DOCTORAATSPROEFSCHRIFT

2010 | Faculteit Wetenschappen

Solid-state NMR relaxometry as a tool to describe and quantify the nanostructured morphology of thin polymer/PCBM films used as photoactive layer in plastic solar cells

Proefschrift voorgelegd tot het behalen van de graad van
Doctor in de Wetenschappen, richting scheikunde, te verdedigen door:

Raoul MENS

Promotor: prof. dr. Peter Adriaensens
Copromotor: prof. dr. Jan Gelan

D/2010/2451/10

universiteit hasselt

Table Of Contents

Aim and Outline

The aim of the research described in this dissertation is to explore the possibilities of alternative and innovative methods to investigate the nanomorphology in organic photovoltaics (OPVs) by solid-state NMR techniques like ^{1}H wide-line NMR, ^{13}C MAS (Magic Angle Spinning) and ^{13}C CP/MAS (Cross Polarization/Magic Angle Spinning). ^{1}H wide-line NMR is fast, but non-chemical selective, so it can only be used for relaxometry. ^{13}C (CP/)MAS experiments, on the other hand, require longer acquisition times but are chemical shift selective, so are appropriate for as well relaxometry as spectroscopy. The use of NMR relaxometry will be evaluated as a quantitative tool to obtain non-invasively bulk information about the nanomorphology of photoactive films. The obtained results will be complemented with more conventional techniques (microscopy, XRD, DSC, …).

The introductory **chapter 1** describes the device characteristics and architectures of actual organic solar cells. Furthermore the process which converts the energy emitted by the sun into electric power is discussed in detail. Finally the parameters that influence the morphology of photoactive layers are listed.

In **chapter 2** a summary about the physical basics of NMR spectroscopy and relaxometry is presented. Extra attention is given to the meaning of the relaxation decay times, the phenomenon of spin diffusion and how to increase the resolution and sensitivity in ^{13}C solid-state spectroscopy.

Chapter 3 focuses on the study of the nanomorphology of photoactive MDMO-PPV/PCBM films casted from toluene solutions. In addition to the blend composition, the influence of two casting techniques (spin-coating versus doctor blading) is reported. As will be demonstrated, the morphology of the MDMO-PPV/PCBM films casted from toluene can be thoroughly described and quantified by the proton wide-line NMR relaxometry technique. The NMR results are complemented by XRD and conventional microscopy (TEM and AFM).

In order to describe and quantify the MDMO-PPV/PCBM chlorobenzene system and other more complex D/A systems properly, the acceptor PCBM is studied in more detail in **chapter 4**. Moreover several procedures were tried out to convert PCBM into the amorphous state. The nanomorphology of differently

treated PCBM samples (acetone-precipitated, thermally quenched from the melt and doctor bladed) was characterized via different relaxation decay time constants obtained by means of several solid-state NMR techniques. The NMR results are complemented by XRD and DSC. Furthermore, the purity of as-received PCBM is discussed.

In more complex D/A systems, i.e. in which phase separation occurs without the formation of large well-defined crystallites, chemical shift selective (but also more time consuming) ^{13}C solid-state NMR techniques are an absolute must, as will be demonstrated for MDMO-PPV/PCBM blends processed from chlorobenzene solutions. The latter system will be discussed in **chapter 5**.

In **chapter 6** the obtained knowledge is used to explain the nanomorphology of thin P3HT/PCBM films casted by doctor blading from chlorobenzene and toluene solutions. Both as-processed and thermally annealed films will be studied. Further a detailed study by means of optical microscopy and TEM is presented in order to confirm these explorative NMR results.

Finally the dissertation is completed with **general conclusion**, a **summary** in English and Dutch, a list of **abbreviations** and the **acknowledgements**.

Chapter One

About Organic Solar Cells

1.1 The challenge of future energy supply

Both the growing awareness of the limited supply of fossil fuels and the observed climatic changes all over the world have triggered great attention for environmentally friendly and inexpensive renewable energy sources in as well the political as scientific community[1]. Nowadays, lots of techniques and sources are explored of which some are already commercialized, while others are still in early stages. Examples are wind turbines, solar energy, hydro-electric power stations, tidal/ocean power, biomass energy and geothermal energy. Among these applications there is an extensive attention for solar energy because the sun is an inexhaustible source: the solar light daily received by the Earth's surface is equivalent to the total amount of energy used by mankind in 16 years at present rates of utilization. Two approaches are possible to harness this carbon-free source of energy. In the case of solar cells, solar energy is converted into an electric current. Another basic concept, especially applicable in areas with dessert climatic conditions, is to focus the sunlight by a series of mirrors and subsequently create steam that can drive turbines. The latter technique offers the supplementary possibility to desalinate water.

At present the on the market dominating solar cells are inorganic in nature, i.e. the active components are inorganic (e.g. silicon p-n junction cells). However, three milestones initiated an extensive study with organic counterparts. Firstly, by the revolutionary discovery of electrical conductivity in polyacetylene (figure 1-1) in 1977 by the teams of Alan J. Heeger, Alan G. MacDiarmid and Hideki Shirakawa[2,3] (Nobel Prize in chemistry, 2000), the new group of semiconducting polymers, i.e. conjugated polymers, was born. The distinguishing feature in comparison with classical polymers (e.g. PVC or polyvinyl chloride) is that the electronic structure of the polymer backbone of conjugated polymers is constituted of alternating single and double bonds (figure 1-1). Each carbon atom of the backbone is in sp^2 hybridization, and the remaining p_z orbital becomes available for

the formation of extended molecular π orbitals. The conducting properties of conjugated polymers after doping are caused by delocalizations in these latter orbitals. In classical saturated polymers on the contrary, all the four valence electrons of the carbon atoms of the backbone are used in the formation of strong covalent σ bonds.

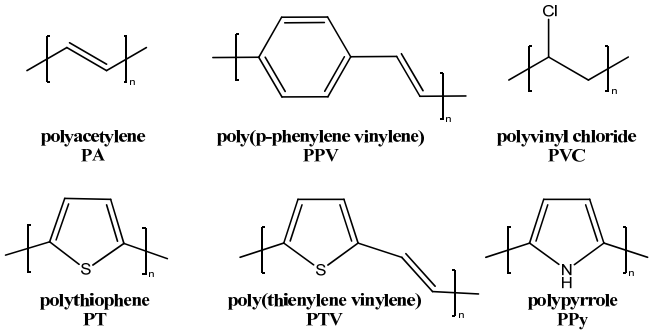

Figure 1-1: *Chemical structure of some conjugated polymers and the not-conjugated polymer polyvinyl chloride.*

A second major step forward was made by Tang[4] at the Eastman Kodak Company in 1986. He introduced organic photovoltaic (OPV) cells in which the active film consists of two layers of organic materials with dissimilar electronic properties. A power conversion efficiency of about 1% (AM2 illumination, 75 mW cm^{-2}) was reported. This significant increase in OPV performance was a consequence of an improved separation of the photogenerated excitons over the created heterojunction.

The third breakthrough was, once again, forced by Heeger *et al*[5-7]. They observed an ultra fast photoinduced electron transfer from the semiconducting polymer MEH-PPV (poly(2-methoxy-5-(2'-ethylhexyloxy)-1,4-phenylene vinylene)) to the semiconducting buckminsterfullerene C_{60} (figure 1-2). The transfer is in the order of a few hundreds of fs, much faster than competing processes like photoluminescence (ps/ns) and back transfer/recombination (μs).

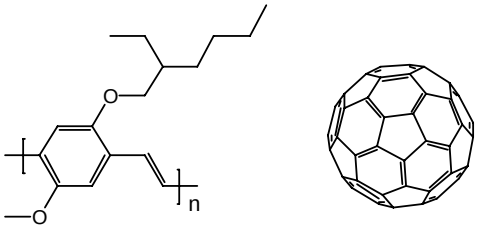

Figure 1-2: *Chemical structure of MEH-PPV (left) and C_{60} (right).*

At present several research groups worldwide combine the benefits of the three mentioned principles (conjugated polymers, heterojunction and ultra fast photoinduced electron transfer) in the so-called bulk heterojunction (BHJ) photovoltaic devices, which consist of a thin film processed from a blend of a strongly light absorbing conjugated semiconducting polymer (electron donor) and a soluble semiconducting fullerene derivative (electron acceptor) deposited onto a transparent substrate by solution processing techniques. This dissertation is accentuating on polymer-based BHJ solar cells. However, it should be noted that a vast variety of possible chemical structures and functionalities of organic materials are available for the construction of organic solar cells: polymers, oligomers, small-sized molecules, dyes, pigments, organo-minerals, dendrimers, liquid crystals, …

Remark that in the last decades conjugated polymers have been the subject of numerous investigations towards their applicability in electro-optical devices, not only hybrid and/or all organic solar cells[8-15], but also others such as polymeric light-emitting diodes (pLEDs)[16-23], organic thin film transistors (oTFTs)[24-29], lasers[30,31] and (bio)sensors[32,33].

1.2 Possible role of organic solar cells

In the next sections, a brief overview of the relevant device characteristics and the occurring energy conversion process[34] is presented. BHJ solar cells are used as a model to describe the energy process, but the general principles apply as well to other types of cells. The aim is not to present an exhaustive study of organic solar cells, the purpose is to outline the state of affairs.

1.2.1 Device characteristics

A lot of terminology about the device characteristics will be encountered throughout this manuscript. The meaning of most of them can be inferred from a current density-voltage curve. Figure 1-3 shows a typical J-V curve for a solar cell under illumination. The active layer of the OPV cell was processed from a MDMO-PPV/PCBM 20/80 wt% solution in chlorobenzene. MDMO-PPV/PCBM is the abbreviation for poly(2-methoxy-5-(3',7'-dimethyloctyloxy)-1,4-phenylene

vinylene)/[6,6]-phenyl-C_{61}-butyric acid methyl ester, of which both the chemical structures are depicted in figure 1-10 and 1-11. Usually only the fourth quadrant of the J-V curve is depicted as it shows the power generation of the device under illumination.

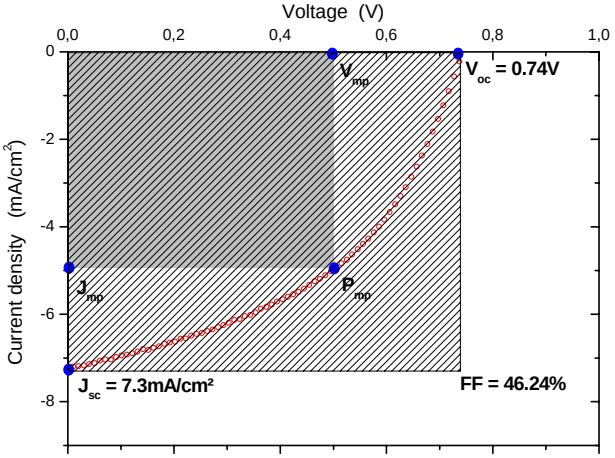

Figure 1-3: *Current density-voltage curve of a MDMO-PPV/PCBM (20/80 wt%) solar cell under illumination. Experimental data are depicted by red circles.*

The intersections of the experimental data curve on the x- and y-axis are the open circuit voltage (V_{OC}) and the short-circuit current density (J_{SC}), respectively. The V_{OC} is the voltage across the solar cell under illumination when no current is flowing. Kim *et al*[35] observed a linear increase of V_{OC} with decreasing HOMO energy level of the donor. However, Ohkita *et al*[36] claimed the existence of a minimum HOMO level for the polymer in order to allow an efficient creation of charge carriers. The above empirical observations, among others, lead to the conclusion that this maximum possible voltage V_{OC} is limited by the energy difference between the HOMO (highest occupied molecular orbital) of the donor and LUMO (lowest unoccupied molecular orbital) of the acceptor comprising the photoactive filmif the electrodes of the device make ohmic contacts with the donor and acceptor materials[37,38]:

$$q.V_{oc} \leq E_{HOMO\text{-}donor} - E_{LUMO\text{-}acceptor}$$

In reality, however, V_{OC} can further be reduced as a consequence of energy level bending close to the electrodes on account of thermal injection of charge carriers from the electrodes into the active layer[37,39].

The I_{SC} is the current that flows when the cell is short-circuited, i.e. when the electrodes are simply connected to each other. This maximum current is correlated to the incident photon to current efficiency (*IPCE)* or external quantum efficiency *(EQE):*

$$I_{SC} = \frac{hc}{q} \int_{\lambda 1}^{\lambda 2} \frac{P_{AM1.5}(\lambda) \cdot EQE(\lambda) \cdot d\lambda}{\lambda}$$

where h is Planck's constant, q is the charge, c is the speed of light in vacuum, λ_1 and λ_2 are the limits of the active spectrum of the solar cell device, EQE (or IPCE) is the amount of absorbed light which is effectively converted into charge carriers and $P_{AM1.5}$ is the power of the sunlight (see also further). Mostly the short-circuit current density (J_{SC}) is presented in curves such as depicted in figure 1-3 in order to remove the dependence of the device area. Nowadays, the J_{SC} in organic solar cells is rather low (e.g. ~ 10 mA cm^{-2} for the P3HT/PCBM 1/1 system *versus* ~ 40 mA cm^{-2} for crystalline silicon) because of (and see also section 1.2.2 for more details):

- not optimized nanomorphology of the photoactive layer which limits exciton dissociation.
- limited spectral absorption window of the organic photovoltaic materials.
- limited optical depth on account of the restricted active layer thickness in order to minimize recombination processes.
- low charge carrier mobilities which increases recombination before charge collection at the electrodes.

The maximum power point (P_{mp}) is the point on the experimental J-V curve, represented by the coordinates V_{mp} and J_{mp}, which corresponds to the maximum possible power. In figure 1-3 this maximum power is depicted by the dark rectangle.

With the said definitions one is now armed to introduce the fill factor (*FF*) and the power conversion efficiency (η_e). Both can be calculated by the following formulas:

$$FF = \frac{J_{mp} \cdot V_{mp}}{J_{SC} \cdot V_{OC}} \qquad \eta_e = \frac{P_{out}}{P_{in}} = \frac{J_{mp} \cdot V_{mp}}{P_{in}} = \frac{J_{SC} \cdot V_{OC} \cdot FF}{P_{in}}$$

The *FF* is the ratio of the actual (defined by P_{mp}) to the theoretical (defined by V_{OC},J_{SC}) maximum power output. In figure 1-3 both maximum powers (experimental and theoretical) are equivalent to the area of the two depicted rectangles. The more the darker rectangle converges to the lighter one, the higher the *FF*. Or stated otherwise, the more oblong the experimental J-V curve, the higher the *FF* and the better the quality of the device. The *FF* particularly depends on the shunt and series resistance of the OPV cell. Ideally, the shunt and series resistance should be high and low, respectively. Next to the morphology of the active layer, the *FF* is mainly influenced by the properties of the electrodes. Poor electrode selectivity leads to shunt losses and so a consequent reduction in *FF* and decrease in photovoltage. Poor conductivity and/or electronic matching of the electrodes, on the other hand, leads to slow charge transfer to the electrodes and so a consequent resistive loss in *FF* and in photocurrent.

The η_e is the most significant parameter. It equals the ratio of output (produced by the cell) to input (originating from the incident sunlight) power. Mostly the value of 100 mW/cm^2 is experimentally taken for P_{in}. To define and compare power conversion efficiencies unambiguously two parameters have to be taken into account, namely the 100 mW/cm^2 corresponding to the spectral integrated power density of the sunlight impinging on the Earth's surface and the incident angle of 48°. The latter is denoted as AM 1.5 (air mass 1.5) and can be calculated according to:

$$AM1.5 = AM\,\frac{1}{\cos 48°}$$

In the example of figure 1-3 η_e evaluates as 2.5 %. Throughout this manuscript, unless stated otherwise, all quoted η_e values are given under standard test conditions of 100 mW/cm^2 simulated AM 1.5 and cell temperature of 25 °C.

1.2.2 Energy conversion process

In this section the basic principles of photovoltaic energy conversion in organic semiconductors will be detailed. The photoactive film in BHJ OPV cells contains two main components. On the one hand, for instance, a conjugated polymer like MDMO-PPV which acts as an electron donor and on the other hand an electron accepter like PCBM or another related functionalized fullerene.

Basically, the energy conversion process consists of four consecutive fundamental steps (figure 1-4). It starts with the absorption of a photon by the conjugated polymer (step 1). Due to this, an electron promotes from the HOMO to the LUMO, creating a strong coulombically bound electron-hole pair on the polymer molecule. This excited state is called a Frenkel exciton and the devices are classified into the category of excitonic solar cells[40,41]. The situation is strikingly different in the case of inorganic, conventional solar cells (e.g. silicon-based p-n junctions). In these devices free charge carriers are generated immediately upon excitation[42,43] as a result of the significant higher dielectric constants for inorganic materials. Fortunately, most conjugated polymers have high absorption coefficients[44], in the order of 10^5 cm^{-1} (generally much higher than for inorganic materials), so efficient absorption in thin films can take place if a reflective back contact metal electrode is used to increase the optical path length of light in the cell. However, the spectral absorption window is rather limited, i.e. most polymers utilize only the blue side of the solar spectrum. Improvements in cell performance can be achieved by designing low band gap (~ 1 eV) polymers, i.e. polymers with an extended spectral absorption window. Note that the spectrum of terrestrial sunlight covers the range of 1 to 4 eV and that only absorption of photons of energy larger than the bandgap between the HOMO and the LUMO leads to the creation of excitons.

In general, after photon absorption, the created singlet exciton can have (depending on its position in the photoactive layer) several fates. It can:

- diffuse to the D/A interface, i.e. the heterojunction (see below, step 2).
- recombine radiatively by emission of a photon or non-radiatively via release of heat.
- convert to a lower-energy and more long-living triplet state.
- dissociate at the D/A interface followed by an electron transfer to the acceptor (step 3), or undergo alternative mechanisms at the D/A interface like RET (resonance energy transfer).
- dissociate via transfer of an electron or hole at one of the electrodes (unwanted processes in solar cells).

Next in the energy conversion process, the exciton has to diffuse to the polymer/fullerene heterojunction, i.e. the D/A interface (step 2). For most organic polymers the diffusion path length is rather limited to about 10 nm[45-48]. Note that excitons are neutral species which means that their motion is not influenced by an electric field, i.e. they diffuse randomly. If the distance of the place of creation to

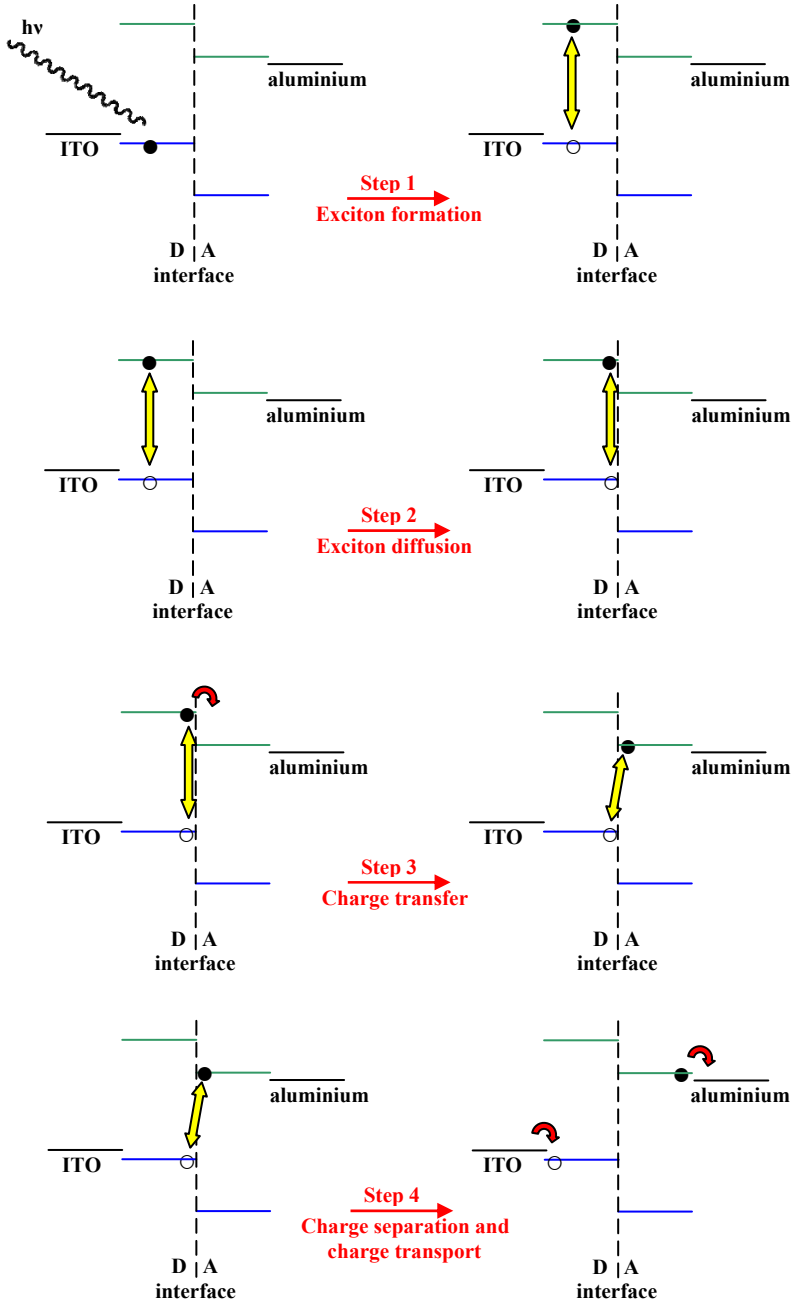

Figure 1-4: *Schematic presentation of the energy conversion process based on fast electron transfer. HOMO and LUMO levels are depicted in blue and green, respectively. Coulombic interactions are represented by yellow arrows, red curled arrows show the direction of electron transfers (holes are presented by ○, electrons by ●).*

the heterojunction exceeds 10 nm, the exciton most likely just recombines by photoluminescence or non-radiative pathways.

If on the other hand the exciton reaches the D/A heterojunction during its lifetime, an ultra fast electron transfer to the fullerene occurs[5-6] (step 3). A prerequisite for this to happen is that the energy differences between the LUMOs of the donor and acceptor exceeds the exciton binding energy. This minimum driving force is estimated to be at least 0.3 eV[49,50], but the actual value in the well performing P3HT/PCBM 1/1 devices is much larger (~ 1 eV). In literature one refers to this as a charge-transfer state with the electron and hole on two different molecules (acceptor and donor molecule, respectively) but still bounded. The existence of this intermediate charge-transfer state has been shown by PIA (photoinduced absorption)[5,51,52] and FTPS (Fourier-transform photocurrent spectroscopy)[53] experiments. Furthermore hole polarons (radical cations) and electron polarons (radical anions), bipolarons and solitons are proposed as additional intermediates[54-56]. These species with longer lifetimes were evidenced by ESR (electron spin resonance) experiments[51]. In the time period between charge transfer and generation of free charge carriers, the geminate polaron pairs can still recombine leading to a loss of photocurrent.

The last step is the generation of free charge carriers (i.e. charge separation) and the charge transport towards collection of the holes at the ITO and the electrons at the aluminium electrode, respectively (step 4; the electrodes are discussed in more detail in section 1.2.3). The driving forces for these transport processes can be provided by two mechanisms, namely field induced drift and diffusion. It is generally assumed that for layers up to ~100 nm in thickness the charge transport is dominated by the former process. The drift is than caused by the electrical field across the active layer induced by the different work functions of the electrodes. It is important at this stage to have ideal, ohmic electrode contacts. Otherwise band bending will have a negative effect. The drift distance of the charge carriers is not solely a function of the electric field, it also depends on the charge carrier mobilities and lifetimes. As the mobilities are relatively low, long charge carrier lifetimes are required. For example, the hole mobility in pure MDMO-PPV[57] equals $5x10^{-11}$ $m^2V^{-1}s^{-1}$ and the electron mobility in pure PCBM[58] equals $2x10^{-7}$ $m^2V^{-1}s^{-1}$. It should be emphasized that the charge carrier mobilities will be different in a BHJ blend and will depend on the blend composition[59] and

nanomorphology. Several studies have suggested that the hole mobility is one of the primary factors limiting the solar cell performance[60,61].

In thicker films, on the other hand, diffusion of charge carriers under the influence of concentration gradients comes into play.

1.2.3 Device architecture

In general, plastic (organic) solar cells have a planar-multilayered architecture[23,62,63]. Figure 1-5 shows a diagram of some standard device configurations. The most relevant components will be described below.

The devices consist of a transparent (e.g. glass or polyethylene terephthalate) substrate with on top an electrode of indium tin oxide (ITO). Increasing the work function of this electrode for hole collection can be achieved by molecular monolayer modifications[64,65] or plasma treatments[66,67].

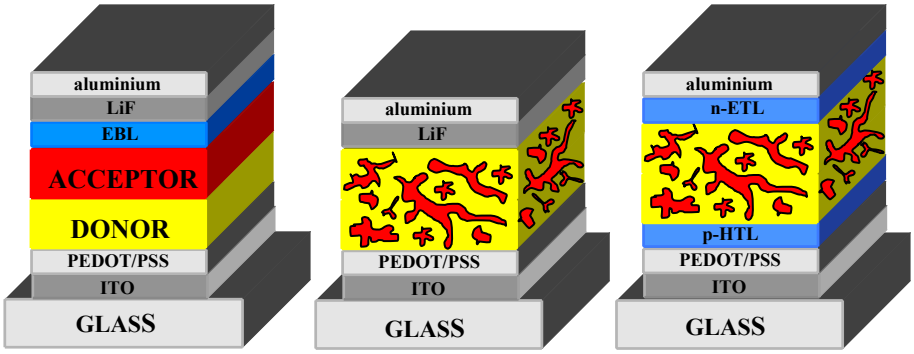

Figure 1-5: *Diagram of the layered structure of different organic solar cell configurations: bilayer (left), BHJ (centre) and pin-BHJ (right) devices. For the sake of clarity thicknesses of the layers are not drawn on scale.*

On this a poly(3,4-ethylenedioxythiophene)/polystyrene sulphonic acid (PEDOT/PSS) film is coated (figure 1-6) as an additional electrode sub-layer. Remark that PEDOT is a conjugated polymer as well. This polythiophene derivative was first synthesised at Bayer AG[68]. PEDOT/PSS behaves like a metal[69,70], improves the surface quality and facilitates the hole extraction[71]. Morphological control by solvent treatment and annealing can enhance its electrical conductivity[72,73].

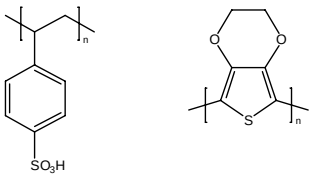

Figure 1-6: *Chemical structure of PPS (left) and PEDOT (right).*

Subsequently the photoactive layer is processed. As the active layer is the principal part of the device it will be further discussed in detail in the next section. Important parameters as constituting materials and layer structure will be examined. In figure 1-5 and 1-9 the components which form the active layer are colored yellow (donor) / red (acceptor).

Finally the cell is completed by evaporating the metallic low-work-function back electrode (e.g. aluminium, silver or gold). However, inserting an ultra thin (~ 0.7 nm) lithium fluoride (LiF) layer between the electrode and the active layer facilitates the electron collection. The exact action of the LiF layer is still under debate but it is observed that it reduces the metal work function[74]. Further, Brabec *et al*[75] reported on the formation of a favorable dipole moment across the junction. An alternative to the LiF layer is the use of a modified ZnO/self-assembled-monolayer/metal electrode with an interfacial dipole directed towards or away from the metal surface[76].

As will be discussed in the next section, the bilayer junction and BHJ are two basic designs for the photoactive layer. In the bilayer structure no work function difference between the ITO and metal electrodes is of absolute necessity for the generation of photocurrent because the asymmetry in the vertical structure already provides a driving force for directed photocurrent[77]. On the contrary, in BHJ cells an electrode work function difference is of utmost importance for device operation since no pronounced vertical compositional gradient is present.

For completeness it should be mentioned that not only single devices are the subject of latest research in order to increase the power conversion efficiency and cell performance; the prospects of multijunction (e.g. tandem) solar cells are explored as well[78-81]. Herein several active layers, which can consist of materials that absorb in different parts of the solar spectrum and so extend the combined spectral absorption window of the photovoltaic cell, are placed as laminates on top of each other.

1.2.4 The photoactive layer

1.2.4.1 Architecture of the photoactive layer

In course of time a number of adaptations regarding the structure of the photoactive layer, with consequent improvement of the power conversion efficiency, were launched. The first generation plastic solar cells were single photoactive layer devices, in which a film of a donor-type organic material was sandwiched between two metal electrodes of different work functions[82]. Merely close in the neighborhood of the electrodes, band bending of the HOMO and LUMO levels takes place, creating an electric field in which excitons can dissociate. This restricted area is referred to as the depletion layer. Such devices are "exciton diffusion limited" because in most organic materials the diffusion path length is below 10 nm and only excitons which can reach the depletion layer, before recombination occurs, can effectively be transformed into charge carriers. So the short exciton diffusion length limits the useful device thickness, and hence the absorbance of the single layer cell.

As already mentioned in section 1.1, a fundamental breakthrough was accomplished by Tang[3]. His bilayer OPV cell acquired a power conversion efficiency of about 1% (75 mW cm^{-2}, AM2). In fact the bilayer architecture was introduced by Tang, but the basics of the occurring working principle, i.e. the ultra fast photo-induced electron transfer from donor to acceptor was demonstrated by Heeger *et al*[5-7]. In a bilayer device an electron-donating material is processed on top of the ITO electrode followed by a second layer of electron-accepting material (figure 1-5-left). Once more, only the excitons that reach the planar heterojunction D/A interface within their lifetime can lead to effective charge carriers. Two important factors contribute to the improved performance in comparison with single layer cells. First the large potential difference at the heterojunction, between donor and acceptor, triggers an efficient charge separation[83]. Secondly, since after the exciton dissociation the holes and electrons travel within different layers, recombination is strongly limited. In current bilayer cells, usually an extra layer is inserted between the acceptor (fullerene) layer and the aluminum electrode[84-86]. This layer is referred to as the exciton blocking layer (EBL, figure 1-5-left). The introduction of the EBL offers some benefits as it provides a reflection barrier for excitons. In order to be efficient the EBL has to be transparent to incident light.

Furthermore EBL materials must be good electron transporters, in other words they should have minimal series resistance. Materials that fulfill these requisites are bathocuproine (BCP) and ruthenium(III)triacetylacetonate ($Ru(acac)_3$) (figure 1-7)[87].

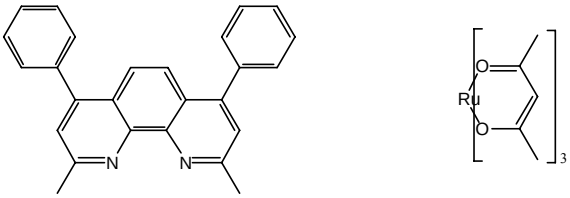

Figure 1-7: *Chemical structure of BCP (left) and $Ru(acac)_3$ (right).*

As a solution for the above described "exciton diffusion limited" devices, the bulk heterojunction (BHJ) concept was introduced[7,88]. Basically the same working principles apply. The main difference is that in BHJ cells the donor and acceptor materials are blended in solution and film casted as a single layer (figure 1-5-centre). In an optimal phase morphology the dimensions of the molecular domains are such that most of the created excitons will reach, within their lifetime, the heterojunction (D/A interface) of which the area is increased enormously in the BHJ concept.

Another possibility is the pin-BHJ configuration in which the photoactive mixed D/A layer is sandwiched between a p-doped hole transport layer (p-HTL) and a n-doped electron transport layer (n-ETL) (figure 1-5-right). The acronym *pin* refers to the coexistence of three layers: the *p*-type (donor), the *i*ntrinsic absorber (mixed donor and acceptor) and the *n*-type (acceptor) layer, respectively. The concept was first introduced by Maennig *et al*[89]. The complete layer sequence in their solar cells was ITO/PEDOT:PPS/HTL/ZnPc:C_{60}(1:2)/ETL/LiF/Al. As HTL p-doped m-MTDATA (4,4',4''-tris(N-3-methylphenyl-N-phenylamino)triphenyl-amine) or p-doped MeO-TPD (N,N,N',N'-tetrakis(4-methoxyphenyl)benzidine) was explored. The materials for the ETL were n-doped Me-PTCDI (N,N'-dimethyl-3,4,9,10-perylenetetracarboxylic diimide) and n-doped C_{60}. The p and n dopants were F4-TCNQ (tetrafluoro-tetracyano-quinodimethane) and rhodamine B chloride, respectively. ZnPc stands for zinc phthalocyanine. The chemical structures of the listed compounds are depicted in figure 1-8. The HTL and ETL are build from wide-bandgap materials. This means that only in the intrinsic

absorber layer (hence the name) excitons can be created. The transport layers behave as semi-permeable membranes. Only one charge carrier species is transmitted, the opposite charge carriers are repelled. In conclusion, the electrons are injected into the conduction band of the ETL, and the holes into the valence band of the HTL. These separated charges can then travel across the respective transport layers towards the electrodes without the risk of recombination. Since the transport layers don't absorb sunlight, also an optical advantage can be utilized. The thickness can be adjusted so that the intrinsic absorption layer is optimally positioned in the layer stack with respect to absorption in the optical interference pattern formed by the reflecting back contact[89].

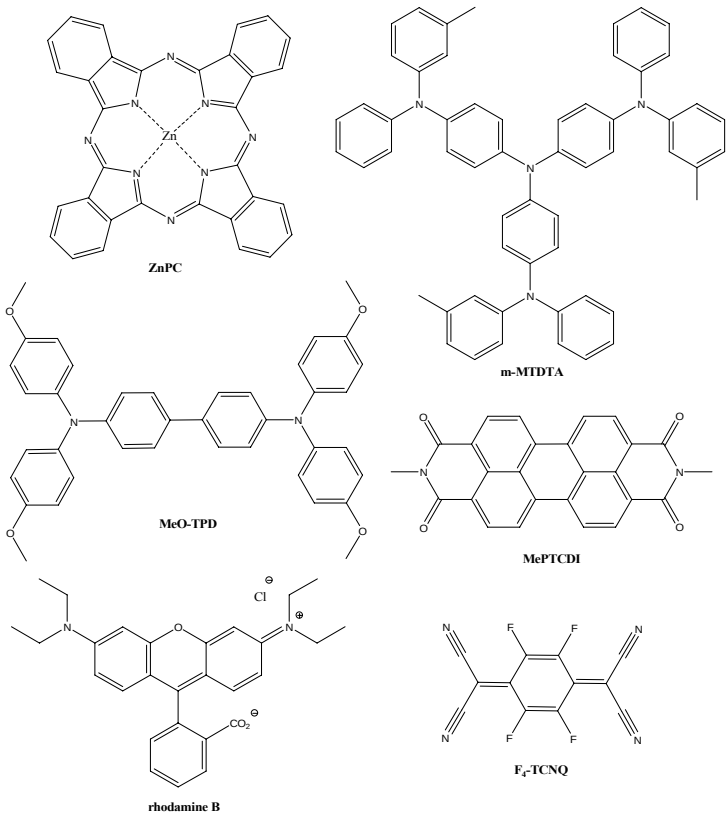

Figure 1-8: *Chemical structure of ZnPc, m-MTDTA, MeO-TPD, MePTCDI, F_4-TCNQ and rhodamine B.*

A last practical configuration is the diffuse bilayer or interdigitated heterojunction[90,91]. Here one attempts to combine the advantages of the bilayer

(spatially separated pathways for opposite charge carriers) and BHJ (maximized donor-acceptor interface) concepts. In these bilayer devices the interface is not planar. The donor and acceptor layers are somewhat diffused into each other. This morphology can be achieved either by pressing together[92] or annealing[93] the from solution processed D/A bilayer films. Alternatively, the acceptor layer can be film casted from a solvent that partially dissolves the donor layer[94].

In an effort to obtain the ideal mixing between the donor and the acceptor, some research groups introduced more exotic and radical approaches in controlling the morphology. Notwithstanding very promising, these applications are still in early stages. In the discotic liquid crystals configuration[95] (figure 1-9-left) the donor and acceptor materials self-align into flat, disc-like configurations which preferentially stack into vertical columns. The vertical stacks offer separated pathways for efficient charge transport, while neighboring columns of donor and acceptor molecules offer an optimal morphology for lateral charge separation.

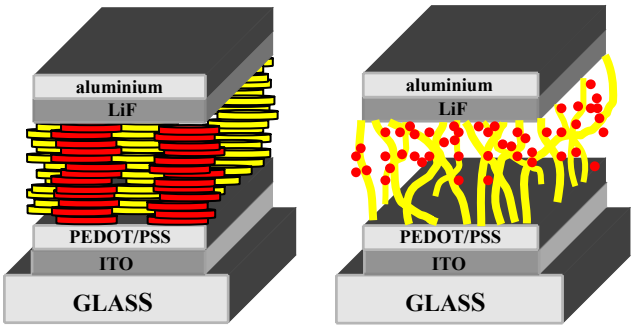

Figure 1-9: *Diagram of the structure of some exotic organic solar cell configurations: discotic liquid crystals (left) and polymer-brush (right) devices.*

In the polymer-brush nanoparticle heterojunction configuration[96] (figure 1-9-right), donor polymers grow vertically using surface-initiated polymerisation techniques. A layer of acceptor nanoparticles (e.g. CdSe) is subsequently deposited on top. In the ideal case, even a vertical composition gradient can be introduced to improve and maximize the photocurrent. Note that for the classical BHJ configuration (figure 1-5-centre) it is not always possible to achieve such vertical composition gradient experimentally, or in general to obtain a desired morphology in which percolated pathways for both donor and acceptor molecules to the right electrodes are present.

1.2.4.2 Constituting materials of the photoactive layer in OPV solar cells

Basically the donor and acceptor organic building blocks can be both small-sized molecules and/or polymers. Small-sized rigid organic molecules have in general a quite high thermal stability and low solubility. This makes them appropriate to be processed by evaporation under high vacuum. On the other hand polymers often decompose at much lower temperatures and evaporation is excluded because of their large molar mass. However, polymers are soluble or can be made soluble by introducing side chains on the backbone. Therefore polymers are mainly processed from solution.

Some examples of popular small-sized acceptor molecules are buckminsterfullerenes like PCBM, NDI (naphthalene diimide), perylene and its derivative PTCDA (3,4,9,10-perylene-tetracarboxylic dianhydride). PCBM is a functionalized fullerene with increased solubility that can be blended with polymers and processed from solution. Small-sized donors are phthalocyanine (figure 1-8) and pentacene. Chemical structures are depicted in figure 1-10.

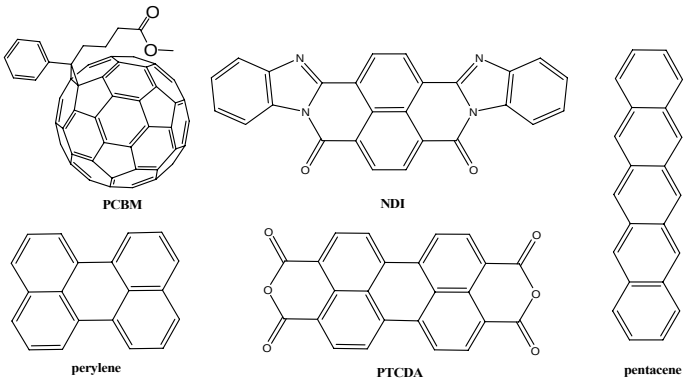

Figure 1-10: *Chemical structure of the acceptors PCBM, NDI, perylene and PTCDA and of the donor pentacene.*

Most of the (co)polymers are build up from the material classes of thiophene, benzene, fluorene and cyclopentadithiophene. Frequently encountered conjugated donor polymers are MDMO-PPV, P3HT, PCPDTBT (poly[2,6-(4,4-bis-(2-ethylhexyl)-4*H*-cyclopenta[2,1-*b*;3,4-*b'*]-dithiophene)-*alt*-4,7-(2,1,3-benzo-thiadiazole)]), PFB (poly[(9,9-dioctylfluorenyl-2,7-diyl)-*alt*-(N,N'-diphenyl-N,N'-di(*p*-butylphenyl)-1,4-diaminobenzene)]), MEH-PPV and PBDTTT (poly(4,8-bis-(2-ethylhexyl)-benzo[1,2-*b*:4,5-*b'*]dithiophene-2,6-diyl-*alt*-4-(2-ethylhexanoyl)-

thieno[3,4-*b*]thiophene-2,6-diyl)). Examples of acceptor polymers, as a substitute for fullerenes, are CN-MEH-PPV (poly(2-methoxy-5-(2'-ethylhexyloxy)-1,4-(1-cyanovinylene)phenylene)), PTPTB (poly-(N-dodecyl-2,5-bis(2'-thienyl)pyrrole-(2,1,3-benzothiadiazole) and PFV (poly(*p*-fluoranthene vinylene)). Chemical structures of the listed polymers are presented in figure 1-11. Fluorene-based (e.g. PFB) OPV cells usual exhibit high V_{OC} (~ 1 V) as a concequence of low-lying HOMO levels. PCPDTBT, made of alternating electron-rich and electron-deficient units, is a very promising member of the novel class of cyclopentadithiophene-based copolymers. It is a low-band gap material (~ 1.45 eV; extended spectral

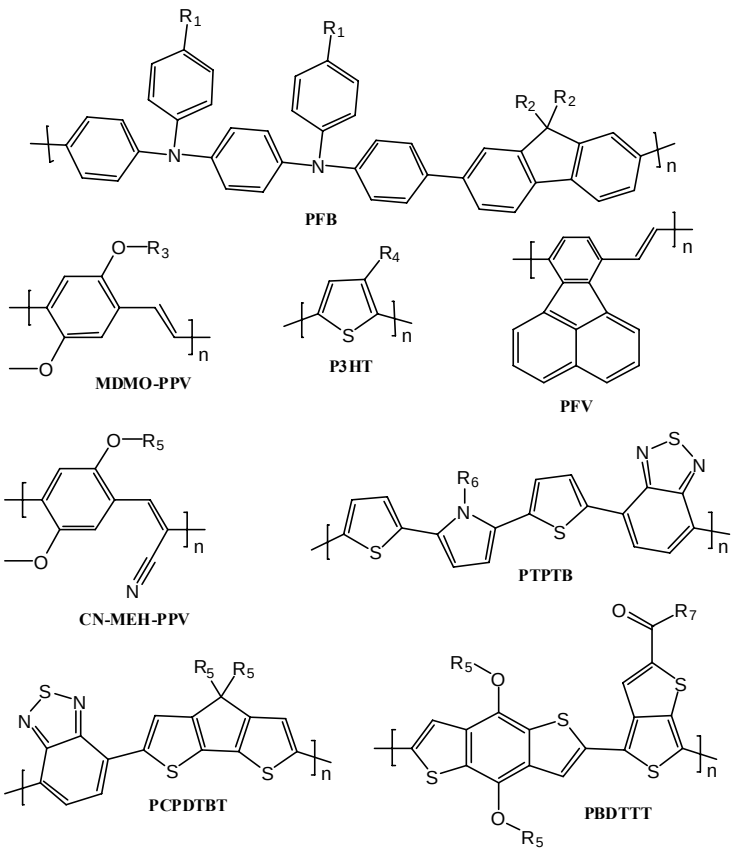

Figure 1-11: *Chemical structure of donor (PFB, MDMO-PPV, PCPDTBT, PBDTTT and P3HT) and acceptor polymers (PFV, CN-MEH-PPV and PTPTB).*

absorption window up to the near infrared region and so increased spectral overlap with the solar radiation spectrum) and shows a high hole mobility ($1.5x10^{-2}$ $cm^2V^{-1}s^{-1}$)[97].

1.2.5 Nanomorphology of the active layer in BHJ solar cells versus η_e

Plastic solar cells bear the potential to compete with their inorganic counterparts in the future. Besides possible economical advantages due to less demanding manufacturing and low production cost, polymer-based materials possess low specific weight and high mechanical film flexibility (figure 1-12), properties that are desired for the production of large-area-applications. Furthermore, it is possible to tune the color of OPV modules which is of particular value both in building design where color is of aesthetic importance, and in dual-function applications as photovoltaic windows where semi-transparency is required.

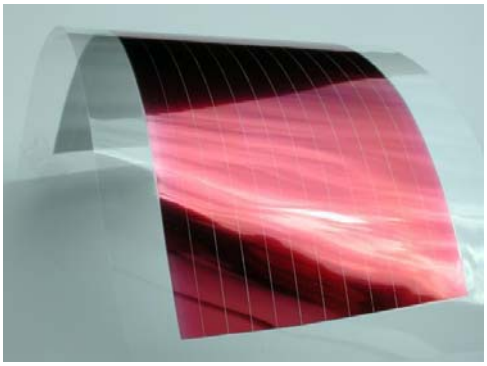

Figure 1-12: *Prototype of a flexible solar cell.*

In any event, the current state-of-the-art maximum power conversion efficiency η_e of about 6 %[98] has to be increased significantly before production and commercialization becomes feasible. Minnaert *et al*[99] described a realistic scenario on the outcome of their effective medium BHJ model based on values which are, with the current state of technology, reached in organic photovoltaics: an absorption window of 200 nm, an external quantum efficiency *EQE* of 70 % and a fill factor *FF* of 60 %. This results in a maximum attainable efficiency of 5.8 % for organic BHJ solar cells, a η_e which is nowadays in fact achieved. In a second

scenario, optimistic values are considered which are credible to be achieved in the future (i.e. an absorption window of 400 nm, an *EQE* of 90 %, and a *FF* of 70 %). According to this optimistic scenario, a power conversion efficiency of 15.2 % could become possible.

At present, research is still done on both bilayer and BHJ devices (next to others as described in section 1.2.4.1). A competition between device architectures is still going on. Currently η_e's of about 5-6 % are reached by both kind of cells (leading devices: metal phthalocyanine/fullerene bilayers *versus* P3HT/PCBM, PCPDTBT/$PC_{70}BM$ and PBDTTT/$PC_{70}BM$ BHJs). As our research group concentrates on BHJ cells, the rest of the manuscript will focus on this configuration.

To optimize BHJ OPV devices one has to act on the complex interplay between the nanomorphology of the photoactive layer and the electronic properties of the comprising organic materials. Comprehensive discussion on the electronic properties (e.g. optimization of the electrodes (ohmic contacts), band gaps and absorption profiles of the organic materials) is outside the scope of this work that focuses on the morphology of the photoactive layer. This nanostructured morphology is determined by the thermodynamics of miscibility of the blend components as well as by the kinetics of the thin film formation. Several, weekly reported scientific publications regarding OPVs with "morphology" as one of the keywords reflect the importance of the nanomorphology of the active components in thin composite films.

In most steps of the energy conversion process (section 1.2.2) the morphology is of paramount importance. The ideal BHJ solar cell nanomorphology is defined as an interpenetrating network of donor and acceptor molecules in combination with an optimized interfacial area and an average domain size in the order of the exciton diffusion length (~ 10 nm)[63,100-103].

The *interpenetrating network* is required to ensure efficient pathways for optimal charge transport (step 4 in the conversion process) as charge recombination has to be avoided as much as possible. It can be visualized as phase separated, percolated network domains which direct the charge carriers efficiently to their respective electrodes. Charge transfer (step 3) and subsequent charge separation can be increased by an *optimized interfacial area*, i.e. an optimal area of the D/A heterojunction. Exciton diffusion (step 2) in organic polymers is limited to a very

short distance. An *average domain size* in the order of the exciton diffusion length can avoid the presence of photovoltaic inactive domains in the active layer.

Two remarks regarding the morphology are here in place. First there seems actually to be a contradiction between the favorable conditions for step 3 and 4 of the working principle. Step 3 requires a fine nanoscale intermixing while for step 4 a certain demixing or phase segregation is advantageous. The optimization of the morphology of the BHJ photoactive layer is indeed of utmost importance with respect to the efficiency of the photovoltaic operation[104,105]. Therefore one has to balance the exciton dissociation and charge transport requirements. This in contrast to the bilayer configuration for which the D and A phases are separated so that after charge transfer the charge carriers can be transferred efficiently to their respective electrodes.

Secondly, and closely related to the η_e's of OPV devices, is the problem of the time ageing process and the chemical stability of the photoactive films. The morphology in BHJ devices, whether or not after optimization, is usually not in a thermodynamically stable state. Coarsening of the nanomorphology is observed with time under working conditions (elevated temperature) which decreases the η_e and operational life time of the BHJ solar cell. The instability as a result of exposure, for example, to oxygen or water vapor can be tackled by the same encapsulation techniques used in the already commercial LEDs. Unfortunately, this requires glass substrates (increase of weight and limitation of flexibility) or expensive multilayer barrier coatings. In the long term solutions can be offered by the design and development of more stable photoactive materials, once the fundamental mechanism and its relationship to chemical structure is well understood. The nanomorphological degradation of polymer/fullerene films, on the other hand, is not yet fully countered. In polymer/PCBM films at elevated temperatures (operational conditions) the PCBM molecules diffuse through the polymer matrix as a consequence of the inherent thermodynamic instability, and start to form crystallites[101,106]. A possible solution, by using high T_g conjugated polymers, is proposed by Bertho *et al*[107]. Post production cross-linking[108,109] of the components to prevent their diffusion is another possibility. Other solutions could be the use of blockcopolymers, compatibilizers and electron acceptor polymers, ...

1.2.6 Parameters that influence the morphology of BHJs

1.2.6.1 Film casting solvent

The morphology and consequently the power conversion efficiency η_e are strongly influenced by the experimental preparation conditions. A first important parameter is the solvent from which the active layer is processed. Already from the pioneering work done by Heeger *et al*[6] it was observed that the performance of BHJ OPV cells was increased by changing the solvent from xylene to 1,2-dichlorobenzene.

It has further been shown by Shaheen *et al*[110] that the photovoltaic performance of devices based on MDMO-PPV/PCBM (20/80 wt%) was strongly dependent on the casting solvent: a decrease in η_e of the solar cells from 2.5 % to 0.9 % was observed in going from chlorobenzene to toluene. This worsening had to arise from changes in the morphology as the absorption spectrum of the film was not affected. The two solvents indeed lead to a significantly different morphology. As compared to chlorobenzene, toluene enhances the phase separation between MDMO-PPV and PCBM. The size of the PCMB rich areas is increased, resulting in a scale of phase separation exceeding the exciton diffusion path length as well as in a reduced interfacial contact area between polymer and PCBM. This was confirmed by Hoppe *et al*[111] who observed a residual PCBM photoluminescence of unquenched photoexcitations at ~735 nm in films processed from toluene. The formation of large PCBM clusters in MDMO-PPV/PCBM (20/80 wt%) films casted from toluene can be considered as a solvent-induced effect attributed to the lower solubility of PCBM in toluene (1 g/100 ml) compared to the solubility in chlorobenzene (4.2 g/100 ml).

Liu *et al*[112] reported upon a second solvent-induced effect on the film morphology. They compared the solvent stabilization effect of MEH-PPV and C_{60} in aromatic (xylene, chlorobenzene and dichlorobenzene) as well as in non-aromatic (tetrahydrofuran and chloroform) solvents. In aromatic solvents the backbone of the polymer is solvated resulting in a polymer packing with better π-π stacking. Non-aromatic solvents preferentially solvate the non-conjugated side-chains of the polymer, resulting in a different polymer packing.

1.2.6.2 Film casting technique

As mentioned before the phase morphology in thin films is not only determined by the thermodynamic miscibility of the blend components. Also the processing solvent and conditions will contribute to the final morphology. Martens *et al*[113] have shown that the solvent evaporation conditions and time dramatically influence the blend morphology. They observed a reduced degree of phase separation if a hot air flow was introduced over the freshly casted film (faster solvent evaporation). Therefore the casting technique used for processing the thin film from solution will determine the morphology as well. Up to date the majority of BHJ solar cells are fabricated by spin-coating[114]. However, since spin-coating is not appropriate for large-area roll-to-roll manufacturing, several other techniques like e.g. doctor blading[115,116], screen printing[117] and inkjet printing[118,119] are under study as well.

1.2.6.3 Donor/acceptor blend ratio

In most D/A systems the morphology further depends strongly on the donor/acceptor blend ratio. As well in MDMO-PPV/PCBM films casted from toluene as from chlorobenzene, 50/50 wt% mixtures give rise to quite homogeneous films on the nanometer scale. In 20/80 wt% films casted from chlorobenzene, on the other hand, phase separated domains up to 100 nm are visible by microscopy. In case of toluene as processing solvent PCBM domains up to 500 nm or more are observed[120]. However, up to date no information is available regarding the quantification of the amount of phase separated and intermixed PCBM.

Remark that the MDMO-PPV/PCBM and the MEH-PPV/PCBM systems obtain the best η_e for a blend ratio of 20/80 wt% processed from chlorobenzene[121,122]. However, this can change dramatically for other donor polymers as e.g. in the P3HT/PCBM system for which the best results are obtained for a PCBM content of 50 wt%[123] or even little less.

Recently, Mayer *et al*[124] reported an interesting theory that predicts the ideal donor/acceptor ratio in polymer/fullerene films. This ideal ratio depends on the possibility of the fullerene to intercalate between the side chains of the

conjugated polymer. The authors proposed the following equation to evaluate the ideal fullerene weight percentage x:

$$x = \frac{100 \cdot n \cdot \zeta + 50}{1 + n \cdot \zeta}$$

where ζ is the molecular weight ratio fullerene/monomer and n is the number of fullerene molecules per monomer in the intercalated phase. However, the appropriate processing conditions still have to be present in order to obtain this intercalated morphology.

1.2.6.4 Film thickness

The thickness of the photoactive layer depends on experimental parameters such as e.g. the spin speed during the spin-coating procedure or the viscosity of the solution from which the thin films are doctor bladed or spin-coated. In general, the thinner the film, the smaller the mean dimensions of phase separated domains[102].

Li *et al*[125] studied the influence of the film thickness on the η_e of P3HT/PCBM 50/50 wt% films spin-coated from 1,2-dichlorobenzene. The film thickness was controlled by changing the spin speeds, and ranged from 35 to 155 nm. In their experimental set-up, the best η_e of 4 % was measured for 63 nm thick films.

1.2.6.5 Post production treatments

Padinger *et al*[126] reported on post production treatments of P3HT/PCBM BHJ OPV devices. The η_e raised from 0.4% to 3.5% after post thermal annealing and applying an external dc voltage. The higher power conversion efficiency η_e of post annealed P3HT/PCBM 50/50 wt% films can be related to improved order/crystallinity in the treated films. At temperatures around 100 °C, especially P3HT crystallizes upon controlled thermal annealing as shown by Zhao *et al*[127]. 2D NMR techniques indicate and confirm a high degree of interaction between the side chains of the polymer and the fullerene cages[128]. Annealing results in the formation of a bi-continuous network with well-developed pathways for charge transport. The formation of large separated PCBM domains is prevented if the annealing temperature is kept below 150°C.

Chirvase *et al*[129] observed a large increase of P3HT light absorption for P3HT/PCBM films after annealing, which was not the case for annealed pristine P3HT or PCBM films. Brown *et al*[130] reported on an improved ordering of P3HT via inter-chain interactions and Ahn *et al*[131] demonstrated that thermal annealing improves the interfacial properties as a result of reduced interfacial defects. All these factors have a favorable effect on the η_e.

Remark that annealing not always has an advantageous effect. Annealing MDMO-PPV/PCBM films at 150°C causes PCBM molecules to evolve in separated domains which strongly reduce the D/A interfacial area. The system is ultimately driven towards complete phase separation between donor and acceptor[132]. The authors sustained these findings by photoluminescence measurements. Initially quenched luminescence of MDMO-PPV is observed again after annealing.

1.2.6.6 Solvent annealing

Slow drying or solvent annealing[133], however strictly speaking not a post production treatment, is closely related to thermal annealing. In this case one tries to prolong the solvent evaporation up to after the film casting. This can result in different morphologies because the constituting molecules have a longer time period to organize (but sometimes also to phase separate) since solvent interactions allow faster molecular motions. For example, this can be achieved by allowing the film to dry for a certain period in a sealed petri dish. Mihailetchi *et al*[134] reported about solvent annealed P3HT/PCBM 50/50 wt% devices casted from dichlorobenzene that reach a respectable η_e of 3.7%. The improved η_e was attributed to the fact that the morphological reorganization increases the hole mobility of the polymer, thereby balancing the transport of the holes and electrons in the composite film.

1.2.6.7 Additives

As an alternative to thermal and solvent annealing, the nanomorphology of the thin film can also be modified and optimized by the use of additives. In that way it is possible to reduce the drying kinetics without removing the device from the spin-coater or without using an enclosed atmosphere during the film formation.

Yao *et al*[135] demonstrated that the D/A components in a P3HT/PCBM photoactive layer can be phase separated into a more optimal morphology if 1,8-octanedithiol (figure 1-13) is added to the solution from which the films are casted.

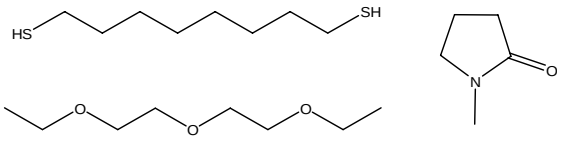

Figure 1-13: *Chemical structure of the additives 1,8-octanedithiol, di(ethylene glycol)-diethyl ether and NMP.*

Other additives (plasticizers) investigated were NMP (N-methyl-2-pyrrolidinone) and di(ethylene glycol)-diethyl ether. Nevertheless, some thermal annealing can still be beneficial to obtain the highest performance.

Recently Chang[136] claimed that simply adding a small amount of P3HT monomer to the processing solution of a P3HT/PCBM blend produces a nanoscaled phase separation and interpenetrating network morphology like this of thermally annealed conventional films. Also similar η_e values were obtained. This should be very feasible and advantageous for large-scale production.

1.3 NMR relaxometry as a tool to describe the morphology

Since the active layer nanomorphology is one of the key points in determining the cell performance, it is important to have dedicated methods to evaluate the state of phase separation in the active layers. While microscopic techniques like Scanning Electron Microscopy (SEM), Atomic Force Microscopy (AFM) and Transmission Electron Microscopy (TEM) are indispensable in this research field[106,111,120,137], solid-state NMR relaxometry is a complementary method to describe and quantify the nanomorphology of polymer/fullerene films. Moreover, this technique allows to describe virtually all polymer/polymer or hybrid systems, independently of microscopic contrast. The latter could become a problem in new systems in which PCBM is replaced by a conjugated acceptor polymer since in such case the donor and acceptor will have similar electron densities.

Solid-state NMR spectroscopy and relaxometry are powerful non-invasive techniques to investigate the segmental chain dynamics and phase morphology of polymer blends on the nanometer scale in the bulk[138-149]. NMR relaxometry can possibly offer new, quantitative insights which might be useful and difficult to obtain by conventional microscopy. Especially if mixed domains co-exist next to phase separated domains, NMR spectroscopy furnishes a unique tool to quantify the distribution of the blend components. However, a relatively large amount of sample (at least 20 mg) is needed to perform the NMR relaxometry measurements since, as compared to optical spectroscopy, NMR spectroscopy is intrinsically a rather unsensitive technique. Therefore the solid-state NMR techniques, certainly ^{13}C NMR, are rather time consuming. The spectrometer time needed for ^{1}H wide-line NMR and ^{13}C relaxometry experiments is typically in the order of a few hours to multiple hours/days, respectively.

An additional advantage of solid-state NMR is that the results are representing the bulk properties, i.e. represent the 3D (dimensional) specimen. Conventional TEM is a 2D superposition technique, in contrast to AFM which provides only information about the surface as it is a SPM (Scanning Probe Microscopy) technique by which the interaction between a tip mounted on a cantilever and the sample under investigation is transduced in topological details of the film. On the other hand, it is nowadays possible to obtain 2D AFM and TEM cross-sections. Recently, 3D tomography TEM is introduced.

As stated before, the inherently thermodynamic instability of the active layers in BHJs can be tackled by post production cross-linking of the components to prevent further diffusion. Changes in dynamics and the degree of cross-linking can be monitored by solid-state NMR.

1.4 References

1. European Commission. Towards a European strategy for the security of energy supply. Green Paper **2000,** 1.
2. Shirakawa, H.; Louis, E.; MacDiarmid, A.; Heeger, A., *Chem. Commun.* **1977**, 578.
3. Heeger, A.J., *Angew. Chem. Int. Ed.* **2001**, 40, 2591.
4. Tang, C.W., *Appl. Phys. Lett.* **1986**, 48, 183.
5. Sariciftci, N.S.; Smilowitz, L.; Heeger, A.J., Wudl, F., *Science* **1992**, 258, 1474.
6. Yu, G.; Heeger, A.J., *J. Appl. Phys.* **1995**, 78, 4510.

7. Yu, G.; Gao, J.; Hummelen, J.C.; Wudl, F.; Heeger, A.J., *Science* **1995**, 270, 1789.
8. Coakley, K.M.; McGehee, M.D., *Chem. Mat.* **2004**, 16, 4533.
9. Brabec, C.J.; Sariciftci, N.S.; Hummelen J.C., *Adv. Funct. Mater.* **2001**, 11, 15.
10. Dennler, G.; Sariciftci, N.S., *Proc. IEEE* **2005**, 93, 1429.
11. Meissner, D., *Photon* **1999**, 2, 34.
12. Yang, C.Y.; Heeger, A.J., *Synth. Met.* **1996**, 83, 85.
13. Hoppe, H.; Sariciftci, N.S., *J. Mater. Chem.* **2006**, 16, 45.
14. Issaris, A.; Vanderzande, D.; Gelan, J., *Polymer* **1997**, 38, 2571.
15. Munters, T.; Martens, T.; Goris, L.; Vrindts, V.; Manca, J.; Lutsen, L.; De Ceuninck, W.; Vanderzande, D.; De Schepper, L.; Gelan, J.; Sariciftci, N.S.; Brabec, C.J., *Thin Solid Films* **2002**, 403-404, 247.
16. Bradley, D.D.C., *Synth. Met.***1993**, 54, 401.
17. Burroughes, J.H.; Bradley, D.D.C.; Brown A.R.; Marks, R.N.; Mackay, K.; Friend, R.H.; Burns, P.L.; Holmes, A.B., *Nature* **1990,** 347, 539.
18. Braun, D.; Heeger, A.J., *Appl. Phys. Lett.* **1991**, 58, 1982.
19. Yu, G., *Synth. Met.* **1996**, 80, 143.
20. Song, S.; Jang, M.S.; Shim, H.; Hwang, D.; Zyung, T., *Macromolecules* **1999**, 32, 1482.
21. Geffroy, B.; Le Roy, P.; Prat, C., *Polym. Int.* **2006**, 55, 572.
22. Müllen, K., *Organic Light Emitting Devices: Synthesis, Properties and Applications* **2006**.
23. Perepichka, I.F.; Perepichka, D.F.; Meng, H.; Wudl, F., *Adv. Mat.* **2005**, 17, 2281.
24. Dimitrakopoulos, C.D.; Malenfant, R.L., *Adv. Mat.* **2002**, 14, 99.
25. Burroughes, J.H.; Jones, C.A.; Friend, R.H., *Nature* **1988**, 335, 137.
26. McCullough, R.D., *Adv. Mater.* **1998**, 10, 93.
27. Newman, C.R.; Frisbie, C.D.; da Silva, D.A.; Bredas, J.L.; Ewbank, P.C.; Mann, K.R, *Chem. Mat.* **2004**, 16, 4436.
28. Horowitz, G., *Adv. Mater.* **1998**, 10, 365.
29. Chen, T.A.; Wu, X.; Rieke, R.D., *J. Am. Chem. Soc.* **1995**, 117, 233.
30. McGehee, M.D.; Heeger, A.J., *Adv. Mat.* **2000**, 12, 1655.
31. Hide, F.; DiazGarcia, M.A.; Schwartz, B.J.; Andersson, M.R.; Pei, Q.B.; Heeger, A.J., *Science* **1996**, 273, 1833.
32. Heeger, P.S.; Heeger, A.J., *Proc. Natl. Acad. Sci. U. S. A.* **1999**, 96, 12219.
33. Gerard, M.; Chaubey, A.; Malhotra, B.D.; *Biosensors & Bioelectronics* **2002**, 17, 345.
34. Koeppe, R.; Sariciftci, *Photochem. Photobiol. Sci.* **2006**, 5, 1122.
35. Kim, H.; Jin, S.H.; Suh, H.; Lee, K., *Proc. SPIE – Int .Soc. Opt. Eng.* **2004**, 5215, 111.
36. Ohkita, H.; Cook, S.; Astuti, Y.; Duffy, W.; Heeney, M.; Tierney, S.; McCulloch, I.; Bradley, D.D.C.; Durrant, J.R., *Chem. Commun.* **2006**, 3939.
37. Brabec, C.J.; Cravino, A.; Meissner, D.; Sariciftci, N.S.; Fromherz, T.; Rispens, M.T.; Sanchez, L.; Hummelen, J.C., *Adv. Funct. Mater.* **2001**, 11, 374.
38. Scharber, M.C.; Mühlbacher, D.; Koppe, M.; Denk, P.; Waldauf, C.; Heeger, A.J.; Brabec, C.J., *Adv. Mater.* **2006**, 18, 789.
39. Mihailetchi, V.D.; Koster, L.J.A.; Blom, P.W.M., *Appl. Phys. Lett.* **2004**, 85, 970.
40. Gregg, B.A., *J. Phys. Chem. B* **2003**, 107, 4688.

41. Pope, M.; Swenberg, C.E., *Electronic Processes in Organic Crystals and Polymers* **1999**, Oxford University Press, Oxford.
42. Gledhill, S.E.; Scott, B.; Gregg, B.A., *J. Mater. Res.* **2005**, 20, 3167.
43. Bube, R.H., *Photoelectronic Properties of Semiconductors* **1992**, Cambridge University Press, Cambridge.
44. Hoppe, H.; Arnold, N.; Meissner, D.; Sariciftci, N.S., *Sol. Energy Mater. Sol. Cells* **2003**, 80, 105.
45. Halls, J.J.M.; Pichler, K.; Friend, R.H.; Moratti, S.C.; Holmes, A.B., *Appl. Phys. Lett.* **1996**, 68, 3120.
46. Savenije, T.J.; Warman, J.M.; Goossens, A., *Chem. Phys. Lett.* **1998**, 287, 148.
47. Stübinger, T.; Brütting, W., *J. Appl. Phys.* **2001**, 90, 3632.
48. Markov, D.E.; Tanase, C.; Blom, P.W.M.; Wildeman, J., *Phys. Rev. B* **2005**, 72, 045217.
49. Halls, J.J.M.; Cornil, J.; dos Santos, D.A.; Silbey, R.; Hwang, D-H.; Holmes, A.B.; Bredas, J.L.; Friend, R.H., *Phys. Rev. B* **1999**, 60, 5721.
50. Bredas, J.L.; Beljonne, D.; Coropceanu, V.; Cornil, J., *Chem. Rev.* **2004**, 104, 4971.
51. Janssen, R.A.J.; Hummelen, J.C.; Lee, K.; Pakbaz, K.; Sariciftci, N.S.; Heeger, A.J.; Wudl, F., *J. Chem. Phys.* **1995**, 103, 788.
52. Hwang, I-W.; Soci, C.; Moses, D.; Zhu, Z.; Waller, D.; Gaudiana, R.; Brabec, J.C.; Heeger, A.J., *Adv. Mater.* **2007**, 19, 2307.
53. Vandewal, K.; Tvingstedt, K.; Gadisa, A.; Inganäs, O.; Manca, J.V., *Nature Materials* **2009**, 8, 904.
54. Morteani, A.C.; Sreearunothai, P.; Herz, L.M.; Phillips, R.T.; Friend, R.H.; Silva, C., *Phys. Rev. Lett.* **2004**, 92, 247240.
55. Koster, L.J.A.; Smiths, E.C.P.; Mihailetchi, V.D.; Blom, P.W.M., *Phys. Rev. B* **2005**, 72, 085205.
56. Mihailetchi, V.D.; Koster, L.J.A.; Hummelen, J.C.; Blom, P.W.M., *Phys. Rev. Lett.* **2004**, 93, 216601.
57. Blom, P.W.M.; de Jong, M.J.M.; van Munster, M.G., *Phys. Rev. B* **1997**, 55, R656.
58. Mihailetchi, V.D.; van Duren, J.K.J.; Blom, P.W.M.; Hummelen, J.C.; Janssen, R.A.J.; Kroon, J.M.; Rispens, M.T.; Verhees, W.J.H.; Wienk, M.M, *Adv. Funct. Mater.* **2003**, 13, 43.
59. Mihailetchi, V.D.; Koster, L.J.A.; Blom, P.W.M.; Melzer, C.; de Boer, B.; van Duren, J.K.J.; Janssen, R.A.J., *Adv. Funct. Mater.* **2005**, 15, 795.
60. Riedel, I.; Dyakonov, V., *Phys. Status Solidi A* **2004**, 201, 1332.
61. Choulis, S.A.; Nelson, J.; Kim, Y.; Poplavskyy, D.; Kreouzis, T.; Durrant, J.R.; Bradley, D.D.C., *Appl. Phys. Lett.* **2003**, 83, 3812.
62. Hoppe, H.; Sariciftci, N.S., *J. Mater. Res.* **2004**, 19, 1924.
63. Günes, S.; Neugebauer, H.; Sariciftci, N.S., *Chem. Rev.* **2007**, 107, 1324.
64. Ganzorig, C.; Fujihira, M., *Organic Optoelectronic Materials, Processing and Devices* **2002**, edited by S.C. Moss, 83.
65. Sarangerel, K.; Ganzorig, C.; Fujihira, M.; Sakomura, M.; Ueda, K., *Chem. Lett.* **2008**, 37, 778.
66. Sugiyama, K.; Ishii, H.; Ouchi, Y.; Seki, K., *J. Appl. Phys.* **2000**, 87, 295.

67. Wu, C.C.; Wu, C.I.; Sturm, J.C.; Kahn, A., *Appl. Phys. Lett.* **1997**, 70, 1348.
68. Jonas, F.; Heywang, G.; Schmidtberg, W., EP0339340, **1989**.
69. Kugler, T.; Salaneck, W.R.; Rost, H.; Holmes, A.B., *Chem. Phys. Lett.* **1999**, 310, 391.
70. Greczynski, G.; Kugler, T.; Salaneck, W.R., *J. Appl. Phys.* **2000**, 88, 7187.
71. Zhang, F.L.; Johansson, M., Andersson, M.R.; Hummelen, J.C.; Inganas, O., *Adv. Mater.* **2002**, 14, 662.
72. Jönssona, S.K.M.; Birgerson, J.; Crispin, X.; Greczynski, G.; Osikowicz, W.; van der Gonc, A.W.D.; Salaneck, W.R.; Fahlman, M., *Synth. Met.* **2003**, 139, 1.
73. Kim, J.Y.; Jung, J.H.; Lee, D.E.; Joo, J., *Synth. Met.* **2002**, 126, 311.
74. Jong, D.; Friedlein, M.P.; Osikowicz, R.W.; Salaneck, W.R.; Fahlman, M., *Mol. Cryst. Liq. Cryst.* **2006**, 455, 193.
75. Brabec, C.J.; Shaheen, S.E.; Winder, C.; Sariciftci, N.S.; Denk, P., *Appl. Phys. Lett.* **2002**, 80, 1288.
76. Yip, H.; Hau, S.K.; Baek, N.S.; Ma, H.; Jen, A.K., *Adv. Mater.* **2008**, 20, 2376.
77. Ramsdale, C.M.; Barker, J.A.; Arias, A.C.; Mac Kenzie, J.D.; Friend, R.H.; Greenham, N.C., *J. Appl. Phys.* **2002**, 92, 4266.
78. Gilot, J.; Wienk, M.M.; Janssen, R.A., *Appl. Phys. Lett.* **2007**, 90, 143512.
79. Hagemann, O.; Bjerring, M.; Nielsen, N.C.; Krebs, F.C., *Sol. Energy Mater. Sol. Cells* **2008**, 92, 1327.
80. Hadipour, A.; de Boer, B.; Wildeman, J.; Kooistra, F.B.; Hummelen, J.C.; Turbiez, M.G.R.; Wienk, M.M.; Janssen, R.A.J.; Blom, P.W.M., *Adv. Funct. Mater.* **2006**, 16, 1897.
81. Ameri, T.; Dennler, G.; Lungenschmied, C.; Brabec, C.J., *Energy & Environmental Science* **2009**, 2, 347.
82. Weinberger, B.R.; Akhtar, M.; Gau, S.C., *Synth. Met.* **1982**, 4, 187.
83. Rostalski, J.; Meissner, D., *Sol. Energy Mater. Sol. Cells* **2000**, 63, 37.
84. Peumans, P.; Bulovic, V.; Forrest, S.R., *Appl. Phys. Lett.* **2000**, 76, 2650.
85. Peumans, P.; Yakimov, A.; Forrest, S.R., *J. Appl. Phys.* **2003**, 93, 3693.
86. Rand, B.P.; Burk, D.P.; Forrest, *Phys. Rev. B* **2007**, 75, 115327.
87. Rand, B.P.; Li, J.; Xue, J.; Holmes, R.J.; Thompson, M.E.; Forrest, S.R., *Adv. Mater.* **2005**, 17, 2714.
88. Halls, J.J.M.; Walsh, C.A.; Greenham, N.C.; Marseglia, E.A.; Friend, R.H.; Moratti, S.C.; Holmes, A.B., *Nature* **1995**, 376, 498.
89. Maennig, B.; Drechsel, J.; Gebeyehu, D.; Simon, P.; Kozlowski, F.; Werner, A.; Li, F.; Grundmann, S.; Sonntag, S.; Koch, M.; Leo, K.; Pfeiffer, M.; Hoppe, H.; Meissner, D.; Sariciftci, N.S.; Riedel, I.; Dyakonov, V.; Parisi, J., *Appl. Phys. A* **2004**, 79, 1.
90. Yang, F.; Shtein, M.; Forrest, S.R., *Nat. Mater.* **2005**, 4, 37.
91. Xue, J.; Rand, B.P.; Uchida, S.; Forrest, S.R., *Adv. Mater.* **2005**, 17, 66.
92. Granström, M.; Petritsch, K.; Arias, A.C.; Lux, A.; Andersson, M.R.; Friend, R.H., *Nature* **1998**, 395, 257.
93. Drees, M.; Premaratne, K.; Graupner, W.; Heflin, J.R.; Davis, R.M.; Marciu, D.; Miller, M., *Appl. Phys. Lett.* **2002**, 81.
94. Brabec, C.J.; Cravino, A.; Meissner, D.; Sariciftci, N.S.; Rispens, M.T.; Sanchez, L.; Hummelen, J.C.; Fromherz, T., *Thin Solid Films* **2002**, 403-404, 368.

95. Schmidt-Mende, L.; Fechtenkotter, A.; Mullen, K.; Moons, E.; Friend, R.H.; MacKenzie, J.D., *Science* **2001**, 293, 1119.
96. Snaith, H.J.; Whiting, G.L.; Sun, B.Q.; Greenham, N.C.; Huck, W.T.S.; Friend, R.H., *Nano Lett.* **2005**, 5, 1653.
97. Morana, M.; Wegscheider, M.; Bonanni, A.; Kopidakis, N.; Shaheen, S.; Scharber, M.; Zhu, Z.; Waller, D.; Gaudiana, R.; Brabec, C, *Adv. Funct. Mater.* **2008**, 18, 1757.
98. Chen, H-Y.; Hou, J.; Zhang, S.; Liang, Y.; Yang, G.; Yang. Y.; Yu, L.; Wu, Y.; Li, G., *Nature Photonics* **2009**, 3, 649.
99. Minnaert, B.; Burgelman, M. *Prog. Photovolt: Res. Appl.* **2007**, 15, 741.
100. Kim, K.; Liu, J.; Namboothiry, M.; Carroll, D.L. *Appl. Phys. Lett.* **2007**, 90, 163511.
101. Hoppe, H.; Glatzel, T.; Niggemann, M.; Schwinger, W.; Schaeffler, F.; Hinsch, A.; Lux-Steiner, M.C., Sariciftci, N.S. *Thin Solid Films* **2006,** 511-512**,** 587.
102. Hoppe, H.; Sariciftci, N.S. *J. Mater. Chem.* **2006**, 16, 45.
103. Thompson, B.C.; Fréchet, J.M.J., *Angew. Chem. Int. Ed.* **2008**, 47, 58.
104. Kim, J.S., Ho, P.K.H.; Murphy, C.E.; Friend, R.H.; *Macromolecules* **2004**, 37, 2861.
105. Moons, E., *J. Phys. Condens. Matter.* **2002**, 14, 12235.
106. Yang, X.; Van Duren, J.K.J.; Janssen, R.A.J.; Michels, M.A.J.; Loos, J., *Macromolecules* **2004**, 37, 2151.
107. Bertho, S.; Janssen, G.; Cleij, T.J.; Conings, B.; Moons, W.; Gadisa, A.; D'Haen, J., Goovaerts, E.; Lutsen, L.; Manca, J.; Vanderzande, D., *Sol. Energy Mater. Sol. Cells* **2008**, 92, 753.
108. Drees, M.; Hoppe, H.; Winder, C.; Neugebauer, H.; Sariciftci, N.S.; Schwinger, W.; Schäffler, F.; Topf, C.; Scharber, M.C.; Zhu, Z.; Gaudiana, R., *J. Mater. Chem.* **2005**, 15, 5158.
109. Miyanishi, S.; Tajima, K.; Hashimoto, K., *Macromolecules* **2009**, 42, 1610.
110. Shaheen, S.E.; Brabec, C.J.; Sariciftci, N.S.; Padinger, F.; Fromherz, T.; Hummelen, J.C., *Appl. Phys. Lett*. **2001**, 78, 841.
111. Hoppe, H.; Niggemann, M.; Winder, C.; Kraut, J.; Hiesgen, R.; Hinsch, A.; Meissner, D.; Sariciftci, N.S., *Adv. Funct. Mater.* **2004**, *14*, 1005.
112. Liu, J.; Shi, Y.; Yang, Y., *Adv. Funct. Mater.* **2001**, *11*, 420.
113. Martens, T.; D'Haen, J.; Munters, T.; Beelen, Z.; Goris, L.; Manca, J.; D'Olieslaeger, M.; Vanderzande, D.; De Schepper, L.; Andriessen, R. *Proc. SPIE-Int. Soc. Opt. Eng.* **2003**, *4801*, 40.
114. Swinnen, A.; Haeldermans, I.; vande Ven, M.; D'Haen, J.; Vanhoyland, G.; Aresu, S.; D'Olieslaeger, M.; Manca, J., *Adv. Funct. Mater.* **2006**, 16, 760.
115. Mens, R.; Adriaensens, P.; Lutsen, L.; Swinnen, A.; Bertho, S.; Ruttens, B.; D'Haen, J.; Manca, J.; Cleij, T.; Vanderzande, D.; Gelan, J., *J. Polym. Sci. Pol. Chem.* **2008**, 46, 138.
116. Padinger, F.; Brabec, C.J.; Fromherz, T.; Hummelen, J.C.; Sariciftci, N.S., *Opto-Electron. Rev.* **2000**, 8, 280.
117. Shaheen, S.E.; Radspinner, R.; Peyghambarian, N.; Jabbour, G.E., *Appl. Phys. Lett*. **2001**, 79, 2996.
118. Hoth, C.N.; Choulis, S.A.; Schilinsky, P.; Brabec, C.J., *Adv. Funct. Mater.* **2007**, 19, 3973.

119. Sirringhaus, H.; Kawase, T.; Friend, R.H.; Shimoda, T.; Inbasekaran, M.; Wu, W.; Woo, E.P., *Science* **2000**, 290, 2123.
120. Martens, T.; D'Haen, J.; Munters, T.; Beelen, Z.; Goris, L.; Manca, J.; D'Olieslaeger, M.; Vanderzande, D.; De Schepper, L.; Andriessen, R., *Synth. Met.* **2003**, *138*, 243.
121. Scharber, M.C.; Schultz, N.A.; Sariciftci, N.S.; Brabec, C.J., *Phys. Rev. B* **2003**, 67, 085202-1.
122. van Duren, J.K.J.; Yang, X.; Loos, J.; Bulle-Lieuwma, C.W.T.; Sieval, A.B.; Hummelen, J.C.; Janssen, R.A.J., *Adv. Funct. Mat.* **2004**, 14, 425.
123. Li, G.; Shrotriya, V.; Huang, J.; Yao, Y.; Moriarty, T.; Emery, K.; Yang, Y., *Nat. Mater.* **2005**, 4, 864.
124. Mayer, A.C.; Toney, M.F.; Scully, S.R.; Rivnay, J.; Brabec, C.J.; Scharber, M.; Koppe, M.; Heeney, M.; McCulloch, I.; McGehee, M.D., *Adv. Funct. Mater.* **2009**, 19, 1173.
125. Li, G.; Shrotriya, V.; Yao, Y.; Yang, Y., *J. Appl. Phys.* **2005**, 98, 043704.
126. Padinger, F.; Rittberger, R.S.; Sariciftci, N.S., *Adv. Funct. Mater.* **2003**, 13, 1.
127. Zhao, Y.; Yuan, G.; Roche, P.; Leclerc, M., *Polymer* **1995**, 36, 2211.
128. Yang, C.; Hu, J.G.; Heeger, A.J., *J. Am. Chem. Soc.* **2006**, 128, 12007.
129. Chirvase, D.; Parisi, J.; Hummelen, J.C.; Dyakonov, V., *Nanotechnology* **2004**, 15, 1317.
130. Brown, P.J.; Thomas, D.S.; Köhler, A.; Wilson, J.; Kim, J.S.; Ramsdale, C.; Sirringhaus, H.; Friend, R.H., *Phys. Rev. B* **2003**, 67, 064203.
131. Ahn, T.; Sein-HoHa, H.L., *Appl. Phys. Lett.* **2002**, *80*, 392
132. Hoppe, H.; Drees, M.; Schwinger, W.; Schäffler, F.; Sariciftci, N.S., *Synth. Met.* **2005**, *152*, 117.
133. Li, G.; Shrotriya, V.; Huang, J.; Yao, Y.; Moriarty, T.; Emery, K.; Yang, Y., *Nat. Mater.* **2005**, 4, 864.
134. Mihailetchi, V.D.; Xie, H.; de Boer, B.; Popescu, L.M., Koster, L.J.A., *Appl. Phys. Lett.* **2006**, *89*, 012107.
135. Yao, Y.; Hou, J.; Xu, Z.; Li, G.; Yang, Y., *Adv. Funct. Mater.* **2008**, 18, 1783.
136. Chang, Y.M.; Wang, L., *J. Phys. Chem. C* **2008**, 112, 17716.
137. Yang, X.; van Duren, J.K.J.; Rispens, M.T.; Hummelen, J.C.; Janssen, R.A.J.; Michels, M.A.J.; Loos, J., *Adv. Mater.* **2004**, 16, 802.
138. Komoroski, R.A., *High Resolution NMR spectroscopy of Synthetic Polymers in Bulk* **1986**, VCH: Florida.
139. Schmidt-Rohr, K.; Spiess, H.W., *Multidimensional solid-state NMR and polymers* **1996**, Academic Press, 402.
140. Adriaensens, P.; Roex, H.; Vanderzande, D.; Gelan, J., *Polymer* **2005**, *46*, 1759.
141. Adriaensens, P.; Dams, R.; Lutsen, L.; Vanderzande, D.; Gelan, J., *Polymer* **2004**, *45*, 4499.
142. Lequieu, W.; Van de Velde, P.; Du Prez, F.E.; Adriaensens, P.; Storme, L.; Gelan, J., *Polymer* **2004**, *45*, 7943.
143. Adriaensens, P.; Rego, R.; Carleer, R.; Ottenbourgs, B.; Gelan, J., *Polymer International* **2003**, 52, 1647.
144. Orza, R.A.; Magusin, P.C.M.M.; Litvinov, V.M.; Van Duin, M.; Michels, M.A.J. *Macromolecules* **2007**, 40, 8999.
145. Collar, E.P.; García-Martínez, J.M.; Garrido, L., *J. Appl. Polym. Sci.* **2008**, 107, 2656.

146. Gandhi, S.; Melian, C.; Demco, D.E.; Brar, A.S.; Blümich, B., *Macromol. Chem. Phys.*, **2008**, 209, 1576.
147. Hedesiu, C.; Demco, D.E.; Kleppinger, R.; Vanden Poel, G.; Gijsbers, W.; Blümich, B.; Remerie, K.; Litvinov., *Macromolecules*, **2007**, 40, 3977.
148. Akbey, U.; Granados-Focil, S.; Coughlin, E.B.; Graf, R.; Spiess, H.W., *J. Phys. Chem. B* **2009**, 113, 9151.
149. Wei, Y.; Graf, R.; Sworen, J.C.; Cheng, C-Y.; Bowers, C.R.; Wagener, K.B.; Spiess, H.W., *Angew. Chem. Int. Ed.,* **2009**, 48, 4617.

Chapter Two

The Physical Basis of NMR Spectroscopy and Relaxometry

2.1 The NMR signal

This section will first explain how a NMR signal is obtained. The succinct description is primarily based on the vector model. Nuclei with an odd number of protons and/or neutrons contain an intrinsic spin angular momentum, mathematically described by the spin quantum number I. Consequently a nuclear spin magnetic moment $\vec{\mu}$ is associated with this angular momentum, i.e. the nucleus generates a small magnetic field. If a molecule containing NMR active nuclei (i.e. with spin quantum number $I \neq 0$) is brought into the external magnetic field B_0 of a NMR spectrometer, the magnetic moments $\vec{\mu}$ associated with the nuclei start to precess around this magnetic field B_0. The magnetic field normally has a vertical direction (determined by spectrometer design) and is defined according to the z-axis in a reference laboratory frame. The precession frequency is called the Larmor frequency ω_0. For example, in nowadays spectrometers generating magnetic field strengths B_0 of 5-20 Tesla, the Larmor frequency for protons is several hundreds of MHz. The Larmor frequency is proportional to the external field B_0:

$$\vec{\omega}_0 = -\gamma \vec{B}_0$$

The proportionality constant γ is called the gyromagnetic ratio and is nucleus specific (e.g. 26.7519×10^7 rad T^{-1} s^{-1} for protons and 6.7283×10^7 rad T^{-1} s^{-1} for carbon-13). It can be shown that the Larmor frequency vector is negative for nuclei with a positive gyromagnetic ratio γ (hence the negative sign in the above equation). In the rest of the discussion a positive γ is always assumed and only the magnitude of $\vec{\omega}_0$ is considered:

$$\omega_0 = \gamma B_0$$

At first glance the spatial distribution of the magnetic moments $\vec{\mu}$ is isotropic and the precession cone can take all angles with respect to the magnetic field B_0. But this would mean that nuclear magnetism is unobservable. However, as a consequence of the random thermal motion of molecules, the individual direction of the magnetic moment $\vec{\mu}$ associated with a particular spin is not static in nature. In the long run the magnetic moment $\vec{\mu}$ of a nucleus can take all directions. But in the presence of an external field B_0 not all directions are equal in energy. Like in the case of a compass needle, the potential energy of the interaction between the magnetic moment $\vec{\mu}$ and the external magnetic field B_0 is minimal if the direction of $\vec{\mu}$ is parallel to the external field B_0. Thus the above described wandering motion of the magnetic moments $\vec{\mu}$ is not completely isotropic. The nuclear spin system evolves towards an anisotropic equilibrium state in which there are more magnetic moments aligned with B_0 as compared to the amount in other directions, resulting at thermal equilibrium into a net macroscopic magnetic moment along B_0. This bulk magnetization of the sample, in the +z direction at equilibrium, can be represented by a macroscopic magnetization vector $\vec{M}_0$. The magnitude of $\vec{M}_0$ depends on the number of spins, their gyromagnetic ratio γ and the magnitude of the external field B_0. The *vector model* is concerned with what happens to this magnetization vector $\vec{M}_0$ during the NMR experiment.

In order to acquire an NMR signal, the macroscopic magnetization vector $\vec{M}_0$ has to be tilted away from the z-axis. The tilting of $\vec{M}_0$ is achieved by feeding a radiofrequency (RF) pulse $2B_1$ to a coil (wound around the sample), which is e.g. orientated along the x-axis. An oscillating current through the coil creates a linearly oscillating magnetic field $2B_1$. This $2B_1$ field of frequency ω_{RF} can be decomposed in two counter-rotating fields B_1^- and B_1^+ both rotating at frequency ω_{RF}. It turns out that only B_1^+, which is rotating in the same sense to the Larmor precession, will interact with the magnetization $\vec{M}_0$. Therefore B_1^- will be ignored and in the next B_1^+ will simply be denoted as B_1. Remark that the applied, rather low frequencies in NMR spectroscopy belong to the radiofrequency (RF) part of the electromagnetic spectrum (TV broadcasts, mobile phones, baby intercom, radio, …). Notice also that in NMR, distinct from other kinds of spectroscopy, it is the magnetic component of electromagnetic radiation that interacts with matter.

For the sake of ease a rotating reference frame (x',y',z'), on top of the laboratory frame (x,y,z), is introduced in order to facilitate the description of the complex motion in space of $\vec{M}_0$ under the influence of the magnetic fields B_0 and

B_1. This x',y',z (=z') frame rotates, by definition, around the z-axis. The rotating field B_1 appears to be stationary in the rotating frame if the rotation frequency of the latter equals ω_{RF}. Moving to the rotating frame removes the time dependency of the field B_1, i.e. it can be considered as a static field.

But how are the magnetic field B_0 and the Larmor frequency ω_0 affected by viewing things in the rotating frame? Suppose that ω_{RF} is close to ω_0. The apparent frequency of the precession in the rotating frame will be ω_0-ω_{RF} (in the order of Hz to kHz). This difference frequency is referred to as the offset frequency Ω_0. In general, a magnetic moment executes a precessional motion around a static magnetic field B_0 defined by:

$$\omega_0 = \gamma B_0 \quad \text{or} \quad B_0 = \frac{\omega_0}{\gamma}$$

Following this line of argument, the apparent magnetic field ΔB in the rotating frame, in which the precessional frequency appears to be Ω_0, is given by:

$$\Delta B = \frac{\Omega_0}{\gamma} \quad \text{or} \quad \Delta B = \frac{(\omega_0 - \omega_{RF})}{\gamma}$$

ΔB is called the reduced field in the rotating frame. In conclusion, the apparent magnetic field ΔB along the z-axis (in the rotating frame) is much weaker than the applied external field B_0. As the reduced field ΔB becomes comparable with the B_1 field, i.e. if the "resonance condition" $\omega_0 \approx \omega_{RF}$ is met, the latter influences the motion of $\vec{M}_0$ even though it is much weaker in magnitude than B_0. In the rotating frame, $\vec{M}_0$ precesses around an effective field B_{eff}, which is the vector addition of ΔB (along the z-axis) and B_1 (along the x'-axis). The magnitude of B_{eff} is given by:

$$B_{eff} = \sqrt{B_1^2 + \Delta B^2}$$

If the offset Ω_0 is small, the effective field B_{eff} will lie close to the x'-axis (figure 2-1-centre). As a consequence B_{eff} will exert a torque on $\vec{M}_0$ by which the magnetization vector will rotate away from the z-axis to the y'-axis. As mentioned before, the offset Ω_0, and so the reduced field ΔB, is small if the frequency of the RF field B_1 is close to the Larmor frequency ($\omega_0 \approx \omega_{RF}$). In the limit that the offset Ω_0 is zero ($\omega_0 = \omega_{RF}$), ΔB disappears and the B_1 field is the only one left in the rotating frame (figure 2-1-left). In that situation, $\vec{M}_0$ simply rotates in the y'z-plane and one refers to it as an on-resonance pulse. The angle θ through which $\vec{M}_0$ is tipped away from the z-axis is called the pulse angle θ:

$$\theta = \gamma B_1 \tau_p$$

were τ_p is the duration of the pulse B_1. Applying a $90°_{x'}$ pulse ($\theta = 90°$) brings $\vec{M}_0$ to the y'-axis, as is demonstrated in figure 2-2.

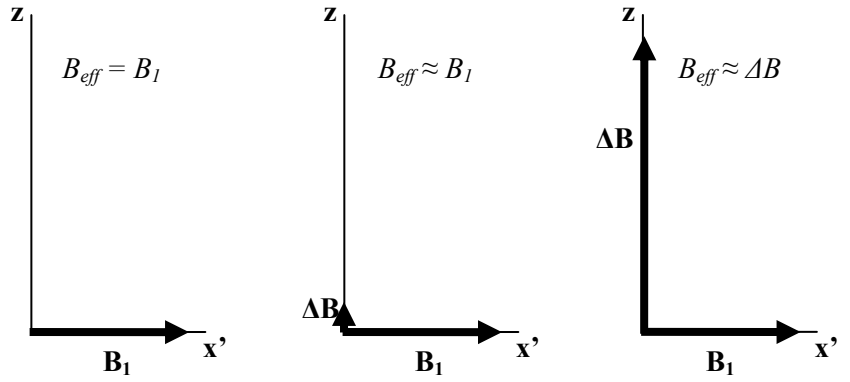

Figure 2-1: *The x'z-plane in the rotating frame. Some possible cases of the reduced field ΔB in relation to the RF pulse B_1: ΔB=0 (left), ΔB is small (centre) and ΔB is large (right). B_{eff}, the effective field around which M_0 precesses, is the vector addition of ΔB and B_1.*

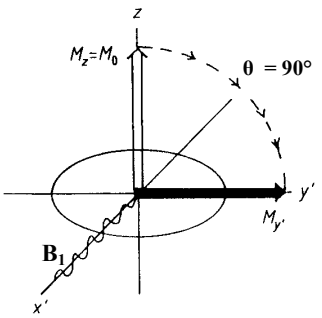

Figure 2-2: *The position of $\vec{M}_0$ after applying a $90°_{x'}$ pulse.*

In the other extreme case, i.e. if the reduced field ΔB becomes much larger than B_1, B_{eff} will lie very close to the z-axis (figure 2-1-right) and will have no effect on $\vec{M}_0$. For example, a hard pulse B_1 applied to ^{13}C spins will have no effect on ^1H spins, as the offset Ω_0 for the latter is in the order of hundreds of MHz. Under these circumstances, it is even impossible to draw ΔB on scale in figure 2-1.

After the B_1 pulse, the magnetization vector $\vec{M}_0$ behaves in the same way as the individual magnetic moments $\vec{\mu}$, i.e. it starts to precess around the external magnetic field B_0. This precessing magnetization vector $\vec{M}_0$, at frequency Ω_0 in

the rotating frame, can subsequently be recorded by a detector positioned in the x'y'-plane in which it induces an oscillating current. This current is amplified and gives a transient time domain signal S(t), referred to as the free induction decay (FID).

On account of the precessing motion of $\vec{M}_0$ in the x'y'-plane, the FID can be considered as a complex function S(t) in which the real and imaginary part correspond to the x' and y' component of $\vec{M}_0$, respectively:

$$S(t) = S_0 \exp(i\Omega_0 t/2\pi)$$

However, as the system is not at equilibrium anymore, S(t) will decay over time. Relaxation processes will drive the spins back to the Boltzmann equilibrium state in which the orientation of $\vec{M}_0$ is again parallel to B_0 (see also section 2.4). If one assumes an exponential decay, as is the case in the liquid state, the FID can be presented as:

$$S(t) = S_0 \exp(i\Omega_0 t/2\pi)\exp(-\lambda t)$$

in which λ is the rate constant for the decay.

After digitization, the complex FID is subjected to a Fourier transformation. The resulting frequency domain signal $S(\Omega)$ is referred to as a Lorentzian function L and is complex as well:

$$S(\Omega) = S_0 L(\Omega;\Omega_0,\lambda)$$

$$L(\Omega;\Omega_0,\lambda) = \frac{1}{\lambda + i(\Omega - \Omega_0)}$$

In the notation $L(\Omega;\Omega_0,\lambda)$ the argument is the frequency coordinate Ω, while λ is the peakwidth parameter and Ω_0 the centre frequency of the peak (L is maximal if $\Omega = \Omega_0$). Recall that Ω_0 is the offset frequency of the oscillating time domain signal (FID) in the rotating frame. The coefficient S_0 is related to the amount of nuclear spins that is represented by the Lorentzian signal. Figure 2-3-left depicts a Lorentzian signal. The peak-width-at-half-height can be obtained from the Lorentzian for the value 1/2 λ^{-1} (solution: $\Omega=\Omega_0\pm\lambda$) and is thus given by 2λ (hence called the peakwidth parameter) in units of rad s^{-1}.
In units of Hz it equals:

$$\Delta\nu_{1/2} = \frac{\lambda}{\pi} \qquad \text{or} \qquad \Delta\nu_{1/2} = \frac{1}{\pi T_2}$$

The inverse of the peakwidth parameter λ is called the relaxation time constant T_2 (see also section 2.4). Recall that λ is also the rate constant for the decay of the FID. One can conclude that the larger the rate constant λ, i.e. the shorter T_2 and the faster the FID decays, the broader the corresponding peak in the frequency spectrum, and vice versa.

In the description above, a Lorentzian signal is considered. This particular lineshape results from an exponential decay of the FID. Such a function is appropriate in liquid-state NMR, but in the case of solid-state NMR the situation is often more complex. In solid-state NMR, the decay of the FID has to be described by other functions, e.g. a Gauss function resulting in a Gaussian lineshape. The main cause can be found in the very strong dipolar interactions between the magnetic moments. The Fourier transformation (FT) of a Gaussian time domain signal results in a Gaussian frequency domain signal S(Ω) (see figure 2-3-right):

$$S(t) = S_0 \exp(-t^2/4\sigma^2) \xrightarrow{\text{FT}} S(\Omega) = S_0' \exp(-\Omega^2/4(1/2\sigma)^2)$$

Here σ is the peakwidth parameter and the widths of the time and frequency domain signals are again in inverse relation to each other.

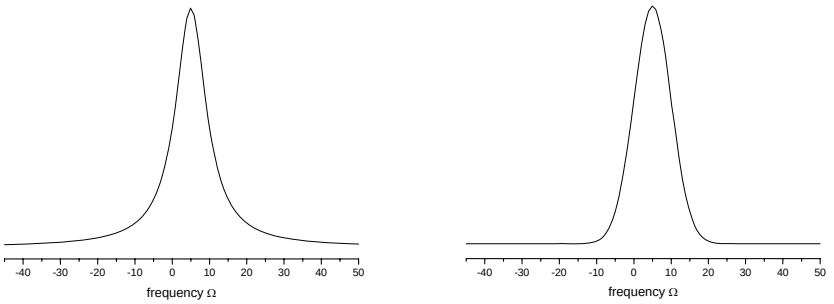

Figure 2-3: *Depiction of a Lorentzian (left) and Gauss (right) signal, both centered around 5 Hz.*

2.2 Signal broadening in solid-state NMR

In solid-state NMR spectra the observed signals are inextricably much broader compared to these obtained in liquid-state NMR as the peak-width-at-half-height $\Delta\nu_{1/2}$ and the relaxation time constant T_2 are inversely proportional quantities, and the latter is inherently very short for solids (see also section 2.4) due to very

strong homonuclear or heteronuclear dipole-dipole interactions and the chemical shift anisotropy (CSA). The resulting broadening can be much larger than the complete spectral range what would make solid-state spectra useless. Both interactions, dipolar coupling and CSA, will be discussed in this section and the differences between liquid-state and solid-state NMR will be pointed out.

2.2.1 Dipolar coupling

As mentioned in section 2.1 magnetic moments start to precess around the external magnetic field B_0 at the Larmor frequency ω_0. However, a particular nucleus under consideration experiences not solely B_0 but also the local fields induced by other nuclei in the vicinity. The magnitude of these local fields depends on the distance and angle between the observed nucleus I and the dipolar coupled spin S. On that account, the local field B_{loc} experienced by the spin is spatially dependent. B_{loc} can be evaluated by:

$$B_{loc} \propto \pm \frac{\gamma_I \gamma_S (3\cos^2 \theta - 1)}{r^3}$$

Here γ_I and γ_S are the gyromagnetic ratios of the spins under consideration and the neighboring spins, respectively, r is the internuclear distance and θ is the angle between the vector joining the spins with respect to B_0 (see figure 2-4).

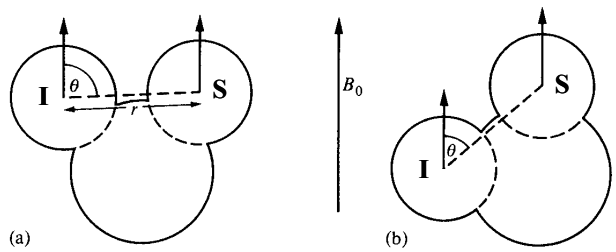

Figure 2-4: *Depiction of two orientations of the spins I and S with different angle θ.*

As a result each spin I is affected in a different way (i.e. it feels not only B_0 but also B_{loc}) and consequently precesses at a slightly different resonance frequency ω_i:

$$\omega_i = \gamma B_{0i}$$

This through space phenomenon is called the dipole-dipole interaction or dipolar coupling[1,2]. In conclusion the dipolar coupling arises from interactions between the

nuclear magnetic moments $\vec{\mu}$ of neighboring spins. For protons the major contribution to this interaction arises from neighboring proton spins as a consequence of the high natural abundance (99.98%) and the large gyromagnetic ratio (26.7519 10^7 rad T^{-1} s^{-1}). On the other hand, ^{13}C spins observed at natural abundance (1.108%) are mainly dipolarly coupled to the nearby ^1H spins as the interaction falls off rather quickly as $1/r^3$ (effective dipolar coupling is only present if r < 10 Å).

Note that for small molecules in solution the dipole-dipole interactions average out to zero due to fast Brownian motions. The reorientation time of fast tumbling molecules in solution is much faster than the time needed for the dipolar coupling to evolve. In the case of solid-state NMR however, it actually gives rise to a strong line broadening in the spectrum. A solution for solid-state ^{13}C spectroscopy can be furnished by high power ^1H-decoupling (see section 2.3.1).

2.2.2 Chemical shift anisotropy

Section 2.1 described how a NMR signal is obtained. Hereto isolated nuclei were considered. In a real sample, however, nuclei are under the influence of both neighboring nuclei (as discussed above in section 2.2.1) and neighboring electronic environments. The contribution of the latter on the resonance frequency of a particular nucleus under observation can be divided into an isotropic and anisotropic component.

When a sample is placed in the external field B_0 of a spectrometer, the latter induces a circulation of the spherically symmetric electrons (e.g. s-electrons) present in the molecules. This circulation of electrons in turn produces a small local magnetic field at the nucleus which opposes the external field B_0. One refers to this phenomenon as "diamagnetic isotropy", i.e. shielding of the nucleus by its surrounding electrons. The higher the electron density around the nuclei, the more shielded it is. This means that nuclei with different electronic environments precess at their specific resonance frequency ω_i:

$$\omega_i = \gamma B_{0i} = \gamma(B_0 - \sigma_i B_0) = \gamma(1 - \sigma_i)B_0$$

where σ_i is the shielding constant of nucleus i; the shielding is a function of the strength of B_0 as can be noticed in the above formula.

However, local fields created by anisotropic electron motions in surrounding groups are also involved. In this case the effective magnetic field experienced by a particular spin, and consequently its specific resonance frequency ω_i, is altered depending on the spatial orientation of the surrounding groups with respect to the B_0 field. The chemical shift Hamiltonian is given by the equation:

$$H_{CS} = \gamma B_0 I_Z \left[\delta_{ISO} + 1/2\delta_{CSA}\left(3\cos^2\theta - 1\right)\right]$$

where δ_{iso} is the isotropic chemical shift. The CSA is a function of the strength of the external field B_0, i.e. the stronger the latter the broader the NMR signals in the frequency spectrum.

In liquid-state NMR, the CSA is averaged out to its isotropic value δ_{iso} as for randomly and rapidly tumbling molecules in solution even strongly asymmetric electron distributions (physical origin of the CSA) will appear spherical if viewed on the NMR timescale. However, the diamagnetic isotropy as well as anisotropy ensure the chemical shift dispersity in (liquid-state) NMR spectra. In addition, chemical shift anisotropy[3,4] is the second major interaction that causes strong line broadening in solid-state spectra. A solution for ^{13}C spectra can be furnished by fast spinning of the sample along the so-called "magic angle" (see section 2.3.2).

2.3 Resolution and sensitivity enhancement in solid-state ^{13}C spectra

Fortunately, experimental techniques are available to obtain much higher resolution in ^{13}C spectra than expected on the basis of broadening by the dipolar coupling and CSA.

2.3.1 High-power proton dipolar decoupling

As stated above the ^{1}H-^{13}C heteronuclear coupling is the dominant dipolar interaction experienced by ^{13}C nuclei. The effect of this interaction can be eliminated by continuously saturating the proton spins by high power continuous-wave (CW) irradiation at the ^{1}H Larmor frequency[5,6]. The technique is referred to as high-power proton dipolar decoupling (DD).

2.3.2 Magic-angle spinning

As the CSA is a result of interactions between spins and local fields induced by anisotropic motions of electrons in neighboring groups, it can not be removed by decoupling (like the dipole-dipole interaction). However, the answer to the problem can be deduced from the chemical shift Hamiltonian equation (see H_{CS} in section 2.2.2). The angular dependency can be eliminated if θ equals 54.74°, resulting in isotropic values δ_{iso} for the chemical shift. In practice this is done by rapidly spinning the sample around an axis which is inclined at 54.74° with respect to the static field B_0. The technique is known as magic-angle spinning (MAS)[7-9]. MAS can be regarded as a dynamic implementation of cubic symmetry that cancels out the anisotropic term[10]. Incomplete averaging at slow spinning speeds results in spinning sidebands appearing at frequency distances of integer multiples of the spinning speed. They can largely be reduced by spinning faster than the width of the CSA pattern. Remark that MAS also partially removes the dipolar interactions (cf. the $(3\cos^2\theta-1)$ factor).

2.3.3 Cross-polarization

Last but not least the frequently used solid-state NMR technique called cross polarization (CP) is introduced[3,4,11]. Its purpose is to increase the sensitivity of low natural abundance and/or low γ nuclei such as ^{13}C or ^{15}N. It involves the transfer of magnetization, known as cross polarization, from sensitive nuclei (protons) to less sensitive nuclei (^{13}C or ^{15}N). In addition, one can benefit from the shorter relaxation decay time T_1 (see section 2.4) of the protons. This allows to cut down the preparation delay time d1, and so the total acquisition time.

Figure 2-5 depicts the pulse sequence diagram used for the CP experiment. The first step is to apply a $90°_{x'}$ pulse of strength $B_{1H,x'}$ in the proton channel which rotates the proton magnetization $M_0^{^1H}$ along the y'-axis. The phase of this B_{1H}-field is then instantaneously 90° shifted so that $B_{1H,y'}$ now lies along the y'-axis collinear with the proton spin magnetization $M_0^{^1H}$. The magnetization is said to be spin-locked by $B_{1H,y'}$ (it will undergo no precession in the rotating frame; $B_{1H,y'}$ is maintained for the duration of the spin-lock period). At this point the RF spin-lock field in the ^{13}C channel, $B_{1C,y''}$, is switched on, and its amplitude is adjusted so that the Hartmann-Hahn[12] condition is fulfilled:

$$\omega_{1H} = \omega_{1C} \qquad \text{or} \qquad \gamma_H B_{1H,y'} = \gamma_C B_{1C,y''}$$

This condition implies that in their respective rotating frames the M_0^{1H} and M_0^{13C} magnetizations vectors precess at equal rates, allowing a rapid transfer of magnetization. In figure 2-5 the magnitude of M_0^{1H} and M_0^{13C} are depicted in blue. As can be noticed in figure 2-5, the magnitude of M_0^{1H} decreases as a consequence of relaxation. This process is called spin-lattice relaxation in the rotating frame or $T_{1\rho H}$ relaxation (see also section 2.4). The magnitude of M_0^{13C} first grows due to the CP, and eventually tracks the proton signal. After the spin-lock period, the ^{13}C FID is acquired under broad band (BB) decoupling of the protons.

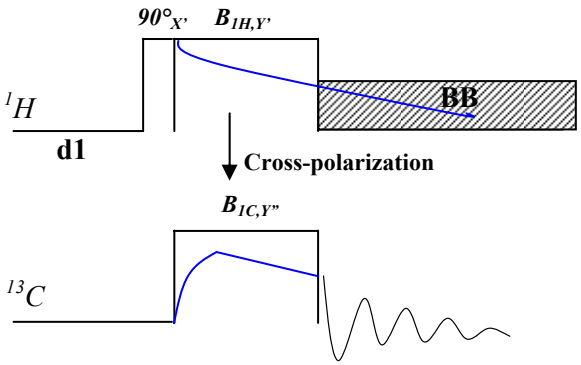

Figure 2-5: *Pulse sequence of the CP experiment.*

Note that the rotation frequencies are determined by the gyromagnetic ratios γ and the amplitudes of the applied RF B_1-fields. The maximum magnetization enhancement is given by γ_{1H}/γ_{13C}. The increase in M_0^{13C} during the CP period depends on the strength of the ^1H-^{13}C dipolar coupling (section 2.2). Directly proton-bonded ^{13}C spins are polarized more rapidly than unprotonated carbon spins. In conclusion, CP is based on matching the frequencies between the two spin systems.

Nowadays, to acquire solid-state ^{13}C spectra with high sensitivity and resolution, all listed techniques (DD, MAS, CP and T_{1H} dependency) mentioned in this section 2.3 are combined in the so-called CP/MAS/DD experiment. In general CP/MAS can be applied to all broadband nuclei. However, for ^1H solid-state NMR the above mentioned combined technique is not applicable. Nonetheless ^1H solid-state NMR also can offer important information regarding molecular dynamics and

miscibility. Hereto the proton wide-line solid-state NMR techniques were developed.

2.3.4 Sample tuning to ensure the sensitivity

One important practical/technical operation concerning the acquisition of NMR signals is the tuning process. The NMR radiofrequency circuit consists of a tuning capacitor (of capacity C (Farad)) wired in parallel with the transmitter/detection coil (of inductance L (Henry)) enclosing the sample. The function of the capacitor is enhancing the currents in the coil by electromagnetic resonance. Indeed, such parallel circuit comprises an electromagnetic oscillator of which the frequency (in rad s^{-1}) is given by:

$$\omega_{osc} = \frac{1}{\sqrt{LC}}$$

Energy in the circuit is stored alternately as an electric and magnetic field. If a RF pulse of frequency ω_{ref} arrives at the parallel circuit, it sets up oscillations in the properly tuned circuit, i.e. in case of $\omega_{RF} \approx \omega_{osc}$ the oscillations build up. The phenomenon is similar to a child's swing[13]: by giving the swing small pushes at instants matching the natural resonant frequency, a large amplitude motion is built up. Mechanical and electrical energy is accumulated in the swing and the tuned circuit, respectively. The reciprocal phenomenon takes place if a NMR signal is detected. The capacitor and coil act together to accumulate the energy of the weak NMR signal. Certainly in the case of ^{13}C experiments tuning is of utmost importance because of the low natural abundance and consequently intrinsic very low sensitivity. Tuning is done by manual adjustment of the capacitor and has to be repeated every time the sample is changed as the electrical properties of the circuit are affected by the nature of the sample.

2.4 Relaxation

After the macroscopic magnetization vector $\vec{M}_0$ is tilted away from the z-axis towards the y'-axis by a RF pulse, relaxation processes will drive the magnetization $\vec{M}_0$ back to its equilibrium state. The rate at which this occurs is

rationalized by the spin-lattice or longitudinal relaxation decay time constant T_1. Spin-lattice relaxation is accompanied by a change in energy, since the energy absorbed from the RF pulse must be given up again to the surrounding (the lattice). The (thermally induced) molecular motions of magnetic dipoles and groups in which anisotropic electron motions occur (e.g. aromatic rings) create fluctuating magnetic fields in the surrounding of the nucleus under observation. If these local fluctuating magnetic fields B_{loc} have components, perpendicular to B_0 and at the Larmor frequency ω_0 of the observed nucleus, the latter will undergo T_1 relaxation. Remark that according to Fourier mathematics a random fluctuating signal can be decomposed in oscillations (cosine and sine waves) of different frequencies and amplitudes (see figure 2-6).

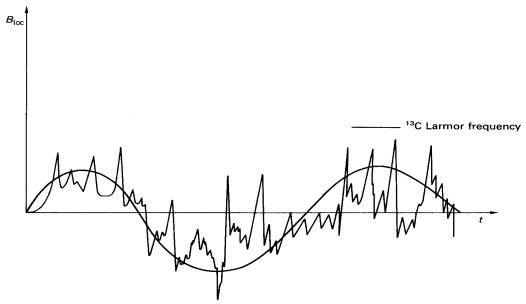

Figure 2-6: *Decomposition of a random fluctuating field in a sine wave.*

The question arises which physical sources can provide the appropriate frequencies. Well, a particular molecule will experience three kinds of motions: vibrations, translations and rotations. However, the frequencies corresponding to vibrations, in the range 10^{11} to 10^{13} Hz, are much higher than the nowadays maximum achievable proton Larmor frequency of around 1000 MHz (determined by the maximum spectrometer external field B_0). No well-defined oscillation frequencies can be associated with translations. In conclusion, only rotations will result in the modulation of local fields generated by mainly the dipole-dipole coupling and the CSA. Therefore chiefly such frequency motions can be a source of T_1 relaxation. The higher the spectral density of the appropriate frequency ω_0 the shorter the relaxation time constant T_1.

Another type of relaxation mechanism is the spin-spin or transverse relaxation characterized by the T_2 decay time constant. A 90° RF pulse $B_{1x'}$

perpendicular to B_0 not only will tilt the macroscopic magnetization vector $\vec{M}_0$ into the x'y'-plane. It also brings the individual magnetic moments $\vec{\mu}$ partly in phase. The rate by which this phase-coherence is lost, i.e. the rate by which the magnetic moments $\vec{\mu}$ fan out in the x'y'-plane (see figure 2-7) is quantified by the spin-spin relaxation decay time constant T_2.

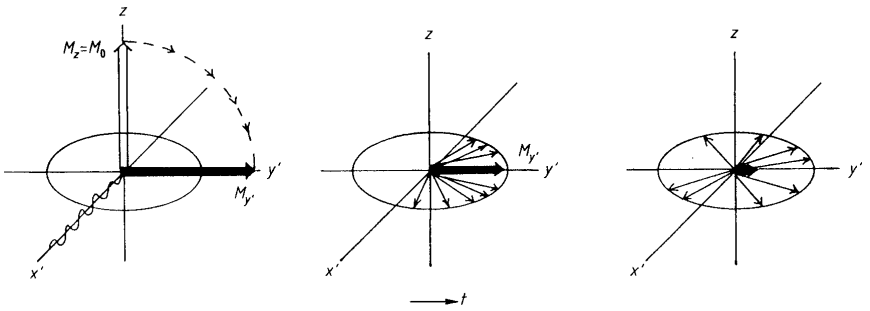

Figure 2-7: *Spin-spin or transverse relaxation: gradual loss of the phase-coherence of the magnetic moments* $\vec{\mu}$.

A number of contributions define the T_2 decay time. Once more fluctuating local fields come into play. Remarkably T_1 also affects T_2. The higher the spectral density of molecular motions with the Larmor frequency ω_0 the shorter the relaxation time constant T_1. This means also a shorter lifetime of the spins in the excited state. Then according to the uncertainty principle of Heisenberg T_2 will be short as well, after all:

$$\Delta E \Delta t \geq \frac{h}{2\pi} \qquad \text{and} \qquad h\Delta\upsilon\Delta t \geq \frac{h}{2\pi} \qquad \text{and} \qquad \Delta\upsilon \geq \frac{1}{2\pi\Delta t}$$

So in the extreme narrowing limit (at the left side in figure 2-8) it holds that the shorter the lifetime Δt (i.e. efficient T_1 relaxation) the broader the resonance or the shorter T_2 (cfr. section 2.1). One refers to this contribution on T_2 as the lifetime broadening.

Secondly, not only components of the fluctuating local fields perpendicular to B_0, but also components parallel to B_0 can affect T_2. As these z-components will reinforce or reduce the field felt by the nuclei, their magnetic moments will precess faster or slower. This causes some line broadening in the corresponding spectrum or T_2 relaxation as well, and is referred to as the adiabatic broadening. However, molecules in solution are tumbling very fast so that on the NMR time scale (during the acquisition time) the effect is averaged out to zero, i.e. the contribution to the

rate of fanning out of the magnetic moments $\vec{\mu}$ in the x'y'-plane is negligible. For molecules in solution (left side in figure 2-8) only the lifetime broadening is relevant and therefore T_2 equals T_1. For solids, on the other hand, a spin with a particular isotropic chemical shift possesses in different molecules within the sample different precessing frequencies due to variations in r and θ (see section 2.2) and consequently the magnetic moments $\vec{\mu}$ will fan out very quickly. The relaxation decay time T_2 will be very short, in the range of tens of μs, and of course T_2 will be much shorter than T_1. Remark that for the adiabatic component of the T_2 relaxation no local magnetic field fluctuations at the Larmor frequency ω_0 are necessary. In addition, the slower the molecular motions, the higher the impact of the adiabatic contribution and the faster the T_2 relaxation. In the solid state, the T_{2H} relaxation is a valuable tool to evaluate the presence of crystallinity since it often induces an oscillation in the initial part of the FID as a consequence of the presence of strong dipolar-dipolar interactions. However, when both amorphous and crystalline phases are present, one should perform measurements at temperatures of at least 70 °C above the glass transition temperature of the amorphous phase in order to sufficiently discriminate between the two phases. Only then a reasonable determination of the crystallinity is feasible.

In the solid-state and for abundant nuclei, like protons, a third contribution to T_2 is relevant. Two proton spins which are close in space can mutually exchange energy via their local fields perpendicular to B_0. During these spin flip-flops the total energy of the spin system is conserved. T_2 relaxation will occur since the mechanism involves short spin lifetimes. Remark that the spins themselves are not displaced but the magnetization is transferred. The flip-flop mechanism forms the basis for the phenomenon of spin diffusion (see section 2.5).

A third relaxation time constant that will be considered is the spin-lattice relaxation time constant in the rotating frame, denoted as $T_{1\rho}$. After a $90°_{x'}$ pulse has brought the magnetization $\vec{M}_0$ parallel to the y'-axis, the B_1 field is instantly phase shifted by 90° to the y'-axis. This will maintain the magnetization along the y'-axis, just as B_0 keeps the magnetization along the z-axis. As already discussed in section 2.3.3, this is called spin-locking of the magnetization. Actually, a competition between B_0 and B_1 arises. However, as B_0 is much higher in strength in comparison with $B_{1y'}$ (typically several T versus a few mT), $M_{y'}$ will decrease through so-called $T_{1\rho}$ relaxation which goes much more slowly (in the order of

tens to hundreds of ms) as compared to T_2 (for solids it is in the order of tens of μs) relaxation.

How the relaxation decay time constants can be measured experimentally will be postponed to the experimental sections of chapters 3, 4 and 5.

For spin-1/2 (i.e. spin quantum number I = ½) nuclei such as ^{1}H and ^{13}C the most important mechanism for relaxation results from the dipole-dipole coupling[14]. The relaxation times are further dependent on the way that the dipolar interactions are varied by molecular motions, which are characterized by a correlation time τ_C. The correlation time τ_C is the averaged time for a molecule or chain fragment to rotate over one radian with respect to its starting position[15]. Rapid molecular motions correspond to short τ_C's and in general the τ_C decreases with increasing temperature according to the following equation in which E_a is the activation energy:

$$\tau_C = \tau_0 \exp(-E_a / kT)$$

Figure 2-8 shows a rudimentary graph of the relaxation time constants T_1, $T_{1\rho}$ and

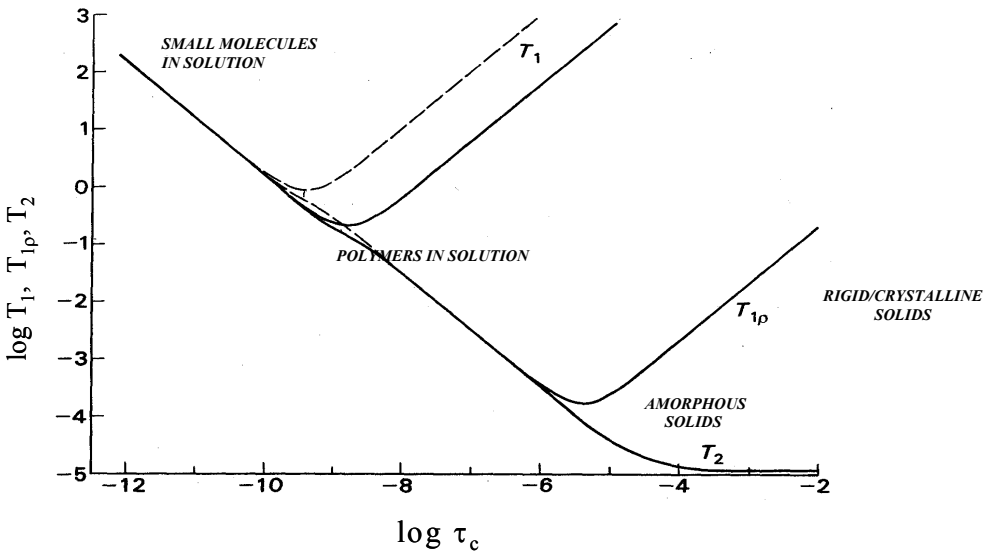

Figure 2-8: *T_1, $T_{1\rho}$ and T_2 as a function of the correlation time τ_C. The solid lines are calculated for ω_0 = 100 MHz and the dashed lines for ω_0 = 400 MHz.*

T_2 as a function of the correlation time τ_C (logaritmic scale for both axises). Notice that as τ_C increases, T_1 and $T_{1\rho}$ pass through a minimum and then increase again. On the other hand, T_2 continues to decrease with increasing τ_C. Furthermore, if B_0

is increased, the T_1 minimum increases as well and moves to shorter τ_C values. The $T_{1\rho}$ minimum depends on the field strength of the B_1-field.

Sometimes other relaxation mechanisms, in addition to the dipole-dipole relaxation, can be important as well. Other mechanisms are the quadrupole interaction (for nuclei with spin quantum number $I > ½$), the chemical shift anisotropy, the spin rotation interaction, the paramagnetic contribution and the scalar relaxation. In each of these cases local fluctuating magnetic fields contribute to the relaxation[16].

2.5 Spin diffusion

In rigid systems below the glass transition temperature T_g and for abundant spins (e.g. protons), the T_{1H} and $T_{1\rho H}$ relaxation is not solely determined by molecular motions but also by the process of spin diffusion[1,17,18]. Proton spin diffusion is not a physical movement of protons but a transfer of nuclear spin energy throughout the spin system by successive energy conserving spin flips (flip-flop mechanism). It allows to judge the degree of phase separation and to make a rough estimation of the size of the molecular domains. For a structure with 3D morphology and 3D spin-diffusion, the maximum diffusive path length L can be approximated by the one-dimensional Fickian diffusion equation $L = (6.D.T_{iH})^{1/2}$ in which T_{iH} is the T_{1H} or $T_{1\rho H}$ decay time and D is the spin-diffusion coefficient ($\sim 4 \times 10^{-16}$ m^2/s for rigid organic polymer systems)[18,19]. The T_{1H} relaxation time, in the order of seconds, is dominated by the spectral density of segmental motions in the MHz region. It provides info regarding the molecular miscibility on a distance scale in the order of tens to hundreds of nm, making it a rather large-scale property. The $T_{1\rho H}$ relaxation time on the other hand, in the order of milliseconds, is mainly affected by slower motions in the kHz region and provides info about the miscibility at the molecular level, i.e. the nanometer level. Phase specific decay times are only observed if the domain sizes exceed the average diffusive path length L (see figure 2-9) and if the intrinsic decay times of the phases differ enough. Otherwise a single averaged decay time is observed.

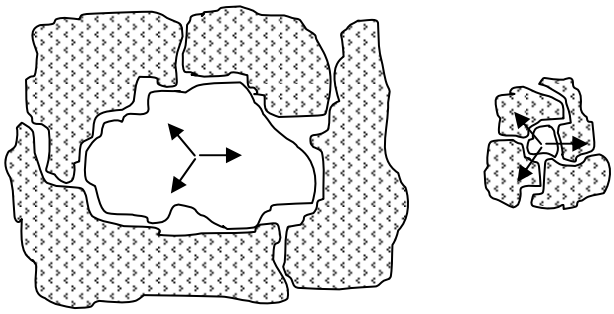

Figure 2-9: *Demonstration of the process of spin diffusion. Assuming that the central domain possesses a much longer decay time constant as compared to the surrounding, the left-hand sketch shows a situation in which the domain size exceeds the average diffusive path length L (visualized by the arrows). Under these circumstances, phase specific decay times will be observed. In the right-hand sketch on the other hand, only a single, averaged decay time constant will be measured.*

Note that T_{1C} (and T_{2H}) are local properties, not influenced by the process of spin diffusion. In principle, and as shown in figure 2-8, it is possible to discriminate between the molecular dynamics of well-defined crystalline and vitrified amorphous phases. On the one hand amorphous phases are characterized by rather short T_{1C} relaxation decay times. Well-ordered crystalline phases on the other hand have typically extremely long T_{1C}'s.

2.6 References

1. Komoroski, R.A., *High Resolution NMR Spectroscopy of Synthetic Polymers in Bulk* **1986**, VCH: Florida.
2. Laws, D.D.; Bitter, H.L.; Jershow, A., *Angew. Chem. Int. Ed.* **2002**, 41, 3096.
3. Mehring, M., *High Resolution NMR in Solids* **1983**, Springer, New York.
4. Haeberlen, U., *Adv. Magn. Reson.* **1976**, suppl. 1.
5. Bloch, F., *Phys. Rev.* **1956**, 102, 104.
6. Bloch, F., *Phys. Rev.* **1958**, 111, 841.
7. Andrew, E.R.; Bradbury, A.; Eades, R.G., *Nature* **1958**, 182, 1659.
8. Lowe, I.J., *Phys. Rev. Lett.* **1959**, 2, 285.
9. Schaefer, J.; Stejskal, E.O., *J. Am. Chem. Soc.* **1976**, 98, 1031.
10. Emsley, L.; Laws, D.D.; Pines, A., *Proc. Int. Sch. Phys. "Enrico Fermi"* **1999**, 129, 45.
11. Pines, A.; Gibby, M.G.; Waugh, J.S., *J. Chem. Phys.* **1973**, 59, 569.
12. Hartmann, S.R.; Hahn, E.L., *Phys. Rev.* **1962**, 128, 2042.

13. Levitt, M.H., *Spin Dynamics-Basics of Nuclear Magnetic Resonance* **2001**, John Wiley & Sons Ltd, 79.
14. Bovey, F.A., *Nuclear Magnetic Resonance Spectroscopy* **1988**, Academic Press, London, 255.
15. Keeler, J., *Understanding NMR Spectroscopy* **2005**, John Wiley & Sons Ltd, 256.
16. Fedotov, V.D.; Schneider, H., *Structure and Dynamics of Bulk Polymers by NMR-Methods* **1989**, Springer-Verlag, Berlin.
17. McBrierty, V.J.; Douglas, D.C.*, J. Polym. Sci., Macromolec. Rev.* **1981**, 16, 295.
18. Schmidt-Rohr, K.; Spiess, H.W., *Multidimensional solid-state NMR and polymers* **1996**, Academic Press, 402.
19. Clauss, J.; Schmidt-Rohr, K.; Spiess, H.W. *Acta. Polym.* **1993**, *44*, 1.

Chapter Three

MDMO-PPV/PCBM Thin Films Casted from Toluene Solutions

3.1 Introduction

Historically, MDMO-PPV (figure 3-1) together with MEH-PPV belongs to the first extensively studied conjugated polymers in the field of BHJ solar cells. Recall that the MDMO side chains on the standard PPV backbone serve to increase the solubility in organic solvents (cf. section 1.2.4.2). In addition, the alkoxy functionalization of the PPV backbone both offers the advantage of band gap tuning of the conjugated polymer (nowadays different PPVs are available with energy band gaps that span the whole visible spectrum[1]) and can have important consequences on the resulting polymer microstructure and morphology of the casted photoactive films.

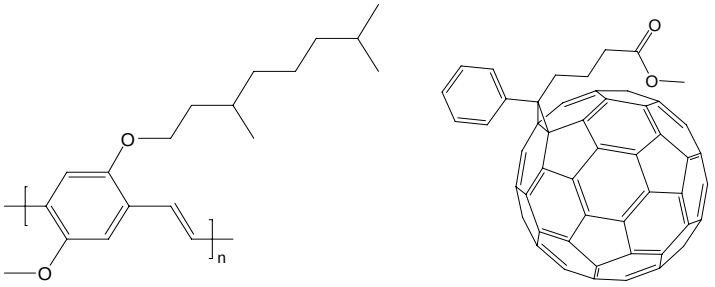

***Figure 3-1**: Chemical structure of MDMO-PPV (left) and PCBM (right).*

In a BHJ plastic solar cell the semiconducting and strongly light absorbing conjugated polymer, which acts as an electron donor, is intimately mixed with an electron acceptor. PCBM is frequently the choice for the latter (figure 3-1). The functionalization on the buckminsterfullerene C_{60} serves again to increase the solubility in processing solvents.

The main goal of this work is to study the nanomorphology of photoactive layers used in BHJ OPV devices by NMR techniques. Since MDMO-PPV/PCBM blends are often still considered as a "work-horse" or reference system for organic polymer based solar cells and are still used in e.g. tandem solar cells[2], we started with this system to evaluate the possibilities of solid-state NMR relaxometry in this field of science.

The nanomorphology of the well-documented MDMO-PPV/PCBM system has already been extensively investigated by XRD (X-ray Diffraction) and microscopic techniques like TEM (Transmission Electron Microscopy), SEM (Scanning Electron Microscopy) and AFM (Atomic Force Microscopy)[3-10].

In this chapter toluene is used as the solvent for processing the thin MDMO-PPV/PCBM films. It has been shown in the above listed references that toluene significantly enhances the phase separation between MDMO-PPV and PCBM. Features of a few hundreds of nanometer in size are visible in TEM and AFM images of films casted from toluene solutions with high PCBM content.

Here, a complementary and innovative method to describe and quantify the morphology of the active layer, based on ^{1}H wide-line solid-state NMR relaxometry, is presented. The obtained results are compared with conventional microscopy and XRD. In ^{1}H wide-line solid-state spectra only one single broad resonance, with a line width in the order of 50 kHz, is noticeable as a consequence of the strong ^{1}H-^{1}H dipolar couplings (see section 2.2 and 2.3). However, information about the segmental chain dynamics, physico-chemical nature, phase structure and molecular miscibility is hidden under this broad signal and can be extracted via the determination of relaxation time constants and molar fractions of the different phases.

Since the phase morphology is not only determined by the thermodynamic miscibility of the blend components but also by the film processing conditions, different casting techniques are evaluated as well. Although most studies concentrate on spin-coating, this technique is rather unacceptable from a commercial and environmental point-of-view since most of the material is wasted. Therefore attention is focused on the influence of the blend composition and the film casting method (spin-coating versus doctor blading) upon the nanomorphology in thin MDMO-PPV/PCBM films prepared from toluene. To start, the individual components were studied first.

3.2 Relaxation behavior of the pure blend components

3.2.1 PCBM

Figure 3-2 shows a XRD pattern of the electron acceptor PCBM. Sharp reflections are observed which clearly point to a semicrystalline structure for as-received Solenne PCBM.

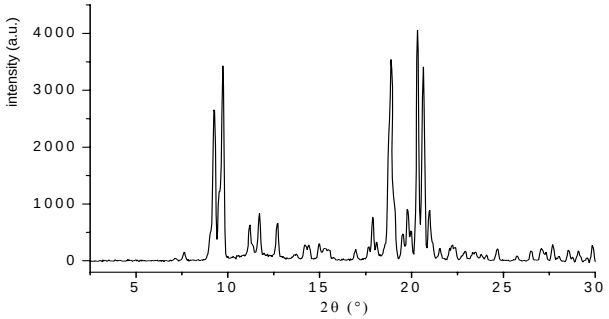

***Figure 3-2**: XRD pattern of as-received Solenne PCBM.*

The time domain NMR signal (see section 2.1), i.e. the experimental FID (Free Induction Decay – T_{2H} relaxation) can be obtained by the solid-echo pulse sequence (cf. section 3.5.2). The FID of as-received PCBM (figure 3-3) is not an ordinary exponential decay but clearly shows an oscillating behavior. This indicates the presence of very strong dipolar interactions, typical for well-defined crystalline systems.

This FID was converted into an ASCII file and read into the PC for data analysis with Origin or Kaleidagraph software. The T_{2H} relaxation time constants were obtained by performing a non-linear least-squares fit of the FID by means of the following equation:

$$I(t) = I_0^A \exp(-(t/T_{2H}^A)^2)\frac{\sin 2\pi\upsilon t}{2\pi\upsilon t} + I_0^G \exp(-(t/T_{2H}^G)^2) + I_0^L \exp(-t/T_{2H}^L)$$

So to determine the phase distribution, the FID had to be fitted by means of an Abragam (damped oscillating function), Gaussian and Lorentzian (i.e. exponential) function, with relaxation decay times T_{2H}^A, T_{2H}^G, T_{2H}^L and corresponding molar fraction I_0^A, I_0^G, I_0^L, respectively. The fractions, presented on the inset in figure 3-3, are normalized to 100 %. In the latter figure not only the experimental FID is

shown, the fitting curve and the three constituting components are shown as well. A first, very coarse estimate of the amount of crystallinity can be made by adding the Abragam and Gaussian fractions together, giving a molar fraction of about 75 %.

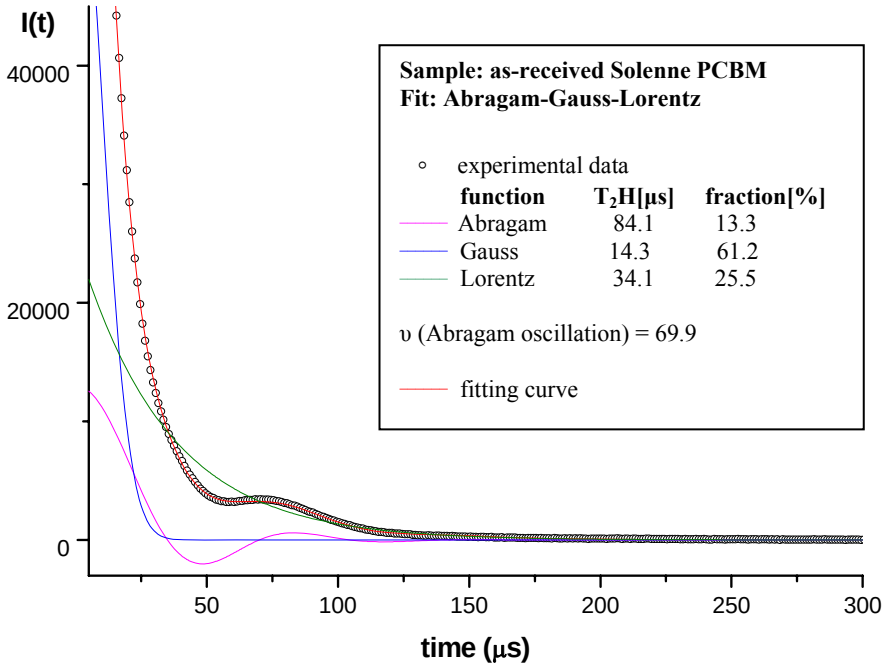

***Figure 3-3**: FID (experimental data) of as-received Solenne PCBM and decomposition of the relaxation curve in Abragam, Gauss and Lorentz components.*

From both observations, XRD and FID, we can infer that as-received PCBM is highly crystalline. Thus if one performs T_{1H} and $T_{1\rho H}$ wide-line relaxation experiments on an as-received PCBM sample, long relaxation decay times might be expected (cf. section 2.4). As a demonstration figure 3-4 shows the results of a $T_{1\rho H}$ wide-line experiment on as-received PCBM. Each experimental data point corresponds to a particular value of the variable spin-lock time t_{SL} in the pulse sequence presented in figure 3-12 (see experimental part, section 3.5.2). With increasing value for t_{SL}, the detected magnetization will decrease as a consequence of $T_{1\rho H}$ relaxation. It is clear that a mono-exponential analysis is inadequate (figure 3-4-left). An appropriate correlation between the experimental data points and the mathematical curve fitting is attained using a bi-exponential analysis (see section 3.5.2 for equations) as demonstrated in figure 3-4-right.

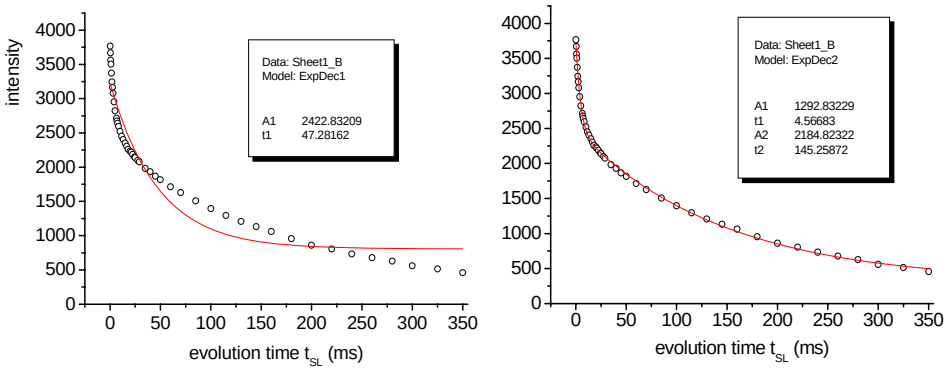

***Figure 3-4**: Data of a $T_{1\rho H}$ experiment on as-received Solenne PCBM analyzed mono-exponentially (left) and bi-exponentially (right).*

The same goes for the T_{1H} experiment in which the magnetization behaves bi-exponentially as well, as demonstrated in figure 3-5-right. In figure 3-5 the observed experimental data points correspond to different values for the variable evolution time t of the pulse sequence presented in figure 3-11. With increasing value for t, the detected magnetization will increase as a consequence of T_{1H} relaxation and, finally, the macroscopic magnetization vector will return to its maximal equilibrium value M_0.

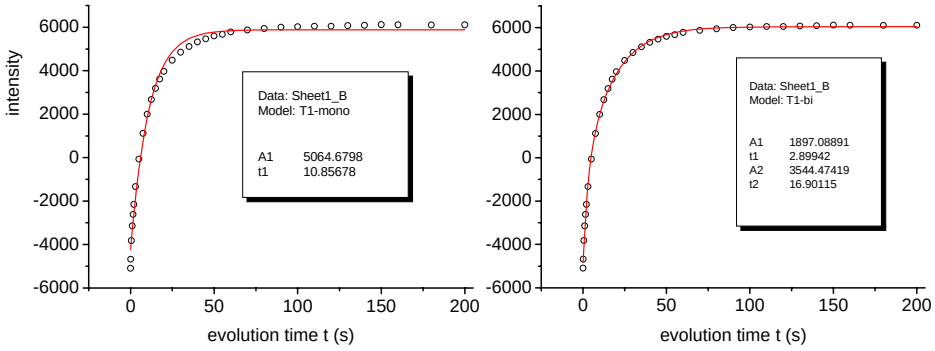

***Figure 3-5**: Data of a T_{1H} experiment on as-received Solenne PCBM analyzed mono-exponentially (left) and bi-exponentially (right).*

A mono-exponential analysis is inadequate (figure 3-5-left): a bad correlation is observed between the data points and the curve fit, especially in the bend and at the initial and end part of the fit.

Table 3-1 shows an overview of the obtained decay times for as-received

PCBM and drop-casted films of PCBM as measured by proton wide-line NMR. Both the T_{1H} and $T_{1\rho H}$ relaxation behave bi-exponentially with a short (s) and long (l) decay time. The short T_{1H}^{s} and $T_{1\rho H}^{s}$ decay times and the corresponding molar proton fractions represent amorphous PCBM.

***Table 3-1**: Relaxation decay times T_{1H} and $T_{1\rho H}$ for as-received Solenne PCBM and drop-casted PCBM film. The normalized molar proton fractions are presented between brackets.*

decay time	as-received PCBM	drop-casted PCBM film
T_{1H}^{s} / T_{1H}^{l} (s)	2.9 (35%) / **16.9 (65%)**	2.0 (50%) / **14.5 (50%)**
$T_{1\rho H}^{s}$ / $T_{1\rho H}^{l}$ (ms)	4.6 (37%) / **145 (63%)**	6.5 (49%) / **70.0 (51%)**
T_{2H}	oscillating FID	oscillating FID

On the other hand, the extremely long T_{1H}^{l} and $T_{1\rho H}^{l}$ decay times (depicted in bold in table 3-1) point to a semi-crystalline structure[11] and the corresponding molar proton fractions represent the amount of crystallinity. Note that with both independent measurements the same, within experimental error, amount of crystallinity of about 65 % is obtained for as-received PCBM. As-received PCBM is indeed highly crystalline and these T_{1H} and $T_{1\rho H}$ results confirm the observations done by T_{2H} relaxometry and XRD. The amount of crystallinity is lower for the drop-casted PCBM film (~50%) as compared to as-received PCBM (~65%). This is probably caused by the fast evaporation of solvent during the drop-casting process. It can be expected that the crystallinity will drop further upon spin-coating. Note that the values (and fractions) of the long time constants look to be good probes to judge the quality and amount of well-defined crystals.

Based on the spin-diffusion equation ($L=(6.D.T_{1H})^{1/2}$), the minimum dimensions of the crystallites can be estimated to be around 200 and 180 nm for as-received and drop-casted PCBM, respectively.

In the next part of the dissertation all experimental relaxation NMR data will be analyzed in the same manner as described above. However, only the resulting relaxation decay times and corresponding molar proton fractions will be presented, without showing the fits.

3.2.2 MDMO-PPV

Table 3-2 shows the decay times for as-received MDMO-PPV as measured by proton wide-line NMR. No differences are observed between as-received

MDMO-PPV and a MDMO-PPV film casted from chlorobenzene (data not shown). Due to spin-diffusion, all protons relax very efficiently with a short T_{1H} decay time of 0.63 s. The short decay time is an indication for a high spectral density of 400 MHz motions (see section 2-4).

The $T_{1\rho H}$ decay on the other hand behaves bi-exponentially, a typical observation for polymers with long flexible side chains and for which the corresponding molar proton fractions can often not be assigned straightforward. Note, however, that both relaxation decay times $T_{1\rho H}^{s}$ and $T_{1\rho H}^{i}$ are rather short (cf. section 2.4). No extremely long $T_{1\rho H}$ decay time, as for PCBM, is measured. So the two decay times do not represent phase separation but incomplete spin diffusion due to weakened dipolar interactions in the long, mobile side-chain. In addition no initial oscillating component can be observed in the FID (data not shown). In conclusion, both as-received and spin-coated MDMO-PPV seem to appear as fully amorphous polymers.

***Table 3-2**: Relaxation decay times T_{1H} and $T_{1\rho H}$ for MDMO-PPV. The normalized molar proton fractions are presented between brackets.*

decay time	MDMO-PPV
T_{1H} (s)	0.63
$T_{1\rho H}^{s}$ / $T_{1\rho H}^{i}$ (ms)	1.4 (27%) / 3.3 (73%)
T_{2H}	no oscillating FID

3.3 Relaxation behavior of the MDMO-PPV/PCBM blends

3.3.1 Spin-coated films

Table 3-3 presents the T_{1H} and $T_{1\rho H}$ relaxation decay times measured by proton wide-line NMR of thin films prepared by spin-coating from solutions in toluene for different MDMO-PPV/PCBM weight ratios (wt%). Thin films with a homogeneous thickness of about 150 nm were investigated. Besides the wt% indication (printed in bold) which is generally encountered in the field of plastic electronics, also the corresponding molar ratios and molar proton ratios of the blends are listed in table 3-3, since especially the latter is more expressive in the case of proton NMR.

***Table 3-3**: T_{1H} and $T_{1\rho H}$ decay times and corresponding normalized proton fractions (between brackets) of thin films spin-coated from solutions in toluene for different MDMO-PPV/PCBM ratios. L is an estimate for the average minimum dimension of the well-defined phase separated PCBM crystallites. Also the mol % of PCBM in well-defined phase separated crystallites and the molar ratio MDMO-PPV/PCBM in the mixed phase are listed.*

	MDMO-PPV/PCBM			
weight ratio (wt%) molar ratio *molar proton ratio*	**50/50** 76/24 *86/14*	**30/70** 58/42 *73/27*	**20/80** 44/56 *61/39*	**15/85** 36/64 *53/47*
T_{1H} (s)	0.71	0.74 (95%) **6.2 (5%)**	0.83 (91%) **13.3 (9%)**	0.63 (84%) **29.8 (16%)**
L (nm)	4 < x <40	> 120	> 180	> 270
$T_{1\rho H}$ (ms)	1.7 (16%) 7.8 (84%)	1.8 (18%) 9.4 (75%) **53.5 (7%)**	1.9 (17%) 9.4 (74%) **76.0 (9%)**	1.9 (22%) 9.9 (64%) **172 (14%)**
mol % PCBM in well-defined crystallites	**0 %**	**19 %**	**23 %**	**34 %**
molar ratio of MDMO-PPV/PCBM in the mixed phase*	100/32	100/59	100/98	100/117

** expressed per 100 repetition units of MDMO-PPV*

For films prepared from blends with 50 wt% PCBM, a single T_{1H} decay time of about 0.7 s is observed. The T_{1H} relaxation seems to be very efficient and a short decay time, as is the case for pure MDMO-PPV, is observed. Due to efficient spin diffusion, the T_{1H} relaxation of PCBM in this spin-coated blend is driven by the molecular motions of MDMO-PPV. Therefore these blends have to be homogeneous on the T_{1H} distance scale (several tens to hundreds of nm). If phase separation of PCBM takes place at all, it means that the molecular PCBM domains should be smaller than about 40 nm. This is already confirmed by AFM, showing a homogeneous morphology as depicted in figure 3-6-a.

Starting from 70 wt% PCBM, the T_{1H} relaxation of the blends becomes bi-exponentially with a short and long T_{1H} decay time. The short decay time represents the mixed MDMO-PPV/PCBM matrix while, as for pure PCBM, the long T_{1H} component represents well-defined phase separated PCBM crystallites. The spin diffusion equation ($L=(6.D.T_{1H})^{1/2}$) indicates PCBM crystallites with minimal average dimensions of 120, 180 and 270 nm for blends with 70, 80 and 85 wt% PCBM, respectively. Such a large-scale phase separation is clearly confirmed by the observed AFM images as shown in figure 3-6-b and 3-6-c. Features with

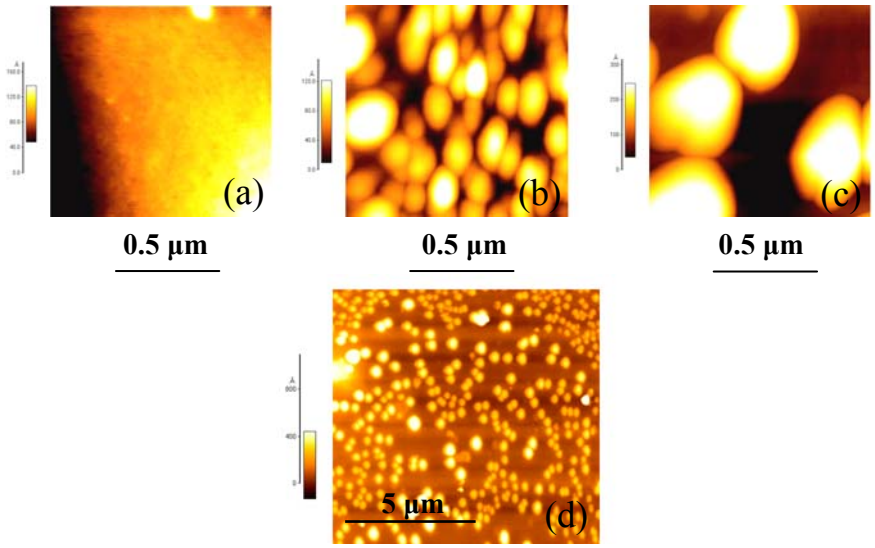

***Figure 3-6**: Top panels: AFM images (1 µm x 1 µm) of thin MDMO-PPV/PCBM films spin-coated from solutions in toluene with 50 wt% (a), 70 wt% (b) and 80 wt% (c) PCBM; bottom panel: 'Zoom-out' AFM image (10 µm x 10 µm) (d) of image (c).*

average dimensions of respectively 150 and 400 nm are noticed in AFM images of the 30/70 wt% and 20/80 wt% blends. However, remark that in figure 3-6-d, a 'zoom-out' of figure 3-6-c, also smaller (< 400 nm) crystals are present. This is in good agreement with the NMR result which represents a bulk average of the minimal crystal dimensions. A summary and comparison between NMR and AFM is given in table 3-4.

***Table 3-4**: Comparison of NMR and AFM results with respect to the average dimensions of well-defined PCBM crystallites.*

MDMO-PPV/PCBM	NMR	AFM
50/50 wt%	if present, than < 40 nm	homogeneous
30/70 wt%	domains ≥ 120 nm	domains ± 150 nm
20/80 wt%	domains ≥ 180 nm	200 nm ≤ domains ≤ 400 nm

The molar amount of PCBM that is phase separated and organized in large well-defined crystallites can be quantified and calculated from the observed proton fractions corresponding to the long relaxation T_{1H} decay time (presented in bold in table 3-3). Taking into account the corresponding molar proton ratios of 73/27 (30/70 wt% blend), 61/39 (20/80 wt% blend) and 53/47 (15/85 wt% blend), this

means that in these blends respectively about 19 mol % (5/27x100%), 23 mol % (9/39x100%) and 34 mol % (16/47x100%) of the PCBM is phase separated (results are summarized in table 3-3). A clear trend is that the amount and size of well-defined PCBM crystallites increases as a function of the PCBM content in the blend.

It can further be calculated that the amount of PCBM in the mixed MDMO-PPV/PCBM matrix also increases as a function of the total PCBM content in the film. For example for the 30/70 wt% blend, the corresponding molar ratio is 58/42 and the molar amount of well-defined phase separated PCBM crystallites is 19 % (see above). Or stated otherwise, 81 mol % of the PCBM can be found in the mixed MDMO-PPV/PCBM matrix. This results in a molar ratio of 58/34 in the mixed matrix. This means that, expressed per 100 repeating units of MDMO-PPV, there are 59 molecules of PCBM in the mixed phase. In conclusion, per 100 repeating units of MDMO-PPV, there are 32, 59, 98 and 118 molecules of PCBM present in the mixed phase of the 50/50, 30/70, 20/80 and 15/85 wt% blends, respectively (see table 3-3).

The semi-crystalline structure of PCBM in thin MDMO-PPV/PCBM films with high PCBM content and spin-coated from toluene is confirmed by XRD as depicted for the 15/85 wt% blend in figure 3-7-a. The XRD clearly shows the same

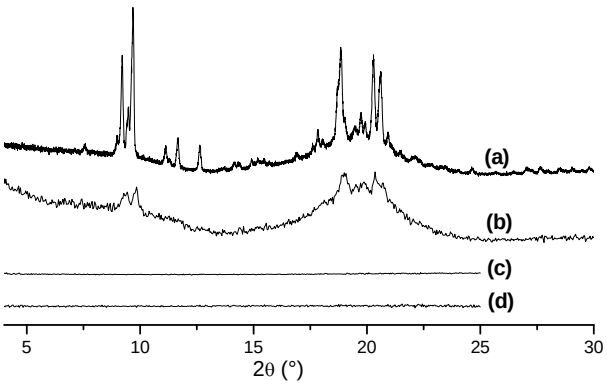

***Figure 3-7**: XRD patterns of toluene casted film samples: 15/85 wt% MDMO-PPV/PCBM powder sample (a), 30/70 wt% MDMO-PPV/PCBM powder sample (b), single thin doctor bladed PCBM film (c) and single thin spin-coated 20/80 wt% MDMO-PPV/PCBM film (d).*

diffraction pattern as for as-received PCBM (figure 3-2) superimposed on a broad halo. Figure 3-7-b shows the XRD pattern of the 30/70 wt% blend which is in agreement with the NMR results, i.e. a long T_{1H} decay time and molar proton

fraction of only 6.2 s and 5 %, respectively. Note that these XRDs were acquired from the same samples as used for the NMR measurements. If XRD measurements are performed directly on 150 nm thin films, no XRD patterns can be obtained due to the limits in sensitivity of detection (figure 3-7-c and 3-7-d).

Regarding the $T_{1\rho H}$ relaxation (table 3-3) the 50/50 w% blend shows two decay times as is the case for pure MDMO-PPV. Remark however that the second, intermediately long, $T_{1\rho H}$ decay time (7.8 ms) is significantly longer as compared to the value of 3.3 ms for pure MDMO-PPV (table 3-2). This might point to the presence of small and irregular PCBM crystals in the MDMO-PPV matrix. Based on the T_{1H} and intermediate $T_{1\rho H}$ values (and spin diffusion equation), it can be concluded that if such nanocrystals are present at all their dimensions should be situated between 4 and 40 nm. Although these 50/50 wt% films apparantly look homogeneous on 2D AFM (figure 3-6-a) and TEM (not shown) images, the presence of nanocrystals will be confirmed in chapter 5 by means of local T_{1C} relaxation measurements.

However, films prepared from blends with PCBM content ≥ 70 wt% show a third and long $T_{1\rho H}$ decay time. Such long $T_{1\rho H}$ decay times are once again indicative of phase separated, well-defined PCBM crystallites. Well-organized crystallites have a low spectral density of molecular motions in the kHz region which explains the long $T_{1\rho H}$ decay times. A clear trend is that the amount of well-defined PCBM crystals, represented by the fraction corresponding to this long decay time, increases with increasing PCBM content. Furthermore, the increase of both the T_{1H} and $T_{1\rho H}$ decay time values with increasing PCBM content can be ascribed to an increase of the average dimensions of the crystallites. Nonetheless, as was demonstrated for T_{1H}, not all of the PCBM is phase separated and crystallized into well-defined crystals. By taking the molar proton fractions of the blends into account, similar molar amounts of well-defined phase separated PCBM crystallites are found as on basis of the T_{1H} results (table 3-3). The remaining part is mixed with MDMO-PPV. To our knowledge, this is the first time that a direct quantitative determination of the amount of phase separated PCBM as well as the amount of PCBM dispersed in the MDMO-PPV matrix is provided. Such information can be important for further fine-tuning of the performance of PCBM-based electro-optical devices. An important contribution to the driving force of the fast phase separation and so crystallization of PCBM can be found in the use of

toluene as the casting solvent, since these well-defined crystallites are not formed if films are casted from chlorobenzene (see chapter 5).

3.3.2 Doctor bladed films

Table 3-5 presents the T_{1H} and $T_{1\rho H}$ relaxation decay times measured by proton wide-line NMR for 150 nm thin films prepared by doctor blading from solutions in toluene for different MDMO-PPV/PCBM ratios. Doctor blading is a more continuous process with much less waste of material that allows to prepare thin films with a homogeneous thickness as well.

***Table 3-5**: T_{1H} and $T_{1\rho H}$ decay times and corresponding normalized proton fractions (between brackets) of thin films casted by doctor blading from solutions in toluene for different MDMO-PPV/PCBM ratios. L is an estimate for the average minimum dimension of the well-defined phase separated PCBM crystallites. Also the mol % of PCBM in well-defined phase separated crystallites and the molar ratio MDMO-PPV/PCBM in the mixed phase are listed.*

	MDMO-PPV/PCBM		
weight ratio (wt%) molar ratio *molar proton ratio*	**50/50** 76/24 *86/14*	**30/70** 58/42 *73/27*	**20/80** 44/56 *61/39*
T_{1H} (s)	0.70	0.71 (94%) **10.7 (6%)**	0.68 (82%) **13.8 (18%)**
L (nm)	4 < x <40	> 160	> 180
$T_{1\rho H}$ (ms)	1.9 (16%) 8.2 (84%)	1.9 (15%) 9.4 (79%) **65.5 (6%)**	2.2 (20%) 8.8 (65%) **131.7 (15%)**
mol % PCBM in well-defined crystallites	**0 %**	**22 %**	**46 %**
molar ratio of MDMO-PPV/PCBM in the mixed phase*	100/32	100/57	100/68

** expressed per 100 repetition units of MDMO-PPV*

Upon changing the processing technique from spin-coating to doctor blading, the same general trends are observed for both the T_{1H} and $T_{1\rho H}$ relaxation. Also here, for the 50/50 wt% doctor bladed films a single short T_{1H} decay time of 0.7 s is observed. The T_{1H} relaxation seems to be very efficient and a short decay time, as is the case for pure MDMO-PPV, is observed. Due to efficient spin

diffusion, the T_{1H} relaxation of PCBM in this doctor bladed blend is driven by the molecular motions of MDMO-PPV. Therefore these blends, as is confirmed by the TEM image in figure 3-8-a, have to be homogeneous on the T_{1H} distance scale. However, as is the case for spin-coating, the intermediately long $T_{1\rho H}$ decay time of 8.2 ms might point to the presence of small and irregular PCBM crystals in the MDMO-PPV matrix. Based on the T_{1H} and intermediate $T_{1\rho H}$ values (and the spin diffusion equation), it can be concluded that if nanocrystals are present at all their dimensions should be situated between 4 and 40 nm. Although these 50/50 wt% doctor bladed films apparantly look homogeneous on 2D AFM (not shown) and TEM (figure 3-8-a) images, the presence of nanocrystals will be confirmed in chapter 5 by means of local T_{1C} relaxation measurements.

Films doctor bladed from blends with PCBM content ≥ 70 wt% show an additional, long T_{1H} and $T_{1\rho H}$ decay time (indicated in bold in table 3-5). Again, such long decay times point to a semi-crystalline structure[11] and their corresponding fractions represent the amount of well-defined PCBM crystallites. Note that within experimental error the same fraction of phase separated crystalline PCBM is obtained by both independent measurements (T_{1H} and $T_{1\rho H}$). Also for these doctor bladed films, the appearance of phase separated PCBM could be confirmed by TEM (Figure 3-8-b and 3-8-c).

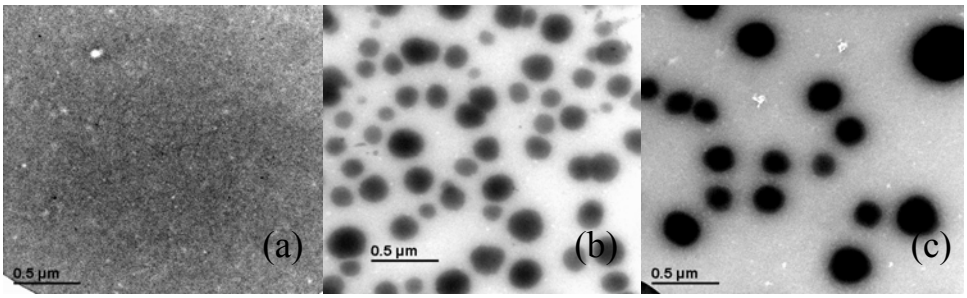

***Figure 3-8**: TEM images of 150 nm thin MDMO-PPV/PCBM films casted by doctor blading from solutions in toluene with 50 wt% (a), 70 wt% (b) and 80 wt% (c) PCBM (marker is 500 nm long).*

3.3.3 Film morphology: spin-coating versus doctor blading

The following conclusions based on microscopy (TEM and AFM) and proton wide-line NMR relaxometry can be drawn regarding the preparation of thin

films from toluene solutions by the two casting techniques discussed (see tables 3-3 and 3-5):

- No differences between spin-coating and doctor blading are observed for 50/50 wt% films.
- Concerning the 30/70 wt% blends, nonetheless for both casting techniques almost the same molar amount of well-defined PCBM crystallites is observed, the value of the T_{1H} as well as the $T_{1\rho H}$ relaxation time is longer for the doctor bladed films. The former implies larger crystallite dimensions, while the latter points to more perfect PCBM crystals.
- A comparison of the films processed from the 20/80 wt% blend by the two casting techniques shows a rather similar T_{1H} decay time and so average minimum dimension for the PCBM crystallites (L > 180 nm). This is confirmed by microscopy in figure 3-6-d and 3-8-c. However, the amount of well-defined PCBM crystallites is doubled for the doctor blading technique. This observation is a clear indication that the solvent evaporation rate, which is much slower for the doctor blade technique, is a parameter that strongly determines the amount of phase separated crystalline PCBM. Furthermore, the $T_{1\rho H}$ decay time is significantly longer for doctor blade films. A slower evaporation rate possibly improves the quality (less defects) of the PCBM crystallites, explaining the longer $T_{1\rho H}$ values observed for the doctor bladed films.
- The 20/80 wt% doctor bladed films already show a much higher amount of well-defined PCBM crystallites as found for the 15/85 wt% spin-coated films.
- In conclusion, depending on the casting solvent the film processing technique can become quite important with respect to the resulting morphology as is demonstrated here for toluene.

3.3.4 Film morphology: film thickness

Figure 3-9 depicts some TEM images of MDMO-PPV/PCBM 20/80 wt% doctor bladed films as a function of the film thickness to demonstrate the influence on the nanomorphology (cf. section 1.2.6.4). TEM images are shown for film thicknesses, as measured by Dektak3ST surface profilometry, of respectively 30 nm (left), 70 nm (middle) and 150 nm (right). It is clear that the thinner the films,

the smaller the observed phase separated PCBM domains. This indicates that not only the processing technique but also the processing conditions are highly determining the final film morphology. Van Bavel *et al*[12] also reported differences in degree of crystallinity as a function of film thickness for P3HT/PCBM films.

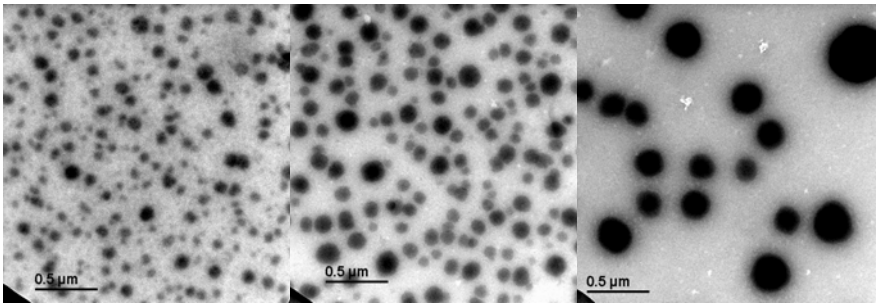

Figure 3-9: *TEM images of doctor bladed MDMO-PPV/PCBM 20/80 wt% films of different thickness:30 nm (left), 70 nm (middle) and 150 nm (right).*

Future perspectives:

The nanomorphology in the "30 nm thick film" (figure 3-9-left) looks quite optimal as phase separation of PCBM occurs into 40-50 nm domains resulting in an increased interfacial contact area between conjugated polymer and PCBM. It could be worthwhile to prepare a sample of such 30 nm doctor bladed 20/80 wt% films from toluene for NMR and XRD measurements. Aims are (i) confirmation of the preservation of phase separated PCBM into small but highly organized PCBM crystallites and (ii) quantification of the phase separated PCBM. It is known from literature that charge carrier transport is increased by mesoscopic order and crystallinity[13-15]. However, also some kind of co-continuous matrix of polymer and PCBM should be present for fast charge carrier mobility and so high η_e. If so, it could be tried to obtain this kind of morphology in thicker films (100-200 nm) by e.g. mixing toluene (driving force for fast phase separation and so crystallization since the solubility of PCBM in toluene is rather low) with other solvents and to compare the η_e's. As will be demonstrated in chapter 5, no well-defined PCBM crystallites but PCBM-rich and polymer-rich domains are observed in MDMO-PPV/PCBM films casted from chlorobenzene.

3.4 Conclusions

In this chapter we evaluated the use of proton wide-line NMR relaxometry as a useful and complementary tool to obtain information about the bulk phase nanomorphology of blends used as active layer in organic semiconducting OPV devices. In order to demonstrate the applicability of NMR relaxometry in this field of science, experiments were started on the "work-horse" reference system MDMO-PPV/PCBM and the influence of two casting techniques on the morphology of toluene-based films is reported.

As is demonstrated, as-received Solenne PCBM is highly semicrystalline. The amount (≈ 65 mol %) of well-defined phase separated PCBM crystallites and their average minimum dimensions (≥ 200 nm) can be quantified via the long T_{1H} and $T_{1\rho H}$ relaxation decay times and their corresponding fraction. Both as-received and spin-coated MDMO-PPV, on the other hand, are fully amorphous polymers.

For the composite films, prepared by spin-coating as well as doctor blading, it is demonstrated that starting from 70 wt% PCBM a fraction of the PCBM is phase separated into well-defined crystalline domains. The remaining part is mixed with MDMO-PPV. It has been shown that the molar amount (%) of PCBM in well-defined phase separated crystallites as well as in the mixed phase increases as a function of the total amount of PCBM in the blend. A detailed quantification of the partition of PCBM among the different phases is provided. To our knowledge, this is the first time that a quantitative determination of the amount of phase separated PCBM and dispersed PCBM is provided. Note that the results obtained by NMR are in good agreement with TEM and AFM.

However, in case of 50/50 wt% MDMO-PPV/PCBM films casted from toluene it could be decided by solid-state proton wide-line NMR relaxometry that these films, although showing a quite homogeneous morphology on microscopy images (AFM and TEM), most likely contain PCBM nanocrystals (with dimensions between 4 and 40 nm) which are embedded in the polymer matrix.

For doctor bladed films, in general a higher amount of well-defined PCBM crystallites is observed as compared to spin-coated films. For films with a 80 wt% PCBM content the molar amount of well-defined PCBM crystals is even doubled in case of doctor blading. Moreover, the quality of the crystals is improved by doctor blading (longer $T_{1\rho H}$ decay times). These differences can be explained by the nature of the processing technique, which determines the solvent evaporation rate.

Concerning NMR relaxometry as a tool to describe the nanomorphology in polymer/fullerene OPV devices, it can be concluded that proton wide-line NMR relaxometry is appropriate to detect and quantify the presence of well-defined crystals in thin photoactive films. However, as will be shown later, for the detection of PCBM nanocrystals the more chemical shift selective and local T_{1C} probe, being the carbon spin-lattice relaxation decay time, will be needed.

The presented quantitative description of the phase morphology further improves the understanding why MDMO-PPV/PCBM devices perform rather weak when prepared from toluene solutions. The reduced interfacial contact area between conjugated polymer and PCBM, on account of the partial phase separation of PCBM in domains of which the dimensions are much larger than the diffusion path length of the created excitons, will certainly play a crucial role (cf. section 1.2.2). Moreover, the continuous "highways" needed for efficient charge transport are interrupted in such phase morphologies. Since polymer/PCBM films form the active layer in bulk heterojunction and multi-junction (e.g. tandem) plastic solar cells, this kind of detailed information can contribute to guide device performances towards economical demands.

3.5 Experimental part

3.5.1 Film preparation

MDMO-PPV (M_w=659500, M_n=88300, PD=7.5, M_w of a repetition unit is 288 g/mol) and PCBM[16] (M_w=910 g/mol) were purchased from Covion and Solenne, respectively. The glass transition temperature of MDMO-PPV[17] and PCBM[18] is situated around 40-50 and ~131°C, respectively. Mixtures with different weight ratios were dissolved in toluene and stirred for at least 4 hours at 50°C. The MDMO-PPV/PCBM blend compositions studied are 15/85, 20/80, 30/70 and 50/50 wt% or 36/64, 44/56, 58/42 and 76/24 mol % (based on the molecular weight of the repetition unit of the polymer). This results in a molar proton ratio of respectively 53/47, 61/39, 73/27 and 86/14 % (PCBM contains 14 protons while a repetition unit of MDMO-PPV contains 28 protons).

Two casting techniques were used for processing the thin films. As a first technique, the solutions where spin-coated, under N_2 atmosphere, using a Karlsuss

RC 8 spin-coater. The viscosity and, consequently the spin-coating conditions of the mixtures, where altered depending on the weight ratios to obtain a homogeneous film thickness of about 150 nm, as determined with a Dektak3ST surface profile measuring system of Veeco Instruments Inc. For the preparation of the 50/50 wt% films, a MDMO-PPV concentration of 8 mg/mL was used while for the 30/70 wt%, 20/80 wt% and 15/85 wt% films the MDMO-PPV concentration was 5 mg/mL. The spin-coating procedure consists of 3 consecutive steps to ensure active layer films with a well-defined thickness[19]. The first step is a deposition step (spinning with open cover for 4 s at 200 rps), followed by a second thickness-determining high speed step with closed cover for 4 s and finally a low speed /drying step with open cover at 500 rps during 150 s. For the thickness-determining step calibration experiments were performed. As shown in table 3-6, in all cases the film thickness increases with decreasing spin rate. This affects the morphology of the thin films as discussed in sections 1.2.6.4 and 3.3.4, so for each blend composition the appropriate spin rate was chosen in order to obtain the desired thickness of 150 nm.

Table 3-6: *Film thickness as a function of the spin rate (thickness-determining step) for different MDMO-PPV/PCBM ratios and casting solvents.*

50/50 wt% toluene		**50/50 wt% chlorobenzene**		**20/80 wt% chlorobenzene**	
spin rate (rpm)	**thickness** (nm)	**spin rate** (rpm)	**thickness** (nm)	**spin rate** (rpm)	**thickness** (nm)
1100	145	800	200	800	165
1300	135	1000	160	900	135
1500	115	1200	155	1000	125
1700	90	1400	140	1300	90

Glass substrates of 10x10 cm^2 were successively cleaned with soap (and afterwards thoroughly rinsed with demineralized water to ensure the removal of the soap), acetone and boiling isopropyl alcohol before use. Eventually the substrates were dried using dust-free high-pressure air. For the NMR measurements, the spin-coated layer is scraped off and collected. An amount of 10-15 mg was used in order to have sufficient NMR sensitivity. Before recording the NMR data, the material was dried under high vacuum (10^{-3} mbar) for at least 2 days.

As spin-coating is rather a material wasting technique it is only suitable on a laboratory scale. Therefore films of the same thickness were prepared by the doctor blade technique[20] as well, using a coatmaster 509 MC of Erichsen (figure 3-10). In this case glass substrates of 20x10 cm^2, analogously cleaned as for spin-coating, were used. Doctor blading is a more continuous, roll-to-roll process with less waste of material and by which the film thickness can also be adjusted easily. Hereto the polymer/fullerene solution was deposited on the edge of a glass substrate and spread out homogeneously by the mechanical movement of a knife (20 mm/s). In this way, 25-35 mg material could be collected with only 1/3 of the initial amount of polymer and fullerene as compared to spin-coating.

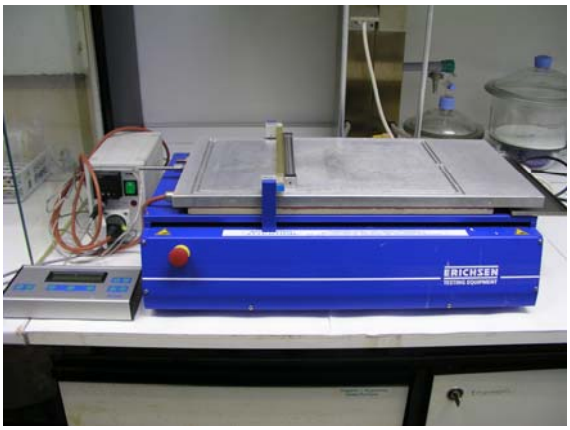

***Figure 3-10**: Picture of a doctor blading apparatus.*

3.5.2 Analytical techniques

For the TEM measurements, thin freestanding films were obtained by putting small pieces of substrate in hydrofluoric acid. Hereby the substrate sinks while the active layer floats on the liquid surface. The floating film was then picked up with a 200-mesh copper TEM grid. Experiments were performed on a Philips CM12-STEM which operates at a voltage of 120 kV in bright field mode and has a point resolution of 0.34 nm. AFM measurements were performed with an Autoprobe CP from Park Scientific Instruments operating in tapping mode under ambient atmosphere. XRD experiments were done on a Siemens D5000 diffractometer with an incident beam Ge(111) monochromator (Cu $K_{\alpha 1}$-1.54056Å).

Solid-state proton wide-line NMR measurements were carried out at ambient temperature on a Varian Inova 400 spectrometer in a dedicated wide-line probe equipped with a 5 mm coil. The number 400 in the spectrometers' name refers to the Larmor frequency (see section 2.1) for protons, i.e. approximately 400 MHz. The samples were placed in 5 mm glass tubes which were closed tightly with teflon stoppers. On-resonance Free Induction Decays (FIDs) were acquired by applying the solid-echo technique ($90°_{x'}$ - $t_{se}/2$ - $90°_{y'}$ - $t_{se}/2$ - acquire) in an effort to overcome the effect of the dead-time of the receiver[21]. The 90° pulse length t_{90} was set to 1.2 μs and spectra were recorded with a spectral width of 2 MHz (0.5 μs dwell time or sampling interval) allowing an accurate determination of the echo maximum. The solid-echo is formed with a maximum at $\tau = (3t_{90}/2 + t_{se}) = 6$ μs. From these FIDs, the T_{2H} decay times are extracted as shown in figure 3.3. A preparation delay d1 of 5 times the T_{1H} relaxation decay time was always respected between successive accumulations to obtain quantitative results. Both probe (20 L/min) and upper-barrel (30 L/min) cooling were used to limit sample heating.

Figure 3-11 depicts the pulse sequence diagram used for the proton wide-line T_{1H} experiment. Symbols under the horizontal time axis refer to intervals of time, some of which are fixed (e.g. *d1*), others are variable (e.g. *t*) (For clarity the length of pulses has been exaggerated). The T_{1H} relaxation decay times were measured by placing an inversion recovery filter in front of the solid-echo part. Hereto the equilibrium magnetization M_0 is first inverted by a $180°_{x'}$ pulse, i.e. M_0 is tilted in the –z direction. Next, during the variable evolution time t T_{1H} relaxation occurs, i.e. the magnitude of the z-component of the macroscopic magnetization gradually returns back to its equilibrium value M_0.

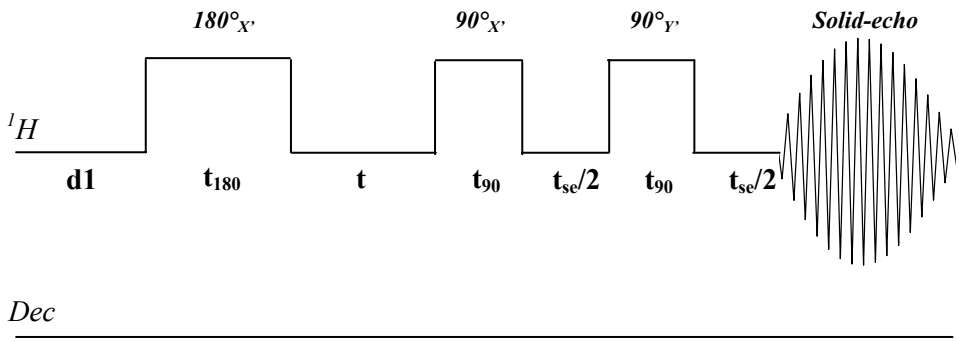

***Figure 3-11**: Pulse sequence of the proton wide-line T_{1H} experiment.*

In the experiments presented in this chapter, the evolution time t was varied between 0.01 and 200 s. The $90°_{X'}$ pulse, after t, serves to bring this actual z-magnetization, along the y'-axis as that is the axis along which detection occurs (cf. section 2.1). For most of the t-values the z-magnetization did not yet reach its equilibrium value, causing a detected signal moving from negative to positive values after the solid-echo part. The T_{1H} is then obtained by analyzing the integrated proton signal intensity I(t) (which is proportional to the magnetization M(t)) mono- or bi-exponentially as a function of the variable evolution time t according to:

$$I(t) = I_0(1 - 2\exp(-t/T_{1H}))$$

or

$$I(t) = I_0^s(1 - 2\exp(-t/T_{1H}^s)) + I_0^l(1 - 2\exp(-t/T_{1H}^l))$$

For the bi-exponential analysis, the superscripts s and l refer to the fractions and T_{1H} values with short and long decay time, respectively. Recall that proton wide-line experiments are acquired without the use of the decoupler channel (see section 2.3).

Figure 3-12 depicts the pulse sequence diagram used for the proton wide-line $T_{1\rho H}$ experiment. The $T_{1\rho H}$ decay times were measured by applying a spin-lock field (45 kHz) of variable duration t_{SL}. Hereto the equilibrium magnetization M_0 is first tilted in the y' direction by a $90°_{x'}$ pulse. The magnetization is then spin-locked (cf. section 2.3). In the experiments presented in this chapter, the variable spin-lock time t_{SL} was varied between 0.25 and 350 ms. During the variable spin-lock time $T_{1\rho H}$ relaxation occurs. Before detection, the magnetization is further subjected to the solid-echo part.

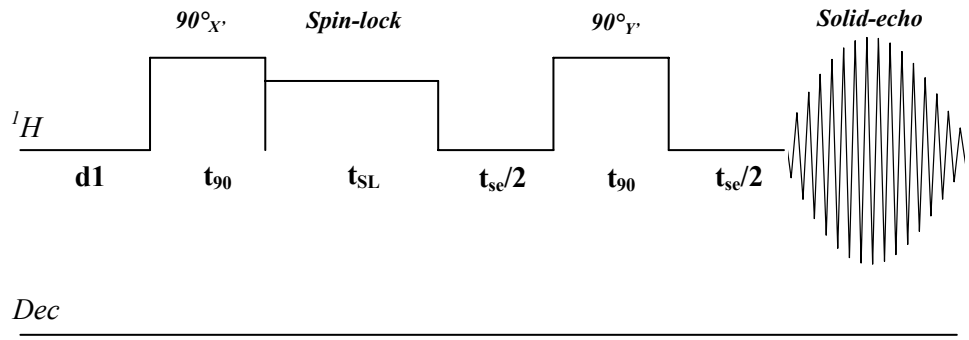

Figure 3-12: *Pulse sequence of the proton wide-line $T_{1\rho H}$ experiment.*

The integrated proton signal intensity $I(t_{SL})$ as a function of the duration of the spin-lock field t_{SL} was analyzed by the sum of two or three exponential functions:

$$I(t_{SL}) = I_0^s \exp(-t_{SL} / T_{1\rho H}^s) + I_0^i \exp(-t_{SL} / T_{1\rho H}^i)$$

or

$$I(t_{SL}) = I_0^s \exp(-t_{SL} / T_{1\rho H}^s) + I_0^i \exp(-t_{SL} / T_{1\rho H}^i) + I_0^l \exp(-t_{SL} / T_{1\rho H}^l)$$

The superscripts s, i and l refer to the fractions and $T_{1\rho H}$ values with short, intermediate and long relaxation decay times, respectively.

All experimental relaxation data were subsequently converted into an ASCII file, read into the Kaleidagraph 3.0.2 or Origin 6.1 program and analyzed by a non-linear least-squares fit (Levenberg-Marquardt algorithm)[22]. The normalized molar proton fractions, with an error of about 2%, are presented between brackets in the tables that summarize the experimental results; the error on T_{1H} and $T_{1\rho H}$ is about 4% and 6%, respectively.

3.6 References

1. Hide, F.; Diaz-Garcia, M.; Schwartz, B. ; Andersson, M.; Pei, Q.; Heeger, A.J., *Science* **1996**, 273, 1833.
2. Hadipour, A.; de Boer, B.; Blom, P.W.M., *Organic Electronics* **2008**, 9, 617.
3. Hoppe, H.; Niggemann, M.; Winder, C.; Kraut, J.; Hiesgen, R.; Hinsch, A.; Meissner, D.; Sariciftci, N.S., *Adv. Funct. Mater.* **2004**, 14, 1005.
4. Martens, T.; D'Haen, J.; Munters, T.; Beelen, Z.; Goris, L.; Manca, J.; D'Olieslaeger, M.; Vanderzande, D.; De Schepper, L.; Andriessen, R., *Synth. Met.* **2003**, 138, 243.
5. Martens, T.; D'Haen, J.; Munters, T.; Beelen, Z.; Goris, L.; Manca, J.; D'Olieslaeger, M.; Vanderzande, D.; De Schepper, L.; Andriessen, R., *Proc. SPIE-Int. Soc. Opt. Eng.* **2003**, 4801, 40.
6. Hoppe, H.; Drees, M.; Schwinger, W.; Schäffler, F.; Sariciftci, N.S., *Synth. Met*. **2005**, 152, 117.
7. van Duren, J.K.J.; Yang, X.; Loos, J.; Bulle-Lieuwma, C.W.T.; Sieval, A.B.; Hummelen, J.C.; Janssen, R.A.J. *Adv. Funct. Mater.* **2004**, 14, 425.
8. Brabec, C.J.; Cravino, A.; Meissner, D.; Sariciftci, N.S.; Fromherz, T.; Rispens, M.T.; Sanchez, L.; Hummelen, J.C. *Adv. Funct. Mater.* **2001**, 11, 374.
9. Mozer, A.J.; Denk, P.; Scharber, M.C.; Neugebauer, H.; Sariciftci, N.S.; Wagner, P.; Lutsen, L.; Vanderzande, D.; Kadashchuk, A.; Staneva, R.; Resel, R. *Synth. Met.* **2005**, 153, 81.
10. Yang, X.; Loos, J., *Macromolecules* **2007**, 40, 1353.

11. Fedotov, V.D.; Schneider, H., *Structure and Dynamics of Bulk Polymers by NMR-Methods* **1989**, Springer-Verlag, Berlin.
12. van Bavel, S.S.; Sourty, E.; de With, G.; Loos, J., *Nano Lett.* **2009**, 9, 507.
13. Schmidt-Mende, L.; Fechtenkötter, A.; Müllen, K.; Moons, E.; Friend, R.H.; MacKenzie, J.D., *Science* **2001**, 293, 1119.
14. Rispens, M.T.; Meetsma, A.; Rittberger, R.; Brabec, C.J.; Sariciftci, N.S.; Hummelen, J.C., *Chem. Commun.* **2003**, 2116.
15. Nishizawa, T.; Tajima, K.; Hashimoto, K., *Nanotechnology* **2008**, 19, 424017.
16. Hummelen, J.C.; Knight, B.W.; LePeq, F.; Wudl, F., *J. Org. Chem.* **1995**, 60, 532.
17. Kim, J. Y.; Frisbie, C.D., *J. Phys. Chem. C* **2008**, 112, 17726.
18. Zhao, J.; Swinnen, A.; Van Assche, G.; Manca, J.; Vanderzande, D.; Van Mele, B., *J. Phys. Chem. B* **2009**, 113, 1587.
19. Martens, T., *Relations between morphology and electro-optical properties of MDMO-PPV:PCBM bulk heterojunction organic solar cells* **2008**, PhD dissertation.
20. Krebs, F.C., *Sol. Energy Mater. Sol. Cells* **2009**, 93, 394.
21. Powles, J.G.; Strange, J.H., *Proc. Phys. Soc.* London **1963**, 82, 6.
22. Marquardt, D.W., *J. Soc. Ind. Appl. Math.* **1963**, 431.

Chapter Four

A Closer Look at the Electron Acceptor PCBM

4.1 Introduction

In spite of the fact that methanofullerene PCBM[1] is one of the first electron acceptors used in the field of BHJ solar cells[2], to date it is still one of the most successful ones. Several other functionalized fullerenes and other materials, including electron-transporting polymers and small molecules as perylene derivatives, have been evaluated as substitute acceptors[3,4]. Nonetheless, photovoltaics built from PCBM consistently achieve the highest power conversion efficiency[5,6]. Therefore it is no surprise that PCBM is the most encountered electron acceptor in studies contributing to the subject of OPVs.

As discussed in chapter three, PCBM turns out to be partly phase separated in MDMO-PPV/PCBM films casted from toluene solutions with high PCBM content. The phase separated PCBM appears as large and well-defined crystalline domains. The PCBM segregation in such photoactive layers was appropriately described on the basis of long T_{1H} as well as $T_{1\rho H}$ relaxation decay times, which are characteristic for crystalline structures. However, as will be demonstrated in the contiguous chapters, the description of the nanomorphology of other D/A systems can be more complex. In MDMO-PPV/PCBM films casted from chlorobenzene for instance, the dimension and organization of the phase separated PCBM clusters are quite different. Yang *et al* claimed the existence of PCBM nanocrystals in composite polymer/fullerene[7] and pure PCBM[8] films casted from chlorobenzene.

On account of the importance of PCBM in the domain of organic solar cells and to obtain reliable reference values which could be useful to tackle more complex morphologies, it was decided to study first the relaxation behavior of PCBM in more detail. Hereto thin (50 and 100 nm) doctor bladed PCBM films were prepared from chlorobenzene solutions. Furthermore, the purity of as-received PCBM will be discussed and attempts were made to convert it into the amorphous state.

For a more extended investigation and description of the NMR relaxation behavior of PCBM, the chemical shift selective ^{13}C solid-state NMR techniques[9] were introduced, next to ^{1}H wide-line NMR. Finally the findings were complemented with XRD and DSC measurements.

4.2 Chemical purity of as-received PCBM

In acquiring proton liquid-state NMR spectra of PCBM it was noticed that the purchased PCBM (Solenne B.V.; Groningen, The Netherlands) was not completely pure. Figure 4-1 shows the proton liquid-state spectra of as-received PCBM dissolved in deuterated acetone, dimethyl sulfoxide (DMSO) and chlorobenzene (CB). In each of these spectra the peaks originating from the residual not-deuterated solvent are indicated by their name, H_2O resonances are indicated by the symbol ◆. The latter were already present in the spectra of the pure deuterated solvents. The resonances indicated by the symbol ■ in the acetone spectrum are the ^{13}C satellites of the solvent peak.

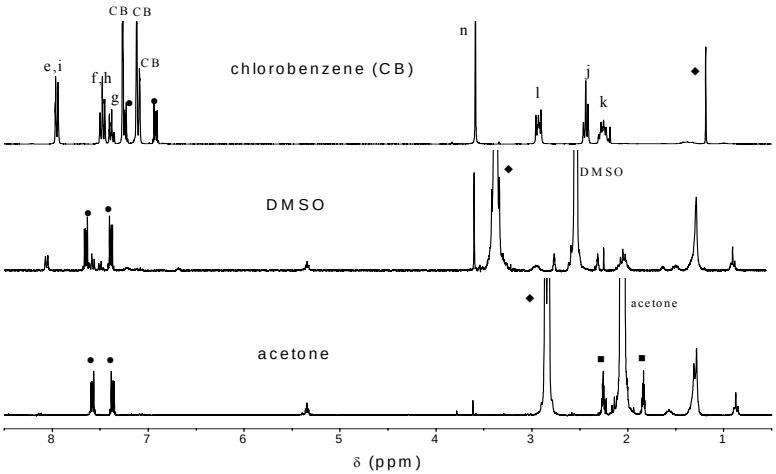

***Figure 4-1**: Proton liquid-state NMR spectra of as-received PCBM in deuterated acetone (bottom), DMSO (centre) and chlorobenzene (top). Symbols are explained in the text.*

Although PCBM is insoluble in acetone and precipitated in the NMR tube, the colorless acetone became red upon adding PCBM. Moreover, in the proton

spectrum acquired from this sample (figure 4-1-bottom) no PCBM resonances were observed. Instead impurities were noticed from which the most important/intense is indicated by the symbol ●. In conclusion PCBM is not soluble in acetone; the dark red color originates from the soluble impurities. Likewise in DMSO the solubility of PCBM is very poor. Nevertheless some resonances of it become noticeable in the corresponding proton spectrum (figure 4-1-centre). Only in chlorobenzene the solubility of PCBM (4.2 g in 100 ml)[10] is sufficient to observe a clear spectrum (figure 4-1-top).

The numbering scheme for PCBM is presented in figure 4-2 and the signal assignment of the proton resonances is indicated in figure 4-1-top. Figure 4-3-left shows a 'zoom-in' on the aromatic region of the PCBM spectrum in deuterated chlorobenzene.

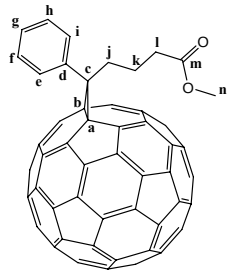

Figure 4-2: *Numbering scheme for PCBM.*

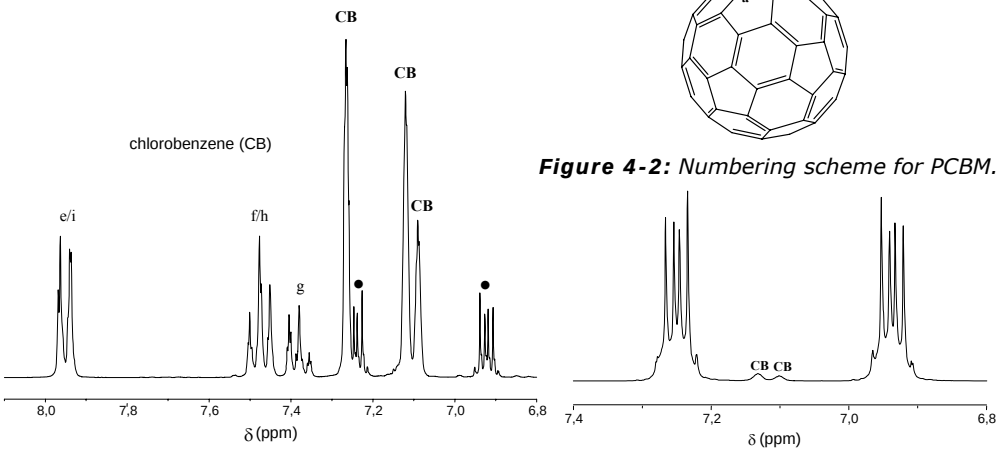

Figure 4-3*: 'Zoom-in' on the aromatic region of the proton liquid-state spectra of as-received PCBM (left) and ortho-dichlorobenzene (right) in deuterated chlorobenzene.*

The 'zoom-in' additionally reveals that the main impurity (indicated by the symbol ●) contains an AA'BB' *ortho*-disubstituted benzene spin system showing resonances perturbed by second order effects. In an AA'BB' system, the A and A' (B and B') protons are chemically equivalent but not magnetically equivalent[11]. The most obvious conclusion is that the main impurity is just residual *ortho*-dichlorobenzene which originates from the synthesis process of PCBM[1]. To check

this, a proton liquid-state spectrum of *ortho*-dichlorobenzene in deuterated chlorobenzene was recorded (figure 4-3-right). As can be noticed, exactly the same chemical shifts (δ (in ppm) : 7.27, 7.26, 7.25, 7.24, 6.96, 6.95, 6.94 and 6.93) and J-coupling pattern are observed. This is further corroborated by thermal desorption–gas chromatography/mass spectrometry (TD-GC/MS). A TD-GC/MS experiment on as-received PCBM revealed dichlorobenzene as the main by-product in the sample (dichlorobenzene represents 81 % of the detected impurities). Remark that with this technique it is not possible to differentiate between the ortho, meta and para isomers. Other by TD-GC/MS identified minor impurities were toluene, xylene, stearic acid and palmitic acid.

The amount of *ortho*-dichlorobenzene in as-received PCBM can be calculated from the quantitative spectrum shown in figure 4-1-top. Both the PCBM signal labeled l and the signal corresponding to the high field protons of *ortho*-dichlorobenzene are representing 2 protons, and are spectroscopically well resolved. The integrated areas of these signals are in the proportion of 2 to 0.9. Taking the molecular weights into account (910 g/mol for PCBM and 147 g/mol for *ortho*-dichlorobenzene), this means that 910 g PCBM corresponds to 66 g *ortho*-dichlorobenzene, i.e. the latter is present for 6.8 wt% in as-received PCBM.

This amount could be confirmed by a TGA (thermal gravimetric analysis) experiment (see figure 4-4). The TGA performed on as-received PCBM (black curve in figure 4-4-left) reveals a loss of weight of about 7 wt% at around 100 °C. This loss of weight can be assigned to the evaporation of *ortho*-dichlorobenzene

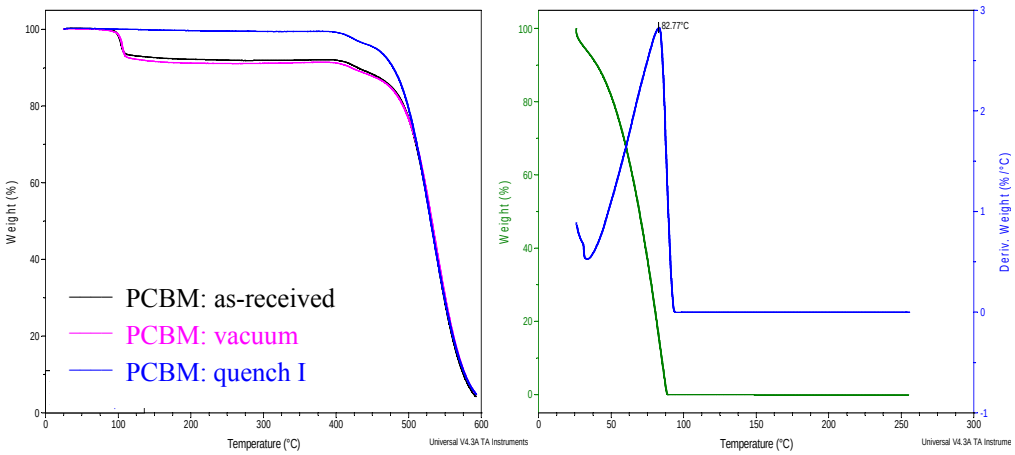

***Figure 4-4**: TGA of different PCBM samples (left) and ortho-dichlorobenzene (right).*

present in as-received PCBM and the observed amount is in very good agreement with the NMR quantification. At first glance it is rather unexpected to observe an evaporation temperature of about 100 °C for *ortho*-dichlorobenzene, knowing that its boiling point is 180 °C[12]. Therefore it was decided to perform a TGA on ortho-dichlorobenzene as well (figure 4-4-right). This TGA experiment reveals that already at 83 °C all the free *ortho*-dichlorobenzene is evaporated. A somewhat higher evaporation temperature of *ortho*-dichlorobenzene that is adsorbed or entrapped between vitrified PCBM can be expected. The reason for the relatively low evaporation temperatures can be found in the experimental set-up: the use of a continuous nitrogen flow over an open sample pan.

Note that *ortho*-dichlorobenzene remains present after putting as-received PCBM for 24 hours under vacuum (10^{-3} mbar) (see violet curve "PCBM vacuum" in figure 4-4-left). During the film processing, however, part of the *ortho*-dichlorobenzene will evaporate. This is demonstrated in figure 4-5 which shows the aromatic part of a proton liquid-state NMR spectrum of a 100 nm thick doctor bladed PCBM film. As indicated by the arrow, the *ortho*-dichlorobenzene is still present in the film, albeit in a decreased quantity of about 2 wt% (the integrated areas of the signals described above are in the proportion of 2 to 0.26).

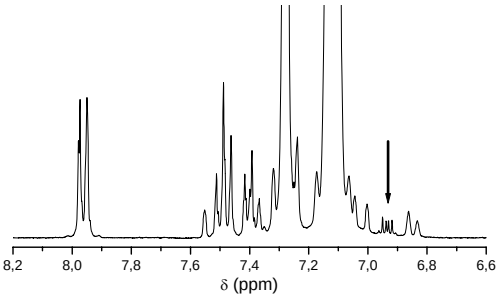

***Figure 4-5**: Aromatic part of a proton liquid-state NMR spectrum in deuterated chlorobenzene of a 100 nm thick doctor bladed PCBM film. The right part of the resonances corresponding to ortho-dichlorobenzene are indicated by an arrow.*

Since PCBM is the most frequently used electron acceptor in active layer blends of organic photovoltaics, it might be worthwhile for scientists involved in the field to check its structure and purity by liquid-state NMR.

4.3 Attempts to obtain amorphous PCBM

In order to achieve reference values for the NMR relaxation experiments in the next chapters, several attempts to obtain fully amorphous PCBM were performed as will be described below. A first trial consisted in heating PCBM above its melting point and quenching it in liquid nitrogen. The maximum heating temperature, in order to avoid degradation, was derived from the TGA experiments presented in figure 4-4-left. No thermal degradation is observed up to 400 °C. Zhao *et al*[13] reported about melting peaks for PCBM at 267.5 °C and 287.7 °C. Therefore as-received PCBM was heated for 10 minutes at 330 °C and quenched in liquid nitrogen ("quench I"). Remark that the *ortho*-dichlorobenzene in the PCBM has disappeared in this quenched sample as confirmed both by TGA (blue curve in figure 4-4-left) and NMR (figure 4-6-bottom).

As will be discussed in section 4.4, sample "quench I" was at first glance not fully amorphous. Therefore two additional quenching experiments were performed in which as-received PCBM was heated for 15 minutes at 360 °C ("quench II") and for 60 minutes at 350 °C ("quench III"), respectively. It is clear that heating the PCBM sample for long time periods above 350 °C results in degradation (figure 4-6-top).

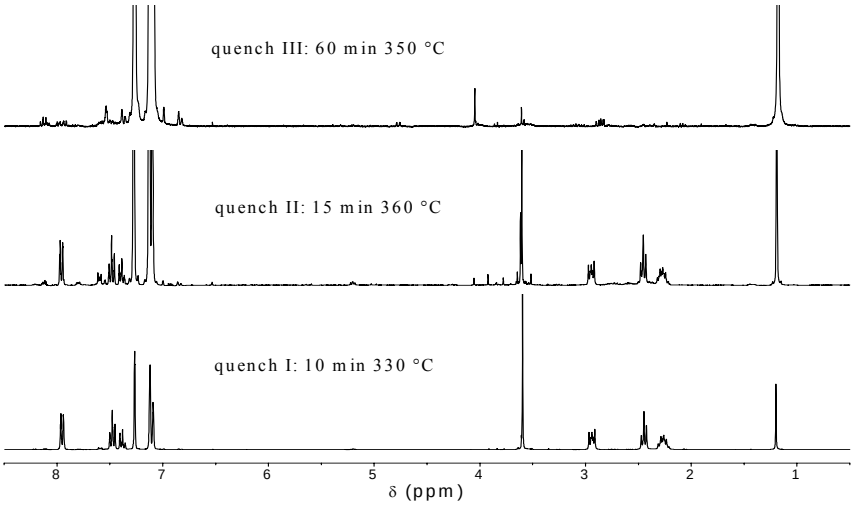

***Figure 4-6**: Proton liquid-state NMR spectra of PCBM samples in deuterated chlorobenzene: "quench I" (bottom), "quench II" (centre) and "quench III" (top).*

A second trial to obtain fully amorphous PCBM was accomplished by fast precipitation of as-received PCBM in an ice-cold non-solvent like acetone. Hereto, as-received PCBM was dissolved in chlorobenzene (4 g per 100 ml) by stirring overnight at 50°C, followed by precipitation in a 50-fold excess of ice-cold acetone. After centrifugation for 10 min at 3000 rpm, the supernatant was removed and the PCBM was dried under vacuum overnight. Note that the acetone also removes the *ortho*-dichlorobenzene impurity as is confirmed by the proton NMR in figure 4-7. In the latter spectrum, the signals at 6.84, 6.87 and 7.01 ppm (indicated by the symbol ■) are no impurities but ^{13}C satellites of the chlorobenzene solvent peaks ($^{1}J_{CH}$ constants of 165, 160 and 159 Hz, respectively).

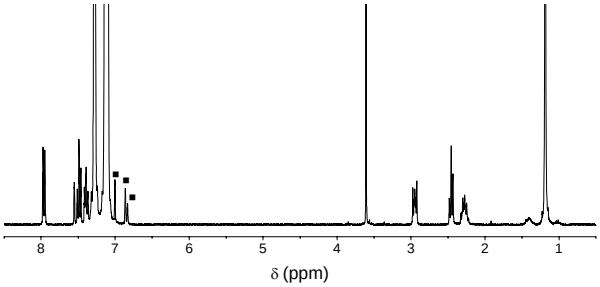

***Figure 4-7**: Proton liquid-state NMR spectrum of PCBM in deuterated chlorobenzene after precipitation in a 50-fold excess of ice-cold acetone.*

4.4 Proton wide-line NMR, DSC & XRD of treated PCBM

Proton wide-line NMR was performed to investigate the morphology and physico-chemical nature of as-received, "Konarka", acetone-precipitated, thermally quenched and doctor bladed (from chlorobenzene solutions) PCBM. Table 4-1 presents the T_{1H} and $T_{1\rho H}$ relaxation decay times and corresponding normalized molar proton fractions. "Konarka" PCBM was a gift of Konarka-Austria. Most of these samples were also studied by differential scanning calorimetry (DSC) and X-ray diffraction (XRD) techniques.

***Table 4-1**: T_{1H} and $T_{1\rho H}$ relaxation decay times measured by proton wide-line NMR of as-received, "Konarka", acetone-precipitated, thermally quenched and doctor bladed PCBM samples.*

PCBM sample:	T_{1H} (s)	$T_{1\rho H}$ (ms)
as-received	2.3 (30%) **21.7 (70%)**	7.1 (27%) **189 (73%)**
Konarka	3.1	3.2 (31%) 22.0 (69%)
precipitated in acetone	1.2	2.1 (36%) 15.1 (64%)
quench I *	1.1 (41%) 4.8 (59%)	3.0 (25%) 17.9 (75%)
quench II *	1.1 (40%) 5.6 (60%)	2.8 (20%) 19.1 (80%)
quench II-aged	1.2	2.1 (18%) 20.0 (82%)
doctor bladed (50nm)	1.1	2.0 (32%) 16.0 (68%)
doctor bladed (100nm)	1.4	2.3 (29%) 18.4 (71%)

* *metastable*

4.4.1 PCBM: as-received from Solenne

The attentive reader will notice slightly different decay times and normalized molar proton fractions for as-received PCBM in table 4-1 with respect to the decay times and fractions listed in table 3-1. This is just the batch to batch variation of commercial PCBM. But in general the same conclusion can be drawn, i.e. as-received PCBM is highly crystalline in nature which can be decided on the basis of the extremely long T_{1H} and $T_{1\rho H}$ decay times[14] and corresponding molar proton fractions (shown in bold in table 4-1).

The DSC thermogram (first run) in figure 4-8 shows the heat flow (HF) of

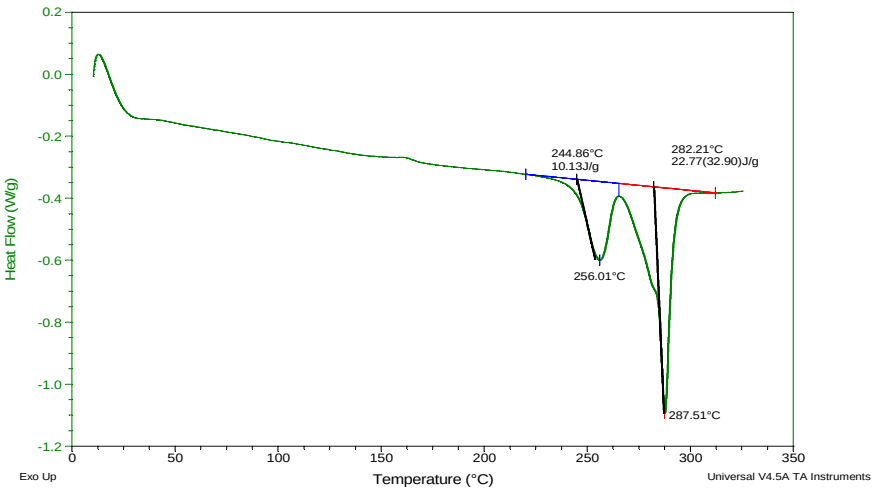

***Figure 4-8:** DSC thermogram (first run) showing heat flow (HF) for as-received PCBM.*

as-received PCBM. Double melting peaks are observed at 256.0 and 287.5 °C with areas of 10.1 and 22.8 Jg^{-1}, respectively. These melting peaks approximately appear at the same temperatures as reported in literature[13,15] and correspond to endothermic phase transitions which originate from the melting of the large well-defined PCBM crystallites. Note that Rispens *et al*[16] reported about a monoclinic and triclinic crystal structure for PCBM. The presence of well-organized PCBM crystals is confirmed by XRD (see figure 3-2) and these are, as measured by proton wide-line NMR, present for about 70 %. Indeed, a certain length of coherence is needed to observe sharp reflection lines in XRD patterns.

4.4.2 PCBM: provided by Konarka

A powder PCBM sample provided by Konarka was investigated as well. No extremely long T_{1H} and $T_{1\rho H}$ decay times were observed for this sample (see table 4-1). Moreover, the T_{1H} relaxation becomes mono-exponential with a decay time of 3.1 s. Based on the values of the T_{1H} and intermediate $T_{1\rho H}$ (cf. the spin diffusion equation $L=(6.D.T_{iH})^{1/2}$), the average dimension of the crystals has to be situated between 7 and 85 nm.

The XRD pattern shows, as demonstrated in figure 4-9, still relatively sharp reflection lines, albeit less pronounced as compared to as-received "Solenne" PCBM (figure 3-2). Based on this wide-line NMR and XRD information, it can be

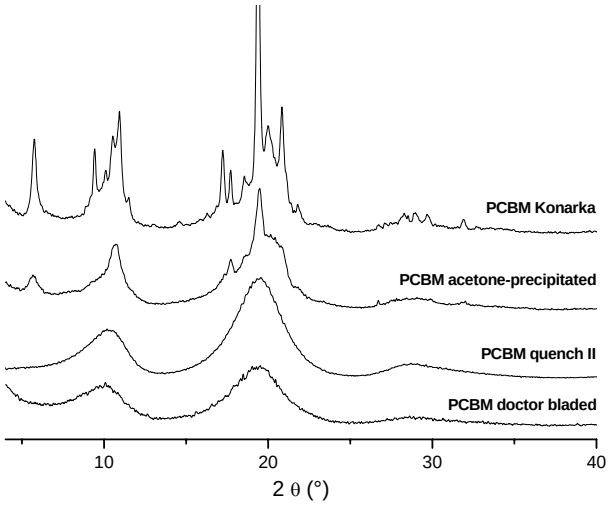

***Figure 4-9**: XRD patterns of different PCBM samples.*

concluded that PCBM crystallites are still present in the "Konarka" PCBM but that the average dimension of the crystals is significantly smaller as compared to as-received "Solenne" PCBM.

The presence of crystallinity is also demonstrated in figure 4-10 showing the first run HF trace of "Konarka" PCBM. Double melting peaks are observed at 259.6 and 285.4 °C with areas of 4.9 and 14.6 Jg^{-1}, respectively. Note that the total area of the enthalpic transitions (19.5 J/g) is only 59 % with respect to the melting enthalpies of as-received PCBM (32.9 J/g).

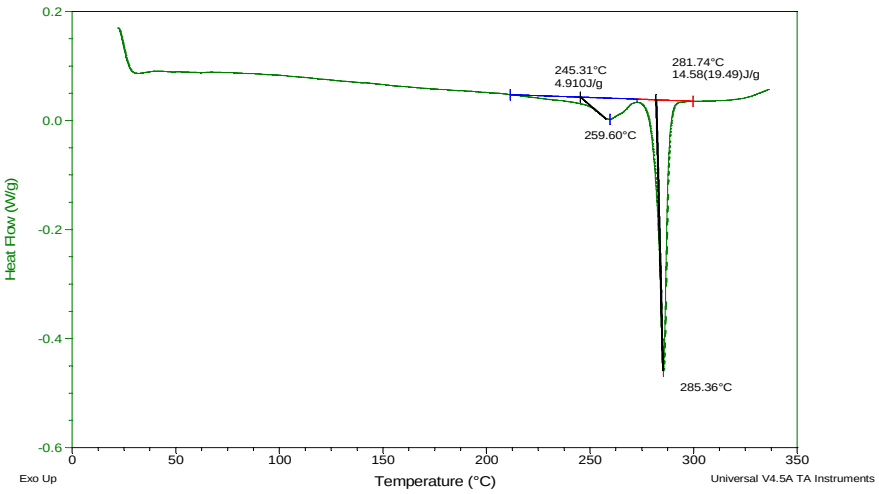

Figure 4-10: *DSC thermogram (first run) showing HF for "Konarka" PCBM.*

4.4.3 PCBM: precipitated in ice-cold acetone

Precipitation in a non-solvent like acetone gives rise to PCBM of which the T_{1H} relaxation behaves mono-exponentially with a short decay time of 1.2 s (table 4-1). This indicates that well-defined crystallites are no longer present. If crystallization of PCBM takes place at all, this means that the molecular domains should be smaller than about 55 nm.

The $T_{1\rho H}$ relaxation, on the other hand, still behaves bi-exponentially with an intermediate $T_{1\rho H}$ decay time of 15.1 ms. Based on the values of the T_{1H} and intermediate $T_{1\rho H}$ decay times, the average dimension of the PCBM clusters has to be situated between 6 and 55 nm. This means that the PCBM molecules appear in a low-order organization, i.e. in so-called nanocrystals. The presence of crystallinity

is also demonstrated in figure 4-11 showing the first run HF trace of acetone-precipitated PCBM. Double melting peaks are observed at 260.9 and 284.5 °C with areas of 4.6 and 13.1 Jg^{-1}, respectively. Note that the total area of the enthalpic transitions (17.8 J/g) is only 54 % with respect to the melting enthalpies of as-received PCBM (32.9 J/g). The transition around 146 °C is probably the glass transition of PCBM.

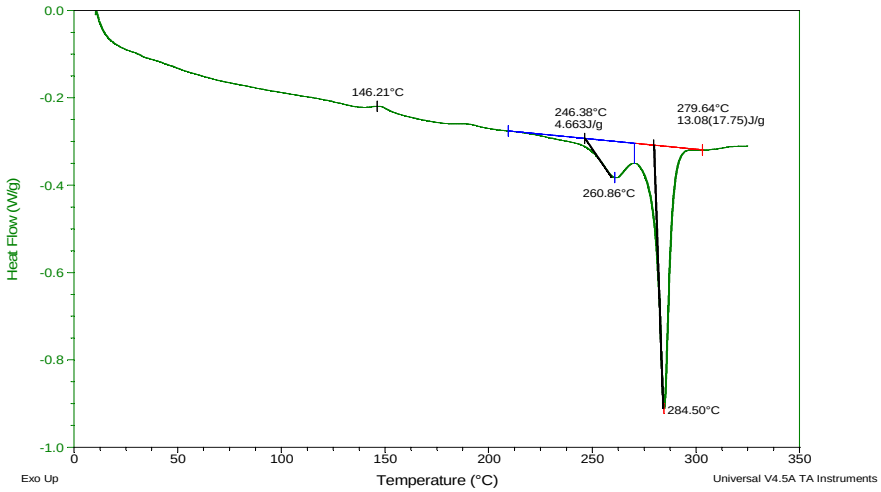

Figure 4-11: *DSC thermogram (first run) showing HF for acetone-precipitated PCBM.*

The nanomorphology of the acetone-precipitated PCBM can therefore be described as nanocrystals surrounded by amorphous PCBM. Such a morphology explains why the T_{1H} relaxation is driven, due to spin diffusion, by the surrounding amorphous PCBM. This conclusion is further supported by the XRD pattern in figure 4-9 showing still some defined reflections although already strongly broadened as compared to the reflections observed for the "Konarka" PCBM. It is most likely that the PCBM coherence reaches the limit for detection by XRD. Further loss of coherence will lead to broad halos in XRD patterns.

4.4.4 PCBM: thermally quenched

The T_{1H} relaxation of the PCBM samples "quench I" and "quench II" is still bi-exponentially with a short and intermediate decay time (see table 4-1). Note that the molar fraction of the intermediate T_{1H} decay time is quite high (60%). However, no extremely long T_{1H} decay times are observed as for well-defined

crystallites. Also the $T_{1\rho H}$ relaxation behaves bi-exponentially, but with an intermediate decay time of only 18-19 ms. The presence of an intermediate T_{1H} decay time (with high molar fraction) without a longer $T_{1\rho H}$ decay time is remarkable. It should be pointed out, however, that quenching the molten PCBM in liquid nitrogen (very abrupt temperature decrease from 360 °C down to –196 °C) results in a metastable PCBM state. Indeed, if the PCBM sample "quench II" was remeasured one week after preparation (referred to as sample "quench II–aged"), only a single short T_{1H} decay time of 1.2 s was observed. So even time ageing at room temperature seems to be enough to induce changes in this metastable phase morphology.

Figure 4-12 gives an overview of the findings by XRD, DSC and T_{1H} NMR for the PCBM samples "quench II" (immediately after preparation) and "quench II-aged" (after 20 days of time ageing at room temperature). As can be noticed in figure 4-12, only broad halos are observed in the XRD pattern of both samples. This indicates that if PCBM nanocrystals are present in these samples, their coherence length should be shorter as in the acetone-precipitated sample. Regarding the bi-exponential T_{1H} behavior of the "quench II" sample, recall that

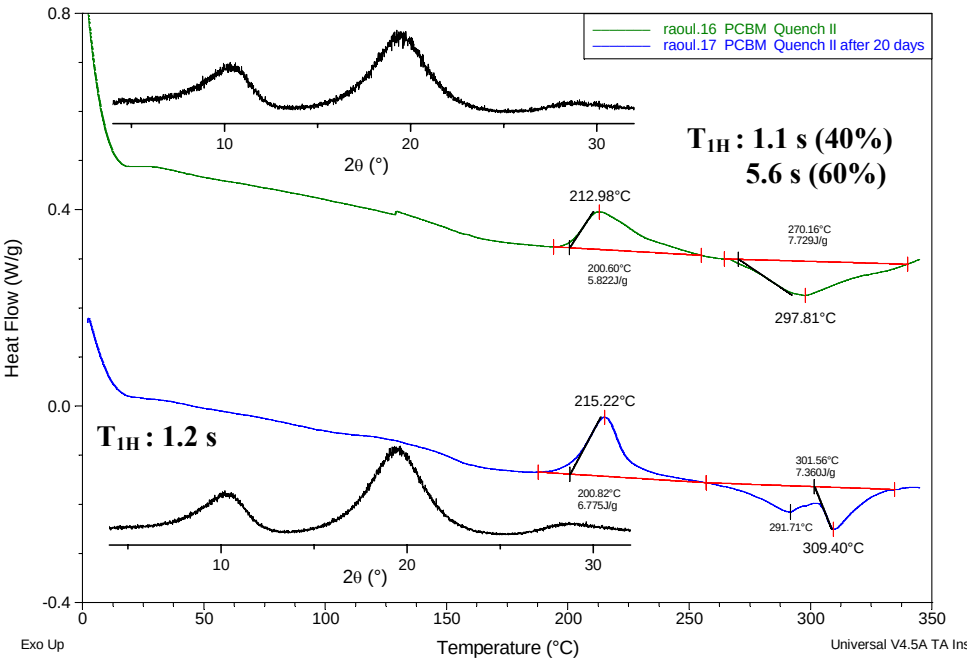

***Figure 4-12**: Overview of the XRD, DSC and wide-line T_1H results of the "quench II" (top) and "quench II-aged" (bottom) PCBM samples.*

for 30/70 wt% MDMO-PPV/PCBM films processed from toluene (chapter 3), having a T_{1H} of 6.2 s, still sharp reflections were observed in XRD. This despite the molar fraction of well-defined crystallites was only 19 % (table 3-3). However, for this 30/70 wt% blend, also a long $T_{1\rho H}$ (53.5 ms) was observed.

Likewise the DSCs are different for the "quench II" and "quench II-aged" PCBM. In the heat flow traces of both samples, an exothermic cold crystallization peak is observed at about 215 °C which is sharper for the aged sample. In addition, after ageing its area is increased from 5.8 to 6.8 Jg^{-1}. Concerning the melting, a broad endothermic melting peak is observed at 298 °C with an area of 7.7 Jg^{-1} for the "quench II" sample, while the aged sample shows double melting peaks at 292 and 309 °C with a total area of 7.4 Jg^{-1}. Although we do not know the molar enthalpy of cold crystallization, we can state that most of the area of the melting peak represents the melting of crystals formed by cold crystallization. In other words, that thermal quenching followed by time ageing results in a highly unorganized PCBM morphology. According to the NMR results, the average dimensions of these nanocrystals should be situated between 6 and 55 nm as is the case for acetone-precipitated PCBM. However, XRD and DSC are clearly pointing to the lower limits of this NMR based dimension interval, i.e. in the order < 20-25 nm. In conclusion, the morphology can be described as very small PCBM clusters surrounded by amorphous PCBM.

4.4.5 PCBM: doctor bladed

Thin doctor bladed PCBM films casted from solutions in chlorobenzene were prepared as well to obtain samples in which the processing resembles the one encountered in organic solar cells. Films of 50 and 100 nm in thickness were casted. For the doctor bladed films the same, within experimental error, T_{1H} and $T_{1\rho H}$ relaxation decay times and molar proton fractions are found as for the acetone-precipitated PCBM sample. This again indicates dimensions between 6 and 55 nm for the nanocrystals. Such a morphology was already quoted by Yang *et al*[8] via SAED (Selected-Area Electron Diffraction) on spin-coated PCBM films. They observed a diffraction pattern which consisted of several blurred and broad diffraction rings. According the authors, these Debye-Scherrer rings could arise from films which (i) are amorphous without any long-distance order, (ii) consist of mesoscopic low-order domains, or (iii) are composed of densely and

homogeneously distributed PCBM nanocrystals. However, arguments were presented that suggest the presence of densely and homogeneously distributed PCBM nanocrystals.

Figure 4-13 shows the first run HF trace of doctor bladed PCBM. In contrast to the "quench II-aged" sample, there is a clear difference between the area

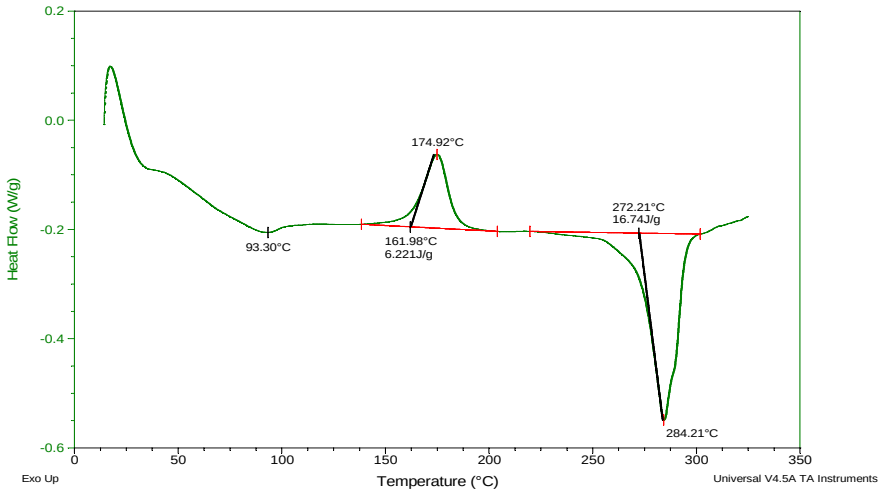

Figure 4-13: *DSC thermogram (first run) showing HF for the 100 nm thick doctor bladed PCBM film.*

of the cold crystallization peak around 175 °C (6.2 Jg^{-1}) and that of the melting peak (16.7 Jg^{-1}). The lower crystallization temperature (175 °C versus 215 °C for the "quench II-aged" PCBM) probably indicates that more/improved crystallization ents are already present in the doctor bladed films. However, no resolved double melting peaks are observed as for the acetone-quenched sample. Moreover, the XRD pattern only shows broad bands indicating that the dimensions of the nanocrystals are also situated at the lower limits of the NMR based dimension interval (figure 4-9). However, DSC points to a higher amount of nanocrystals.

4.4.6 Conclusions

As a conclusion of this, non-chemical shift selective, proton wide-line NMR relaxometry study one can state that:

- In general PCBM has a very high tendency to crystallize. It will therefore be very difficult, if possible at all, to prepare fully amorphous PCBM.

- Only the observation of a long T_{1H} as well as a long $T_{1\rho H}$ relaxation decay time indicates the presence of well-defined crystals.
- Nanocrystals are likely present in all treated PCBM samples. However, proton wide-line NMR results have to be supported by DSC and XRD to situate the dimension of the nanocrystals within the NMR based dimension interval. Therefore the treated samples were further investigated by means of local T_{1C} probes and the chemical shift selective ^{13}C-MAS technique as will be discussed in the next section. The main goal is twofold: besides attempting to further refine the dimensions of the nanocrystals, the focus will be on the quantification of the molar amount of nanocrystalline PCBM.

4.5 Solid-state ^{13}C MAS NMR of treated PCBM

As demonstrated in section 4.4, the nanomorphology of PCBM films can be qualitatively described by proton wide-line NMR in combination with DSC and XRD. However, in order to quantify the blend morphology of complex D/A systems in more detail, the local carbon spin-lattice relaxation decay times T_{1C} were determined via the chemical shift selective ^{13}C MAS technique (see pulse sequence in figure 4-20) to obtain quantitative information. Recall that T_{1C} is a very local parameter since this decay time is not influenced by the process of spin diffusion. In addition, since the dipolar mechanism falls off rather fast with the distance between the observed carbon spins and the neighboring protons (as $1/r^3$; effective dipolar coupling if $r \leq 10$ Å) it is only efficient at short distance (cf. chapter 2). Remark that the T_{1C} fractions presented in this section are mol % fractions here as the T_{1C} is measured via a PCBM carbon signal.

Figure 4-14 shows a typical CP/MAS spectrum of PCBM. The numbering scheme for the carbons is presented in figure 4-2. Although the signal assignment of PCBM is already described in literature[17] some discrepancies were noticed. Therefore it was decided to study first the solution carbon-13 spectrum of PCBM in somewhat more detail, i.e. by analyzing a quantitative carbon spectrum and an APT spectrum (figure 4-15). In an APT spectrum (see figure 4-19 for the pulse sequence) non-protonated and methylene carbons show negative intensities while methyl and methine carbons show positive intensities.

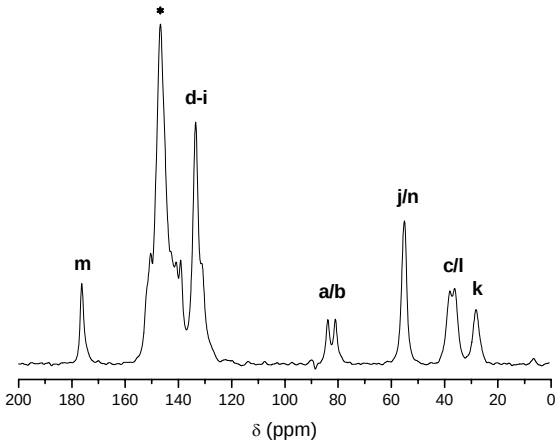

***Figure 4-14**: Solid-state ^{13}C CP/MAS NMR spectrum of as-received PCBM taken with a contact time of 3.5 ms. The signal marked with an * arises from the main resonance of PCBM at 146 ppm.*

Based on the solution spectra, the signals at 173 and 51 ppm can easily be assigned to the carbonyl (C_m) and methoxy carbons (C_n is the only signal with a positive intensity in the APT spectrum), respectively. Yang *et al*[17] assigned the methoxy carbon to a signal at 62 ppm, a position were no signal appears in our spectra (figure 4-14 and 4-15). The origin of this 62 ppm signal remains unclear. The signal at 81 ppm with double intensity in the quantitative carbon spectrum results from the quaternary bridge carbons C_a and C_b of PCBM which were not noticed in literature due to overlap with the spinning side bands of the aromatic resonances. These bridge carbon signals are clearly observed in the solid state spectrum of figure 4-14 since the spinning side bands fall completely out of the ^{13}C spectral range due to fast rotor spinning at 14 kHz. Remark that the chemical shift anisotropy (cf. section 2.2.2) of the C_a and C_b carbons is not averaged out by fast molecular motions in the solid state. The signals at 52, 34 (integrates for 2) and 23 ppm can be assigned to C_j, C_c/C_l and C_k, respectively. The resonances between 125 and 150 ppm can be attributed to the phenyl carbons C_d, C_e/C_i, C_f/C_h, C_g and the fullerene C_{60} carbons of which the highest intensity is situated around 146 ppm (indicated by an ∗ in figure 4-14).

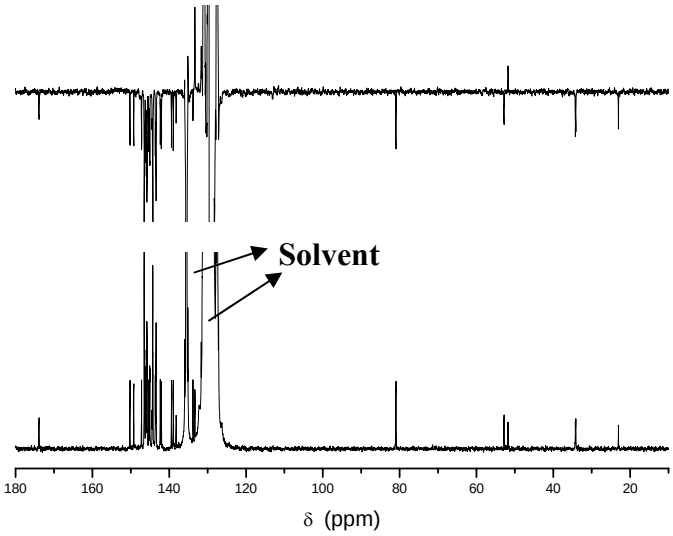

Figure 4-15: *Attached Proton Test (APT) spectrum (top) and quantitative ^{13}C spectrum (bottom) of PCBM dissolved in a 1:2 mixture of chlorobenzene/C_6D_6 containing 20 mM of $Cr(acac)_3$ as a relaxation agent.*

In the following ^{13}C solid-state NMR part, attention is focused on the T_{1C} relaxation behavior of the main PCBM resonance at 146 ppm. The results for the investigated PCBM samples, i.e. as-received, "Konarka", acetone-precipitated, "quench II-aged" and 100 nm thick PCBM films prepared by doctor blading from solutions in chlorobenzene are summarized in table 4-2. As can already be read out from table 4-2 for the last four PCBM samples, the discriminating power of the T_{1C} probe is much higher as compared to the $T_{1\rho H}$ probe (table 4-1). This holds for the decay times as well as for the molar fractions. Notice that the T_{1C} decay time values are in the order of tens of seconds while the $T_{1\rho H}$ decay times are in the order of only milliseconds to tens of milliseconds.

Table 4-2*: T_{1C} relaxation decay times of the main signal at 146 ppm of different PCBM samples measured by means of the ^{13}C MAS technique. Due to the extremely long decay time of PCBM crystallites, no fully quantitative measurement was performed on as-received Solenne PCBM.*

PCBM sample:	**T_{1C} (s)**	
as-received	±35	**±380**
Konarka	14.0 (23%)	58.2 (77%)
precipitated in acetone	16.0 (49%)	61.4 (51%)
quench II-aged	13.2 (42%)	49.8 (58%)
doctor bladed (100 nm)	11.2 (26%)	42.7 (74%)

4.5.1 As-received PCBM

As expected an extremely long T_{1C} relaxation decay time (presented in bold in table 4-2) is observed for as-received PCBM which corroborate the proton wide-line NMR experiments described in section 4.4.1. Note that for as-received PCBM no fully quantitative analysis was performed (due to time reasons) as the only goal was to assign the very long relaxation decay time to well-defined crystallites. Moreover, a second intermediate decay time of about 35 s is detected. This intermediate T_{1C} decay time (probably) represents the nanocrystals as well as the surrounding amorphous PCBM. The intermediate decay time is then the averaged value of two phase specific decay times, i.e. these corresponding to nanocrystals (T_{1C} ~ 40-60 s) and to unorganized, amorphous PCBM (T_{1C} ~ 10-15 s). Since the experiment was not carried out quantitatively (due to the presence of the extremely slow relaxing component), it was impossible to discriminate them mathematically.

4.5.2 "Konarka" PCBM

Regarding the T_{1C} relaxation, "Konarka" PCBM shows a relatively short and intermediate T_{1C} relaxation decay time. Recall that T_{1C} is a local parameter, not influenced by spin diffusion, which explains why the T_{1C} relaxation is not averaged out as it is for the T_{1H} relaxation. A short T_{1C} of 14 s is observed for amorphous PCBM. This value is already quite long since it concerns the relaxation of non-protonated C_{60} carbons (cf. section 2-4). The longer decay time of about 60 s on the other hand, represents the small, ordered PCBM clusters (i.e. the nanocrystals). On no account extremely long decay times, as observed for as-received PCBM, are detected. In conclusion, the T_{1C} findings further support the morphological description of the "Konarka" PCBM as already provided before (section 4.4.2). In addition, the molar amount of PCBM organized into nanocrystals could be quantified as being 77 %.

As can be observed in figure 4-9, relatively sharp reflections are still present in the XRD pattern of "Konarka" PCBM. This agrees well with the T_{1H} value of 3.1 s (table 4-1) as well as with the high molar amount (77 %) and relatively high value of about 60 s of the intermediate T_{1C} decay time (table 4-2). It can be inferred from the combination of XRD and T_{1C} relaxometry that most likely

the dimensions of the nanocrystals are situated around the upper limit of the proton wide-line NMR based dimension interval of 7 – 85 nm.

4.5.3 Acetone-precipitated PCBM

Acetone-precipitated PCBM basically shows the same T_{1C} relaxation behavior as "Konarka" PCBM, i.e. a relatively short and intermediate T_{1C} relaxation decay time is measured. A short T_{1C} of 16 s is observed for amorphous PCBM while the intermediate decay time of about 60 s represents the PCBM nanocrystals. No extremely long decay times are detected. Furthermore, the molar amount of PCBM organized into nanocrystals could be quantified as being 51 %. A lower amount, as compared to "Konarka" PCBM, is in agreement with the differences in melting enthalpy observed by DSC (figures 4-10 and 4-11). Also here, the T_{1C} findings further support the morphological description of the acetone-precipitated PCBM as already provided in section 4.4.3.

For the acetone-precipitated PCBM, the XRD lines become less pronounced and more broadened (see figure 4-9). Such a XRD pattern correlates well with the reduced T_{1H} decay time of 1.2 s and the reduced molar fraction (51 %) of the intermediate T_{1C} decay time of about 60 s. For this PCBM sample the dimensions of the nanocrystals are most likely situated around the upper limit of the proton wide-line NMR based dimension interval of 6 – 55 nm.

4.5.4 "Quench II-aged" and doctor bladed (100 nm) PCBM

The same general trend is observed for the T_{1C} relaxation of the "quench II-aged" and doctor bladed PCBM samples (see table 4-2). Regardless of the treatment method, the relaxation behavior is always bi-exponentially with a short and intermediate T_{1C} decay time. In addition, the molar amount of PCBM organized into nanocrystals could be quantified as being 58 and 74 %, respectively. The higher amount of nanocrystals for the doctor bladed sample is further in good agreement with DSC (figures 4-12 and 4-13). The DSC of "quench II-aged" PCBM shows double melting peaks with a total area of 7.4 Jg^{-1}, which is significantly lower as compared to the area of the melting endotherm of 16.7 Jg^{-1} for doctor bladed PCBM.

Moreover, it can be noticed that the value of the intermediate T_{1C} decay time observed for the "quench II-aged" as well as the doctor bladed PCBM is significantly shorter (40-50 s) as compared to the "Konarka" and acetone-precipitated PCBM (around 60 s). This points to decreased dimensions of the nanocrystals. This lower degree of crystalline order is corroborated by XRD (figure 4-9) in which only broad halos are discerned for the "quench II-aged" and doctor bladed PCBM. This observation seems to correlate well with the value of the intermediate T_{1C} decay time. For PCBM samples showing an intermediate T_{1C} decay time exceeding 50-55 s, the degree of coherence of the nanocrystals is still sufficient enough to be observed as sharp reflections in XRD. On the other hand, only broad halos show up in the XRD of PCBM samples with an intermediate T_{1C} below 50 s. For the two samples described in this section, the dimensions of the nanocrystals seem to be situated at the lower limits of the proton wide-line NMR based dimension interval of 6 – 55 nm.

4.5.5 Conclusions from ^{13}C MAS T_{1C} relaxometry

As a conclusion, it can be stated that the local and chemical shift selective T_{1C} probe is able to differentiate further between samples which look rather similar from a point of view of the proton relaxation decay times:

- A further refinement of the by proton wide-line NMR provided dimensional interval for the nanocrystals could be derived based on the value of the intermediate T_{1C} relaxation decay time obtained by ^{13}C MAS relaxometry. This conclusion is strengthened by complementary XRD measurements.
- A quantification of the amount of PCBM nanocrystals is furnished via the fraction corresponding to this intermediate T_{1C} relaxation decay time. This conclusion is qualitatively (due to cold crystallization) supported by DSC.

4.6 TEM & SAED of thin doctor bladed PCBM films

Figure 4-16 shows the bright-field TEM image and corresponding Selected-Area Electron Diffraction (SAED) pattern of a 100 nm thick PCBM film prepared by doctor blading from a solution in chlorobenzene. The TEM image

reveals a rather homogeneous morphology on this distance scale (the marker represents 1000 nm). Nonetheless several clear but broad Debye-Scherrer rings can be distinguished in the corresponding SAED pattern. Yang *et* al[8] noticed a similar SAED pattern in spin-coated thin PCBM films and ascribed these diffraction rings to the presence of a large number of densely and homogeneously distributed PCBM nanocrystals. The TEM and SAED observations for thin PCBM films are in agreement with the proton wide-line NMR and ^{13}C MAS T_{1C} NMR results which indicate a morphology in which nanocrystals are imbedded in the amorphous PCBM phase. But the added value of ^{13}C MAS NMR is that the technique allows to quantify the amount of these nanocrystals.

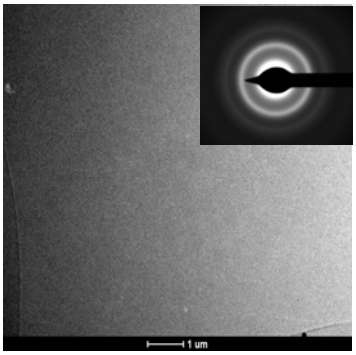

Figure 4-16: *TEM image and corresponding SAED pattern of a 100 nm thick PCBM film prepared by doctor blading from a solution in chlorobenzene.*

4.7 Influence of other solvents on the tendency of PCBM to crystallize

In the kinetic theory of crystallization[18], nucleation of crystals starts with the formation, at a certain temperature, of small but unstable embryo clusters. Some of these embryos shrink while others survive and eventually grow and reach a critical size beyond which they are more likely to grow than to dissolve again, and thus become stable nuclei. After reaching some critical size, the nucleus can provide a growth surface for continued crystallization. The crystallization kinetics of a compound depend on the crystallization conditions (temperature, time, solvent, …) as well as on its molecular architecture.

Since solvent-induced effects (e.g. solubility of PCBM, evaporation rate,…) can be very important with respect to the kinetically determined morphology in thin films casted from solution, the following efforts were further accomplished to obtain fully amorphous PCBM. Hereto, as-received PCBM was dissolved in different solvents before precipitation in ice-cold acetone. The investigated aromatic solvents were *o*-dichlorobenzene, chlorobenzene, *p*-xylene, 1,2,4-trichlorobenzene and *o*-chlorotoluene. The crystallization behavior was monitored by DSC. Unfortunately, as can be inferred from figure 4-17, substantial crystallization endotherms of PCBM are observed for all solvents used. This again indicates that it is difficult to obtain fully amorphous PCBM, if possible at all. Note that the thermograms presented in figure 4-17 were acquired by fast initial heating of the sample up to 150 °C to prevent cold crystallization as much as possible, followed by a heating rate of 10 °C/min.

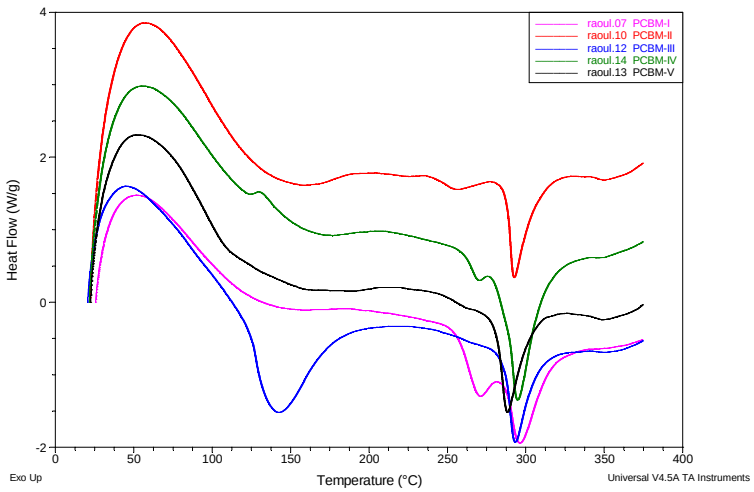

Figure 4-17: *DSC thermograms showing HF for as-received PCBM after precipitation in ice-cold acetone from different solvents: o-dichlorobenzene(I), chlorobenzene(II), p-xylene(III), 1,2,4-trichlorobenzene(IV) and o-chlorotoluene(V).*

4.8 Conclusions

It is demonstrated that commercial PCBM can contain significant amounts of impurities. Based on independent measurements by proton liquid-state NMR and TGA, about 7 wt% *ortho*-dichlorobenzene (next to other minor by-products)

was detected in “Solenne” PCBM.

To achieve appropriate reference values towards the understanding of the relaxation behavior of more complex D/A systems described in the contiguous chapters, several attempts were performed to obtain fully amorphous PCBM. Hereto the as-received “Solenne” PCBM was precipitated in an excess of ice-cold acetone or thermally quenched from the melt. Unfortunately, since PCBM has a very high tendency to crystallize it will be very difficult, if possible at all, to prepare fully amorphous PCBM.

The nanomorphology of differently treated PCBM samples (as-received from “Solenne”, “Konarka”, acetone-precipitated, thermally quenched from the melt and doctor bladed) was characterized and quantified via the relaxation decay time constants obtained by several solid-state NMR techniques like proton wide-line NMR and ^{13}C MAS T_{1C} relaxometry. Furthermore the NMR results were complemented by conventional techniques like XRD, DSC and TEM.

It can be concluded that NMR relaxometry is an appropriate method to detect and quantify the presence of well-defined PCBM crystals in thin photoactive films, based on the detection of long T_{1H} and $T_{1\rho H}$ relaxation decay times. Based on these findings, our research revealed that only as-received PCBM contains such well-defined crystallites.

All other PCBM samples on the other hand lack these long and characteristic T_{1H} and $T_{1\rho H}$ decay times, i.e. no large well-defined PCBM crystals are present in these PCBM samples. However, at least a substantial fraction of PCBM nanocrystals embedded in the amorphous phase is present in the doctor bladed as well as in the other treated PCBM samples. This conclusion was based on the presence of an intermediate $T_{1\rho H}$ decay time. This statement is clearly corroborated by DSC as in all recorded thermograms endothermic transitions show up. By means of proton wide-line NMR it was possible to estimate the limits of the dimensions of the PCBM nanocrystals, i.e. to determine an average dimension interval.

However, proton wide-line NMR results have to be supported by DSC and XRD to situate the dimension of the nanocrystals within the NMR based dimension interval. Therefore the treated samples were also investigated via the chemical shift selective and local T_{1C} ^{13}C-MAS technique. A further refinement of the dimension interval, strengthened by XRD, could be derived from the intermediate T_{1C} decay

time. And last but not least, a quantification of the amount of PCBM nanocrystals, qualitatively supported by DSC, could be furnished via this T_{1C} decay time.

It is demonstrated that for PCBM samples which show a T_{1C} decay time exceeding 50-55 s (e.g. "Konarka" and acetone-precipitated PCBM), the dimensions of the nanocrystals seem to be situated around the upper limit of the proton wide-line NMR based dimension interval. This is confirmed by XRD as still resolved reflection lines can be observed in the patterns of these PCBM samples. The broadening of the XRD lines seems to correlate well with the measured fraction of the intermediate T_{1C} decay time. On the other hand, PCBM samples which show a T_{1C} decay time below 50 s (e.g. "quench II-aged" and doctor bladed PCBM), are built up from PCBM nanocrystals of which the dimensions seem to be situated at the lower limits of the wide-line NMR based dimension interval. Here only broad halos are noticed in the corresponding XRDs.

Armed with these reference relaxation decay time values of PCBM, we can now tackle the more complicated D/A BHJ morphologies encountered in the next chapters.

4.9 Experimental part

4.9.1 Sample preparation

Different PCBM samples were prepared as described here. For *the quenched PCBM samples*, as-received PCBM was wrapped up in aluminum foil. It was first heated in an oven above its melting temperatures and subsequently immediately quenched in liquid nitrogen. The heating times and temperatures were 10 minutes at 330 °C, 15 minutes at 360 °C and 60 minutes at 350 °C for the samples quench I, quench II and quench III, respectively.

For *the acetone precipitated PCBM sample*, as-received PCBM was dissolved in chlorobenzene (4 wt%) by stirring it overnight at 50 °C. Next it was precipitated in a 50-fold excess of ice-cold acetone. The latter is a non-solvent. After centrifugation for 10 min at 3000 rpm, the supernatant was removed and the PCBM was dried under high vacuum overnight.

The preparation method of *the doctor bladed samples* was discussed in section 3.5.1. A concentration of 2 and 3.5 wt% of as-received PCBM in

chlorobenzene was used for the 50 and 100 nm thick films, respectively. Self-supported free-standing films were obtained as described in section 3.5.2.

The additional samples for the DSC experiments were prepared by dissolving as-received PCBM in *o*-dichlorobenzene, chlorobenzene, *p*-xylene, 1,2,4-trichlorobenzene and *o*-chlorotoluene, respectively. After stirring overnight at 50 °C the PCBM was precipitated by pouring the solution in an excess acetone/dry ice mixture (-75 °C).

The sample refered to as *"Konarka"* was kindly provided by Dr. Markus Scharber of Konarka-Austria.

4.9.2 Analytical techniques

For TEM & XRD see section 3.5.2. TA-GC/MS (thermal adsorption-gas chromatography/mass spectrometry) experiments were performed on a Voyager DSQ mass spectrometer (ThermoQuest Scientific Equipment Group Ltd) and an external thermal desorption system (Unity, Markes Int.). Thermal gravimetric analysis (TGA) was acquired on a TA Instruments TGA 2950 thermogravimetric analyzer with a continuous flow of nitrogen (80 mL/minute) and a heating rate of 10 °C/min. Differential scanning calorimetry (DSC) was carried out on a DSC 2920 TA instrument with a continuous flow of nitrogen (50 mL/minute). A heating rate of 20 °C/min was used to obtain the thermograms depicted in figures 4-8, 4-10, 4-11, 4-12 and 4-13. The thermograms presented in figure 4-17 were acquired by fast initial heating of the sample up to 150 °C to prevent cold crystallization as much as possible, followed by a heating rate of 10 °C/min.

The experimental procedure for proton wide-line solid-state NMR is discussed in section 3.5.2. The only parameters that had to be adapted were the variable evolution time t (see figure 3-11) and the spin-lock time t_{SL} (see figure 3-12) in the pulse sequence for the T_{1H} and $T_{1\rho H}$ experiment, respectively. Here, t varies from 0.01 up to 50 s and t_{SL} varies from 0.25 up to 200 ms; apart from the as-received PCBM for which the longer values of section 3.5.2 had to be used.

Quantitative liquid-state ^{1}H-NMR spectra were acquired on a Varian Inova 300 spectrometer (B_0 = 7.2 Tesla; Larmor frequency for ^{1}H about 300 MHz) in a dedicated proton probe with a spectal width of 5 kHz, a 90° pulse length of 4 μs, an acquisition time of 2.5 s and a preparation delay of 10 s. Quantitative ^{13}C and Attached Proton Test (APT)[19,20] liquid-state NMR spectra of PCBM were recorded

on the same Varian Inova 300 spectrometer in a 5 mm four-nucleus PFG probe (Larmor frequency for ^{13}C about 75 MHz). Experimental parameters were a spectral width of 17 kHz, a 90° pulse length t_{90} of 7 µs, an acquisition time (at) of 1.5 s and a preparation delay time d1 of 9 s. The solution was prepared in a 1:2 (v/v) mixture of chlorobenzene/C_6D_6. 20 mM of $Cr(acac)_3$ (chromium(III)triacetylacetonate) was added as a paramagnetic T_1-relaxation agent in order to acquire a fully quantitative, high signal-to-noise ^{13}C NMR spectrum in a relatively short period of time[21]. Figure 4-18 depicts the pulse sequence diagram of the standard ^{13}C experiment.

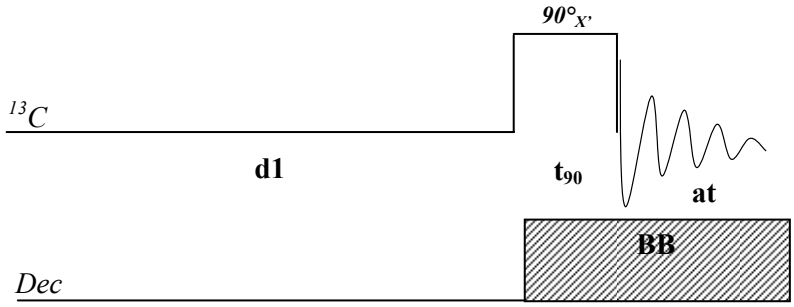

***Figure 4-18**: Pulse sequence of the standard liquid-state ^{13}C NMR experiment.*

Notice in figure 4-18 the use of broad-band (BB) proton decoupling only during the 90° pulse and acquisition time (inverse gated decoupling) in order to ensure a quantitative spectrum. In this rather short time span the Nuclear Overhauser Effect (NOE) cannot build up.

However, by applying BB decoupling all information with regard to the carbon multiplicity is lost. Therefore an APT experiment was performed to regain the carbon multiplicity information. Figure 4-19 depicts the pulse sequence diagram of an APT experiment. As for many pulse sequences, the refocusing $180°_{X'}$ pulse is very essential. Depending on the number of hydrogens bound to a particular ^{13}C atom, the corresponding magnetic moments will evolve differently after the initial $90°_{X'}$ pulse**.** The delay τ is set to the inverse of the carbon proton coupling constant $^1J_{CH}$. For aliphatic sp^3 carbon atoms this $^1J_{CH}$ is at average about 140 Hz so the delay τ is around 7 ms. In that way non-protonated and methylene carbons show negative intensities while methyl and methine carbons show positive intensities in the APT spectrum.

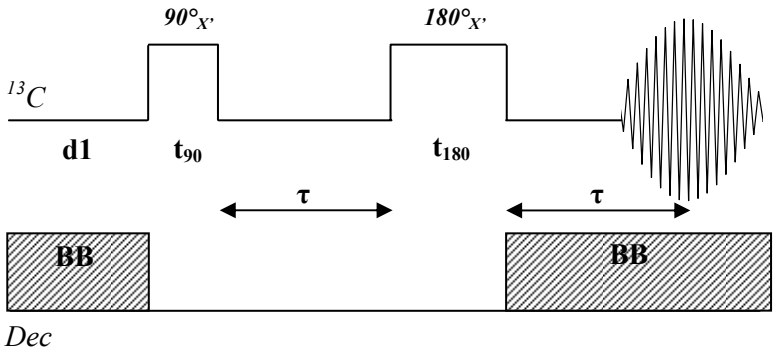

***Figure 4-19**: Pulse sequence of the APT experiment.*

Solid-state ^{13}C CP/MAS and MAS relaxation NMR experiments were accomplished on a Varian 400 DirectDrive 9.4 T spectrometer with a Varian T3 MAS probe (Transmission Line Technology) dedicated for small sample volumes and high power dipolar decoupling. Magic angle spinning (MAS) was performed at 14 kHz in 3.2 mm (diameter) ceramic rotors (22 µL volume). The higher the spin speed the better the resolution and signal-to-noise ratio and the smaller the spinning side bands. Both probe (20 L/min) and upper-barrel (30 L/min) cooling was used to limit sample heating. The aromatic signal of hexamethylbenzene was used to determine the Hartmann-Hahn condition for cross-polarization (CP) and to calibrate the carbon chemical shift scale (132.1 ppm). All spectra were acquired with a spectral width of 50 kHz and a preparation delay time d1 of 5 times T_1. All relaxation data were analyzed by a non-linear least-squares fit (Levenberg-Marquardt algorithm).

The relaxation decay times T_{1C} were measured via direct carbon observation (MAS; no CP) under high power DD (100 kHz) by means of the saturation recovery method (figure 4-20) in which the evolution time d2 was varied between 1 and 330 s. Only for the experiment on the as-received PCBM sample, d2 was varied up to 3000 s. The 90° pulse length t_{90} and the acquisition time (at) were 3.2 µs and 25 ms, respectively. After the first $90°_{x'}$ RF pulse the transversal magnetization is dephased by a spoiling gradient. Longitudinal magnetization M_z (the magnitude of the z-component of the macroscopic magnetization) gradually grows back to its equilibrium value M_0 during the variable evolution time d2 after which a second $90°_{x'}$ RF pulse brings the magnetization again along the detection y'-axis. Signal detection occurs under BB-decoupling. In that way a preparation delay d1 of 5 times the T_{1C} relaxation decay time (as for the inversion recovery

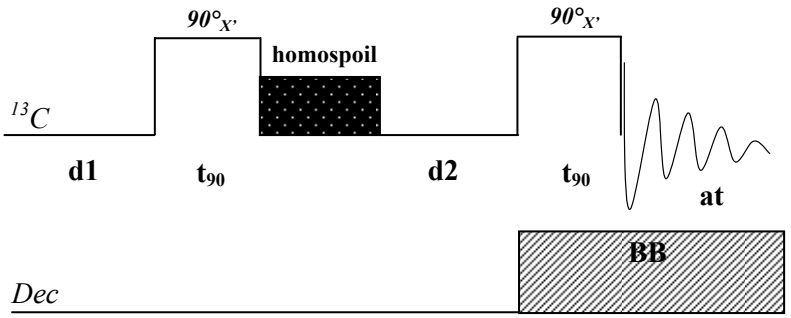

***Figure 4-20**: MAS pulse sequence for the determination of T_{1C} via the saturation recovery method.*

technique) has not to be respected between successive accumulations to obtain quantitative results (in practice: d1 was set to 5 s). The T_{1C}'s are then obtained by analyzing the integrated carbon signal intensity bi-exponentially as a function of the variable inversion time d2 according to:

$$I(t) = I_0^s(1-\exp(-d2/T_{1C}^s)) + I_0^i(1-\exp(-d2/T_{1C}^i))$$

The superscripts s and i refer to the fractions and T_{1C} values with short and intermediate decay time, respectively.

The solid-state ^{13}C NMR spectrum of as-received Solenne PCBM presented in figure 4-14 was recorded by means of the CP/MAS technique (figure 4-21) in which first the proton magnetization was brought along the y'-axis by a $90°_{x'}$ pulse before it is cross-polarized to the carbon nuclei during a fixed contact time cntct of 3.5 ms. The spectrum was than acquired under high power DD (100 kHz) on the proton channel.

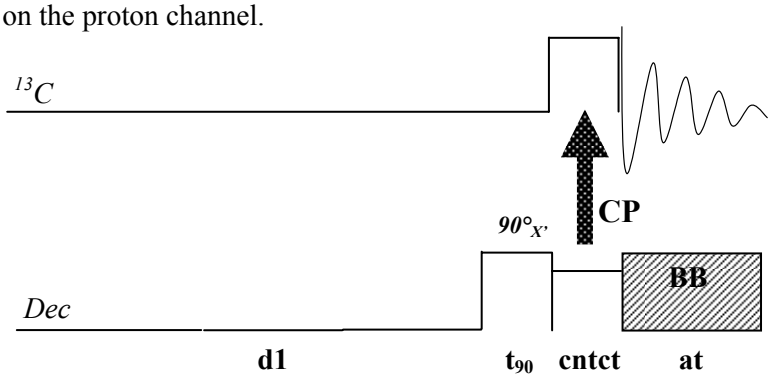

***Figure 4-21**: ^{13}C CP/MAS pulse sequence.*

Based on repeated experiments, the average 95% confidence limit for the (CP)/MAS experiments is about 4% for the normalized molar (proton) fractions and 5-7% for the time constants. Small deviations between experimental points and curve fits (correlation coefficients > 0.999) were attained.

4.10 References

1. Hummelen, J.C.; Knight, B.W.; LePeq, F.; Wudl, F., *J. Org. Chem.* **1995**, 60, 532.
2. Yu, G.; Gao, J.; Hummelen, J.C.; Wudl, F.; Heeger, A.J., *Science* **1995**, 270, 1789.
3. Helgesen, M.; Søndergaard, R.; Krebs, F.C., *J. Mater. Chem.* **2009**, 20, 36.
4. Cheng, Y-J.; Yang, S-H.; Hsu, C-S., *Chem. Rev.* **2009**, 109, 5868.
5. Jo, J.; Na, S.; Kim, S-S.; Lee, T-W.; Chung, Y.; Kang, S-J.; Vak, D.; Kim, D-Y., *Adv. Funct. Mater.* **2009**, 19, 2398.
6. Dennler, G.; Scharber, M.C.; Brabec, C.J., *Adv. Mater.* **2009**, 21, 1323.
7. Yang, X.; van Duren, J.K.J.; Janssen, R.A.J.; Michels, M.A.J.; Loos, J., *Macromolecules* **2004**, 37, 2151.
8. Yang, X.; van Duren, J.K.J.; Rispens, M.T.; Hummelen, J.C.; Janssen, R.A.J.; Michels, M.A.J.; Loos, J., *Adv. Funct. Mater.* **2004**, 16, 802.
9. Stejskal, E.O.; Memory, J.D., *High Resolution NMR in the Solid State-Fundamentals of CP/MAS* **1994**, Oxford university press, New York.
10. Thompson, B.C.; Fréchet, J.M.J., *Angew. Chem. Int. Ed.* **2008**, 47, 58.
11. Levitt, M.H., *Spin Dynamics-Basics of Nuclear Magnetic Resonance* **2001**, John Wiley & Sons Ltd.
12. Aldrich Chemistry, *Handbook of Fine Chemicals* **2009-2010**.
13. Zhao, J.; Swinnen, A.; Van Assche, G.; Manca, J.; Vanderzande, D.; Van Mele, B., *J. Phys. Chem. B* **2009**, 113, 1587.
14. Fedotov, V.D.; Schneider, H., *Structure and Dynamics of Bulk Polymers by NMR-Methods* **1989**, Springer-Verlag, Berlin.
15. Müller, C.; Ferenczi, T.A.M.; Campoy-Quiles, M.; Frost, J.M.; Bradley, D.D.C.; Smith, P.; Stingelin-Stutzmann, N.; Nelson, J., *Adv. Mater.* **2008**, 20, 3510.
16. Rispens, M.T.; Meetsma, A.; Rittberger, R.; Brabec, C.J.; Sariciftci, N.S.; Hummelen, J.C., *Chem. Commun.* **2003**, 2116.
17. Yang, C.; Hu, J.G.; Heeger, A.J. *J. Am. Chem. Soc.* **2006**, *128*, 12007.
18. Erukhimovitch, V.; Baram, J., *Phys. Rev. B.* **1994**, 50, 5854.
19. Lecocq, C.; Lallemand, J., *J. Chem. Soc., Chem. Commun.* **1981**, 150.
20. Patt, S.L.; Ruben, D.; Shoolery, J.N., *J. Magn. Reson.* **1982**, *46*, 535.
21. Adriaensens, P.J.; Karssenberg, F.G.; Gelan, J.M.; Mathot, V.B.F., *Polymer* **2003**, 44, 3483.

Chapter Five

MDMO-PPV/PCBM Thin Films Casted from Chlorobenzene Solutions

5.1 Introduction

In this chapter once more MDMO-PPV and PCBM are the electron donor and acceptor of the BHJ photoactive films. However, this time the film casting solvent is chlorobenzene. The influence of the blend composition and the casting technique, i.e. spin-coating versus doctor blading, on the thin film morphology is investigated by solid-state NMR spectroscopy. Although the main focus of the discussion will be on blends casted from chlorobenzene, occasionally comparisons with films casted from toluene will be presented in order to place the discussion in a global picture. The nanomorphology of chlorobenzene casted films is already as intensively studied with conventional microscopic techniques like TEM, SEM and AFM as their toluene casted counterparts[1-8].

As is the case for toluene casted films, films processed from chlorobezene also show phase segregation. However, as will be shown, the phase separated domains do not consist of large well-defined PCBM crystallites. The dimensions of the phase separated domains, mentioned in the above cited literature, are not all in agreement with each other. Dimensions in the range of 30 to 200 nm are reported. A lot of parameters come into play in defining the nanomorphology of BHJs. Apart from the experimental parameters enumerated in section 1.2.6, the observed differences in morphology and related power conversion efficiency η_e can be a consequence of the intrinsic properties of the conjugated polymer and fullerene as for instance, the molecular weight of the polymer, the number of structural defects in the polymer depending upon the synthetic route, the regioregularity of the polymer, the purity of the materials.... However, also the film thickness is of utmost importance. In the case of spin-coating, the thickness can be controlled by changing the spin rate during the film processing and the viscosity of the blend solution (see tabel 3-6 and figure 3-9). If doctor blading is used as the casting

technique, the viscosity of the polymer/fullerene solution mainly determines the film thickness.

It has been shown by Shaheen *et al*[9] that the performance of devices based on MDMO-PPV/PCBM strongly depends on the casting solvent (cf. 1.2.6.1). The choice of solvent for the MDMO-PPV/PCBM (20/80 wt%) mixture leads to a significantly different morphology and striking effect on the photovoltaic performance: an increase in efficiency η_e of the solar cell from 0.9% (toluene) to 2.5% (chlorobenzene) was observed. As compared to toluene, chlorobenzene reduces the phase separation between MDMO-PPV and PCBM resulting in an increased interfacial contact area between polymer and PCBM as well as in an increased charge carrier mobility. In addition, a much smoother surface of the active layer leads to a better interfacial contact with the electron collecting electrode. The authors further demonstrated that the optical absorption spectra of the active layer films are nearly identical for both solvents, i.e. the morphology of the chlorobenzene-based device is much more efficient in converting photons to charge carriers. It can be stated that the nanomorphology of the BHJ active layer is of utmost importance and can be highly controlled by the processing.

In addition to the pionering work of Shaheen on the MDMO-PPV/PCBM D/A system, Yang *et al*[10] already pointed to the possible existence of PCBM nanocrystals in composite polymer/fullerene. Indications for the presence of substructures in the PCBM-rich domains observed in PCDTBT/PC_{70}BM films were presented by Peet *et al*[11] by means of high-resolution TEM. The authors showed that the 100-200 nm PCBM-rich domains are clearly intermixed with PCDTBT fibrils. Very recently Dante *et al*[12] reported that the "two-phase" morphology of PCDTBT/PC_{70}BM films contains smaller internal domains. These substructures were described, based on cross-sectional AFM images, to have dimensions of only 5 to 8 nm.

First the morphology of the chlorobenzene casted films will be studied by means of ^{1}H wide-line solid-state NMR relaxometry and the obtained results will be compared with TEM and XRD as complementary techniques. However, as the phase separated domains do not consist of well-defined crystallites when film processing takes place from chlorobenzene, the use of the chemical shift selective (but also more time consuming) ^{13}C solid-state NMR techniques becomes an absolute must to describe the morphology in detail. Especially the quantification

aspect and the description of the differences of the nanomorphologies are the main research questions.

5.2 Microscopy, proton wide-line NMR and XRD

Figures 5-1-A-C show some microscopy images of 150 nm thick films prepared by doctor blading from solutions in chlorobenzene. While the TEM image of the 50/50 wt% film looks quite homogeneous (figure 5-1-A), the TEM image of the 20/80 wt% film clearly shows phase separated domains in the order of 100-150 nm (figure 5-1-B). Higher PCBM contents result in even larger aggregates as shown for the 15/85 wt% film (figure 5-1-C). Similar domain sizes are observed for spin-coated films, as is demonstrated for the 20/80 wt% film by AFM (figure 5-1-E). Figures 5-1-D shows as a comparison a TEM image of a 150 nm thick 20/80 wt% film prepared by doctor blading from a solutions in toluene. By comparing

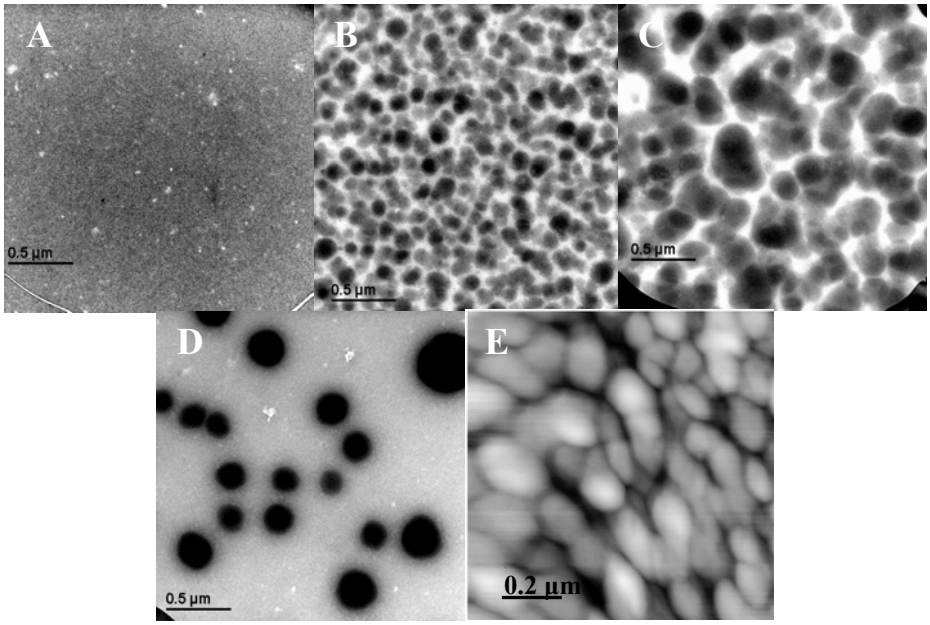

Figure 5-1: *TEM images (A-D) of 150 nm thick films prepared by doctor blading from solutions in chlorobenzene with a PCBM content of 50 wt% (A), 80 wt% (B) and 85 wt% (C) and from a solution in toluene with 80 wt% PCBM (D). AFM image of a film prepared by spin-coating from a solution in chlorobenzene with a PCBM content of 80 wt% (E). Scale bars are 500 nm for the TEM images and 200 nm for the AFM image.*

figures 5-1-B and D, it is noticeable that the 'grey-value' of the phase separated domains is rather uniform for the toluene casted film (figure 5-1-D) while the image of the chlorobenzene casted film clearly shows multiple grey-values (figure5-1-B). Multiple grey-values are also observed in the image of the 15/85 wt% film (figure 5-1-C). Remark that the film surface, as verified by AFM (rms roughness of only ~ 5-15 nm), is quite homogeneous for the chlorobenzene casted films.

Table 5-1 presents the spin-lattice T_{1H} and $T_{1\rho H}$ relaxation decay times as

***Table 5-1**: T_{1H} and $T_{1\rho H}$ relaxation decay times measured by proton wide-line NMR of 150 nm thick films prepared by spin-coating and doctor blading from solutions in chlorobenzene for different MDMO-PPV/PCBM weight ratios (wt%). The normalized molar proton fractions are presented between brackets.*

	MDMO-PPV/PCBM			
	chlorobenzene	**chlorobenzene**	**chlorobenzene**	**chlorobenzene**
wt%	**80/20**	**50/50**	**20/80**	**15/85**
molar ratio	93/7	76/24	44/56	36/64
molar proton ratio	*96/4*	*86/14*	*61/39*	*53/47*
	T_{1H} (s)			
spin-coating	---	0.64	0.80	0.77
doctor blading	0.65	0.64	0.78	0.80
	$T_{1\rho H}$ (ms)			
spin-coating	---	1.8 (22%) 8.4 (78%)	2.6 (20%) 11.9 (80%)	2.4 (26%) 12.4 (74%)
doctor blading	1.4 (25%) 4.4 (75%)	2.2 (24%) 8.4 (76%)	3.0 (21%) 11.8 (79%)	2.8 (23%) 11.5 (77%)

***Table 5-2**: T_{1H} and $T_{1\rho H}$ relaxation decay times measured by proton wide-line NMR of 150 nm thick films prepared by spin-coating and doctor blading from solutions in toluene for a MDMO-PPV/PCBM weight ratio of 20/80 wt%. The normalized molar proton fractions are presented between brackets.*

	MDMO-PPV/PCBM
	toluene
wt%	**20/80**
molar ratio	44/56
molar proton ratio	*61/39*
	T_{1H} (s)
spin-coating	0.83 (91%) **13.3 (9%)**
doctor blading	0.68 (82%) **13.8 (18%)**
	$T_{1\rho H}$ (ms)
spin-coating	1.9 (17%) 9.4 (74%) **76.0 (9%)**
doctor blading	2.2 (20%) 8.8 (65%) **131.7 (15%)**

measured by wide-line NMR for films spin-coated and doctor bladed from solutions in chlorobenzene and with MDMO-PPV/PCBM compositions of 80/20, 50/50, 20/80 and 15/85 wt%. As a comparison, the decay times of the 20/80 wt% films casted from solutions in toluene are shown in Table 5-2.

5.2.1 T_{1H} relaxation

For the 80/20 and 50/50 wt% blends, a single short T_{1H} decay time of 0.64 s is observed, irrespective of the casting technique. Definitely the T_{1H} relaxation seems to be very efficient with the same short decay time as for pure MDMO-PPV (see table 3-2). Due to efficient spin diffusion, the T_{1H} relaxation of PCBM in these blends is driven by the molecular motions of MDMO-PPV. This means further that if domains of pure PCBM are present in these films, they should, according to the spin diffusion equation, be smaller than about 40 nm explaining why the T_{1H} relaxation is averaged out via the process of spin diffusion. Although taking the TEM images into account maybe surprisingly at first sight, a single short T_{1H} decay time is also observed for the 20/80 and 15/85 wt% blends (table 5-1). The value of the T_{1H} decay time (about 0.8 s) indicates that if domains of pure PCBM are present in these films, they should be smaller than about 45 nm.

This T_{1H} relaxation behavior of chlorobenzene-based MDMO-PPV/PCBM films is completely different to the relaxation observed for films prepared from solutions in toluene for which an additional long decay time is observed for PCBM contents ≥ 70 wt% (table 5-2). As discussed in chapter 3, that long decay time corresponds to a fraction of PCBM which is phase separated and organized in well-defined crystallites (~200-400 nm; see also figure 5-1-D) of which the amount can be quantified by taking the molar proton ratio of the blend into account. For example, since the 20/80 wt% blend has a molar proton ratio of 61/39 it can be easily calculated, based on the molar proton fraction of the long decay time, that the molar amount of well-defined PCBM crystals is about 23% in the spin-coated films (9 mol out of 39 or 23%) and 46% in the doctor bladed films (18 mol out of 39 or 46%). The reason for a lower amount of phase separation in spin-coated films can be found in the processing conditions, i.e. the faster solvent evaporation during the spin-coating process. The remaining PCBM was demonstrated to be highly unorganized and mixed with MDMO-PPV. As mentioned above, MDMO-

PPV/PCBM films casted from chlorobenzene clearly lack this long T_{1H} relaxation decay time, related to well-defined PCBM crystals.

5.2.2 $T_{1\rho H}$ relaxation

Table 5-1 further shows the proton spin-lattice relaxation decay times in the rotating frame ($T_{1\rho H}$) as determined by proton wide-line NMR. Similar observations appear as for T_{1H}. Only two decay times (a short and intermediate one) are observed for films casted from chlorobenzene, independent of the blend composition and casting technique. Even for films with PCBM contents ≥ 80 wt%, no third, long decay time is observed. This in contrast to films prepared from solutions in toluene having a PCBM content ≥ about 70 wt% for which a third, long decay time (tens of ms) was clearly demonstrated in chapter 3 (tables 5-2 and 3-3, 3-5). This third, long decay time was attributed to phase separated PCBM that is organized into well-defined crystallites of which the amount can be quantified on basis of the molar proton fractions. The fact that comparable films casted from chlorobenzene clearly lack this long $T_{1\rho H}$ decay time further confirms the absence of well-defined PCBM crystallites.

5.2.3 Presence of nanocrystals ?

The values of the T_{1H} (0.64-0.8 s) and intermediate $T_{1\rho H}$ (5-12 ms) decay times strongly indicate that if domains of pure crystalline PCBM are present in these films, their dimensions have to be situated, based on the spin diffusion equation, between minimal 5 nm and maximal 45 nm, i.e. nanocrystals. Recall that a third $T_{1\rho H}$ decay time in the order of 50 ms can easily be discriminated matematically as demonstrated for the 30/70 wt% films casted from toluene (cf. Chapter 3; section 3.3). The presence of nanocrystals instead of well-defined crystallites would explain the higher performance of BHJ solar cells of which the active layer is casted from chlorobenzene since it results in a much larger interfacial contact area between donor and acceptor and so higher efficiency of exciton dissociation.

Starting from 50 wt% PCBM the intermediate $T_{1\rho H}$ decay time (in the range from 8.4 upto 12.4 ms, table 5-1) becomes significantly longer as compared to the value of 3.3 ms for pure MDMO-PPV (see section 3.2.2, table 3-2). As was

the case for the 50/50 wt% film casted from toluene, this might point to the presence of small and irregular PCBM crystals. Although these 50/50 wt% films apparently look homogeneous on 2D TEM (figure 5-1-a), the presence of nanocrystals will be confirmed for all blend compositions studied in section 5-3-2 by means of local T_{1C} relaxation measurements. Note that the 80/20 wt% blend, on the other hand, shows an intermediate $T_{1\rho H}$ which is significantly lower in value, indicating that the amount of PCBM nanocrystals, if present at all, must be smaller as a consequence of the very low PCBM content in this blend.

The absence of well-defined PCBM crystallites in films prepared from solutions in chlorobenzene, even for high PCBM contents, is further confirmed by XRD. Figure 5-2 shows the XRD patterns of the 20/80 and 15/85 wt% blend materials obtained from 150 nm thick films that were prepared by spin-coating from solutions in chlorobenzene. No sharp reflections are present - only broad halos are observed (compare with figures 3-2 and 3-7 of chapter 3). However, as was demonstrated for doctor bladed PCBM in chapter 4, the dimensions of coherence of PCBM nanocrystals can be too small to observe them by XRD.

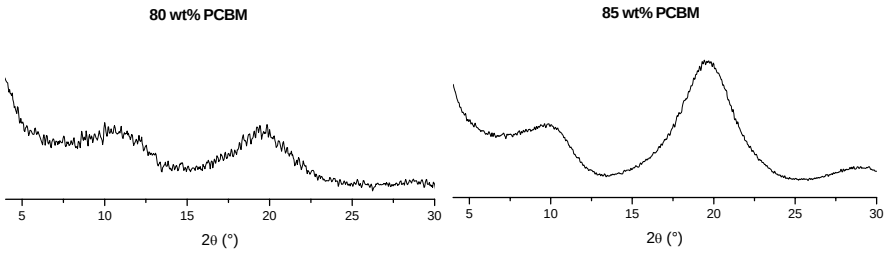

***Figure 5-2**: XRD patterns of 20/80 wt% (left) and 15/85 wt% (right) blend materials obtained from 150 nm thick films prepared by spin-coating from chlorobenzene.*

The above combined information allows to conclude that the 'black-grey' aggregates observed by TEM for films casted from solutions in chlorobenzene with high PCBM content (≥ 80 wt%) can be attributed to PCBM-rich domains rather than to well-defined PCBM crystals. PCBM-rich domains appear as 'dark' in the TEM images since the electron density of PCBM is higher than this of MDMO-PPV[13]. The fact that quite similar T_{1H} and $T_{1\rho H}$ relaxation decay times as well as molar proton fractions are observed for films prepared by spin-coating and doctor blading from solutions in chlorobenzene (table 5-1) indicates that phase separation into PCBM-rich and polymer-rich domains is rather independently of the casting

technique. A possible explanation might be that no fast phase separation between polymer and PCBM takes place in chlorobenzene. It can be imagined that chlorobenzene acts as a kind of compatibilizer, due to e.g. dipole-dipole interactions between the ester function of PCBM and CB, and in this way reduces the driving force for phase separation. This might explain why the phase separation in MDMO-PPV/PCBM films casted from chlorobenzene becomes independent on the solvent evaporation rate.

5.2.4 Literature information regarding PCBM nanocrystals in polymer/fullerene blends

There are several reasons to expect PCBM nanocrystals in the MDMO-PPV/PCBM films casted from chlorobenzene:

- MDMO-PPV/PCBM based BHJ solar cells of which the active layer is composed of a 20/80 wt% mixture and which are casted from solutions in chlorobenzene yield relatively good power conversion efficiencies. It is hard to believe that this could be achieved without any form of PCBM crystallization, since the crystals form the 'highways' for fast transport of electrons to the metal electrode.
- Photoluminescence measurements done by Hoppe *et al*[1] show the detection of PCBM photoluminescence in films casted from toluene which was attributed to radiative recombination of photogenerated PCBM excitons within the large PCBM domains before they could reach the heterojunction. This means that these PCBM domains have to be very pure since fast charge transfer to embedded MDMO-PPV would certainly quench this PCBM photoluminescence. In chapter three of this thesis, these domains were characterized as large, well-defined PCBM crystallites. This in contrast to films casted from chlorobenzene for which no photoluminescence was noticed by Hoppe *et al* which is a clear indication for exciton dissociation at the D/A interface. These photoluminescence experiments point to the presence of nanocrystals with maximum dimensions of about 30-40 nm, i.e. the diffusion path length of excitons in PCBM[14,15].
- Peet *et al*[11] showed that the 100-200 nm PCBM-rich domains (dark) in PCDTBT/PC_{70}BM films are clearly intermixed with PCDTBT fibrils

(white) by means of high-resolution TEM. Moreover, the XRD pattern shows no sharp diffraction peaks which would be expected for large domains of pure PCBM.

- Very recently Dante *et al*[12] reported that the originally observed two phases (i.e. the PCBM-rich and polymer-rich domains) in PCDTBT/$PC_{70}BM$ films contain a mixture of smaller internal domains. These substructures were described, based on cross-sectional AFM images, to have dimensions of only 5 to 8 nm.
- In this respect, we want to refer to Van Bavel *et al*[16] who pointed out that "since conventional TEM images are essentially 2D projections of the actual 3D object, multiple stacking of relatively thin features throughout the thickness of the specimen will inevitably result in images which look blurred…". To describe the film morphology in nanometer detail, high-resolution TEM and/or cross-sectioning would be essential.
- Yang *et al* already pointed to the existence of PCBM nanocrystals in composite MDMO-PPV/PCBM[10].

The proton wide-line NMR results show a tendency of the T_{1H} and the intermediate $T_{1\rho H}$ relaxation decay time to increase as a function of the PCBM content. The decay times evolve towards values observed for PCBM nanocrystals in Chapter 4, i.e. towards 1-1.4 s and 16-20 ms for the T_{1H} and intermediate $T_{1\rho H}$ decay time, respectively. An increasing amount of nanocrystals could explain this and will be demonstrated in section 5.3.2. Despite this, we have to conclude that the $T_{1\rho H}$ decay times as determined via proton wide-line NMR are not sensitive enough to detect clear differences, at least not with the spin-lock field used (45 kHz). Therefore, it was decided to go for a more selective NMR analysis of the MDMO-PPV/PCBM active layers by means of ^{13}C-NMR spectroscopy and relaxometry.

5.3 Carbon-13 solid-state NMR

5.3.1 ^{13}C CP/MAS spectra of PCBM, MDMO-PPV and their blends

To describe the morphology of thin films processed from chlorobenzene in

more detail, relaxation decay times were also determined via the chemical shift selective carbon resonances. In order to decide which carbon resonances are of use for selective relaxometry studies, the necessary solid-state spectra were acquired via the CP/MAS (Cross-Polarization / Magic Angle Spinning) technique. Figure 5-3. shows CP/MAS spectra of the pure components and the 50/50 wt% blend as well as the numbering scheme for the carbons of MDMO-PPV and PCBM. The signal assignment of MDMO-PPV, based on solution NMR spectra, is already described by our group[17] and the assignment for PCBM was discussed in chapter 4. The spectra show that the main resonance of PCBM at 146 ppm (in figure 5-3 marked with an *) does not overlap with signals of the polymer and so is an excellent, local probe to study the relaxation of PCBM. Attention will be focused on this signal in the following sections.

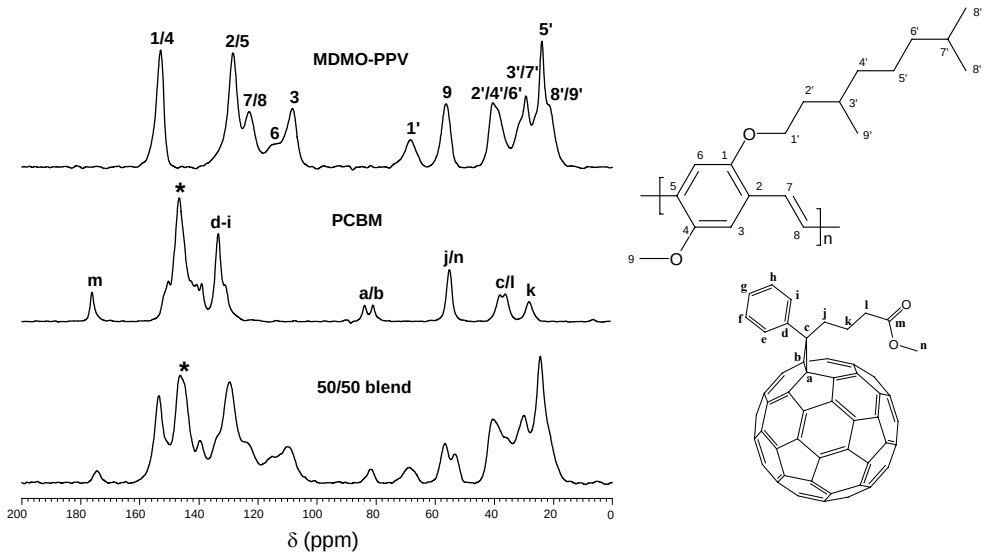

***Figure 5-3**: Solid-state ^{13}C-CP/MAS NMR spectra taken with a contact time of 3.5 ms of MDMO-PPV, PCBM and a 150 nm thick MDMO-PPV/PCBM film prepared by doctor blading from a solution in chlorobenzene with 50 wt% PCBM. The signal marked with an * arises from the main resonance of PCBM at 146 ppm. The inset on the right presents the chemical structure and numbering scheme of MDMO-PPV (top) and PCBM (bottom).*

5.3.2 Study of the T_{1C} relaxation by ^{13}C MAS relaxometry

The T_{1C} relaxation is a local probe since it is not influenced by the process of spin diffusion. If the dipole-dipole interaction is the dominant mechanism, the

T_{1C} relaxation rate is mainly determined by the distance r to neighboring proton spins and the correlation time of motion, τ_c[18]:

$$\frac{1}{T_{1,DD}} = \frac{1}{10}\frac{\gamma_C^2\,\gamma_H^2\,\hbar^2}{r_{CH}^6}\tau_C\left[\frac{1}{1+(\omega_H-\omega_C)^2\tau_C^2}+\frac{3}{1+\omega_C^2\tau_C^2}+\frac{6}{1+(\omega_H+\omega_C)^2\tau_C^2}\right]$$

The relaxation of carbon spins mainly takes place via local fluctuating magnetic fields which arise from the fluctuation of magnetic moments of neighboring proton spins induced by molecular motions. Mainly local magnetic fields that fluctuate with frequencies around the carbon resonance frequency (100 MHz on a 9.4 T magnet) cause relaxation. So, in the solid-state ($\tau_c >> 1/\omega_i$ or $\omega_i^2\tau_c^2 >> 1$), the longer the correlation time of motion τ_c, the longer the T_{1C} decay time (less efficient relaxation).

Table 5-3 presents the T_{1C} decay times measured by ^{13}C-MAS and determined via the main PCBM resonance at 146 ppm for 100 nm thick PCBM films and 150 nm thick films of MDMO-PPV/PCBM with different weight ratios (wt%). Remark that the T_{1C} fractions are molar fractions as the T_{1C} is measured via a PCBM carbon signal. All films were prepared by doctor blading from solutions in chlorobenzene.

***Table 5-3**: T_{1C} decay times measured by ^{13}C-MAS and determined via the main PCBM resonance at 146 ppm for 100 nm thick PCBM films and 150 nm thick composite films of MDMO-PPV/PCBM with different weight ratios (wt%). All films were prepared by doctor blading from solutions in chlorobenzene. The normalized molar fractions are presented between brackets. Also the mol % of PCBM in nanocrystals and the molar ratio MDMO-PPV/PCBM in the mixed phase are listed.*

	MDMO-PPV/PCBM				
weight ratio (wt%) molar ratio	**80/20** 93/7	**50/50** 76/24	**20/80** 44/56	**15/85** 36/64	**0/100** 0/100
T_{1C} (s)	16.3	11.6 (73%) 40.2 (27%)	11.5 (50%) 41.3 (50%)	10.0 (36%) 42.0 (64%)	11.2 (26%) 42.7 (74%)
mol % of PCBM in nanocrystals	**19 % ***	**27 %**	**50 %**	**64 %**	**74 %**
molar ratio of MDMO-PPV/PCBM in the mixed phase**	100/6	100/23	100/64	100/64	---

** estimated from figure 5-4*

*** expressed per 100 repetition units of MDMO-PPV*

Independent of the blend composition, a short and intermediate decay time of about 11 s and 41 s is measured. As described in chapter 4, the short decay time can be assigned to unorganized PCBM which is mixed with the polymer in the MDMO-PPV/PCBM matrix. The intermediate decay time, on the other hand, represents small PCBM clusters organized into so-called nanocrystals. Remark that a T_{1C} of 41 s corresponds to nanocrystals of which the dimensions of coherence are already too short to be detected by XRD (see figure 5-2). As shown in chapter 4-table 4-2, XRD reflections only start to appear from a T_{1C} of around 60 s. This morphology is in agreement with the observations made by Yang *et al*[10]. These authors presented arguments that suggest the presence of densely and homogeneously distributed PCBM nanocrystals in the film matrix. The longer T_{1C} decay time (less efficient relaxation) of the phase separated PCBM nanocrystals can be rationalized by (i) the longer correlation time of motion τ_c in the nanocrystals and (ii) the larger distance to mobile proton magnetic dipoles, i.e. these of the mobile chain fragments of the polymer which are the main source of local magnetic fields fluctuating around 100 MHz. The T_{1C} relaxation of PCBM molecules in the co-existing mixed phase on the other hand is more efficient due to the shorter correlation time of motion τ_c and the higher spectral density of 100 MHz molecular motions generated by the surrounding MDMO-PPV chain fragments and PCBM tail.

Table 5-3 shows that the amount of PCBM in nanocrystals (given in mol % in table 5-3) increases with the total content of PCBM in the blends. A plot of 'mol PCBM in nanocrystals' versus 'mol PCBM in the blend', as presented in figure 5-4, allows to estimate the amount of PCBM in nanocrystals in the 80/20 wt% (93/7 molar ratio) films. For example, the 50/50 wt% blend contains 24 mol PCBM of which 27 %, i.e. 6.5 mol, is phase separated into nanocrystals. A reversed calculation for the 80/20 wt% blend, based on a value of 1.33 mol of PCBM in nanocrystals as obtained from figure 5-4, results in an amount of 19 mol % of phase separated PCBM nanocrystals. Note that for the T_{1C} relaxation of the 80/20 wt% blend only a single average value of 16.3 s is measured (table 5-3), not due to spin diffusion but because the amount of PCBM (7 mol %) becomes very small. However, the experimentally measured T_{1C} value of 16.3 s for the 80/20 wt% blend is in very good agreement with the mol fraction weighted average calculated on basis of the estimated amount of 19 mol % of nanocrystalline PCBM and the T_{1C} values of about 11 and 40 s for mixed and nanocrystalline PCBM respectively, i.e.

(0.81 x 11) + (0.19 x 40) = 16.5 s.

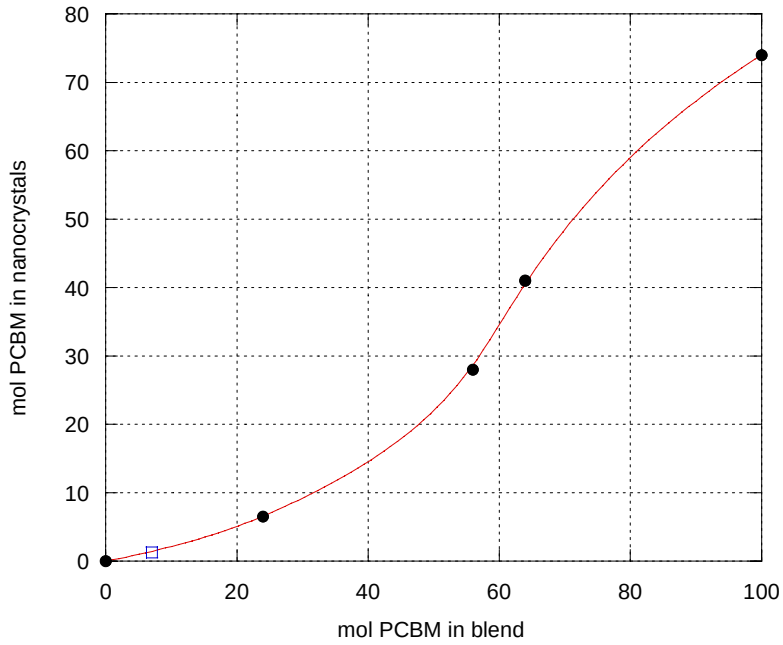

Figure 5-4: *Plot of 'mol PCBM in nanocrystals' versus 'mol PCBM in the blend'.*

The following conclusions can already be drawn:

- The amount of PCBM in nanocrystals (in mol % in table 5-3) increases upon increasing the total content of PCBM in the blends.
- Regarding the optimal active layer of MDMO-PPV/PCBM casted from chlorobenzene, i.e. having a 20/80 wt% ratio, this means that 50 mol % of the PCBM is present in nanocrystals while the other half seems to be unorganized as it is homogeneously mixed with the polymer. For the mixed phase, this can be translated in the presence of 64 molecules of PCBM per 100 monomer units of polymer.

5.3.3 Further confirmation of nanocrystals and corroboration by DSC

Important to notice is that in the 50/50 wt% films, which look quite homogeneous on TEM images (figures 5-1-A), already 27 mol % of the PCBM is organized into nanocrystals. Therefore, it was decided also to determine the T_{1C} relaxation characteristics for films casted from toluene with a 50/50 wt% blend

ratio (which also looked homogeneous on TEM images – see figures 3-8-a). For these toluene casted films once more, the T_{1C} behaves bi-exponentially with a short decay time of 11.8 s (78 %) and an intermediate decay time of 40.8 s (22 %). This means that in 50/50 wt% films casted from toluene about 22 mol % of the PCBM is organized in nanocrystals. As can be noticed in the DSC thermograms presented in figure 5-5, both 50/50 wt% films show a cold crystallization peak at around 169 °C (area of 5.0 and 3.9 Jg^{-1} for toluene and chlorobenzene casted films, respectively). As was the case for pure doctor bladed PCBM films, a rather low crystallization temperature of 169 °C is observed, pointing to the presence of crystallization ents

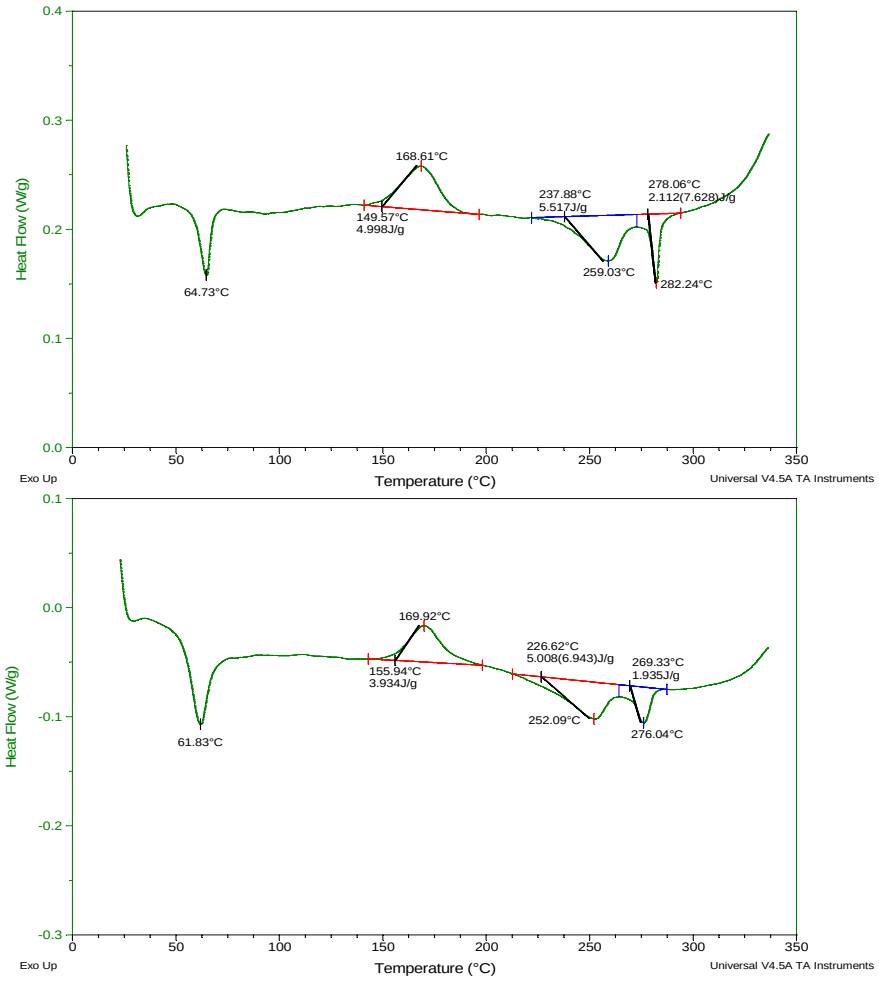

***Figure 5-5**: DSC thermograms (first run) showing HF for thin doctor bladed 50/50 wt% MDMO-PPV/PCBM films casted from toluene (top) and chlorobenzene (botom).*

in the films. In addition broad, double melting endotherms are observed around 260 and 280 °C with total areas of 7.6 and 6.9 J/g for toluene and chlorobenzene casted films, respectively. These observations support the presence of nanocrystals in 50/50 wt% doctor bladed films. Within experimental error, about the same amount of crystallinity is found by DSC for both films.

Further confirmation for the absence of well-defined crystallites in films processed from chlorobenzene, and so for the assignment of the intermediate decay time of 41 s to PCBM nanocrystals, can be found in the T_{1C} results obtained for 20/80 wt% MDMO-PPV/PCBM films casted from solution in toluene. Figure 5-6 presents the T_{1C} fits obtained for 20/80 wt% films casted from toluene and 15/85 wt% films casted from chlorobenzene as a comparison. As the carbon spins are clearly back in thermal Boltzmann equilibrium after an inversion recovery evolution time of 200 s for the chlorobenzene casted film (see section 5.7.2 for details of the pulssequence), this is even not the case after an evolution time of 400 s for the film casted from toluene. For the film casted from chlorobenzene, two decay times of 10 and 42 s are found (table 5-2). Although far from completely

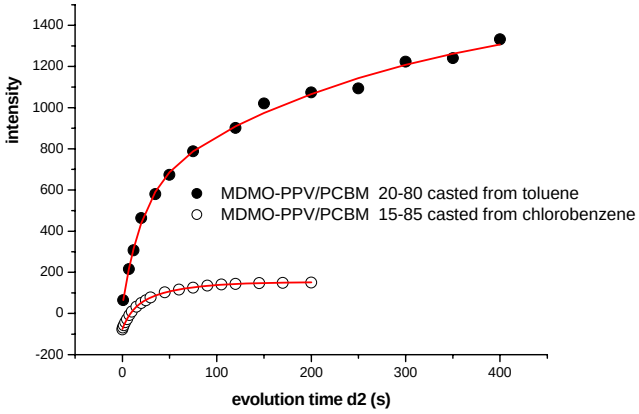

Figure 5-6: *Fits of the ^{13}C MAS data of the T_{1C} experiment on thin films of MDMO-PPV/PCBM casted by doctor blading from solutions in toluene (●) and in chlorobenzene (○).*

relaxed, a bi-exponential fit of the experimental data of the toluene casted film results in decay times of 22 and 325 s. It are these long T_{1C} decay times which can be attributed to the well-defined crystallites described in chapter 3 for films casted from toluene with PCBM contents ≥ about 70 wt%. Remark however that, since the T_{1C} relaxation is far from completed for the toluene casted film, the results are

estimates and for sure not-quantitative – it might even be possible that 'a fully relaxed' inversion recovery experiment would lead to three time constants, i.e. that the 22 s observed here would split into two values of around 10 and 40 s.

The difference in PCBM organization in thin MDMO-PPV/PCBM films processed from chlorobenzene and toluene is further demonstrated by DSC. Figure 5-7 shows the first run HF trace of a 15/85 wt% film casted from chlorobenzene and of a 20/80 wt% film casted from toluene. The total melting enthalpies are as expected higher for the toluene casted film (14.2 J/g), despite of the lower PCBM content, as compared to the chlorobenzene casted film (12.3 J/g) since well-defined

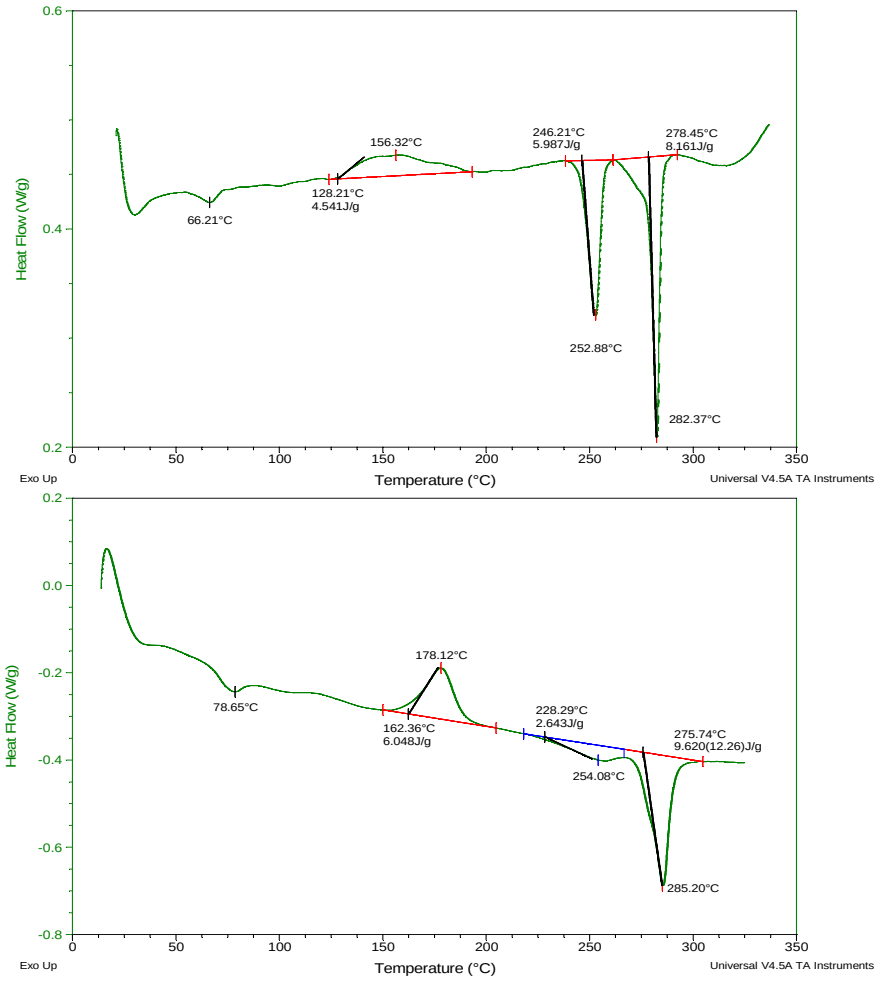

***Figure 5-7**: DSC thermograms (first run) showing HF for thin 20/80 wt% doctor bladed MDMO-PPV/PCBM films casted from toluene (top) and 15/85 wt% casted from chlorobenzene (bottom).*

crystals were only observed (by proton wide-line NMR and XRD) in the toluene-based films. In addition, both films clearly show a cold crystallization peak at around 156 and 178 °C, respectively. Remember that it was calculated in chapter 3 that in the 20/80 wt% film doctor bladed from toluene still 54 mol % of the PCBM was dispersed in the mixed phase, of which apparently a part is subjected to further crystallization during the heating of the DSC experiment. In conclusion, the combination of a lower amount of PCBM, a lower area of cold crystallization and a larger melting enthalpy for the toluene film reflects the higher degree of ordering into well-defined crystallites. For chlorobenzene casted films, all information points to a low order PCBM organization.

5.3.4 Study of the T_{1H} and $T_{1\rho H}$ relaxation via ^{13}C CP/MAS

As discussed above, the T_{1C} relaxation characteristics allows to quantify the amount of PCBM organized in nanocrystals for films casted from chlorobenzene. However, the main disadvantage of this technique is the time duration of the experiments, which can easily become a few days. Therefore, it was decided to measure the proton relaxation decay times again but this time via the chemical shift selective and more sensitive ^{13}C-CP/MAS (Cross-Polarization/Magic Angle Spinning) technique. Cross-polarization of magnetization from the sensitive proton spins to the less sensitive carbon spins occurs mainly by local protons. Concerning the T_{1H} relaxation of these local protons (which is measured via the 146 ppm carbon signal of PCBM), their magnetization is of course expected to be averaged out by long-range spin diffusion before it is cross-polarized to the PCBM carbons, as can be seen in table 5-4. However, for the $T_{1\rho H}$ relaxation, it can be expected that the magnetization of these local protons is also averaged out by short-range spin diffusion for the intimately mixed PCBM, but not for the PCBM in nanocrystals. The bucky ball carbons of PCBM in nanocrystals will sense the $T_{1\rho H}$ relaxation of only the local protons of its own ester tail.

Table 5-4 shows that this is indeed the case for the films with 80 and 85 wt% PCBM. Two $T_{1\rho H}$ decay times of about 4 and 16 ms are detected. The short decay time represents PCBM molecules which are intimately mixed with MDMO-PPV. Their bucky ball carbons sense, via cross-polarization, the spin diffusion averaged $T_{1\rho H}$ relaxation of the C_{60} tail protons and the neighboring MDMO-PPV

protons. The intermediate decay time of about 16 ms represents the phase separated PCBM nanocrystals. The bucky ball carbons of these nanocrystals only sense the $T_{1\rho H}$ relaxation of the C_{60} tail protons. The $T_{1\rho H}$ decay time of PCBM in nanocrystals is longer (less efficient relaxation) since the spectral density of local oscillating magnetic fields with kHz frequencies (caused by kHz molecular motions) is much lower in these organized clusters as compared to this in a polymer.

***Table 5-4**: T_{1H} and $T_{1\rho H}$ relaxation decay times measured by ^{13}C-CP/MAS and determined via the main resonance of PCBM at 146 ppm for 100 nm thick PCBM and 150 nm thick composite films of MDMO-PPV/PCBM with different weight ratios (wt%). All films were prepared by doctor blading from solutions in chlorobenzene. The normalized molar fractions are presented between brackets. Also the mol % of PCBM in nanocrystals and the molar ratio MDMO-PPV/PCBM in the intimately mixed phase are listed.*

	MDMO-PPV/PCBM				
weight ratio (wt%) molar ratio	**80/20** 93/7	**50/50** 76/24	**20/80** 44/56	**15/85** 36/64	**0/100** 0/100
T_{1H} (s)	0.69	0.78	1.0	1.1	1.4
$T_{1\rho H}$ (ms)	6.8	6.4	4.0 (49%) 16.4 (51%)	3.5 (39%) 16.6 (61%)	2.3 (29%) 18.4 (71%)
T_{1C} (s)	16.3	11.6 (73%) 40.2 (27%)	11.5 (50%) 41.3 (50%)	10.0 (36%) 42.0 (64%)	11.2 (26%) 42.7 (74%)

Table 5-4 further shows that the molar amounts of PCBM in nanocrystals are in good agreement with those detected via the T_{1C} relaxation experiments, i.e. 51 mol% and 61 mol % for the 20/80 and 15/85 films, respectively. Questioning why this selectivity was not obtained by proton wide-line NMR can be answered in twofold: a possible reason can be found in the selective cross-polarization step in the CP/MAS method but another reason might be the stronger spin-lock field used for the CP/MAS experiments, i.e. 75 kHz versus 45 kHz for the proton wide-line NMR experiments.

Analysis of the $T_{1\rho H}$ relaxation of the films with 20 and 50 wt% PCBM results in a single decay time of around 6.5 ms. The fraction of the intermediate decay time probably becomes too small to be differentiated efficiently by a bi-exponential fit analysis. For these blend ratio's, a molar weighted average is obtained but in this case due to mathematical reasons.

5.4 Film processing and the 20/80 wt% blend

The relationship between the casting solvent and processing technique on the morphology of the 20/80 wt% blends is interesting. Recall that this blend composition results in the best performing MDMO-PPV/PCBM BHJ solar cells if processing takes place from a solution in chlorobenzene. Microscopy demonstrates that 150 nm thick films, prepared from chlorobenzene and processed by spin-coating (AFM; figure 5-1-E) as well as by doctor blading (TEM; figure 5-1-B), contain PCBM-rich domains with dimensions in the order of 100-150 nm. As shown by NMR and corroborated by photoluminescence measurements[1], these domains contain substructures consisting of small PCBM clusters, i.e. nanocrystals with dimensions between 5 nm and 45 nm and in a molar amount around 50 % (table 5-3).

Films casted from toluene on the other hand contain larger domains of pure, phase separated PCBM (200-400 nm) which is organized in well-defined crystallites as shown by NMR and XRD. The molar amount of well-organized PCBM is in the order of 23% and 46% for spin-coated and doctor bladed films, respectively (chapter three). Both the amount and the dimensions of the phase separated PCBM explain why spincoated active layers perform much less when casted from toluene (efficiencies η_e of 2.5% and 0.9% for chlorobenzene and toluene, respectively[9]): the rather low amount and large size of the PCBM crystallites are highly unfavorable since both result in a strongly reduced interfacial contact area between the polymer (electron-donor) and PCBM (electron acceptor).

These observations indicate that the amount and organization of phase separated PCBM is strongly determined by the physico-chemical interactions between PCBM and the casting solvent. Recall that the solubility of PCBM in toluene is 1 g / 100 ml versus 4.2 g / 100 ml in chlorobenzene[19-21]. If these interactions are weak, as is the case for toluene, fast phase separation into well-defined crystallites is enhanced and becomes, especially for low boiling point solvents, strongly dependent on the casting technique since the solvent evaporation rate is faster for spin-coating as compared to doctor blading. These observations might suggest that further improvements in active layer nanomorphologies might be achieved by applying well-selected solvent mixtures.

5.5 Conclusions

A quite different nanomorphology is observed by TEM for thin MDMO-PPV/PCBM films casted from chlorobenzene depending on the amount of PCBM, as schematically is presented below for films containing 50 and 80 wt% PCBM.

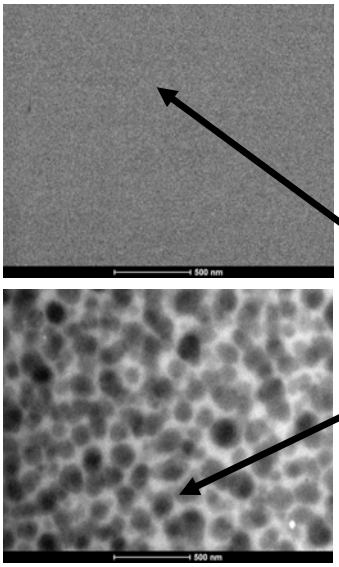

MDMO-PPV /PCBM CB (wt%)	T_{1C}^{s} (s) (short)	T_{1C}^{i} (s) (intermediate)
50/50	11.6 (73 %)	40.2 (27 %)
20/80	11.5 (50 %)	41.3 (50 %)

Concerning MDMO-PPV/PCBM films containing a PCBM amount of 50 wt% and which look homogeneous on TEM images, only an indirect indication for the presence of PCBM nanocrystals is provided by proton wide-line NMR. Their existence however, could only be clearly established based on the intermediate T_{1C} relaxation decay time obtained by ^{13}C MAS relaxometry. A quantification of the amount of PCBM nanocrystals is furnished via the molar fraction of this intermediate T_{1C} decay time.

For films with higher PCBM content PCBM-rich domains clearly show up in the TEM images. Yet the presence of large well-defined PCBM crystals can however be excluded as evidenced by proton wide-line NMR as well as by ^{13}C MAS and CP/MAS. The by TEM observed PCBM-rich domains are demonstrated to consist of nanocrystalline substructures. Their amount can be derived from the molar fraction of the intermediate T_{1C} decay time decay (^{13}C MAS) as well as from the mol fraction of the intermediate $T_{1\rho H}$ decay time (^{13}C CP/MAS).

For the 80/20 wt% MDMO-PPV/PCBM film on the other hand, only an estimation of the amount of PCBM nanocrystals could be derived from a plot of 'mol PCBM in nanocrystals' versus 'mol PCBM in the blend'.

Summarized, independent of the blend composition, all chlorobenzene casted composite films contain PCBM nanocrystals of which the amount increases with increasing PCBM content in the blend. The average dimensions of the PCBM nanocrystals were estimated to be situated between about 5 and 50 nm. This rather small NMR based dimension interval is indirectly supported by XRD patterns showing only broad halos, indicative for the presence of short lengths of coherence. Last but not least DSC experiments further support the NMR findings.

In chapter three and five we evaluated the use of NMR relaxometry as a quantitative and complementary tool to obtain, in a non-destructive way bulk information about the nanomorphology in films used as active layer in organic semi-conducting PV devices. By means of the well-studied MDMO-PPV/PCBM blends, it was shown that proton wide-line NMR relaxometry is a very sensitive tool (few hours acquisition time to determine all relaxation decay times) if phase separation results in well-defined crystallization, as was demonstrated for blends with high PCBM content and processed from toluene solutions. However, in case this phase separation occurs without the formation of well-defined crystals, the more chemical shift selective (but also more time consuming) ^{13}C solid-state NMR techniques are an absolute must, as shown for blends processed from chlorobenzene solutions. For both solvents, a fraction of the PCBM is phase-separated from the co-existing mixed phase and the amount of phase separated PCBM could be determined by NMR relaxometry.

5.6 Experimental part

5.6.1 Materials and film preparation

For details of the purchased materials and the film preparation techniques see section 3.5.1. The MDMO-PPV/PCBM blend compositions studied in this chapter are 15/85, 20/80 and 50/50 wt% or 26/74, 44/56 and 76/24 molar%. This results in a molar proton ratio of respectively 53/47, 61/39 and 86/14 %.

5.6.2 Analytical techniques

For details of DSC, TEM, AFM and XRD see experimental part of the previous chapters. The experimental procedure for solid-state proton wide-line NMR is discussed in section 3.5.2. The only parameters that had to be adapted are the variable evolution time t (see figure 3-12) and the spin-lock time t_{SL} (see figure 3-13) in the pulse sequence for the T_{1H} and $T_{1\rho H}$ experiment, respectively. Here, t varies from 0.01 up to 15 s and t_{SL} varies from 0.25 up to 190 ms.

For the ^{13}C CP/MAS and MAS NMR experiments see section 4.7.2. In this chapter the saturation recovery method (figure 4-15) was replaced by the inversion recovery method (figure 5-8) for determing the T_{1C} relaxation decay times. Hereby the evolution time d2 was varied between 1 and 200 s. The 90° pulse length t_{90} and the acquisition time (at) were 2.5 µs and 25 ms, respectively. In this method the magnetization vector M_0 is first brought by the $180°_{x'}$ pulse parallel to the –z axis.

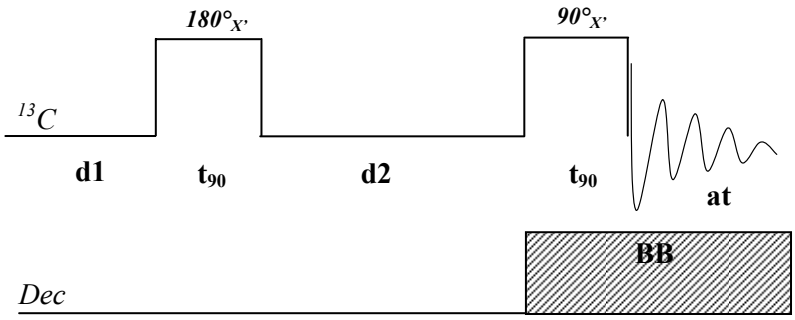

Figure 5-8: *MAS pulse sequence for the determination of T_{1C} via the inversion recovery method.*

During the variable evolution time d2 T_{1C} relaxation occurs, i.e. the macroscopic magnetization gradually returns to its equilibrium value. The $90°_{x'}$ pulse, after d2, serves to bring this actual z-magnetization, for the most values of d2 not yet in the equilibrium value, in the xy-plane as that is the plane where detection of the signal occurs. The T_{1C} decay time is then obtained by analysing the integrated carbon signal intensity I(t) bi-exponentially as a function of the variable inversion time d2 according to:

$$I(t) = I_0^s(1 - 2\exp(-d2/T_{1C}^s)) + I_0^i(1 - 2\exp(-d2/T_{1C}^i))$$

where the superscripts s and i refer to the fractions with short and intermediate decay time, respectively.

For the CP/MAS experiments, the $T_{1\rho H}$ relaxation decay times were obtained using the delayed cross-polarization method (figure 5-9) described by Aujla *et al*[22] in which, after an initial proton 90° pulse (length t_{90} = 2.45 µs), the proton magnetization is kept in spin lock (B_{1H} field of 75 kHz) for a variable time t_{SL} between 0.25 and 150 ms before it is cross-polarized to the carbon nuclei during a fixed contact time cntct of 3.5 ms. The acquisition time (at) was lowered to 8 ms in order to prevent damage of the probe. The $T_{1\rho H}$ decay time is then obtained indirectly by analyzing the integrated carbon signal intensity (see figure 5-9: signal detection on the ^{13}C channel) mono-exponentially according to:

$$I(t_{SL} + \text{cntct}) = I_0 \exp(-(t_{SL} + \text{cntct}) / T_{1\rho H})$$

The variable parameter in the fitting equation is the sum of t_{SL} and cntct as the relaxation processes continue during the CP contact time cntct.

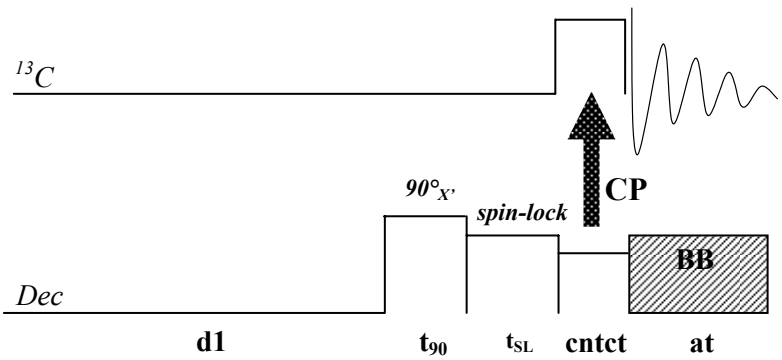

***Figure 5-9**: CP/MAS pulse sequence for the determination of $T_{1\rho H}$.*

The relaxation decay times T_{1H} were measured under high power DD (100 kHz) by means of the inversion recovery method (figure 5-10) in which the evolution time d2 was varied between 0.01 and 7 s. The 90° pulse length t_{90} and the acquisition time (at) were 2.45 µs and 25 ms, respectively. In this method the proton magnetization vector M_0 is first brought parallel to the –z axis by the $180°_{X'}$ pulse. During the variable evolution time d2 T_{1H} relaxation occurs, i.e. the magnitude of the z-component of the proton macroscopic magnetization M_z gradually returns back to its equilibrium value M_0. The $90°_{X'}$ pulse, after d2, serves

to bring this actual z-component, for the most part not yet in the equilibrium value, in the xy-plane. Next the proton magnetization is cross-polarized to the carbons during a fixed contact time cntct of 3.5 ms. Finally the T_{1H} decay time is then obtained by analyzing the integrated carbon signal intensity mono-exponentially according to:

$$I(d2) = I_0(1 - 2\exp(-d2 / T_{1H}))$$

In spite of the fact that T_{1H} relaxation is also occurring during the fixed contact time cntct of 3.5 ms, the latter can safely be omitted in the above equation as the T_{1H} relaxation time constants are in the order of seconds.

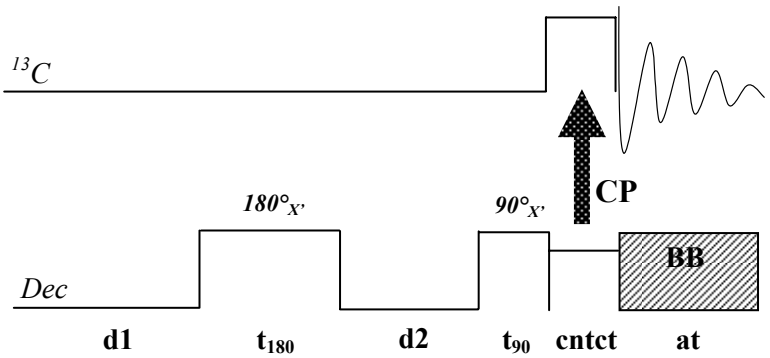

***Figure 5-10**: CP/MAS pulse sequence for the determination of T_{1H}.*

5.7 References

1. Hoppe, H.; Niggemann, M.; Winder, C.; Kraut, J.; Hiesgen, R.; Hinsch, A.; Meissner, D.; Sariciftci, N.S., *Adv. Funct. Mater.* **2004**, 14, 1005.
2. Martens, T.; D'Haen, J.; Munters, T.; Beelen, Z.; Goris, L.; Manca, J.; D'Olieslaeger, M.; Vanderzande, D.; De Schepper, L.; Andriessen, R., *Synth. Met.* **2003**, 138, 243.
3. Martens, T.; D'Haen, J.; Munters, T.; Beelen, Z.; Goris, L.; Manca, J.;D'Olieslaeger, M.; Vanderzande, D.; De Schepper, L.; Andriessen, R., *Proc. SPIE-Int. Soc. Opt. Eng.* **2003**, 4801, 40.
4. Hoppe, H.; Drees, M.; Schwinger, W.; Schäffler, F.; Sariciftci, N.S., *Synth. Met*. **2005**, 152, 117.
5. van Duren, J.K.J.; Yang, X.; Loos, J.; Bulle-Lieuwma, C.W.T.; Sieval, A.B.; Hummelen, J.C.; Janssen, R.A.J. *Adv. Funct. Mater.* **2004**, 14, 425-434.
6. Brabec, C.J.; Cravino, A.; Meissner, D.; Sariciftci, N.S.; Fromherz, T.; Rispens, M.T.; Sanchez, L.; Hummelen, J.C. *Adv. Funct. Mater.* **2001**, 11, 374-380.

7. Mozer, A.J.; Denk, P.; Scharber, M.C.; Neugebauer, H.; Sariciftci, N.S.; Wagner, P.; Lutsen, L.; Vanderzande, D.; Kadashchuk, A.; Staneva, R.; Resel, R. *Synth. Met.* **2005**, 153, 81-84.
8. Yang, X.; Loos, J., *Macromolecules* **2007**, 40, 1353.
9. Shaheen, S.E.; Brabec, C.J.; Sariciftci, N.S.; Padinger, F.; Fromherz, T.; Hummelen, J.C., Appl. Phys. Lett. 2001, 78, 841.
10. Yang, X.; van Duren, J.K.J.; Janssen, R.A.J.; Michels, M.A.J.; Loos, J., *Macromolecules* **2004**, 37, 2151.
11. Peet, J.; Kim, J.Y.; Coates, N.E.; Ma, W.L.; Moses, D.; Heeger, A.J.; Bazan, G.C., *Nature Mat.* **2007**, 6, 497.
12. Dante, M.; Garcia, A.; Nguyen, T-Q, *J. Phys. Chem.* **2009**, 113, 1596.
13. Bulle-Lieuwma, C.W.T.; van Gennip, W.J.H.; van Duren, J.K.J.; Jonkheijm, P.; Janssen, R.A.J.; Niemantsverdriet, J.W., *Appl. Surf. Sci.* **2003**, 203, 547.
14. Peumans, P.; Yakimov, A.; Forrest, S.R., *J. Appl. Phys.* **2003**, 93, 3693.
15. Ferenczi, T.A.M.; Nelson, J.; Belton, C.; Ballantyne, A.M.; Campoy-Quiles, M.; Braun, F.M.; Bradley, D.D.C., *J. Phys.:Condens. Matter.* **2008**, 20, 475203.
16. van Bavel, S.S.; Sourty, E.; de With, G.; Loos, J., *Nano Lett*. **2009**, 9, 507.
17. Roex, H.; Adriaensens, P.; Vanderzande, D.; Gelan, J. *Macromolecules* **2003**, *36*, 5613.
18. Harris, R.K., *Nuclear Magnetic Resonance Spectroscopy-A Physicochemical View* **1983**, Pitman Books Limited, London.
19. Li, G.; Shrotriya, V.; Huang, J.; Yao, Y.; Moriarty, T.; Emery, K.; Yang, Y., *Nat. Mater.* **2005**, 4, 864.
20. Kim, Y.; Choulis, S.A.; Nelson, J.; Bradley, D.D.C.; Cook, S.; Durrant, J.R., *Appl. Phys. Lett.* **2005**, 86, 063502.
21. Hoppe, H.; Sariciftci, N.S., *J. Mater. Chem.* **2006**, 16, 45.
22. Aujla, R.S.; Harris, R.K.; Packer, K.J.; Parameswaran, M.; Say, B.J.; Bunn, A.; Cudby, M.E.A., *Polym. Bull.* **1982**, *8*, 253.

Chapter Six

P3HT/PCBM Thin Films Doctor Bladed from Chlorobenzene and Toluene

6.1 Introduction

This chapter deals with a morphology study of thin P3HT/PCBM films obtained by doctor blading from chlorobenzene and toluene solutions. Roman *et al*[1] first reported in 1997 on OPV devices comprising polythiophene/fullerene BHJ films. Since then plastic solar cells built from this D/A system consistently achieve the highest power conversion efficiencies (efficiencies beyond 5 % are reported). The power conversion efficiencies η_e are significantly higher if e.g. MDMO-PPV is replaced by P3HT as the donor material, and this improvement can be related to its intrinsic properties. It is demonstrated that the hole mobility is much higher in P3HT: up to $1x10^{-5}$ $m^2V^{-1}s^{-1}$ for P3HT[2-4] versus $5x10^{-11}$ $m^2V^{-1}s^{-1}$ for MDMO-PPV[5]. The higher hole mobility is a consequence of a more efficient interchain transport made feasible by the self-organization into a microcrystalline structure for regioregular P3HT[6]. Furthermore, an improved overlap is observed with the solar emission spectrum as a consequence of a red shift in the absorption spectrum of P3HT caused by interchain π-π stacking interactions. Note that for completeness it should be mentioned that very recently a new generation of donor polymers like e.g. PCPDTBT and PBDTTT (see figure 1-11 for chemical structures) outperform the P3HT-based OPV devices. Today's state-of-the-art maximum power conversion efficiency η_e of 6.77 % in organic BHJ solar cells is reached in PBDTTT/PC_{70}BM devices[7].

It was initially reported by Chirvase *et al*[8] and Savenije *et al*[9] that, upon thermal annealing, small PCBM structures appeared in P3HT/PCBM layers casted from chloroform. Later on it was observed that the best power conversion efficiencies η_e were only achieved by performing a post-production thermal annealing step, eventually accompanied by applying an external voltage[10-12] (see section 1.2.6.5). The increased performance upon annealing is attributed to less

charge recombination, higher hole mobility and improved charge transport[13,14]. As a result a higher external quantum efficiency (EQE) is achieved[15], which benefits the I_{SC} (see section 1.2.1).

Yang *et al*[16] started by reporting in detail on the differences in nanomorphology between as-processed and thermally annealed films of P3HT/PCBM using TEM and SAED (Selected-Area Electron Diffraction), and several morphology studies by microscopic techniques followed[17-21]. The authors concluded that post-production thermal annealing enhances not only the crystalline nature of the photoactive film but also the controlled demixing of the active components therein. Optimally, a controlled thermal annealing of P3HT/PCBM 1/1 films improves the efficiency of the device by a factor of almost ten. As already discussed thoroughly in chapter one, one of the requisites to obtain high performance BHJ solar cells is an optimized nanoscaled interpenetrating network with crystalline order for both donor and acceptor components, as charge carrier transport and mobility in organic and polymer semiconducting materials are increased by mesoscopic order and crystallinity[22-24]. Furthermore the annealing process ensures that geminate recombination of charge pairs is much more reduced by the formation of larger crystalline domains of both P3HT and PCBM, as compared to native films[25].

Remark that, as mentioned in section 1.2.6, the optimal morphology of P3HT/PCBM films with increased power conversion efficiency can likewise be achieved by several other methods as there are the use of chemical additives[20,15,26], a reduced drying speed of the film[27-29] and the choice of the casting solvent[30]. The influence of the latter will be demonstrated at the end of this chapter.

The aim of the research described in this chapter is to find out if the nanostructured morphology of P3HT/PCBM based films can also be quantitatively described by solid-state ^{1}H wide-line, ^{13}C MAS and ^{13}C CP/MAS NMR relaxometry. As discussed in chapter 1 (section 1.3), NMR relaxometry is a well-established technique to study polymers but only a few studies have been reported on the investigation of the complex 3D morphology of BHJ donor/acceptor films[31,32]. Yang *et al*[32] studied P3HT/fullerene 1/1 films using 2D NMR techniques. The authors observed a higher degree of interaction between the P3HT hexyl side chains and the fullerenes for native films as compared to annealed films.

In this chapter, doctor bladed P3HT/PCBM films are studied by solid-state NMR relaxometry. Both as-processed and post-production thermally annealed

films has been extensively studied by means of NMR relaxometry, optical microscopy and TEM. Finally, the influence of the casting solvent and the purity of PCBM on the performance of doctor bladed solar cells are discussed.

6.2 Explorative study of the thin film P3HT/PCBM nanomorphology by microscopy

6.2.1 Optical microscopy

A detailed study by optical microscopy was performed on 130 nm thick P3HT/PCBM films prepared by doctor blading from chlorobenzene solutions. Both as-processed and thermally annealed films were investigated. Optical microscopy is an appropriate tool to evaluate the film quality and morphology at low magnification. It can be considered as a "first screening" technique to judge the morphology as a function of varying experimental conditions. Optical microscopy images of films with weight ratios 1/1, 1/2 and 1/4 are presented in figures 6-1, 6-2 and 6-3, respectively. The annealing temperature was varied from 75 °C up to 225 °C, while the annealing time was kept constant at 10 minutes. Each presented image is, unless stated otherwise, taken from a new film. As can be noticed in the corresponding figures, quite uniform films are obtained for all annealing temperatures and weight ratios, demonstrating the quality of films obtained by doctor blading. In order to achieve uniform and reproducible annealing results, it is important to work with a dedicated heating system, i.e. in which the temperature is spatially independent (no thermal gradients) and well-controlled over the entire film (see section 6.7.2 for a detailed description).

Independently of the blend composition, optical microscopy images of native films as well as films annealed up to 125 °C look quite homogeneous, i.e. no large-scale phase separation is noticed. It is known from the literature that the native film morphology of the blends results from a dual crystallization behavior in which the crystallization of each component is hindered by the other component[33]. Nonetheless, several arguments for the presence of small PCBM nanocrystals in these films will be presented in sections 6.2.2 and 6.3. However for all blend compositions studied, needle-like structures start to form at an annealing temperature of 150 °C. Annealing at this temperature results in needles with avera-

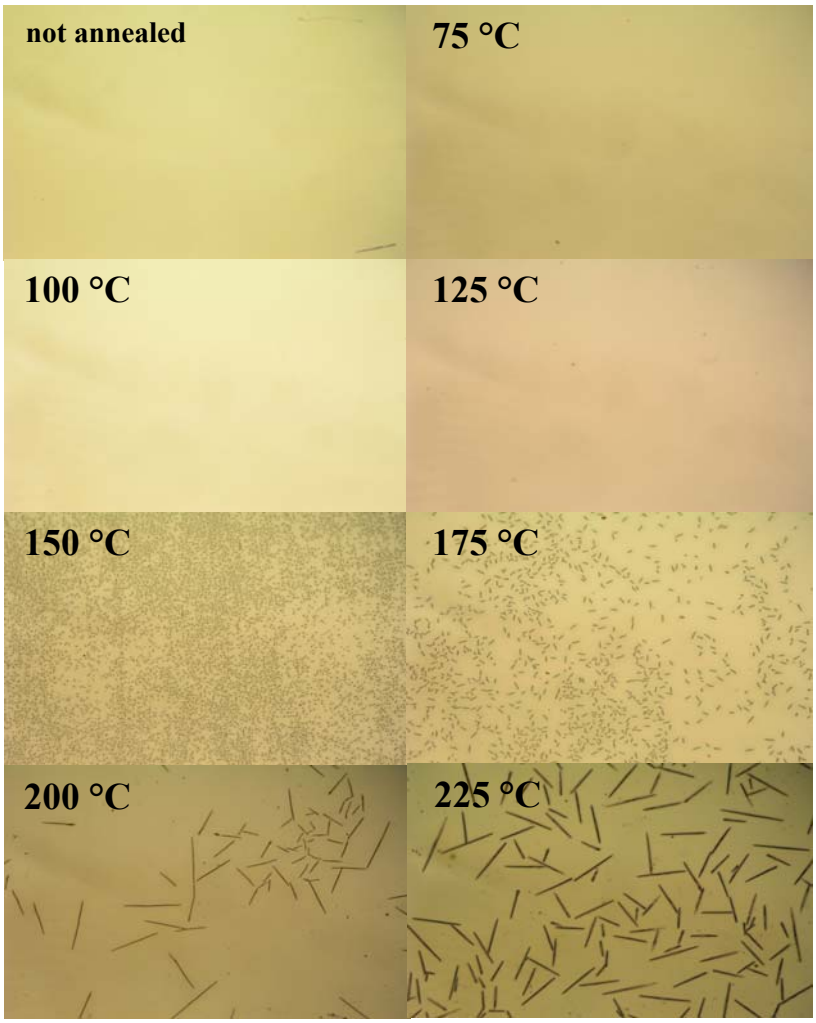

Figure 6-1: *Optical microscopy images of 130 nm thick P3HT/PCBM 1/1 films doctor bladed from chlorobenzene solutions and annealed for 10 minutes at different annealing temperatures (image dimensions: 465 x 630 µm).*

ge dimensions of 2 x 4 µm, 2 x 25 µm and 2 x 20 µm for the 1/1, 1/2 and 1/4 blends, respectively. By comparing the optical images in the series 1/1 → 1/2 → 1/4, it can be inferred that the needle-like structures originate from PCBM as their dimensions clearly grow with increasing PCBM content. The needles observed for the 1/1 blend unmistakable become longer for increasing annealing temperatures but their width of around 2 µm remains more or less the same (e.g. 2 x 80 µm at 225 °C). Higher annealing temperatures result in longer needles for the 1/2 films while fan-shaped PCBM structures appear in the 1/4 blends.

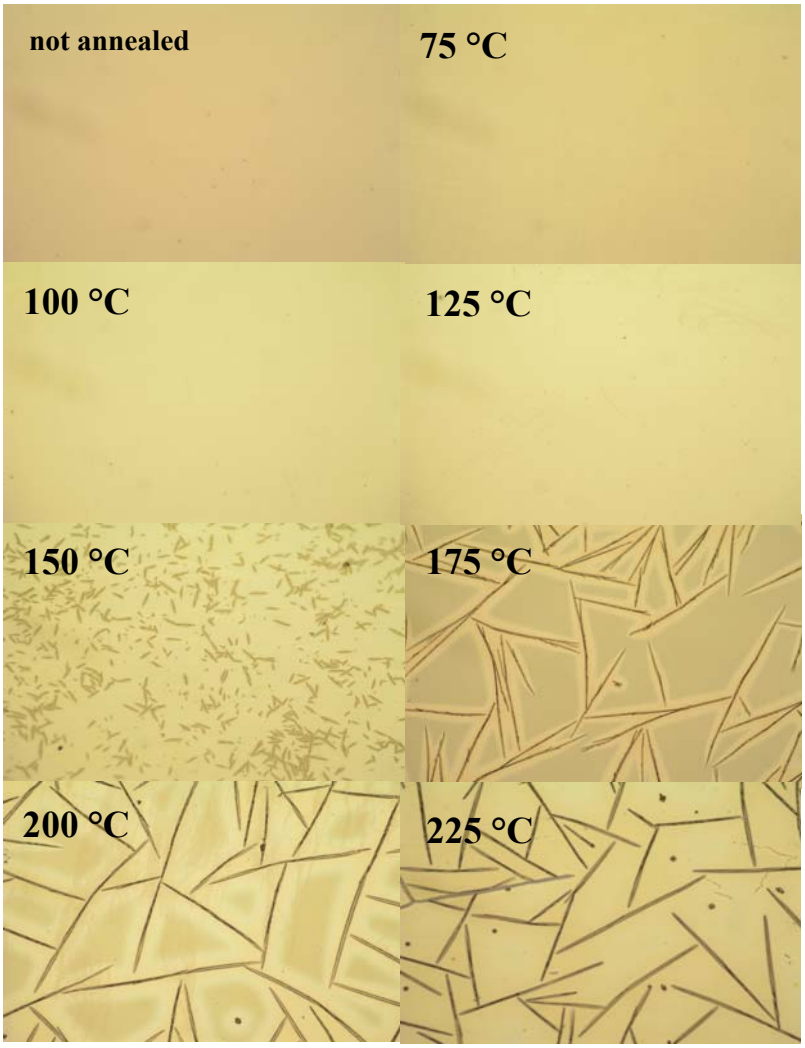

Figure 6-2: *Optical microscopy images of 130 nm thick P3HT/PCBM 1/2 films doctor bladed from chlorobenzene solutions and annealed for 10 minutes at different annealing temperatures (image dimensions: 465 x 630 µm).*

Basically similar optical microscopy images were already observed by Swinnen *et al*[34] and Miyanishi *et al*[35] for spin-coated P3HT/PCBM films. However, Schilinsky *et al*[36] also reported on the performance of doctor bladed versus spin-coated BHJ solar cells. According to these authors, one of today's challenges is the up scaling from the small-area laboratory devices to large-area modules. This requires large-area high-quality films. Changing from spin-coating to large-scale roll-to-roll techniques, e.g. doctor blading, will be inevitably. Films processed from

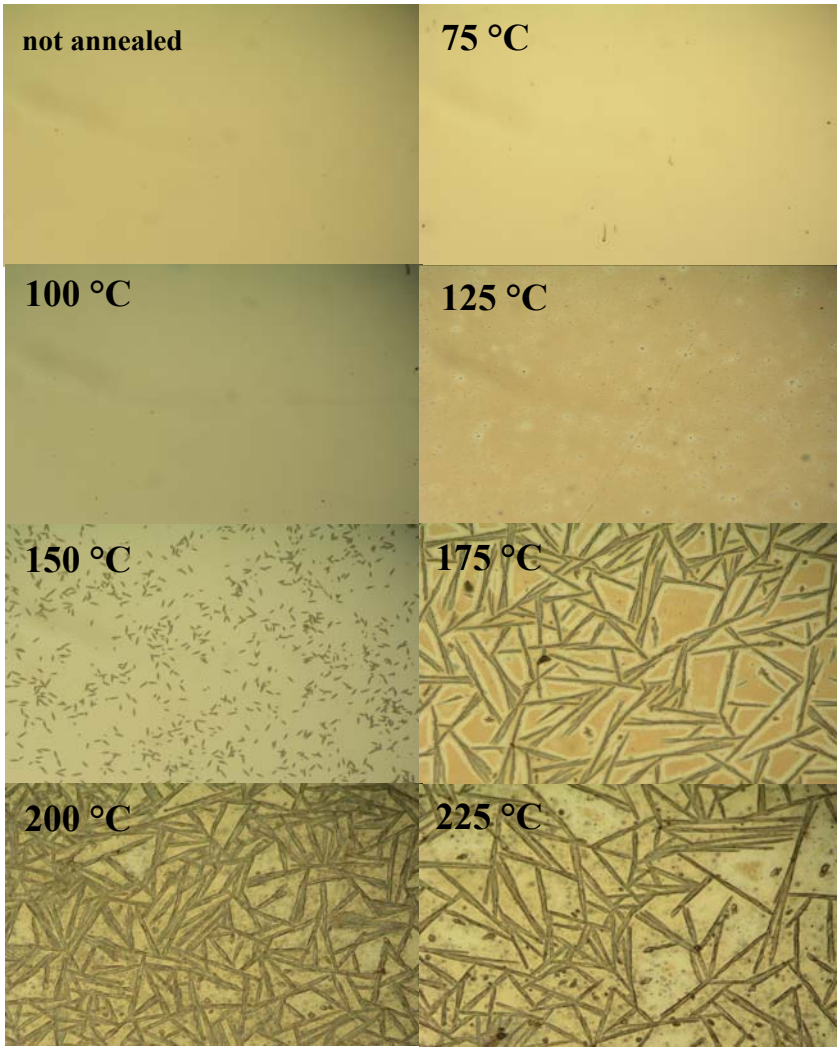

Figure 6-3: *Optical microscopy images of 130 nm thick P3HT/PCBM 1/4 films doctor bladed from chlorobenzene solutions and annealed for 10 minutes at different annealing temperatures (image dimensions: 465 x 630 µm).*

xylene solutions with both techniques (spin-coating and doctor blading) were compared towards their performance in solar cells. The authors reported reproducible PCEs beyond 4 % for doctor bladed BHJ cells in which the thickness of the active layer was between 100 and 200 nm. Recall that in our study large-scale active layers were processed by doctor blading (~ 20x10 cm^2). Most published results on the other hand are based on small-area films, typically only a few square centimetres or even less[37].

How can these observations and especially the critical annealing temperature of 150 °C at which, irrespective of the blend ratio, needle-like PCBM structures start to appear be explained? Obviously the glass transition temperature T_g plays an important role. It is well known from literature (and observed by our experimental work described in section 6.2) that thermal annealing above the T_g's of the polymer and PCBM drives the PCBM molecules to diffuse into separated domains and simultaneously allows the P3HT to grow into elongated fibrillar-like crystals[8,16,38,39]. The T_g of PCBM is reported to be ~ 131 °C[33]. Remark that the T_g of P3HT is still under debate (since the T_g is not a thermodynamic property it depends on the processing history, molecular weight, regioregularity, … of the polymer). Zhao *et al*[33] proposed a single T_g for the P3HT/PCBM blends which decreases with increasing polymer content towards the value of the pure P3HT, being 12.1 °C. Based on the measurements of these authors, the T_g's of the blends studied in this chapter are situated between 40 °C (1/1 blend) and 80 °C (1/4 blend). From our optical microscopy study however, it can be concluded that only temperatures above the T_g of PCBM (131 °C) allow PCBM to diffuse into phase separated domains of which the dimensions are sufficiently large to be detected by optical microscopy. This might be a first indication that the blends consist of a mixed P3HT/PCBM phase (T_g of 40-80 °C) as well as phase separated PCBM (T_g of 131 °C), which could explain why only starting from the "critical" annealing temperature of 150 °C phase separated PCBM needles are observed. Regarding the formation of larger PCBM structures (exceeding 100 μm) at higher annealing temperatures, this seems to require annealing above the melting temperature T_m of the P3HT. According to Zhao *et al*[33] the T_m of P3HT in the blends decreases with increasing PCBM content and is reported to be ~ 185 and ~ 175 °C for the 1/1 and 1/2 blends, respectively. With respect to the solar cell performance, uncontrolled annealing in which large PCBM needles show up in the films, dramatically lowers the interfacial area between donor and acceptor resulting in a less efficient exciton dissociation. Kim *et al*[30] reported that the optimal annealing temperature for spin-coated P3HT/PCBM 1/1 films is 140 °C which is consistent with our observations by optical microscopy.

Figure 6-4-A-C depicts optical microscopy images of a P3HT/PCBM 1/1 film which was subjected to a number of successive annealing steps at 175 °C. Image A was taken after annealing for 10 minutes and the same morphology as in figure 6-1 is observed, i.e. phase separated PCBM needles with an average length

of 4 µm. Image B shows that the nanomorphology does not change after two additional annealing steps of 10 minutes. Moreover after a series of three additional annealing steps of 10 minutes, no changes were noticed in the microscopic morphology (image C). Last but not least, even an additional treatment of 15 minutes at 225 °C had no further impact (image D). On the other hand, the film morphology observed in image D is clearly different from the one observed after a single annealing of 10 minutes at 225 °C (see figure 6-1). It looks that after the first annealing step (10 min at 175 °C) a fixed morphology, at least on a µm scale , is formed.

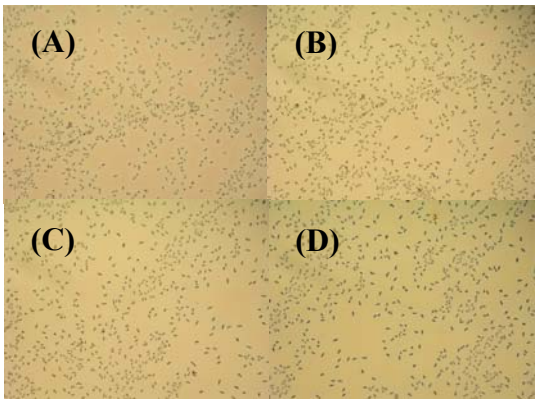

Figure 6-4: *Optical microscopy images of a P3HT/PCBM 1/1 film doctor bladed from a solution in chlorobenzene and subjected to a number of successive annealing steps: 10 minutes at 175 °C (A), followed by 2 extra steps of 10 minutes at 175 °C (B), another 3 extra steps of 10 minutes at 175 °C (C) and finally a last additional step of 15 minutes at 225 °C (D) (image dimensions: 465 x 630 µm).*

Figure 6-5 depicts images of a P3HT/PCBM 1/1 film subjected to a number of successive annealing steps of 10 minutes at increasing temperatures. The images were taken on the same spot of the film, as monitored by a marker stripe at the right-under corner. Also in this way PCBM needles are formed starting at 150 °C. As will be shown later by NMR relaxometry, the polymer matrix still contains a significant molar amount of PCBM at this stage. An additional annealing step at 175 °C only slightly increases the amount of PCMB needles but not their average size. Most likely further phase separation of PCBM from the matrix occurs in this second annealing step at 175 °C. Extra annealing steps at 200 °C and 225 °C did not result in further changes, neither in amount nor in size of the phase separated PCBM, as was also observed for the experiment described in figu-

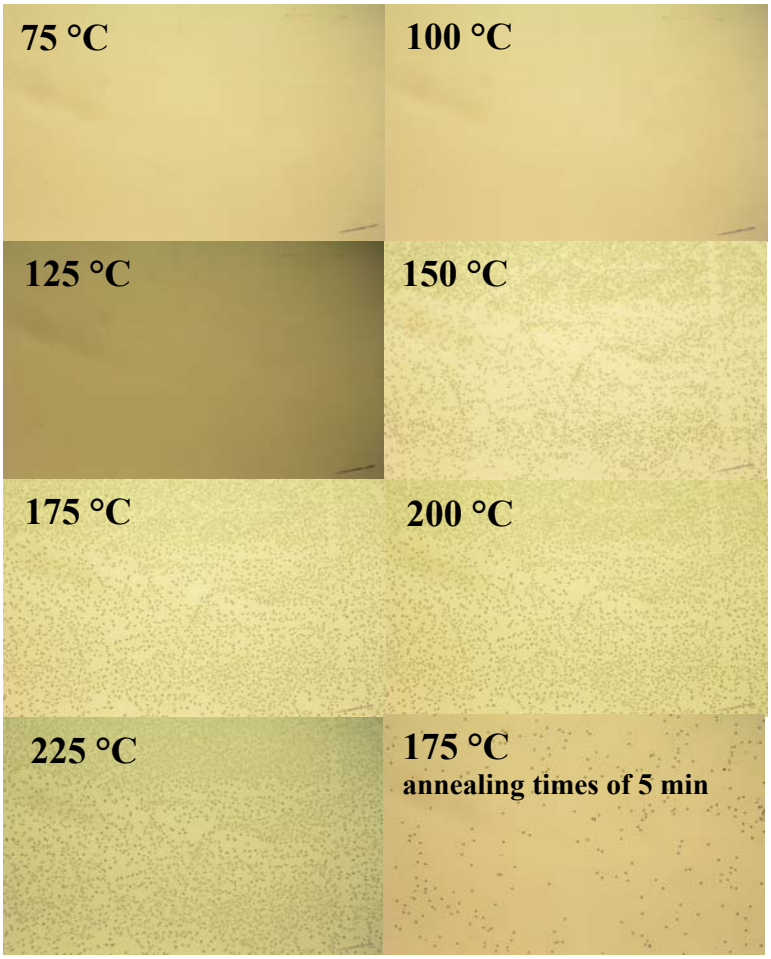

Figure 6-5: *Optical microscopy images of a P3HT/PCBM 1/1 film doctor bladed from a solution in chlorobenzene subjected to a number of successive annealing steps of 10 minutes. The last image shows a 1/1 film subjected to a number of successive annealing steps of 5 minutes at 75, 100, 125, 150 and 175 °C (image dimensions: 465 x 630 µm).*

re 6-4. Starting from 150 °C the initial annealing temperature dictates the amount and dimensions of phase separation. Once a dense physical network of P3HT fibers and PCBM needles is formed, it fixes the blend morphology at least at the µm level. This behavior can be understood in terms of surface energy minimization, being the driving force for the molecules to aggregate. Annealing above a critical temperature of 150 °C initiates the diffusion of PCBM molecules (high surface energy) into local PCBM needles (low surface energy). However once these µm needles are formed, they have become too large to be further organized by

molecular diffusion (at least in this time period) explaining why additional annealing at higher temperatures has no further influence.

The same trends are observed if the annealing time is reduced from 10 to 5 minutes. However a shorter annealing time leads to a significant reduction in the amount of PCBM needles, as demonstrated in the last image of figure 6-5.

6.2.2 Transmission electron microscopy

In this section the nanomorphology of the thin doctor bladed P3HT/PCBM films is further scrutinized by TEM and Selected-Area Electron Diffraction (SAED) experiments. Firstly the "P3HT/PCBM matrix", which is that part of the films in between the observed PCBM needles, as exemplified in figure 6-6 for a 1/2 film annealed for 10 minutes at 200°C, will be examined. In addition, attention

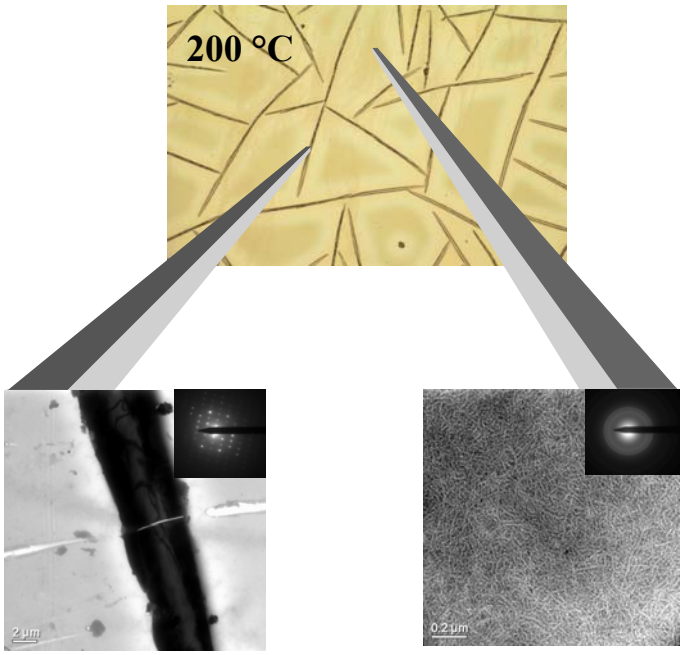

Figure 6-6: *Designation of the film areas which were subjected to a closer look by means of TEM and SAED, as demonstrated here for the optical microscopy image of a 130 nm thick doctor bladed P3HT/PCBM 1/2 film annealed for 10 minutes at 200 °C.*

will also be paid to the needle-like PCBM structures themselves. In order to interpret the SAED patterns some characteristics of it are pointed out. Note first that the diameters of the field-limiting apertures applied in our experiments are 6 μm and 1.2 μm for the matrix and needles, respectively. It is important to realize that the observed SAED pattern is strongly dependent on this parameter[40]. Brighter and sharper Debye-Scherrer diffraction rings in general represent a higher degree of crystallinity. Furthermore the diameter of the diffraction ring inversely corresponds to the associated distance in the crystal lattice.

6.2.2.1 Morphology of the "P3HT/PCBM matrix"

Figure 6-7 shows the bright-field TEM images and corresponding SAED patterns of as-processed, native 130 nm thick P3HT films and P3HT/PCBM 1/1 films doctor bladed from chlorobenzene. In the SAED pattern of the P3HT film (inset of figure 6-7-left) an intense Debye-Scherrer diffraction ring is observed which points to the semi-crystalline nature of the polymer. The diffraction ring corresponds to a distance of 3.8 Å and represents the superposition of the (020) and (002) reflections of the P3HT crystals[41]. The Miller indices (020) are associated with the π-π stacking distance of the P3HT chains, which is referred to in the literature as the lattice parameter b[6,7,42]. The bright-field TEM image of the native P3HT film shows the presence of bright and dark regions. Hugger *et al*[41] concluded that the state of P3HT obtained in thin spin-coated P3HT films is a trapped non-equilibrium state with reduced order and orientation. The authors also showed by DSC and XRD that around 225 °C an endothermic phase transition takes place for regioregular P3HT from the crystalline state into a layered, smectic liquid crystalline structure with the layers parallel to the substrate. Annealing of spin-coated P3HT films in this liquid crystalline state leads to the formation of a well-developed needle-like P3HT morphology (bright regions) next to amorphous P3HT (dark regions), i.e. a morphology as observed for native drop-casted P3HT films by AFM. It can be expected that the dimensions of the P3HT fibres present in our native doctor bladed films are situated between these of spin-coated and drop-casted films. As described by Hugger *et al*, the bright regions can be assigned to P3HT fibre-rich domains while the dark regions arise from P3HT amorphous-rich domains.

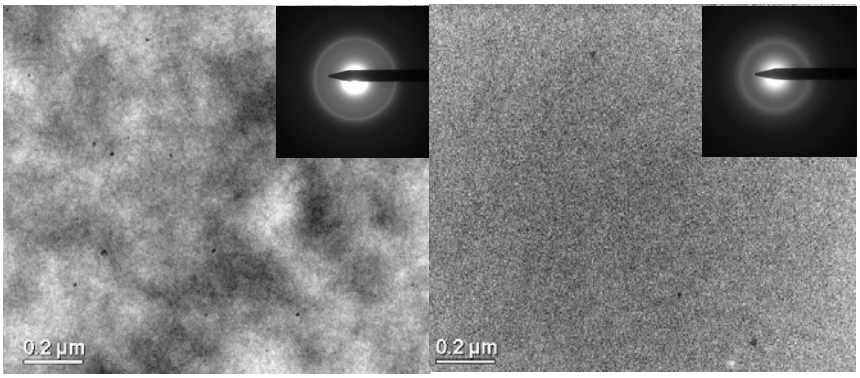

Figure 6-7: *TEM images and SAED patterns of as-processed 130 nm thick P3HT (left) and P3HT/PCBM 1/1 (right) films doctor bladed from chlorobenzene.*

The SAED of the native P3HT/PCBM 1/1 film (inset of figure 6-7-right) contains a blurred and broader Debye-Scherrer ring corresponding to a distance of 4.6 Å and which originates from PCBM. Yang *et al*[40] proposed two possible morphologies for this PCBM diffraction ring. Or it arises from PCBM molecules in mesoscopic low-order domains or, alternatively from PCBM that is organized in densely stacked, small nanocrystals. The latter organization inhibits a pronounced bright-field contrast as many nanocrystals with different crystallographic orientations are simultaneously selected in the region of the field-limiting aperture. Note that such a blurred and broad PCBM Debye-Scherrer ring was also observed in the SAED pattern of a 100 nm thick PCBM film prepared by doctor blading from chlorobenzene (see figure 4-16). As shown in figure 6-7-right, the Debye-Scherrer ring originating from the P3HT crystals is not discernible anymore in the native 1/1 composite film. It is well known from the literature that the presence of PCBM strongly suppresses the crystallization of P3HT in untreated composite films[33,42,43] with PCBM content ≥ 40 wt%. This statement is further supported by the bright-field TEM image in which hardly well-developed P3HT fibers are noticed. Instead, the film shows a quite homogeneous morphology over the whole image range.

Regarding the influence of thermal annealing, figure 6-8 shows the bright-field TEM images and corresponding SAED patterns of the "P3HT/PCBM matrix" of thin films prepared by doctor blading from solutions in chlorobenzene for the different blend weight ratios (1/1, 1/2 and 1/4) and annealing temperatures of 100, 150 and 200 °C. The annealing time was always 10 minutes. The morphology of

the P3HT/PCBM matrix of 1/1 films annealed at 100 °C looks quite similar on TEM images and SAED patterns as for native 1/1 films. Recall that optical microscopy reveals that both films show no phase separated PCBM needles. This in contrast to 1/1 films annealed at 150 °C which show bright-field TEM images containing P3HT fibrils of which the microscopic contrast and average length is increased, indicating an improved crystallinity. The effect is even more pronounced upon annealing at 200 °C, by which the lateral width of the fibrils seems to increase significantly as well. These fibrils, relatively bright in contrast, can be attributed to P3HT because of the lower density of P3HT (1.10 g cm^{-3})[7] as compa-

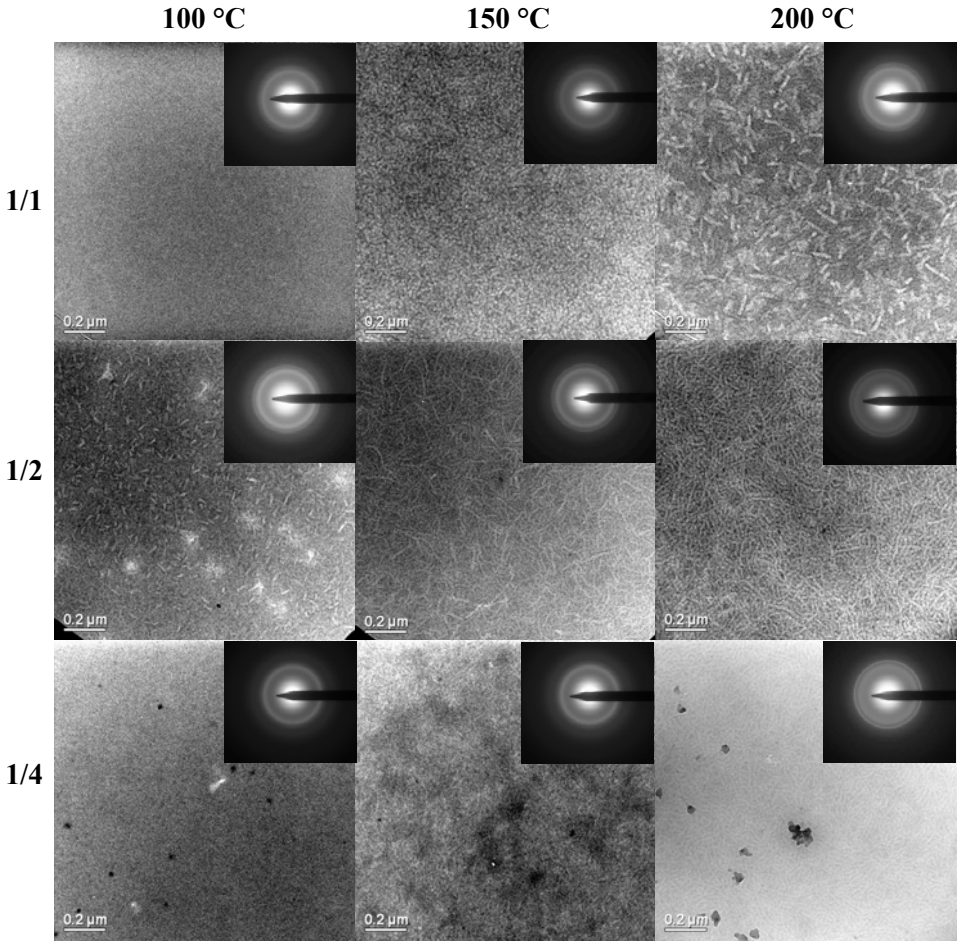

Figure 6-8:*TEM images and corresponding SAED patterns of the P3HT/PCBM matrix of films prepared by doctor blading for different blend weight ratios and annealed for 10 minutes at different temperatures.*

red to PCBM (1.50 g cm^{-3})[44]. These observations are in accordance with the above mentioned findings of Hugger *et al*[41] for P3HT films. Indeed also, Zhao *et al*[33] reported a melt crystallization temperature of P3HT in 1/1 P3HT/PCBM blends of about 125 °C. The same dependency of the degree of P3HT crystallization on the annealing conditions is observed for spin-coated films[9,16,45]. Summarizing, it may be stated that annealing of 1/1 films at moderate temperatures (<140-150 °C) results in fibrillar-like P3HT crystals which constitute an interpenetrating network providing continuous pathways for efficient hole transport in the conjugated polymer. Because of the high aspect ratio of the P3HT fibrils, there is an optimal interfacial area with the PCBM and a lateral average size in the order of the exciton diffusion length is ensured. In this way a more optimal morphology is attained which ensures the improved power conversion efficiencies in the corresponding plastic solar cells. Remark that the darker regions in figure 6-8 can represent PCBM as well as amorphous P3HT. However, at higher annealing temperatures (≥ 150 °C; see figure 6-1) the PCBM starts to phase separate and crystallize into large needles by which this optimal morphology is destroyed.

Although the degree of P3HT crytallinity can be qualitatively monitored by means of TEM (figure 6-8), nothing can be concluded from it regarding the physico-chemical nature of the PCBM in the matrix. For this purpose it is more appropriate to make an appeal to the corresponding SAED patterns. Figure 6-9 shows a magnification of the SAED's taken from the 1/1 composite films. A blurred and broad Debye-Scherrer ring originating from the PCBM and corresponding to a distance of 4.6 Å can be noticed for all films, independently of the annealing temperature. From this it can be concluded that at least a part of the PCBM in the "P3HT/PCBM matrix" appears in a low-order organization, i.e. in nanocrystals as indicated by Yang *et al*[40]. Furthermore for the 1/1 composite films annealed at 150 °C as well as 200 °C, which both show phase separation of PCBM into large needles on optical microscopy images, one can decide that not all the PCBM is segregated into this needle-like structures. Note also that only for an annealing temperature of 200 °C a pronounced Debye-Scherrer ring from P3HT shows up in figure 6-9. Although TEM clearly displays P3HT fibres after annealing the 1/1 blend at 150 °C, the corresponding Debye-Scherrer ring is probably too diffuse to be observed by SAED. Often the SAED patterns suffer from a strong contribution from inelastic scattering. In order to improve the signal-to-noise ratio, an integration over the complete diffraction ring was done (by ad-

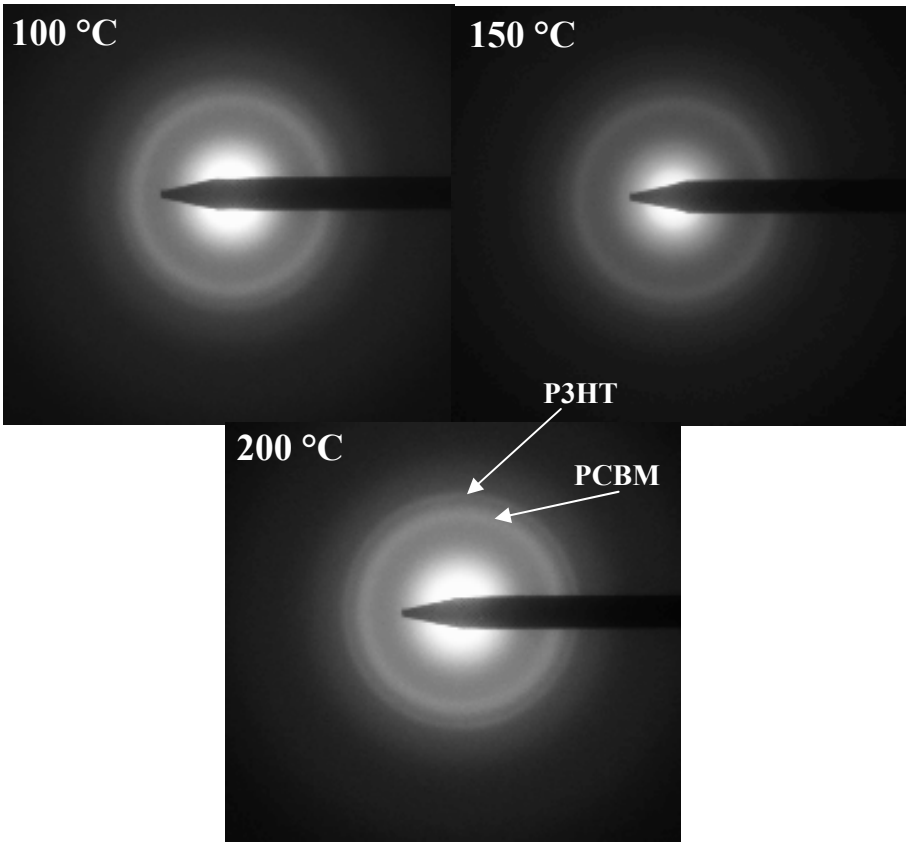

Figure 6-9: *SAED patterns of the P3HT/PCBM matrix of 1/1 films prepared by doctor blading and annealed for 10 minutes at different temperatures.*

ding the intensity of the complete diffraction rings at constant distances from the center point), from which the calculated inelastic scattering background was subtracted. Figure 6-10 shows the resulting residual profiles as a function of the *d*-spacing (related to the radius of the ring) for some selected films. In the profile of the native P3HT/PCBM 1/1 film, *d*-spacings of 4.6, 3.1 and 2.1 Å are noticed which correspond to nanocrystalline PCBM. These values are in agreement with the reported *d*-spacings observed in SAED patterns of PCBM films casted from chlorobenzene and toluene[40]. The same *d*-spacings are present in the profile of the 1/1 composite film which was annealed for 10 minutes at 200 °C. However, the latter also shows a peak at 3.8 Å which originates from the P3HT fibres. This peak at 3.8 Å is barely visible as a shoulder in the profile of the native 1/1 film. So the SAED information (figures 6-9 and 6-10) is in agreement with the observations

seen in BF-TEM of figure 6-8.

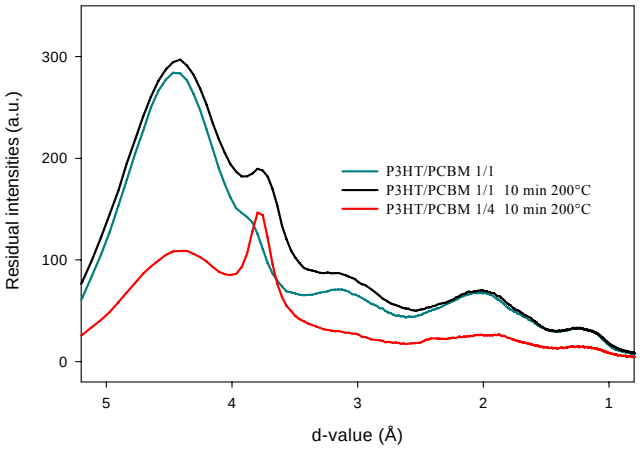

Figure 6-10: *Graph of residual SAED intensity versus d-spacing for some selected P3HT/PCBM films.*

Thermal annealing does not only increase the P3HT crystallinity in P3HT/PCBM films. Pristine P3HT powder is also sensitive to annealing as is demonstrated in the diffractograms of figure 6-11. Herein, the annealed P3HT samples show, next to an amorphous halo, an intense peak at $2\theta = 5.4°$ and a weak second order reflection at 10.8° (Miller indices (100) and (200), respectively). The lattice constant d which corresponds to this reflection can be evaluated by using Bragg's law:

$$2d \sin\theta = n\lambda$$

where n is the interference order, $\lambda = 1.54056$ Å is the wavelength of the incident

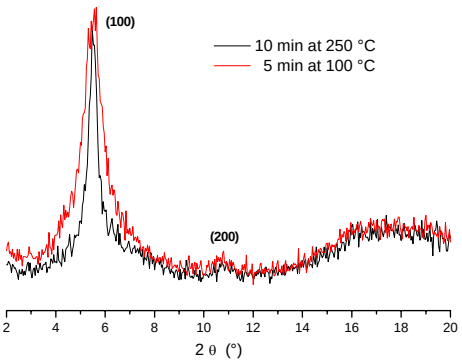

Figure 6-11: *XRD powder diffraction measurements on annealed P3HT samples.*

radiation and 2θ is the angle between the through and scattered X-rays. The obtained d value of 16.3 Å corresponds to the *a*-axis orientation of the P3HT crystals (crystal lattice with orthorhombic unit cel and interchain distance *a* of 16. 3 Å)[46-48]. Longer annealing times and/or at higher temperature increases the crystallinity as can be monitored by the decrease in width of the diffraction peaks.

Regarding the P3HT/PCBM matrix, the same general trends are observed for the 1/2 films: the higher the annealing temperature, the longer the P3HT fibrils (figure 6-8). However, some differences in morphology are visible as compared to the 1/1 films. Firstly, larger P3HT fibrils are already present in the interpenetrating network for films annealed at 100 °C. Furthermore, the average length of the P3HT fibrils is increased upon annealing at 150 °C and the lateral width of the fibrils seems to be tempered upon annealing at 200 °C. This results in a finer P3HT network as can be noticed in the respective bright-field TEM images of figure 6-8. Also for this blend composition, PCBM nanocrystals should be present in the P3HT/PCBM matrix as evidenced by the SAED patterns of figure 6-12. In addition, all patterns contain a clearly resolved Debye-Scherrer ring originating from the P3HT crystals in accordance with the observed P3HT crystallinity in the corresponding TEM images.

Likewise an interpenetrating network of P3HT fibres is noticed in the P3HT/PCBM matrix for the 1/4 films. Furthermore, in such high PCBM content films small PCBM clusters appear in the matrix. In addition, Debye-Scherrer rings for P3HT as well as PCBM show up in the SAED patterns for all films. This means that even for the 1/4-200 °C films not all of the PCBM is phase separated into the dense network of fan-shaped PCBM structures which were noticed by optical microscopy (figure 6-3). Note that the P3HT fibers are barely noticeable in the corresponding TEM image on account of the very bright contrast of the 1/4-200 °C films. This is a consequence of an “automatic-auto-contrast” adjustment. Nonetheless, the P3HT crystallinity is plainly corroborated by the SAED pattern of the 1/4-200 °C films which clearly shows the sharp and intense Debye-Scherrer diffraction ring of P3HT (see figure 6-13) as well as in the corresponding SAED residual profile of figure 6-10 in which a very pronounced peak at 3.8 Å, originating from the P3HT crystals, is observed.

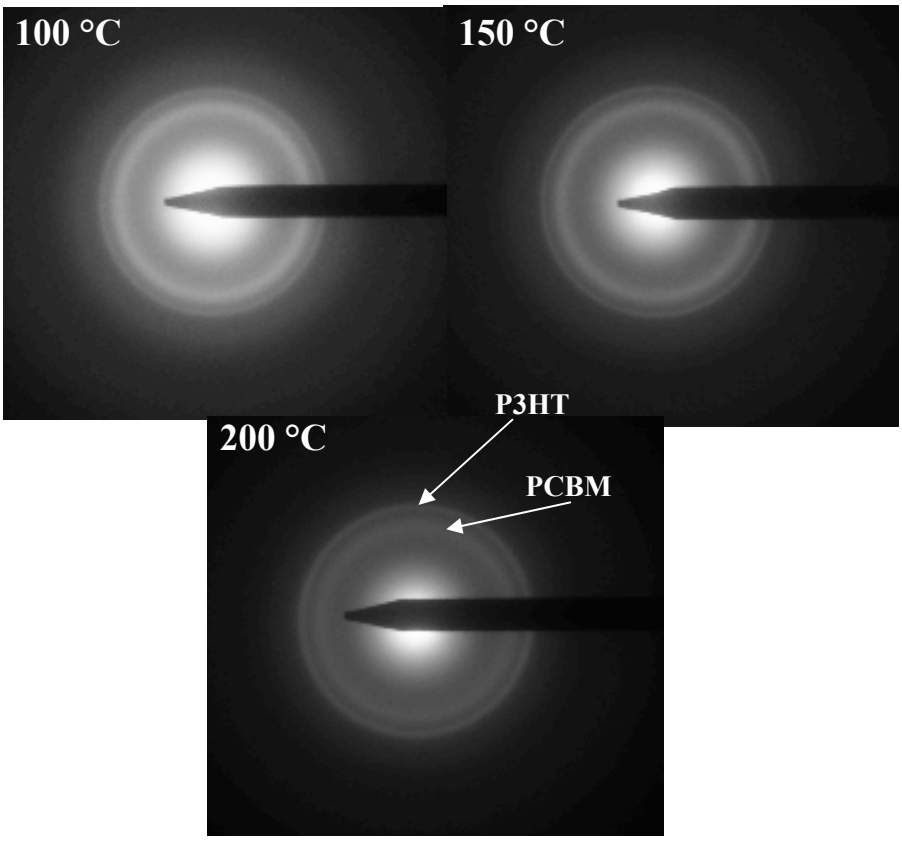

Figure 6-12: *SAED patterns of the P3HT/PCBM matrix of 1/2 films prepared by doctor blading and annealed for 10 minutes at different temperatures.*

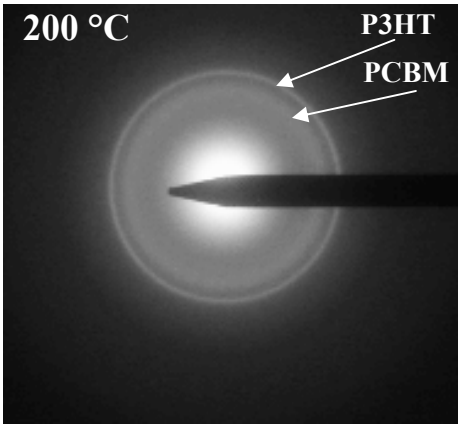

Figure 6-13: *SAED pattern of the P3HT/PCBM matrix of a 1/4 film prepared by doctor blading and annealed for 10 minutes at 200 °C.*

To end this section, the combined information of SAED and TEM allows to conclude that the P3HT/PCBM matrix of all composite films, independently of blend composition and annealing temperature, contains PCBM in a low-order organization. According to Yang *et al*[40], PCBM might be organized into small nanocrystalline domains. Regarding P3HT, pronounced crystallinity is only encountered after annealing at relatively high temperature.

6.2.2.2 Morphology of the PCBM needle-like structures

Bright-field TEM images of the PCBM needle-like structures observed in figures 6-1 to 6-3 are shown in figure 6-14. As demonstrated in the previous section, thermal annealing at 100 °C yields homogeneously looking films without large-scale phase separation for all P3HT/PCBM blend compositions as was also the case for as-processed 1/1 films (figure 6-7-right). Only a network of fine crystalline P3HT fibrils is discernible on a closer look. However, starting from an annealing temperature of 150 °C, phase separation of PCBM takes place.

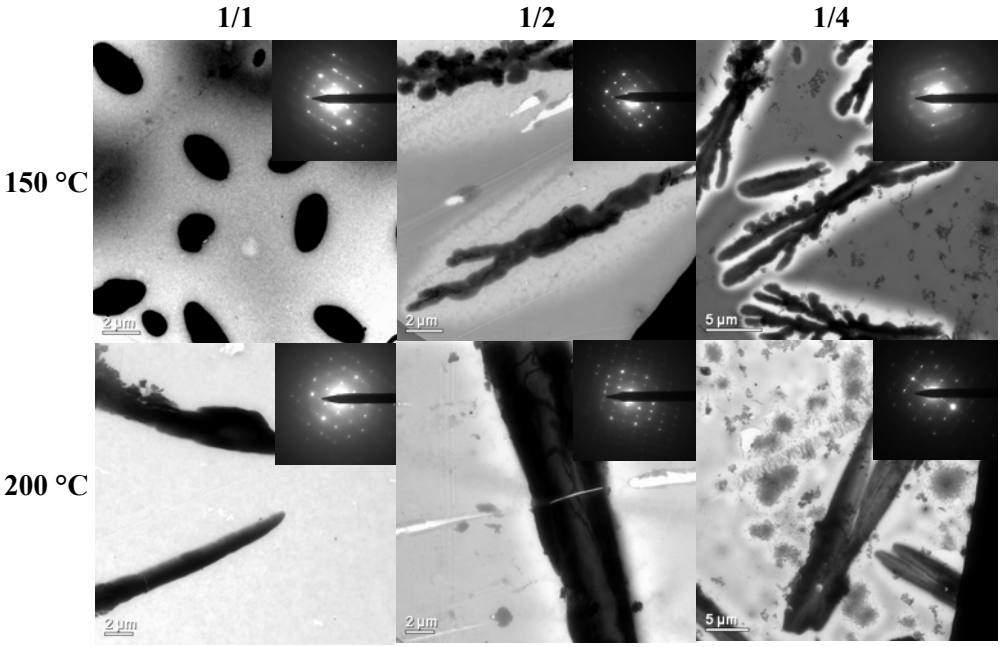

Figure 6-14: *TEM images and corresponding SAED patterns of the needlelike PCBM structures observed in P3HT/PCBM thin films after thermal annealing. For the acquisition of the SAED patterns, the electron beam was focussed on the needles.*

The PCBM needles clearly grow in size with increasing annealing temperature and PCBM content, in agreement with the observations made by optical microscopy (figures 6-1, 6-2 and 6-3). SAED analysis of the PCBM needles, presented in the insets of figure 6-14, results in clear electron-diffraction patterns composed of well-aligned spots which indicates that these needles (partially) consist of PCBM single crystals[40]. However, the regular electron diffraction pattern is superimposed onto a very blurred ring pattern in the SAED's.

6.3 NMR relaxometry study of P3HT/PCBM blends

In this section the nanomorphology of a few selected P3HT/PCBM films doctor bladed from chlorobenzene solutions will be studied by several solid-state NMR techniques. In the following part the selected films will be denoted as 1/1, 1/1-150 °C, 1/1-200 °C, 1/2-175 °C and 1/4-175 °C films. For thermally annealed films the annealing temperature is indicated at the end of the shorthand notation and the annealing time was always 10 minutes. An overview of the optical microscopy images of the considered films is presented in figure 6-15. It was demonstrated by optical microscopy as well as by TEM that certain annealing conditions led to the formation of very large PCBM needles. Due to the grey-value fluctuations noticed in the by TEM and optical microscopy visualized PCBM need-

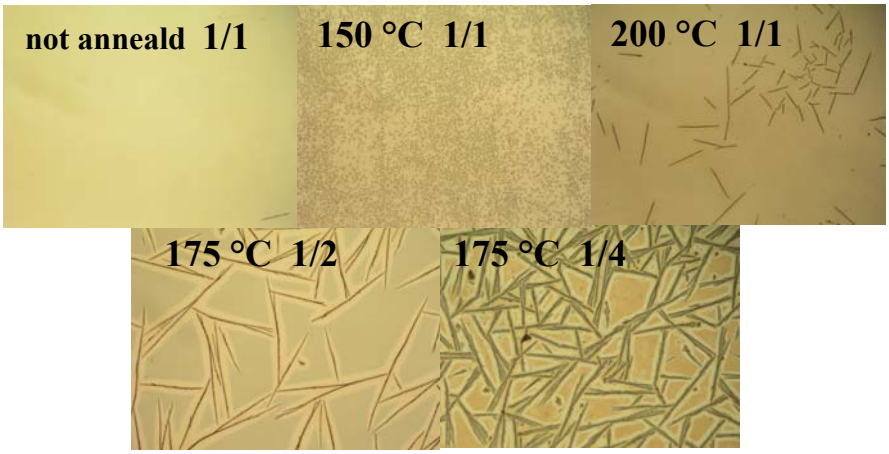

Figure 6-15: *Summary of the optical microscopy images of the blends which were studied by solid-state NMR techniques (image dimensions: 465 x 630 µm).*

les and the blurred background present in the SAED patterns of these needles, an important question remains whether or not these phase separated PCBM needles have a uniform degree of crystalline order. In order to obtain more detailed and complementary information, these films were further analyzed by NMR relaxometry and XRD. In cases where no long T_{1H} and $T_{1\rho H}$ relaxation decay times were detected by means of wide-line NMR, the more local (but also time-consuming) ^{13}C MAS technique was used in an attempt to describe and quantify the complex morphology of these P3HT/PCBM films.

6.3.1 Proton wide-line NMR analysis of P3HT

In this section the proton wide-line NMR relaxation behavior of the donor polymer P3HT, purchased from Rieke Metals Inc., is described as a reference. The regioregularity was specified as > 98.5 %, but our liquid-state proton NMR measurements indicated a slightly lower regioregularity of about 94 % as determined from the signals of the α-methylene protons (see section 6.7.1). Table 6-1 presents the spin-lattice relaxation decay times T_{1H} and the spin-lattice relaxation decay times in the rotating frame $T_{1\rho H}$ of P3HT as measured by proton wide-line NMR. The same T_{1H} and $T_{1\rho H}$ relaxation behavior, within experimental error, is observed for pristine P3HT and P3HT doctor bladed from chlorobenzene.

***Table 6-1**: Relaxation decay times T_{1H} and $T_{1\rho H}$ as determined by proton wide-line NMR for P3HT. The normalized molar proton fractions are presented between brackets.*

decay time	Rieke P3HT	doctor bladed P3HT film
T_{1H} (s)	0.65	0.65
$T_{1\rho H}$ (ms)	2.3 (25%) 8.9 (75%)	2.1 (28%) 8.3 (72%)

Only one short T_{1H} decay time of 0.65 s is measured. On the T_{1H} distance scale the poorly developed P3HT fibers, as evidenced for doctor bladed P3HT films by BF-TEM and SAED, are not detected. Due to efficient spin diffusion the relaxation of all P3HT molecules is driven by the fast molecular motions of the long side chains of the amorphous P3HT in the semicrystalline matrix.

Regarding the $T_{1\rho H}$ relaxation, a short and intermediate decay time is observed for regioregular P3HT. As is the case for MDMO-PPV, at first glance two $T_{1\rho H}$ decay times could be expected as a consequence of incomplete spin diffusion in the long, mobile hexyl side-chain due to weakened dipolar interactions.

However, since regiorandom P3HT only shows a single short $T_{1\rho H}$ decay time (table 6-2), it can be inferred that the intermediate $T_{1\rho H}$ decay time of 8.9 ms represents the P3HT fibers of which, based on the spin diffusion equation, the minimal dimensions can be estimated to be more than 4 nm. This is further confirmed by a study of $T_{1\rho H}$ as a function of the regioregularity performed on P3HT samples which were prepared in our lab (note that for the preceding and following sections only Rieke P3HT was used). A decrease of the regioregularity (rr) from 97 % down to 70 % clearly results in a decreased fraction of the intermediate $T_{1\rho H}$ decay time (table 6-2). Note that for Rieke P3HT, the higher fraction but shorter value of this intermediate $T_{1\rho H}$ time constant is an indication for more but smaller fibres, respectively.

***Table 6-2**: Relaxation decay times $T_{1\rho H}$ as determined by proton wide-line NMR for P3HT as a function of its regioregularity. The normalized molar proton fractions are presented between brackets.*

P3HT	$T_{1\rho H}^{s}$ (ms)	$T_{1\rho H}^{i}$ (ms)
regiorandom	3.2 (100%)	-
rr 70 %	3.0 (53%)	10.5 (47%)
rr 97 %	2.9 (33%)	11.8 (67%)

6.3.2 Proton wide-line NMR analysis of P3HT/PCBM thin films

Table 6-3 presents the T_{1H} and $T_{1\rho H}$ relaxation decay times as measured by proton wide-line NMR for P3HT/PCBM films doctor bladed from solutions in chlorobenzene. Optical microscopy images of the 1/2-175 °C and 1/4-175 °C films clearly show phase separation for PCBM into large needle-like structures (figure 6-15). So one might expect at least two dynamically different molecular environments. This is indeed observed via the T_{1H} relaxation of these films which behaves bi-exponentially with a short and intermediate T_{1H} decay time of 0.68 and 2 s, respectively. However, no long decay times are observed. This is a first indication that the crystalline order is not uniform in these PCBM needle-like structures. If large-scale crystallinity would be present in these films, phase specific long decay times should be observed as the domain sizes would certainly exceed the spin diffusion path length L. This was definitely the case for as-received PCBM (table 3-1) and MDMO-PPV/PCBM films casted from toluene solutions with high PCBM content (table 3-3 and 3-5). This despite the dimensions of the

***Table 6-3**: T_{1H} and $T_{1\rho H}$ relaxation decay times measured by proton wide-line NMR for 130 nm thick P3HT/PCBM films doctor bladed from CB. Also the molar amount of PCBM organized in needles is listed in %. The normalized molar proton fractions are presented between brackets.*

P3HT/PCBM **wt ratio** molar ratio *molar proton ratio*	**1/1** 85/15 85/15	**1/1** 85/15 85/15	**1/1** 85/15 85/15	**1/2** 73/27 73/**27**	**1/4** 58/42 58/**42**
annealing	***none***	***10 min 150°C***	***10 min 200°C***	***10 min 175°C***	***10 min 175°C***
T_{1H} (s)	0.82	0.76	0.78	0.68 (81%) 2.1 (**19%**)	0.69 (70%) 2.0 (**30**%)
mol % of PCBM in needles				**70 %**	**71 %**
$T_{1\rho H}$ (ms)	2.1 (27%) 8.9 (73%)	2.0 (29%) 8.6 (71%)	2.3 (29%) 9.4 (71%)	2.4 (26%) 11.3 (74%)	2.6 (29%) 11.8 (71%)

phase separated PCBM needles in P3HT/PCBM films are undisputed larger as compared to these of the well-defined crystals observed in MDMO-PPV/PCBM films casted from toluene. In order to confirm the absence of a long T_{1H} decay time a last-ditch, time-consuming experiment was accomplished on the 1/4-175 °C films. Hereto a preparation delay of 300 s and an evolution time array up to 1000 s were set in the T_{1H} inversion recovery pulse sequence in order to exclude the possibility of missing extremely long T_{1H} decay times. Notwithstanding these precautions the same NMR results as reported in table 6-3 were obtained.

The short T_{1H} decay time of 0.68 s can be ascribed to the protons of the P3HT/PCBM matrix which relax very efficiently via the fast oscillating magnetic fields generated by the side-chain motions of amorphous P3HT. Remark that also the PCBM nanocrystals which are dispersed in the P3HT/PCBM matrix relax via this efficient relaxation pathway, and so are included in this fraction. This attribution is based on (i) unpublished work of our group in which it was demonstrated that the T_{1H} of P3HT fibres equals this of Rieke P3HT and doctor bladed P3HT[49] and (ii) the fact that almost the same decay time as for pure P3HT (0.65 s) is measured. The intermediate T_{1H} must originate from phase separated PCBM. Based on the intermediate decay time value of 2 s, the average minimal dimension of this ordered PCBM has to be around 70 nm. This is in agreement with the XRD diffractogram of the 1/4-175 °C films as depicted in figure 6-16. A diffraction pattern of large-scale PCBM crystallinity is plainly not observed. Only

some broad signals are superimposed on the amorphous halo. Remark that the broad reflection at 2θ = 5.4° in the XRD pattern of the 1/4-175 °C film originates from the *a*-axis organization in the fibrillar-like P3HT crystals (cf. figure 6-11). By

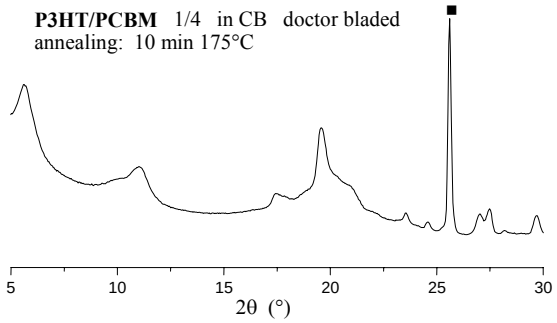

***Figure 6-16**: XRD diffractogram of the 1/4-175 °C films. The signal denoted with an ■ originates from corundum in the sample holder.*

comparing with the XRD patterns presented in figure 4-9, it might be expected that the dimension of PCBM coherence in the 1/4-175 °C films is somewhat larger as for acetone-precipitated PCBM. For this PCBM sample, showing a T_{1H} of 1.2 s, the dimensions of the PCBM crystals were estimated to be situated around the upper limit of the proton wide-line NMR based dimension interval of 6 – 55 nm (section 4.5.3). In conclusion, XRD and NMR provide a second indication that the large needle-like PCBM structures do not fully consist of well-developed PCBM single crystals. Therefore these single crystals (which cause well-aligned spots in the SAED's) have to be in close contact with less organized, mesoscopic low order PCBM regions. As a result, a T_{1H} decay time of only 2 s is observed due to spin diffusion within these PCBM needles. The molar amount of PCBM organized in needle-like structures for the 1/2-175 °C and 1/4-175 °C films is, based on the fraction corresponding to the intermediate T_{1H} decay time, in the order of 70 % (table 6-3). This means that the remaining 30 mol % of PCBM must be situated in the P3HT/PCBM matrix, whether or not partly organized in PCBM nanocrystals.

For the 1/1-150 °C and 1/1-200 °C films, on the other hand, in spite of optical microscopy images that still demonstrate phase separation (figure 6-15), only one single short T_{1H} decay time of about 0.77 s is observed (table 6-3). It can be expected that a reduced dimension of the PCBM single crystals results in a higher molecular mobility of the mesoscopic low order PCBM (T_{1H} decay time

shorter than 2s), so that the phase specific T_{1H} decay time of the PCBM needles becomes close to this of the P3HT/PCBM matrix. On that account it is not possible anymore to extract the two decay times from the experimental relaxation data (due to the similarity of the two decay time values). Most presumably also these films have a nanostructured morphology in which PCBM appears in needle-like structures (partly as single crystals and partly in a mesoscopic low order organization) and in the P3HT/PCBM matrix (partly in an unorganized amorphous state and partly as nanocrystals). The latter is in good agreement with the estimated PCBM aggregate size of 50-60 nm in annealed (at 150 °C for 15 minutes) spin-coated 1/1 P3HT/PCBM films based on XRD experiments reported by Chiu *et al*[50]. However, to describe and quantify the amount of PCBM in single crystals and nanocrystals in the 1/1-150 °C and 1/1-200 °C blends, the more local ^{13}C MAS technique was tried out as will be described in section 6.3.3.

Last but not least, the native 1/1 films show a single short T_{1H} decay time of 0.82 s. The T_{1H} relaxation seems to be very efficient, i.e. due to spin-diffusion the T_{1H} relaxation of all the PCBM is driven by the molecular side-chain motions of P3HT. Optical microscopy (figure 6-15) and TEM images (figure 6-7-right) corroborate this intimate mixing (and so single averaged T_{1H} decay time). Therefore these blends have to be homogeneous on the T_{1H} distance scale (tens to hundreds of nm). If phase separation of PCBM takes place at all, this means that the PCBM domains should be smaller than about 45 nm. Notice that the T_{1H} relaxation decay time of the native 1/1 films is slightly increased as compared to the one of pure P3HT: 0.82 s versus 0.65 s. The intimate contact between P3HT and PCBM in native films disrupts the P3HT chain packing (and π-π stacking) and so creates an increase of the molecular chain dynamics of the polymer. The close interaction between P3HT and PCBM in native films was also observed via 2D NMR by Yang[32]. This reduces the spectral density of Larmor frequency motions and subsequently results in an increase of the T_{1H} value. Proof for this is provided by measuring the T_{1H} decay time of pristine P3HT as a function of temperature (figure 6-17). As the temperature increases, which is related to shorter correlation times of motion τ_C, the T_{1H} increases as well. So the T_{1H} relaxation of P3HT is situated at the left side of the T_{1H} minimum of the correlation diagram (section 2.4). This indicates that in native 1/1 films the molecular motions of the P3HT side-chains are less restricted as a consequence of the close contact with PCBM (which suppresses the crystallization of the P3HT in composite films, as has been shown

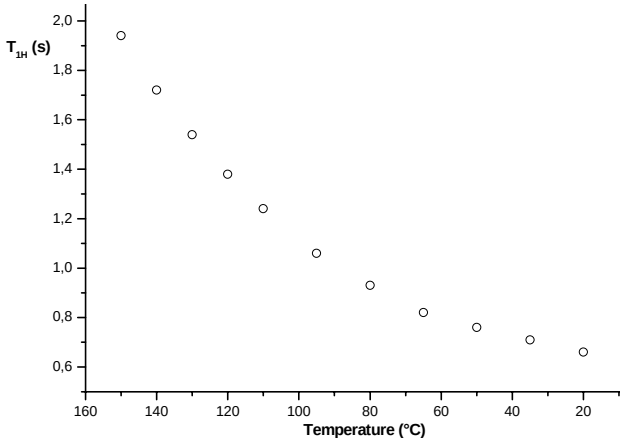

Figure 6-17: *T_{1H} decay time of pristine P3HT measured by proton wide-line NMR as a function of decreasing temperature.*

by XRD[42] and our TEM images of section 6.2.2.1) and accounts for the slight increase of the T_{1H} value. However, thermal annealing causes part of the PCBM to diffuse out of the polymer matrix and allows more pronounced crystallization of the P3HT. This molecular reorganization is coupled with a red shift in the UV/Vis absorption spectra as a consequence of (i) improved π-π stacking in the P3HT fibres and (ii) a more planar arrangement of the polymer backbone which increases the overall effective conjugation length. These effects can already be observed visually by just looking at the thin films since the color changes from yellow into red upon annealing.

Table 6-3 further shows the proton spin-lattice relaxation decay times in the rotating frame $T_{1\rho H}$ as determined by proton wide-line NMR. As for native P3HT and doctor bladed P3HT films, only two decay times are observed. The same main conclusion appears as for T_{1H}, i.e. independently of the blend composition and annealing temperature no long $T_{1\rho H}$ decay times, indicative for well-defined PCBM crystallites, are noticed. The fact that only two decay times are detected for the blends showing phase separation by microscopy indicates that the value of the $T_{1\rho H}$ decay time of the phase separated needle-like PCBM structures and the P3HT fibres in the co-existing matrix become too similar to be differentiated mathematically. This averaged $T_{1\rho H}$ value, however, is significantly increased upto about 11.5 ms for the 1/2-175 °C and 1/4-175 °C films, which is an indirect indication for increased P3HT and PCBM ordering.

At first glance it is somewhat surprising that all films have roughly the same distribution of the $T_{1\rho H}$ fractions (~ 30/70), independently of the blend composition and annealing temperature. On reflection this is expected as both doctor bladed PCBM (table 4-1) and doctor bladed P3HT (table 6-1) have a similar $T_{1\rho H}$ fractional distribution.

6.3.3 ^{13}C solid-state NMR & DSC analysis of P3HT/PCBM thin films

Figure 6-18 depicts typical CP/MAS spectra of PCBM and of 1/4-175 °C and P3HT films doctor bladed from chlorobenzene as well as the numbering scheme for the P3HT carbon atoms. The signal assignment of P3HT, based on solution NMR spectra, has already been described in literature[48]. By comparing the ^{13}C solid-state spectra it can be deduced that the main resonance at 146 ppm (indicated by an ∗ in figure 6-18 and representing the C_{60} carbons) is highly selective for PCBM. The remainder of the discussion will be focused on this fullerene resonance signal.

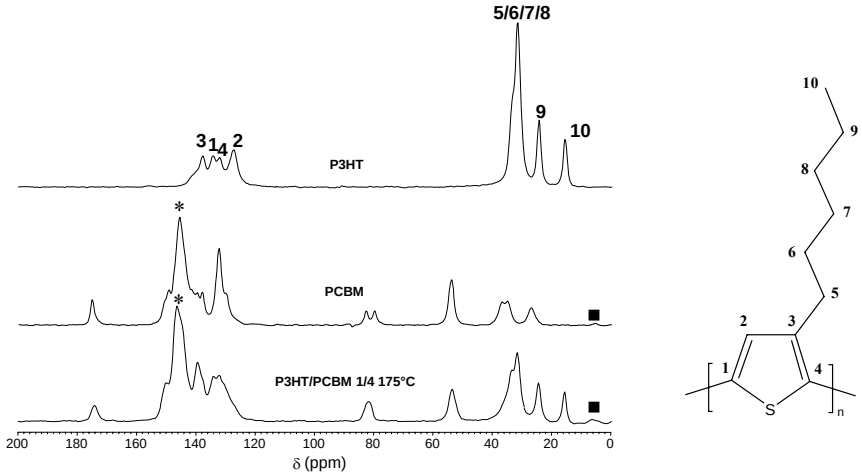

***Figure 6-18**: Solid-state ^{13}C CP/MAS NMR spectra taken with a contact time of 3.5 ms of as-received PCBM (centre) and 130 nm thick P3HT (top) and P3HT/PCBM 1/4 (bottom) films prepared by doctor blading from chlorobenzene solutions. The signals marked with an ∗ arise from the main resonance of PCBM at 146 ppm. The signals marked with an ▪ are spinning side bands. The inset on the right presents the chemical structure and numbering scheme of P3HT.*

Table 6-4 summarizes the T_{1C} (by ^{13}C MAS) and T_{1H} and $T_{1\rho H}$ (by ^{13}C CP/MAS) relaxation decay times. Regarding T_{1C}, independently of the blend composition and annealing temperature, a short and intermediate time constant of around 11-14 and 40-50 s is attained. The intermediate T_{1C} and corresponding molar fraction arise from organized PCBM and can be straightforward attributed to nanocrystals in the P3HT/PCBM matrix as well as single crystals in the needle-like structures. Except of course, for the native 1/1 composite films for which they only

***Table 6-4**: Relaxation decay times for the main signal at 146 ppm of P3HT/PCBM films doctor bladed from chlorobenzene solutions. T_{1C} is measured by carbon-13 MAS and T_{1H} and $T_{1\rho H}$ by ^{13}C CP/MAS. Also the mol % of PCBM in crystals, as determined by the T_{1C} measurement, is listed. The normalized molar fractions are presented between brackets.*

P3HT/PCBM					
wt ratio molar ratio	**1/1** 85/15	**1/1** 85/15	**1/1** 85/15	**1/2** 73/27	**1/4** 58/42
annealing	***none***	***10 min 150°C***	***10 min 200°C***	***10 min 175°C***	***10 min 175°C***
T_{1C} (s)	13.4 (65%) 50.1 (35%)	12.2 (53%) 43.2 (47%)	13.8 (56%) 45.9 (44%)	11.0 (41%) 39.5 (59%)	12.1 (36%) 42.8 (64%)
mol % of PCBM in crystals	**35 % ****	**47 % ***	**44 % ***	**59 % ***	**64 % ***
T_{1H} (s)	0.90	0.96	0.99	1.5	1.9
$T_{1\rho H}$ (ms)	12.1	19.1	17.2	22.9	24.5

*** nanocrystals in the P3HT/PCBM matrix*

** nanocrystals in the P3HT/PCBM matrix as well as single crystals in the needle-like structures*

represent nanocrystals as no PCBM needles are observed for this blend. The remaining PCBM is highly unorganized and/or situated in mesoscopic low-order domains. Very recently, Kalita *et al*[51] demonstrated via high resolution TEM the existence of PCBM nanocrystals in spin-coated P3HT/PCBM films with blend compositions of 1/0.5, 1/1 and 1/2 after annealing for 15 minutes at 150 °C. Although the SAED patterns are significantly different for the PCBM nanocrystals in MDMO-PPV/PCBM films (Debye-Scherrer rings) as compared to the needle-like PCBM structures in P3HT/PCBM films (well-aligned spots), the local dynamics, as probed by the T_{1C} relaxation behavior, are apparently rather similar. Notice further that the amount of crystals (given in mol % in table 6-4) increases upon annealing temperature and/or total PCBM content in the photoactive film. For

the 1/4-175 °C composite films almost a doubled quantity is measured as compared to the native 1/1 films.

Differential scanning calorimetry confirms the semi-crystalline nature of the P3HT/PCBM films. Figure 6-19 shows, as an example, the thermogram of the 1/4-175 °C films. Notice the double melting endotherm originating from PCBM at about 261 and 284 °C with a total area of only 9.6 J/g. This rather low melting enthalpy further supports the hypothesis that the needle-like PCBM structures which are observed by optical microscopy and TEM consist of mesoscopic low order PCBM in addition to single crystals. Remember that as-received "Solenne" PCBM, for which large, well-organized PCBM crystallites were observed, has a melting enthalpy of 32.9 J/g (figure 4-8). The melting peak at 210 °C originates from the fibrillar-like P3HT crystals[52].

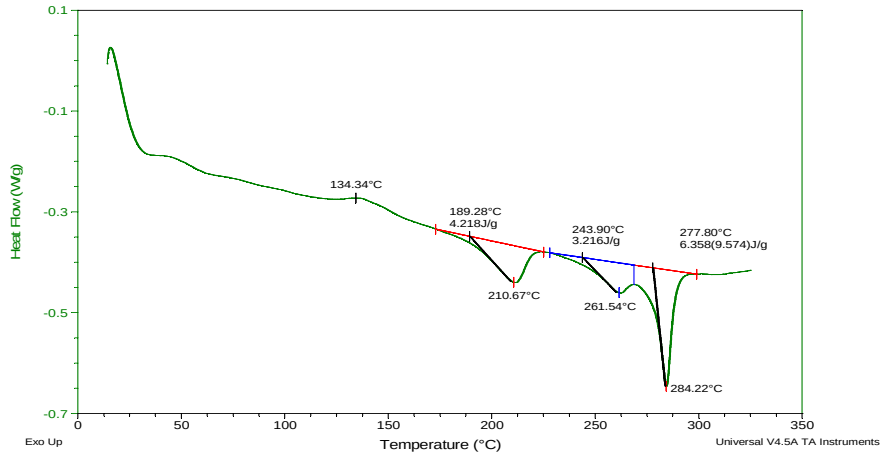

Figure 6-19: *DSC thermogram (first run) showing HF for P3HT/PCBM 1/4-175 °C films.*

Regarding the T_{1H} relaxation, for all blend compositions and annealing conditions one single T_{1H} is observed by CP/MAS as a consequence of efficient spin diffusion. The T_{1H} value increases as a function of the amount of organized PCBM (PCBM crystals) that induces an increased rigidity (see table 6-4).

Concerning the $T_{1\rho H}$ relaxation, all samples show only one single decay time. For the native 1/1 blend a value of 12.1 ms is detected. Annealing of this blend for 10 minutes at 150 °C results in a significant increase of the $T_{1\rho H}$ decay time upto 19.1 ms. This is in accordance with the T_{1H} relaxation behavior observed for these two blends on account of the enhanced phase separation between P3HT

(fibre formation) and PCBM upon annealing. In case of more extreme annealing temperature and higher PCBM content, the same general trend is observed as for T_{1H}, i.e. an increased value of $T_{1\rho H}$ which is reflecting the higher degree of P3HT and PCBM crystallinity.

6.4 Influence of the casting solvent on the P3HT/PCBM film morphology

6.4.1 P3HT/PCBM 1/1 films doctor bladed from toluene

In most published studies performed on P3HT/PCBM BHJ plastic solar cells chlorobenzene or dichlorobenzene are the solvents applied for the film processing. This historically choice of solvent probably arises from the fact that in the first D/A systems studied (e.g. MDMO-PPV as the donor polymer) the best power conversion efficiencies η_e were obtained for these solvents. However as was discussed in section 1.2.6.1, the η_e is highly dependent on this experimental parameter. Therefore we investigated whether or not the nanomorphology of P3HT/PCBM 1/1 films is influenced upon changing the processing solvent from chlorobenzene to toluene.

6.4.1.1 Optical microscopy, TEM and SAED

Figure 6.20 shows some explorative images taken by optical microscopy of 130 nm thick P3HT/PCBM 1/1 films doctor bladed from toluene and annealed at temperatures between 150 and 225 °C for 10 minutes. Each image is taken from a new doctor bladed film. As was the case for chlorobenzene casted films, only starting from an annealing temperature of 150 °C PCBM needles are observed. Although these needles also grow in size with increasing annealing temperature, their dimensions are significantly smaller as compared to annealed films casted from chlorobenzene, especially for the high annealing temperatures (> 175 °C, compare with figure 6-1). From this “first screening” at low magnification it is already clear that the use of toluene as casting solvent results in different morphologies for P3HT/PCBM 1/1 films.

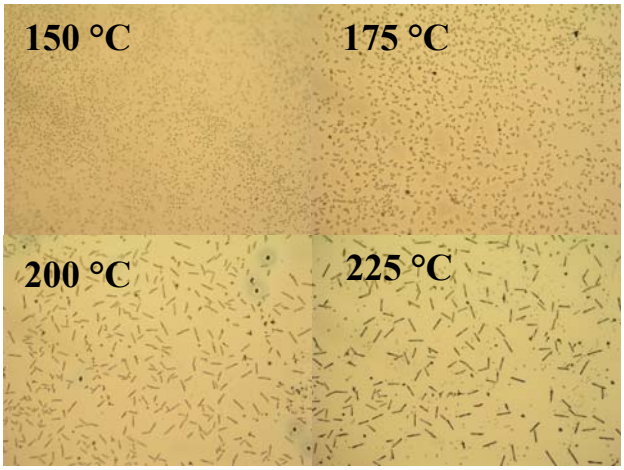

Figure 6-20: *Optical microscopy images of 130 nm thick P3HT/PCBM 1/1 films doctor bladed from toluene solutions and annealed for 10 minutes at different annealing temperatures (image dimensions: 465 x 630 µm).*

Bright-field TEM images and corresponding SAED patterns of the annealed P3HT/PCBM 1/1 films casted from toluene are very similar to the ones obtained for their counterparts casted from chlorobenzene (data not shown). Only in the native film some difference were noticed: in the SAED pattern presented in figure 6-21-right already a more resolved P3HT Debye-Scherrer ring, in addition to the broader PCBM ring, is visible (compare with figure 6-7-right). As this diffraction ring is hardly discernible, the residual SAED profile from which the calculated inelastic scattering background was subtracted is presented in figure 6-

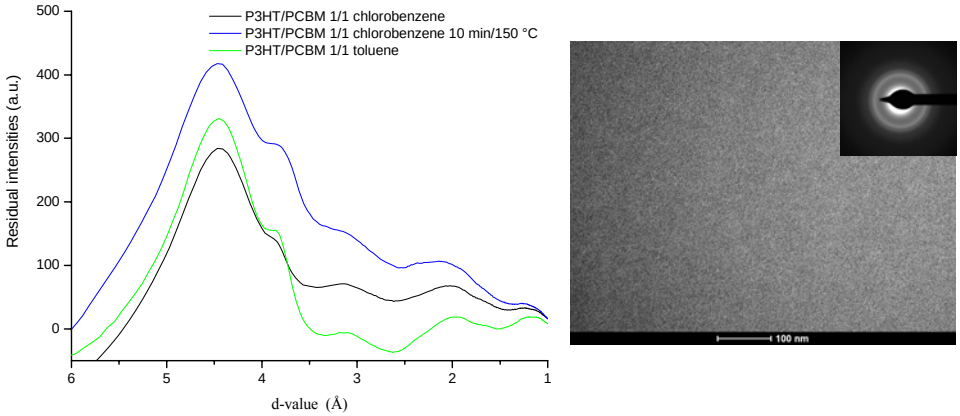

Figure 6-21: *Graph of residual SAED intensity versus d-spacing for some P3HT/PCBM 1/1 films (left) and TEM image and SAED pattern of a P3HT/PCBM 1/1 film doctor bladed from toluene (right).*

21-left. It is clear that the native toluene-casted film already shows a more pronounced diffraction peak at 3.8 Å originating from π-π stacked P3HT fibres. Chlorobenzene-casted films only show this diffraction peak after annealing for 10 minutes at 150 °C.

6.4.1.2 Solid-state ^{13}C (CP)/MAS and proton wide-line NMR relaxometry

Table 6-5 presents the T_{1H} and $T_{1\rho H}$ as well as the T_{1C} relaxation decay times measured via the main PCBM resonance at 146 ppm by ^{13}C CP/MAS and ^{13}C MAS NMR, respectively, for 130 nm thick doctor bladed P3HT/PCBM 1/1 films casted from (i) chlorobenzene, (ii) chlorobenzene and annealed for 10 minutes at 150 °C and (iii) toluene. In the following part these selected films will be denoted as 1/1-CB, 1/1-CB-150 °C and 1/1-Tol, respectively. As listed in table 6-5, points of similarity between the 1/1-CB-150 °C and 1/1-Tol films are noticed. These two blends show the same T_{1H} and $T_{1\rho H}$ relaxation behavior. A value of 0.96 s and 19.1 ms is detected for the T_{1H} and $T_{1\rho H}$ decay times, respectively. These values are significantly different from the values of 0.90 s and 12.1 ms observed for the 1/1-CB blend. Furthermore, roughly the same intermediate T_{1C} decay time and fraction is found for the 1/1-CB-150 °C and 1/1-Tol films. As demonstrated in section 6.3.3, the fraction of this intermediate T_{1C} decay time represents the total amount of PCBM crystals. Remark however that the native 1/1-Tol films only contain PCBM nanocrystals (as no PCBM needle-like structures are observed by microscopy) while the 1/1-CB-150 °C films contain PCBM nanocrystals as well as single crystals. Nevertheless these identical relaxation decay times, the TEM and optical microscopy images are clearly different.

***Table 6-5**: : Relaxation decay times determined via the main PCBM signal at 146 ppm for 130 nm thick P3HT/PCBM 1/1 films doctor bladed from chlorobenzene and toluene. T_{1C} is measured by carbon-13 MAS and T_{1H} and $T_{1\rho H}$ by ^{13}C CP/MAS.*

P3HT/PCBM wt ratio	**1/1**	**1/1**	**1/1**
solvent	**chlorobenzene**	**chlorobenzene**	**toluene**
annealing	***none***	***10 min 150°C***	***none***
T_{1C} (s)	13.4 (65%) 50.1 (35%)	12.2 (53%) 43.2 (47%)	10.6 (49%) 41.0 (51%)
T_{1H} (s)	0.90	0.96	0.95
$T_{1\rho H}$ (ms)	12.1	19.1	19.1

Table 6-6 presents the T_{1H} and $T_{1\rho H}$ relaxation decay times as measured by proton wide-line NMR for the 1/1-CB, 1/1-CB-150 °C and 1/1-Tol films. Also by this technique the same T_{1H} is obtained for 1/1-Tol and 1/1-CB-150 °C films. This indicates that the P3HT chain packing is already less hindered by PCBM. Or in other words, that the P3HT is already more allowed to phase separate into crystalline fibres. This conclusion is corroborated by the color of the as-processed toluene films, being red as was the case for chlorobenzene films only after annealing. This is also in agreement with the higher fraction of the intermediate T_{1C} decay time being the consequence of a higher amount of PCBM nanocrystals. Concerning the $T_{1\rho H}$ relaxation no large differences are noticed by means of proton wide-line NMR, only a slight increase of the intermediate decay time upto 9.5 ms is measured.

***Table 6-6**: T_{1H} and $T_{1\rho H}$ relaxation decay times measured by proton wide-line NMR of P3HT/PCBM 1/1 films doctor bladed from chlorobenzene and toluene. The normalized molar proton fractions are presented between brackets.*

P3HT/PCBM wt ratio	**1/1**	**1/1**	**1/1**
solvent	**chlorobenzene**	**chlorobenzene**	**toluene**
annealing	***none***	***10 min 150°C***	***none***
T_{1H} (s)	0.82	0.76	0.77
$T_{1\rho H}$ (ms)	2.1 (27%) 8.9 (73%)	2.0 (29%) 8.6 (71%)	2.1 (25%) 9.5 (75%)

As a conclusion it can be stated that NMR relaxometry indicates that native P3HT/PCBM 1/1 films casted from toluene already show increased P3HT as well as PCBM nanocrystallinity, which only is achieved in chlorobenzene casted films after e.g. a post-production thermal annealing step. So, it looks feasible to obtain a more optimized nanomorphology in these films without additional cost-raising actions. Such actions (see section 6-1) are indispensable to improve the efficiency of the solar cells by a factor of almost two in case of processing from chlorobenzene. Up to now, most studies regarding this D/A system almost exclusively focused on chlorobenzene and ortho-dichlorobenzene as the casting solvent.

In order to confront these NMR results with solar cell performance, photovoltaic devices of which the 1/1 active layer was prepared from chlorobenzene and toluene were fabricated and compared. To correlate the NMR

findings with the PCE's, P3HT/PCBM BHJ active layers were composed with a thickness of 130 nm. Ambient-air-processed active layers were fabricated. It was opted for mild annealing conditions, i.e. 10 minutes at 110 °C, to prevent the formation of large PCBM needles in the films. Furthermore, it should be noted that the devices fabricated were not optimized for maximum performance; rather, they were produced using the same procedure with the aim of maximizing the comparability between different series. Figure 6-22 shows the current density-voltage curves of P3HT/PCBM 1/1 solar cells, of which the photoactive layers were doctor bladed from chlorobenzene and toluene. Plots are presented for native and annealed (10 minutes at 110 °C) cells and are obtained under simulated AM1.5 illumination. The corresponding device characteristics are summarized in table 6-7. The native chlorobenzene-casted cells have very low efficiencies of about 0.25 %, due to a low J_{SC} of 0.99 mA/cm^{-2}. After annealing, a significantly higher efficiency of 1.58 % is obtained, primarily because of a considerable increase of the J_{SC} as a result of the presence of a more continuous, interpenetrating network of the hole-conducting phase (P3HT fibres) and the electron-conducting phase (PCBM nanocrystals) which is required for optimal extraction of holes and electrons from the device. In keeping with the NMR results, J_{SC} as well as *FF* increase considerably for cells of which the active layer is processed from toluene instead of chlorobenzene. A 5-fold increase of the η_e is obtained. Nevertheless, for these 'first

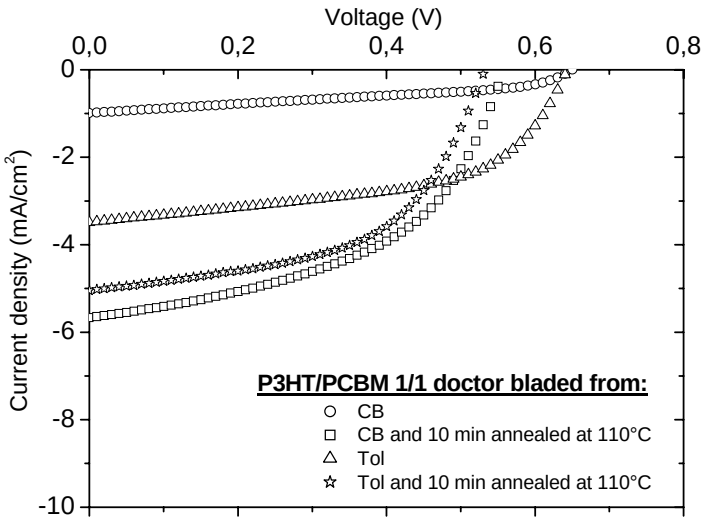

Figure 6-22: *Plot of current density versus voltage for solar cells under illumination.*

***Table 6-7**: Device characteristics J_{sc}, V_{oc}, FF and η_e for solar cells under illumination.*

P3HT/PCBM 1/1 active layer doctor bladed from:	J_{sc} (mA cm^{-2})	V_{oc} (V)	FF (%)	efficiency η_e (%)
CB	0.99	0.65	39	0.25
CB and 10 min annealed at 110 °C	5.67	0.56	50	1.58
Tol	3.49	0.64	55	1.22
Tol and 10 min annealed at 110 °C	4.76	0.53	56	1.40

trial' processing conditions thermal annealing still leads to a further improvement of the performance from 1.22 to 1.40 %. Therefore, as a future perspective, it might be worthwhile to evaluate the performance of organic solar cells in which the P3HT/PCBM active layer is optimized for processing from toluene.

6.4.2 P3HT/PCBM 1/4 films doctor bladed from toluene

Also the influence of the PCBM content was investigated for toluene-casted films. As was shown in chapter 3 for toluene-casted MDMO-PPV/PCBM films, starting from 70 wt% PCBM a fraction of the PCBM is phase separated into well-defined crystallites. Table 6-8 presents the T_{1H} and $T_{1\rho H}$ relaxation decay times as measured by proton wide-line NMR for P3HT/PCBM 1/4 films doctor bladed from toluene (referred to as 1/4-Tol). For comparison the results obtained for the 1/4-CB-175 °C films is repeated.

Plainly, the T_{1H} and $T_{1\rho H}$ relaxation behavior of toluene-based P3HT/PCBM films is completely different to this of MDMO-PPV/PCBM films prepared from toluene for which a long decay time is observed for PCBM contents ≥ about 70 wt%. This indicates that no well-defined PCBM crystallites are present in the 1/4-Tol films. However, the T_{1H} relaxation still behaves bi-exponentially with an intermediate T_{1H} decay time of 2.6 s. For the 1/4-CB-175 °C films an intermediate T_{1H} of 2 s was measured as well and it was attributed to PCBM needles (single crystals and mesoscopic low-order PCBM). For the 1/4-Tol films it should be pointed out however that the film morphology is not fully homogeneous as PCBM aggregates are observed in the TEM images (figure 6-23-left) most likely as a consequence of the low solubility of PCBM in toluene. In the "P3HT/PCBM matrix" (between the aggregates) small P3HT fibres are observed (figure 6-23-right). Based on the fraction corresponding to the intermediate T_{1H} it can be calculated that about 33 mol % of the PCBM is phase separated in the 1/4-Tol film.

***Table 6-8**: T_{1H} and $T_{1\rho H}$ relaxation decay times measured by proton wide-line NMR of P3HT/PCBM 1/4 films doctor bladed from chlorobenzene and toluene. The normalized molar proton fractions are presented between brackets. The mol % of phase separated PCBM is listed as well.*

P3HT/PCBM wt ratio *molar proton ratio*	**1/4 58/42**	**1/4 58/42**
solvent	**toluene**	**chlorobenzene**
annealing	***none***	***10 min 175°C***
T_{1H} (s)	0.77 (86%) 2.6 **(14%)**	0.69 (70%) 2.0 **(30%)**
mol % of phase separated PCBM	**33 %**	**71 %**
$T_{1\rho H}$ (ms)	2.5 (29%) 12.3 (71%)	2.6 (29%) 11.8 (71%)

We conjecture that this rather low amount, as compared to the 71 % for the 1/4-CB-175 °C film, represents the highly mesoscopic low-order PCBM aggregates which are visible in figure 6-23-left. This information indicates that not only the toluene (casting solvent) but also the nature of the polymer (e.g. P3HT versus MDMO-PPV) highly determines whether or not well-defined PCBM crystallites are formed in polymer/PCBM composite films. Note that for the native 1/4-Tol films a similar value for the intermediate $T_{1\rho H}$ decay time (~ 12 ms) is observed as for the 1/4-CB-175 °C films, indicating already a higher crystalline order in the matrix of the toluene-casted films.

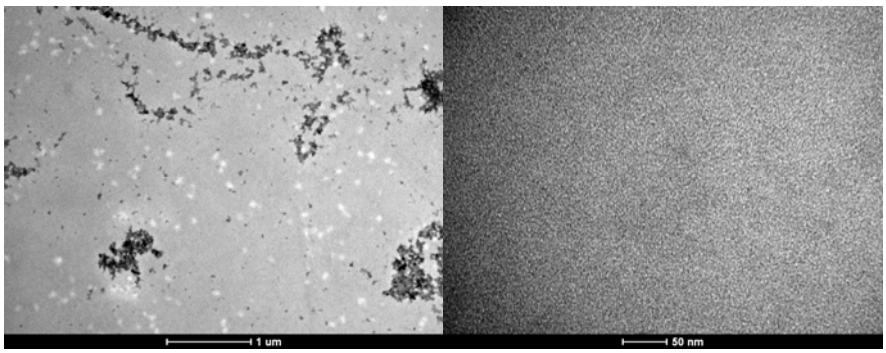

***Figure 6-23:** TEM images of a 130 nm thick P3HT/PCBM 1/4 film doctor bladed from toluene. Scale bar of 1 µm (left) and 50 nm (right).*

6.5 *Purity of PCBM versus performance of P3HT/PCBM solar cells*

As a last experiment the influence of the purity of PCBM on the performance of solar cells will be discussed. The presence of *ortho*-dichlorobenzene as a co-solvent for example might have an influence on e.g. the PCBM solubility and accordingly also on the film morphology and power conversion efficiency η_e [6,7]. To obtain insight on the influence of impurities, solar cells prepared from as-received "Solenne" PCBM were compared to cells prepared from acetone-washed PCBM. Figure 6-24 shows the current density-voltage curves for P3HT/PCBM solar cells casted from chlorobenzene, before and after annealing for 10 minutes at 110 °C. The corresponding device characteristics are summarized in table 6-9. Remarkably, the J_{SC} as well as so *FF* increases considerably if as-received PCBM is replaced by purified PCBM. After annealing, while the V_{OC} is basically unaffected, the highest J_{SC} (6.44 mA/cm^2) is obtained for the solar cells that contain purified PCBM. The higher *FF* for the latter cells can be observed from the more oblong experimental J-V curve (cf. section 1.2.1).

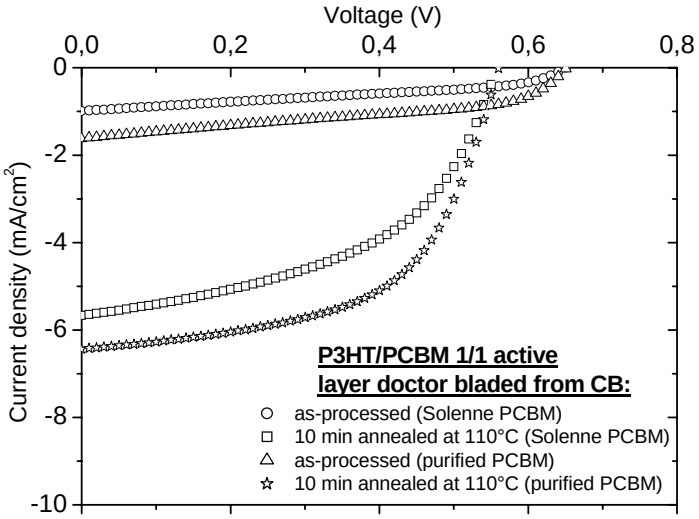

Figure 6-24: *Plot of current density versus voltage for solar cells prepared with as-received and purified PCBM.*

***Table 6-9**: Device characteristics J_{sc}, V_{oc}, FF and η_e for solar cells prepared with as-received and purified PCBM.*

P3HT/PCBM 1/1 active layer doctor bladed from CB:	J_{sc} (mA cm^{-2})	V_{oc} (V)	FF (%)	efficiency η_e (%)
as-processed (Solenne PCBM)	0.99	0.65	39	0.25
10 min annealed at 110 °C (Solenne PCBM)	5.67	0.56	50	1.58
as-processed (purified PCBM)	1.62	0.65	45	0.48
10 min annealed at 110 °C (purified PCBM)	6.44	0.56	57	2.03

6.6 Conclusions

In this chapter the influence of the blend composition as well as the annealing temperature on the nanostructured morphology of thin doctor bladed P3HT/PCBM chlorobenzene-casted films was first studied in detail by microscopy. A first screening by optical microscopy showed that, independently of the blend composition, the films look homogeneous on the μm scale in case of annealing for 10 minutes upto 125 °C. However, annealing at temperatures ≥ 150 °C results in the formation of large (micrometer long) needle-like PCBM structures. Annealing above the melting point of P3HT in the blend results in larger needles for 1/1 and 1/2 blends and fan-shaped PCBM structures for 1/4 films. It was further demonstrated that the blend morphology is fixed once the P3HT fibres and PCBM needles are formed. The combined information of SAED and TEM allows to conclude that the "P3HT/PCBM matrix" of all studied films contains PCBM densely stacked in small nanocrystals. Native P3HT/PCBM films only show rather small P3HT fibres. Pronounced P3HT crystallinity is only encountered in the P3HT/PCBM matrix at relatively high annealing temperatures. The SAED analysis of the PCBM needles results in clear electron-diffraction patterns composed of well-aligned spots which means that these needles (partially) consist of PCBM single crystals. However, this regular electron diffraction pattern is superimposed onto a blurred ring pattern arising from PCBM in a mesoscopic low-order organization.

Next, the nanomorphology of some selected P3HT/PCBM films was further scrutinized by means of solid-state NMR relaxometry. In general proton wide-line NMR is not sensitive enough to describe this complex morphology in detail. Only for films with high PCBM content and annealed at high temperatures

the T_{1H} relaxation behavior is bi-exponentially and the molar fraction of the detected intermediate T_{1H} decay time provides an estimation of the amount of PCBM that is phase separated into the large needle-like structures. However, on no account long T_{1H} decay times are observed indicating that the crystalline order is not uniform in these PCBM needle-like structures. This statement is supported by the XRD pattern, showing only broad peaks.

Regarding the T_{1C} relaxation as investigated via ^{13}C MAS, a short and intermediate decay time constant is attained for all films. The molar fraction of the intermediate T_{1C} represents the more densely ordered PCBM crystals. For the native 1/1 blends it stands for the PCBM nanocrystals that are embedded in the film matrix. In case of blends which show large phase separated PCBM needles by microscopy, the PCBM crystals quantified via the intermediate T_{1C} decay time represent nanocrystals in the P3HT/PCBM matrix as well as single crystals present in the needle-like structures. The needle-like structures on the other hand do not exclusively consist of single crystals, but of single crystals that are surrounded by mesoscopic low order PCBM. This finding is supported by DSC since only a rather low melting enthalpy is obtained for the 1/4-CB-175 °C film. In conclusion it is possible to quantify the amount of PCBM that is phase separated in a densely ordered state for this complex D/A system (PCBM single crystals and nanocrystals). The CP-MAS results (T_{1H} and $T_{1\rho H}$) further corroborate the above described nanostructured morphology in P3HT/PCBM films.

The influence of the casting solvent on the morphology of P3HT/PCBM films was studied as well. It was shown that thin P3HT/PCBM 1/4 films doctor bladed from toluene lack long relaxation decay times. This indicates that not only the casting solvent but also the nature of the polymer highly determines whether or not well-defined PCBM crystallites are formed in polymer/PCBM composite films. Concerning P3HT/PCBM 1/1 films, it can be stated that NMR relaxometry indicates that native films casted from toluene already show increased P3HT as well as PCBM crystallinity, which only is achieved in chlorobenzene-casted films after a post-production thermal annealing step. Notwithstanding roughly the same relaxation behavior is observed for the native toluene-casted and the annealed chlorobenzene-casted films, microscopy clearly shows different nanomorphologies. Native toluene-casted films show a finer morphology, without long PCBM needles. However, the amount of densely ordered PCBM (only nanocrystals for the toluene-casted films) is comparable, explaining the relatively good performances of these

films in solar cells.

Last but not least, in chapter 4 it was demonstrated that commercial PCBM can contain significant amounts of impurities. The influence of the purity of PCBM on the solar cell performances was therefore studied. While the V_{OC} remains basically unaffected, the use of purified PCBM leads to a significant improvement of the J_{SC} of the solar cells.

6.7 Experimental part

6.7.1 Materials

Regioregular P3HT (poly(3-hexylthiophene-2,5-diyl)) (M_w=56000, M_n=25100, PD=2.2, as determined by GPC (gel permeation chromatography) in THF using polystyrene standards; M_w of a repetition unit is 166 g/mol) was purchased from Rieke Metals Inc. These properties of P3HT are well matched to the proposed M_w range of 30000-70000 and polydispersity of around 2 by Ma *et al*[53], to ensure an ideal film morphology upon annealing, i.e. a mix of crystalline regions formed by low-M_w P3HT embedded in a high-M_w amorphous P3HT matrix. For the characterization and solid-state properties of P3HT is referred to the literature[48,54]. The regioregularity of the polymer, quantified by the number of head-to-tail linkages, was checked by ^{1}H and ^{13}C liquid-state NMR (figure 6-25). In the ^{1}H spectrum the resonances at 2.79 and 2.58 ppm represent the α-methylene

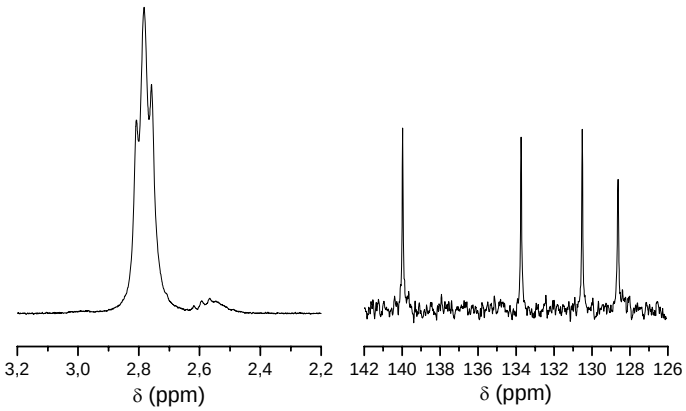

***Figure 6-25**: Part of the ^{1}H (left) and ^{13}C (right) liquid-state NMR spectrum of P3HT.*

protons of the hexyl side-chain in a head-to-tail and head-to-head configuration, respectively. From the integrated proton signal intensities a regioregularity of 94 % can be calculated. In the ^{13}C spectrum only four sharp bands for the thiophene carbons at 139.9, 133.7, 130.5 and 128.7 ppm, which also denotes the head-to-tail structure, are observed.

6.7.2 Film preparation

Mixtures with different weight ratios where dissolved in chlorobenzene and stirred overnight at 50 °C. The weight ratios of the P3HT/PCBM blends studied are 1/1, 1/2 and 1/4. This results in a molar and molar proton ratio of respectively 85/15, 73/27 and 58/42 % (both PCBM and a repetition unit of P3HT contain 14 protons). In order to investigate the influence of the casting solvent, additional 1/1 and 1/4 films casted from toluene were prepared under the same conditions as well. For the preparation of the 1/1 films a P3HT concentration of 1.5 wt% was used while for the 1/2 and 1/4 films the concentration was 1 and 0.6 wt%, respectively.

See section 3.2 for details on the film preparation by doctor blading. A film thickness of about 130 nm, as determined with a Dektak3ST surface profile measuring system of Veeco Instruments Inc, was obtained. Annealing of the thin films was performed under precisely controlled temperature and atmosphere conditions, using a Präzitherm-high temperature hot plate (600°C). The stability of the temperature was controlled within 0.1 °C. The annealing experiments were conducted by putting the film coated glass plate on the hot plate which was stabilized at the desired annealing temperature.

6.7.3 Plastic solar cells

Based on the BHJ configuration, plastic solar cells were fabricated from a blend of P3HT as donor and PCBM as acceptor component, respectively. Hereto a solution of the polymer and PCBM in a 1/1 ratio by weight was prepared in chlorobenzene (or toluene) with a total concentration of 30 mg/mL. The devices were prepared starting from indium tin oxide (ITO, 100 nm) coated glass substrates which were successively cleaned in a soap solution, demineralized water and acetone, each for 10 minutes in an ultrasonic bath. This was followed by cleaning

in boiling isopropyl alcohol for 10 minutes. A 25 nm thick PEDOT/PSS (Bayer) layer was spin-coated on top of the clean glass/ITO substrates. Next the substrates were dried for 20 minutes on a hot plate at 120 °C. Then 130 nm thick photoactive layers were doctor bladed under ambient-air conditions on the PEDOT/PPS. A 20 nm Ca / 80 nm thick Al electrode was deposited on the active film by thermal evaporation at ~ 1 x 10^{-6} mbar. Device annealing was carried out inside a glove box at 110 °C for 10 minutes. Current density-voltage (J-V) characteristics of the OPV devices were measured under inert nitrogen atmosphere using a Newport class A solar simulator (model 91195A) calibrated with a silicon solar cell to give an AM1.5 spectrum and with an input of 100 mW/cm^2 light illumination.

6.8 References

1. Roman, L.S.; Andersson, M.R.; Yohannes, T.; Inganäs, O., *Adv. Mater.* **1997**, 9, 1110.
2. Bao, Z.; Dodabalapur, A.; Lovinger, A., *Appl. Phys. Lett.* **1996**, 69, 4108.
3. Sirringhaus, H.; Tessler, N.; Friend, R.H., *Science* **1998**, 280, 1741.
4. Sirringhaus, H.; Brown, P.J.; Friend, R.H.; Nielsen, M.M.; Bechgaard, K.; Langeveld-Voss, B.M.W.; Spiering, A.J.H.; Janssen, R.A.J.; Meijer, E.W.; Herwig, P.; de Leeuw, D.M., *Nature* **1999**, 401, 685.
5. Blom, P.W.M.; de Jong, M.J.M.; van Munster, M.G., *Phys. Rev. B* **1997**, 55, R656.
6. Prosa, T.J.; Winokur, M.J.; Moulton, J.; Smith, P.; Heeger, A.J., *Macromolecules* **1992**, 25, 4364.
7. Chen, H-Y.; Hou, J.; Zhang, S.; Liang, Y.; Yang, G.; Yang. Y.; Yu, L.; Wu, Y.; Li, G., *Nature Photonics* **2009**, 3, 649.
8. Chirvase, D.; Parisi, J.; Hummelen, J.C.; Dyakonov, V., *Nanotechnology* **2004**, 15, 1317.
9. Savenije, T.J. ; Kroeze, J.E.; Yang, X.N.; Loos, J., *Adv. Funct. Mater.* **2005**, 15, 1260.
10. Camaioni, N.; Ridolfi, G.; Casalbore-Miceli, G.; Possamai, G.; Maggini, M., *Adv. Mater.* **2002**, 14, 1735.
11. Padinger, F.; Rittberger, R.S.; Sariciftci, N.S., *Adv. Funct. Mater.* **2003**, 13, 85.
12. Kim, K.; Liu, J.; Namboothiry, M.A.G.; Carroll, D.L., *Appl. Phys. Lett.* **2007**, 90, 163511.
13. Pivrikas, A.; Juska, G.; Mozer, A.J.; Scharber, M.; Arlauskas, K.; Sariciftci, N.S.; Stubb, H; Österbacka, R., *Phys. Rev. Lett.* **2005**, 94, 176806.
14. Ai, X.; Beard, M.C.; Knutsen, K.P.; Shaheen, S.E.; Rumbles, G.; Ellingson, R.J., *J. Phys. Chem.* **2006**, 110, 25462.
15. Peet, J.; Kim, J.Y.; Coates, N.E.; Ma, W.L.; Moses, D.; Heeger, A.J.; Bazan, G.C., *Nat. Mater.* **2007**, 6, 497.
16. Yang, X.; Loos, J.; Veenstra, S.C.; Verhees, W.J.H.; Wienk, M.M.; Kroon, J.M.; Michels, M.A.J.; Janssen, R.A.J., *Nano Lett.* **2005**, 5, 579.

17. Nguyen, L.H.; Hoppe, H.; Erb, T.; Günes, S.; Gobsch, G.; Sariciftci, N.S., *Adv. Funct. Mater.* **2007**, 17, 1071.
18. Ma, W.; Yang, C.; Gong, X.; Lee, K.; Heeger, A.J., *Adv. Funct. Mater.* **2005**, 15, 1617.
19. Kim, K.C.; Park, J.H.; Park, O.O., *Sol. Energy Mater. Sol. Cells* **2008**, 92, 1188.
20. Moulé, A.J.; Meerholz, K., *Adv. Mater.* **2008**, 20, 240.
21. Yao, Y.; Hou, J.; Xu, Z.; Li, G.; Yang, Y., *Adv. Funct. Mater.* **2008**, 18, 1783.
22. Schmidt-Mende, L.; Fechtenkötter, A.; Müllen, K.; Moons, E.; Friend, R.H.; MacKenzie, J.D., *Science* **2001**, 293, 1119.
23. Rispens, M.T.; Meetsma, A.; Rittberger, R.; Brabec, C.J.; Sariciftci, N.S.; Hummelen, J.C., *Chem. Commun.* **2003**, 2116.
24. Nishizawa, T.; Tajima, K.; Hashimoto, K., *Nanotechnology* **2008**, 19, 424017.
25. McNeill, C.R.; Westenhoff, S.; Groves, C.; Friend, R.H.; Greenham, N.C., *J. Phys. Chem. C* **2008**, 111, 19153.
26. Cook, S.; Furube, A.; Katoh, R., *Jap. J. Appl. Phys.* **2008**, 40, 1238.
27. Vanlaeke, P.; Vanhoyland, G.; Aernouts, T.; Cheyns, D.; Deibel, C.; Manca, J.; Heremans, P.; Poortmans, J., *Thin Solid Films* **2006**, 511, 358.
28. Mihailetchi, V.D.; Xie, H.; de Boer, B.; Popescu, L.M., Koster, L.J.A., *Appl. Phys. Lett.* **2006**, *89*, 012107.
29. Li, G.; Shrotriya, V.; Huang, J.; Yao, Y.; Moriarty, T.; Emery, K.; Yang, Y., *Nat. Mater.* **2005**, 4, 864.
30. Kim, Y.; Choulis, S.A.; Nelson, J.; Bradley, D.D.C.; Cook, S.; Durrant, J.R., *Appl. Phys. Lett.* **2005**, 86, 063502.
31. Adriaensens, P.; Dams, R.; Lutsen, L.; Vanderzande, D.; Gelan, J., *Polymer* **2004**, 45, 4499.
32. Yang, C.; Hu, J.G.; Heeger, A.J., *J. Am. Chem. Soc.* **2006**, 128, 12007.
33. Zhao, J.; Swinnen, A.; Van Assche, G.; Manca, J.; Vanderzande, D.; Van Mele, B., *J. Phys. Chem. B* **2009**, 113, 1587.
34. Swinnen, A.; Haeldermans, I.; vande Ven, M.; D'Haen, J.; Vanhoyland, G.; Aresu, S.; D'Olieslaeger, M.; Manca, J., *Adv. Funct. Mater.* **2006**, 16, 760.
35. Miyanishi, S.; Tajima, K.; Hashimoto, K., *Macromolecules* **2009**, 42, 1610.
36. Schilinsky, P.; Waldauf, C.; Brabec, C.J., *Adv. Funct. Mater.* **2006**, 16, 1669.
37. Tipnis, R.; Bernkopf, J.; Jia, S.; Krieg, J.; Li, S.; Storch, M.; Laird, D., *Sol. Energy Mater. Sol. Cells* **2009**, 93, 442.
38. Moon, J.S.; Lee, J.K.; Cho, S.; Byun, J.; Heeger, A.J., *Nano Lett.* **2009**, 9, 230.
39. van Bavel, S.S.; Sourty, E.; de With, G.; Loos, J., *Nano Lett.* **2009**, 9, 507.
40. Yang, X.; van Duren, J.K.J.; Rispens, M.T.; Hummelen, J.C.; Janssen, R.A.J.; Michels, M.A.J.; Loos, J., *Adv. Mater.* **2004**, 16, 802.
41. Hugger, S.; Thomann, R.; Heinzel, T.; Thurn-Albrecht, *Colloid polym. Sci.,* **2004**, 282, 932.
42. Erb, T.; Zhokhavets, U.; Gobsch, G.; Raleva, S.; Stühn, B.; Schilinsky, P.; Waldauf, C.; Brabec, C.J., *Adv. Funct. Mater.* **2005**, 15, 1193.
43. Vanlaeke, P.; Swinnen, A.; Haeldermans, I.; Vanhoyland, G.; Aernouts, T.; Cheyns, D.; Deibel, C.; D'Haen, J.; Heremans, P.; Poortmans, J.; Manca, J.V., *Sol. Energy Mater. Sol. Cells* **2006**, 90, 2150.

44. Bulle-Lieuwma, C.W.T.; van Gennip, W.J.H.; van Duren, J.K.J.; Jonkheijm, P.; Janssen, R.A.J.; Niemantsverdriet, J.W., *Appl. Surf. Sci.* **2003**, 203, 547.
45. Drees, M.; Hoppe, H.; Winder, C.; Neugebauer, H.; Sariciftci, N.S.; Schwinger, W.; Schäffler, F.; Topf, C.; Scharber, M.C.; Zhu, Z.; Gaudiana, R., *J. Mater. Chem.* **2005**, 15, 5158.
46. Aasmundtveit, K.E.; Samuelsen, E.J.; Guldstein, M.; Steinsland, C.; Flornes, O.; Fagermo, C.; Seeberg, T.M.; Pettersson, L.A.A.; Inganäs, O.; Feidenhans'l, R.; Ferrer, S., *Macromolecules* **2000**, 33, 3120.
47. Erb, T.; Raleva, S.; Zhokhavets, U.; Gobsch, G.; Stühn, B.; Spode, M.; Ambacher, O., *Thin Solid Films* **2004**, 450, 97.
48. Chen, T.; Wu, X.; Rieke, R.D., *J. Am. Chem. Soc.* **1995**, 117, 233.
49. Chambon, S.; Oosterbaan, W.; Vrindts, V.; Mens, R.; Ruttens, B.; Lutsen, L.; Vanderzande, D.; Adriaensens, P., *Effect of the Alkyl Side-Chain Length on the Organization of Poly(3-alkylthiophene): a Combined NMR and XRD Study,* in preparation.
50. Chiu, M-Y.; Jeng, U-S.; Su, M-S.; Wei, K-H., *Macromolecules* **2010**, 43, 428.
51. Kalita, G.; Masahiro, M.; Koichi, W.; Umeno, M., *Solid State Electron.* **2009**, available online.
52. Kim, J. Y.; Frisbie, C.D., *J. Phys. Chem. C* **2008**, 112,17726.
53. Ma, W.; Kim, J.Y.; Lee, K.; Heeger, A.J., *Macromol. Rapid. Commun.* **2007**, 28, 1776.
54. Yamamoto, T.; Komarudin, D.; Arai, M.; Lee, B.; Suganuma, H.; Asakawa, N.; Inoue, Y.; Kubota, K.; Sasaki, S.; Fukuda, T.; Matsuda, H., *J. Am. Chem. Soc.* **1998**, 120, 2047.

Summary & General Conclusion

Both the growing awareness of the limited supply of fossil fuels and the observed climatic changes all over the world have triggered great attention for environmentally friendly and inexpensive renewable energy sources in as well the political as scientific community. Nowadays lots of techniques and sources are explored of which some are already commercialized, others are still in early stages. Among these applications there is an extensive attention for solar energy because the sun is an inexhaustible source. Two approaches are possible to harness this carbon-free source of energy. In the case of solar cells, solar energy is converted into an electric current. Another basic concept is to focus the sunlight by a series of mirrors and subsequently create steam that can drive turbines. Regarding solar cells currently a lot of research is focussed on plastic solar cells as a possible cheaper alternative for their already commercial inorganic counterparts.

In **chapter 1** a short historical background and a definition of organic solar cells are presented. The devices characteristics are discussed and the in the field encountered planar-multilayered architectures are listed. The major component of such a plastic solar cell consists of a thin photoactive layer in which the photovoltaic process occurs. The description of the cells is based on the so-called bulk hetero junction (BHJ) configuration as a model for the photoactive film, but the general principles apply as well to other types of configurations. Furthermore the energy conversion process, starting with the absorption of a photon by the conjugated polymer and eventually resulting in the release of holes and electrons at the respective electrodes, is discussed in detail. The interplay between the power conversion efficiency of the device and the nanostructured morphology of the photoactive film is considered. However, the state-of-the-art maximum efficiency for plastic solar cells of about 6.8 % has to be increased significantly before production and commercialization on a large scale becomes realistic. From that point of view the morphology of the active layer is one of the primary factors which determine the efficiency. Therefore it is important to have dedicated methods to evaluate, describe and quantify the state of the phase morphology in these active layers. The main goal of this work is a study to evaluate the

possibilities of solid-state NMR spectroscopy and relaxometry as a complementary and innovative method in this field of science.

The physical basis of NMR spectroscopy and relaxometry is summarized in **chapter 2.** First it is explained how a NMR signal is created and detected. Next, the meaning of the different relaxation decay times is described and it is discussed how these experimental parameters can be measured by means of several solid-state NMR techniques like proton wide-line, ^{13}C MAS en ^{13}C CP/MAS NMR. Contiguous it is explained, including the important phenomenon of spin diffusion, how the obtained information can be used in order to describe the nanostructured morphology of the active films in plastic solar cells.

Historically, MDMO-PPV/fullerene blends belong to the first extensively studied BHJ donor/acceptor (D/A) systems and are still often considered as 'work-horse or reference system' for organic polymer based solar cells. It is well known from literature that toluene as casting solvent significantly enhances the phase separation of PCBM in these composite films. **Chapter 3** describes this phase separation between MDMO-PPV and PCBM in toluene-casted blends by means of proton wide-line NMR. The influence of parameters like the D/A blend composition and casting technique (spin-coating versus doctor blading) on the film morphology are discused. The NMR relaxometry results furnish an estimation of the average minimum dimension as well as a quantification of the phase separated PCBM crystallites. The high degree of PCBM crystallinity is rationalized via the observation of very long relaxation decay times. In addition, the findings done by NMR are in very good agreement with conventional techniques like TEM, AFM en XRD. However, so-called PCBM nanocrystals were also detected by T_{1C} relaxation time measurements in films which look homogeneous on TEM images (e.g. 50 wt% PCBM films). Differences between the two casting techniques are noticed on account of the solvent evaporation rate, which is much slower for the doctor blade technique. E.g. the well-defined crystallites present in 20/80 wt% films casted with both techniques have roughly the same average dimension but a doubled amount and an improved quality (less defects) of the PCBM crystallites is detected in case of doctor blading.

As will be demonstrated in the contiguous chapters, the description of the nanomorphology of other D/A systems can be more complex. Therefore it was decided to study first the relaxation behavior of the electron acceptor PCBM in more detail in **chapter 4**. In addition it is shown that purchased PCBM contains a

significant amount of *ortho*-dichlorobenzene (next to other minor impurities) and a straightforward method to purify it is offered. A number of different samples were prepared in order to obtain fully amorphous PCBM. Although, the lack of very long relaxation decay times for these samples implies the absence of well-defined PCBM crystals, the nanomorphology is defined as being one in which nanocrystals are imbedded in an amorphous PCBM phase. By means of proton wide-line NMR it is only possible to provide a dimensional interval for the PCBM nanocrystals, supported by DSC and XRD measurements. In order to give a more detailed description of the nanostructured morphology we invoked on the local and chemical shift selective ^{13}C MAS NMR technique. A further refinement of the, by proton wide-line NMR provided dimensional interval, could be derived based on the value of the intermediate T_{1C} relaxation decay time obtained via ^{13}C MAS. This conclusion was strengthened by complementary XRD measurements. A quantification of the amount of PCBM nanocrystals is furnished via the fraction corresponding to this intermediate T_{1C} relaxation decay time. This conclusion is qualitatively (due to cold crystallization) supported by DSC.

Chapter 5 focuses on MDMO-PPV/PCBM films casted from chlorobenzene solutions. Nonetheless TEM images of films with high PCBM content clearly shows phase separated domains, no long relaxation decay times were detected. In addition, more or less the same results were noticed by wide-line NMR for the two casting techniques. Films obtained by doctor blading were further studied by ^{13}C MAS. Once more the amount of PCBM nanocrystals in the composite films could be quantified via the fraction of the intermediate T_{1C} decay time. For films with high PCBM content this quantification could be confirmed via the fraction corresponding to the intermediate $T_{1\rho H}$ decay time as determined by means of much faster ^{13}C CP/MAS relaxometry experiments. The 50/50 wt% films, looking quite homogeneously on TEM images, also contain PCBM nanocrystals of which the amount could be quantified by the fraction of the intermediate T_{1C} as well, as supported by DSC. For films with low PCBM content (e.g. 80/20 wt% films) on the other hand, the presence of nanocrystals could only indirectly be detected via ^{13}C MAS.

Last but not least, **chapter 6** deals with the nanostructured morphology of thin P3HT/PCBM films, native as well as post production thermally annealed, obtained by doctor blading. A first screening by optical microscopy of chlorobenzene-casted films showed, independently of the blend composition and

for annealing temperature below 150 °C, a quite homogeneous morphology, i.e. the absence of large-scale phase separation. However for all blend compositions studied, needle-like structures start to form at an annealing temperature of 150 °C. TEM images further demonstate that annealing above 150 °C results in an enhanced interpenetrating network of P3HT fibres and PCBM. The presence of PCBM nanocrystals in the P3HT/PCBM matrix, or in other words the incomplete phase separation of PCBM into the observed needle-like structures, was revealed by SAED analysis of this matrix. Analysis of the SAED patterns of these PCBM needles on the other hand resulted in clear electron-diffraction patterns composed of well-aligned spots which is a strong indication that these needles, at least partially, consist of PCBM single crystals. However, the regular electron diffraction pattern is superimposed onto a blurred ring pattern. The hypothesis that the PCBM needles are exclusively build from large single crystals was further negated by the absence of very long NMR relaxation decay times. Only for films with high PCBM content and annealed at 175 °C, the T_{1H} relaxation behaves bi-exponentially, albeit with a short and intermediate decay time. The intermediate decay time of 2 s is representing the PCBM needles. Based on the value of this intermediate time constant and XRD it could be decided that the needle-like PCBM stuctures consist of single crystals which are surrounded by a mesoscopic low order PCBM phase. In order to quantify the amount of PCBM crystals in composite films we once more took advantage of the ^{13}C MAS technique. In case of films which showed no PCBM needles in optical microscopy images, the amount of the intermediate T_{1C} relaxation time could be attributed to the PCBM nanocrystals that are dispersed in the film matrix. For films which showed phase separation on the other hand, the intermediate T_{1C} represents the nanocrystals in the P3HT/PCBM matrix as well as single crystals in the needle-like structures. P3HT/PCBM 1/4 films processed from toluene solutions did not show long relaxation decay times. This indicates that not only the film casting solvent but also the nature of the polymer primarily determines wether or not wel-defined PCBM crystallites are formed. A comparison of the relaxation characteristics for P3HT/PCBM films with 1/1 weight ratio processed from chlorobenzene and toluene revealed that roughly the same decay times were attained for native toluene films as for annealed chlorobenzene films, nonetheless the fact that no PCBM needles were noticed in the former. This means that already a higher amount of crystallinity (nanocrystals) is present in the native toluene-casted films, which was corroborated by comparing

the power conversion efficiencies of plastic solar cells in which the photoactive layer was prepared by doctor blading. The PCE of devices in which native toluene-casted films were used as active layer are already approaching the PCE of annealed-chlorobenzene-casted devices. Finally photovoltaic cells in which purified or as-received PCBM was used were constructed. Surprisingly cells build from purified PCBM yielded the best efficiencies. This indicates that it is highly beneficial to purify the PCBM by a simple precipitation in acetone.

As a **general conclusion** it can be stated that the nanostructured morphology of BHJ D/A systems can be very complex. Hereby the electron acceptor PCBM can appear in several fysico-chemical states like e.g. well-defined crystallites, nanocrystals, needle-like structures consisiting of single crystals surrounded by mesoscopic low-order PCBM as well as in the amorphous state. The film morphology originates from the complex interplay between the PCBM, the film casting solvent and the donor polymer. Only D/A systems for which large well-defined PCBM crystallites are observed, as for MDMO-PPV/PCBM films casted from toluene solutions, can be accurately described and quantified by means of solid-state ^{1}H wide-line NMR relaxometry. However, a satisfactory description of the nanomorphology of more complex D/A systems requires, in addition to ^{13}C MAS relaxometry, a combination of analytical techniques like TEM, XRD, DSC, SAED, … In conclusion, NMR results can provide a valuable supplement to the (quantitative) description of the nanomorphology of photoactive layers used in OPVs. Nevertheless each individual D/A system needs a set of complementary techniques in order to describe, and so to optimize, the nanostructured film morphology.

Samenvatting & algemeen besluit

De wereldwijde vraag naar energie ligt nog steeds in stijgende lijn, hoofdzakelijk vanwege de ontwikkeling van economische groeipolen zoals China, India, Zuid-Afrika, Brazilië, enz… Echter de eindige voorraden aan fossiele brandstoffen en de verwachte problemen ten gevolge van het broeikaseffect hebben in zowel de politieke als academische wereld een groeiend moreel besef doen ontstaan aan de noodzaak voor milieuvriendelijke alternatieven om aan deze energiebehoefte te voldoen. Een van de mogelijkheden hiertoe is gebruik te maken van zonne-energie. Voor het oogsten van deze onuitputtelijke bron zijn twee benaderingen mogelijk. Enerzijds kan men zonnelicht omzetten in elektrische stroom (de zogenaamde zonnecellen), anderzijds kan zonne-energie gebruikt worden om stoom te produceren. Wat betreft de zonnecellen wordt er tegenwoordig veel onderzoek gedaan omtrent organische cellen als mogelijk goedkoper alternatief voor de reeds commerciële anorganische tegenhangers.

In **hoofdstuk 1** werd een korte historische schets gegeven en werd er gespecifieerd wat organische zonnecellen juist zijn. Hierbij werden de relevante cel karakteristieken gedefinieerd en de mogelijke architecturen opgesomd. Het hart van zulke cel is een dunne fotoactieve laag waarin het fotovoltaische proces gebeurt. Voor de beschrijving van de zonnecellen maakten we gebruik van de zogenaamde “bulk hetero junction” (BHJ) configuratie als model voor deze fotoactieve laag. Eveneens werd het energie omzettingsproces, startend met de opname van een foton tot de uiteindelijke vrijgave door middel van ladingsdragers aan de elektrodes, in detail besproken. Verbanden werden gelegd tussen het rendement van de cel en de nanogestructureerde morfologie van de actieve film. Het is immers zo dat het rendement van de huidige generatie van organische zonnecellen onvoldoende is opdat deze vanuit commercieel standpunt een realistisch antwoord op de vraag naar energie zouden kunnen geven. De morfologie van de actieve laag is één van de belangrijke factoren die het rendement bepalen. Het is daarom belangrijk om over specifieke methoden te beschikken die ons in staat stellen deze morfologie te beschrijven en te kwantificeren. Het doel van deze thesis was dan ook een studie naar de mogelijkheden van een complementaire en innovatieve methode gebaseerd op vaste stof NMR technieken.

De fysische basis van NMR spectroscopie en relaxometrie werd weergegeven in **hoofdstuk 2**. De nadruk lag op relaxatietijden en hoe deze bepaald kunnen worden aan de hand van verschillende vaste stof NMR technieken zoals proton wide-line, ^{13}C MAS en ^{13}C CP/MAS NMR. Ook werd uitgelegd, met inbegrip van het belangrijke fenomeen van spin diffusie, hoe de bekomen informatie gebruikt kan worden om de morfologie van de actieve film in zonnecellen te beschrijven.

MDMO-PPV/PCBM films, historisch gezien één van de eerst bestudeerde BHJ donor/acceptor (D/A) systemen, worden nog steeds beschouwd als referentie voor polymeer-gebaseerde organische cellen. Het is gekend dat fasescheiding van PCBM plaatsgrijpt in zulke actieve filmen met een hoog PCBM gehalte (≥ 70 m/m %). **Hoofdstuk 3** beschreef deze PCBM segregatie voor filmen gevormd uit tolueen oplossingen aan de hand van proton wide-line NMR relaxometrie. De invloed van experimentele parameters zoals D/A verhouding en filmvormingstechniek (spin-coating of doctor blading) op de morfologie kwamen aan bod. De NMR resultaten laten zowel een goede schatting van de minimale afmetingen als een kwantitatieve bepaling van de hoeveelheid PCBM in fasescheiding toe. De hoge graad van kristalliniteit van deze fasegescheiden PCBM wordt vertaald in zeer lange relaxatietijden. De NMR bevindingen zijn bovendien in goede overeenstemming met deze bekomen door meer conventionele technieken zoals TEM, AFM en XRD. Echter, ook in filmen die homogeen lijken op TEM beelden (vb. 50 m/m % PCBM) werd de aanwezigheid van zogenaamde PCBM nanokristallen aangetoond via T_{1C} relaxatiemetingen. Verschillen in nanomorfologie tussen filmen gevormd via spin-coating en doctor blading werden waargenomen omwille van een verschil in verdampingssnelheid gedurende de filmvorming: bvb. de kristallen in de 80 m/m % PCBM filmen hadden in beide gevallen wel dezelfde gemiddelde afmetingen, doch een verdubbelde hoeveelheid en hogere perfectie werden waargenomen voor de kristallen in geval van doctor blading.

Omdat de film morfologie in de meeste gevallen veel complexer is, werd geopteerd om eerst het relaxatiegedrag van de acceptor PCBM zelf in detail te bestuderen. In **hoofdstuk 4** werd aangetoond dat aangekochte PCBM een aanzienlijke hoeveelheid *ortho*-dichloorbenzeen (naast andere kleine onzuiverheden) bevat en hoe men deze eenvoudig kan verwijderen. Desondanks zijn grote kristallen erin aanwezig. Bewerkingen om volledig amorfe PCBM te

bekomen resulteerden in een reeks stalen waarin geen lange relaxatietijden werden gedetecteerd en dus geen uitgesproken PCBM kristallieten aanwezig zijn. De morfologie kan worden omschreven als PCBM nanokristallen die verspreid zijn in een amorfe PCBM fase. Met behulp van wide-line NMR was het alleen mogelijk een schatting te maken van de minimale en maximale afmetingen van deze PCBM nanokristallen. DSC en XRD metingen ondersteunen deze schatting. Om de nanogestructureerde morfologie verder in detail te beschrijven werd een beroep gedaan op vaste stof ^{13}C MAS NMR. Steunend op de waarde van de gemeten intermediaire T_{1C} relaxatietijd kan men de geschatte dimensies verder verfijnen en de hoeveelheid van deze PCBM nanokristallen kwantitatief bepalen aan de hand van de corresponderende fractie.

Hoofdstuk 5 behandelde MDMO-PPV/PCBM filmen gevormd vanuit chloorbenzeen oplossingen. Niettegenstaande TEM beelden van filmen met hoge PCBM inhoud duidelijk fasescheiding vertonen, werden er geen zeer lange relaxatietijden gedetecteerd. Bovendien geven de 2 filmvormingstechnieken (spin-coating en doctor blading) hier hetzelfde resultaat. De films bekomen met behulp van doctor blading worden verder bestudeerd via ^{13}C MAS. Ook hier konden de aanwezige PCBM nanokristallen gekwantificeerd worden aan de hand van de fractie behorende bij de intermediaire T_{1C} relaxatietijd. Voor filmen met hoge PCBM inhoud kon deze hoeveelheid aan nanokristallen bevestigd worden via de fractie van de intermediaire $T_{1\rho H}$ relaxatietijd bepaald door ^{13}C CP/MAS metingen. Ook de 50/50 m/m % filmen, die op TEM beelden een vrij homogene morfologie lijken te bezitten, bevatten nanokristallen zoals gemeten via de intermediare T_{1C} relaxatietijd en ondersteund door DSC. Voor filmen gemaakt met weinig PCBM (vb. 80/20 m/m % filmen) kon de aanwezigheid van PCBM nanokristallen alleen onrechtstreeks gedetecteerd worden met behulp van ^{13}C MAS relaxometrie.

Tenslotte werd in **hoofdstuk 6** de nanomorfologie van dunne P3HT/PCBM filmen vervaardigd door doctor blading bestudeerd. Zowel natieve als thermisch geannealde filmen kwamen aan bod. Een eerste screening voor filmen gevormd uit chloorbenzeen oplossingen door middel van optische microscopie bracht een vrij homogene nanomorfologie (althans op deze schaal) aan het licht ongeacht de samenstelling, zolang de annealingstemperatuur onder 150 °C blijft. Vanaf 150 °C ontstaan er in de film grote naaldvormige PCBM structuren. Dit laatste werd aangetoond aan de hand van optische microscopie en TEM beelden. Niet alle PCBM is echter fasegescheiden in naaldvormige structuren. Dat er daarnaast ook

nog PCBM nanokristallen aanwezig zijn in de P3HT/PCBM matrix werd aangetoond in de SAED patronen van deze matrix. SAED analyse van de naalden resulteerde (gedeeltelijk) in regelmatige puntpatronen, wat een indicatie is voor de aanwezigheid van PCBM éénkristallen. Echter, de hypothese dat de PCBM naalden volledig zijn opgebouwd uit zuivere kristallen werd ontkracht door het niet waarnemen van zeer lange relaxatietijden. Voor filmen met hoge PCBM inhoud die geanneald werden op 175 °C gedraagt de T_{1H} relaxatie zich bi-exponentieel, zij het met een korte en een intermediare relaxatietijd. De intermediaire tijdsconstante van 2 s vertegenwoordigt de PCBM naalden. Gebaseerd op de waarde van deze intermediaire relaxatietijd en XRD kon besloten worden dat deze naaldvormige structuren zijn opgebouwd uit éénkristallen van PCBM die omgeven zijn door een mesoscopische lagere-orde PCBM fase. Voor een kwantificering van de PCBM kristallen werd opnieuw een beroep gedaan op de intermediare T_{1C} relaxatietijd, bepaald door ^{13}C MAS. Voor filmen die homogeen lijken op optische microscopie beelden staat deze laatste voor PCBM nanokristallen verspreid in de film. Anderzijds voor filmen die naaldvormige PCBM structuren vertonen, vertegenwoordigt deze intermediaire T_{1C} zowel de PCBM nanokristallen in de P3HT/PCBM matrix als de PCBM éénkristallen in de fasegescheiden naalden. P3HT/PCBM 1/4 filmen gemaakt vanuit tolueen vertoonden eveneens geen zeer lange relaxatietijden. Dit betekent dat niet enkel het oplosmiddel gebruikt voor de filmvorming maar ook de aard van het polymeer bepalen of er al dan niet grote PCBM kristalstructuren gevormd worden. Een vergelijkende studie tussen de NMR relaxatietijden, bekomen voor filmen met gewichtsverhouding 1/1 gemaakt vanuit chloorbenzeen en tolueen, onthulde dat ruwweg dezelfde relaxatietijden worden bekomen voor de “natieve tolueen” en de “geannealde chloorbenzeen” filmen. Dit niettegenstaande er geen PCBM naalden aanwezig zijn in filmen gemaakt vanuit tolueen als oplosmiddel. Dit wijst erop dat er reeds van nature een grotere hoeveelheid kristalliniteit (nanokristallen) aanwezig is in de “natieve tolueen” filmen, hetgeen gestaafd werd door de verhoogde performantie van zonnecellen gebaseerd op “natieve tolueen” filmen die reeds de performantie van zonnecellen gemaakt met “geannealde chloorbenzeen” filmen benaderd. Tenslotte werd ook de invloed van de PCBM zuiverheid op de performantie van zonnecellen nagegaan. Verrassend leverden de cellen met de gezuiverd PCBM de beste rendementen op. Dit betekent dat PCBM best eerst gezuiverd wordt door eenvoudige precipitatie in aceton.

Als **algemeen besluit** kunnen we stellen dat de nanogestructureerde morfologie in BHJ D/A systemen zeer complex kan zijn. Wat betreft de acceptor PCBM kan deze laatste voorkomen in meerdere fysico-chemische toestanden zoals o.a. in grote kristallieten, nanokristallen, naaldachtige structuren bestaande uit éénkristallen omgeven door mesoscopische lagere-orde PCBM als ook in de amorfe toestand. De uiteindelijke film morfologie komt tot stand door een onderlinge wisselwerking tussen zowel PCBM, het oplosmiddel voor filmvorming en het donor polymeer. Alleen D/A systemen waarin grote PCBM kristallieten ontstaan, zoals in het geval van MDMO-PPV/PCBM filmen gevormd uit tolueen oplossingen, kunnen voldoende nauwkeurig beschreven en gekwantificieerd worden met behulp van ^{1}H wide-line NMR relaxometrie. Echter, de volledige beschrijving van de nanomorfologie van meer complexe D/A systemen vereist naast ^{13}C MAS relaxometrie een combinatie van conventionele technieken zoals TEM, XRD, DSC, SAED, …. Dus algemeen kan besloten worden dat NMR gegevens een waardevolle aanvulling zijn voor de (kwantitatieve) beschrijving van de film morfologie van de fotoactieve laag van OPV's, maar dat ieder systeem best wordt bestudeerd met de nodige complementaire technieken om een goed beeld, en dus optimalisatie, van de nanomorfologie te bekomen.

List of Abbreviations

AFM	atomic force microscopy
AM	air mass
B_0	external magnetic field
$2B_1 / B_1^- / B_1^+ / B_1$	magnetic fields
BB	broad band
B_{eff}	effective field
BHJ	bulk heterojunction
B_{loc}	local field
C_{60}	buckminsterfullerene
CP/MAS	cross polarization
CSA	chemical shift anisotropy
CW	continuous-wave
D	spin-diffusion coefficient
D/A	donor/acceptor
DD	dipolar decoupling
δ_{iso}	isotropic chemical shift
ΔB	reduced magnetic field in the rotating frame
$\Delta\nu_{1/2}$	peak-width-at-half-heigt
DSC	differential scanning calorimetry
η_e	power conversion efficiency
ESR	electron spin resonance
EQE	external quantum efficiency
FF	fill factor
FID	free induction decay
FTPS	fourier-transform photocurrent spectroscopy
γ	gyromagnetic ratio
HF	heat flow
HOMO	highest occupied molecular orbital
H_{CS}	chemical shift Hamiltonian
I	spin quantum number
IPCE	incident photon to current efficiency
I_{SC}	short-circuit current
ITO	indium tin oxide
J_{SC}	short-circuit current density
J-V curve	current density-voltage curve
L	diffusive path length
LED	light-emitting diode
LUMO	lowest unoccupied molecular orbital
$\vec{M}_0$	macroscopic magnetization vector
MAS	magic angle spinning
MDMO-PPV	poly(2-methoxy-5-(3',7'-dimethyloctyloxy)-1,4-phenylene vinylene)

MEH-PPV	poly(2-methoxy-5-((2'-ethylhexyloxy)-1,4-phenylene vinylene)
$\vec{\mu}$	magnetic moment
NMR	nuclear magnetic resonance
ω_0	Larmor frequency
ω_i	resonance frequency
OPV	organic photovoltaic
oTFT	organic thin film transistor
P3HT	poly-3-hexylthiophene-2,5-diyl
PCBM	[6,6]-phenyl-C_{61}-butyric acid methyl ester
PCDTBT	poly[2,6-(4,4-bis-(2-ethylhexyl)-4H-cyclopenta[2,1-b;3,4-b']-dithiophene)-alt-4,7-(2,1,3-benzo-thiadiazole)]
PCE	power conversion efficiency
PIA	photoinduced absorption
P_{in}	power originating from the incident sunlight
pLED	polymeric light-emitting diode
p-n junction	p-type / n-type junction
r	internuclear distance
RF	radiofrequency
σ_i	shielding constant of nucleus i
SAED	selected-area electron diffraction
SEM	scanning electron microscopy
Ω_0	precessional frequency in the rotating frame / offset / centre frequency
θ	angle between the vector joining the spins with respect to B_0
TEM	transmission electron microscopy
T_1	spin-lattice or longitudinal relaxation decay time constant
$T_{1\rho}$	spin-lattice relaxation decay time constant in the rotating frame
T_2	spin-spin or transverse relaxation decay time constant
T_g	glass transition temperature
TGA	thermal gravimetric analysis
t_{SL}	spin-lock time
τ_C	correlation time
τ_p	the duration of the pulse B_1
V_{OC}	open circuit voltage
wt%	weight percentage
XRD	X-ray diffraction

Dankwoord

Het is passend om bij de voltooiing van deze thesis een gemeend dankwoord te richten tot een aantal personen die belangrijk zijn geweest bij de totstandkoming ervan. Het begon allemaal ongeveer 14 jaar geleden toen ik besliste om terug te studeren, de leraren van de avondopleiding graduaat scheikunde Gunther Decock, Gert Hurkmans en Luk Luyten bedank ik voor het opfrissen van mijn basiskennis na een sabbatperiode van 10 jaar. Niettegenstaande het maar "avondschool" was werd een hoog niveau van onderwijs aangeboden, bovendien stimuleerde Gert Hurkmans mij om verder te gaan studeren aan de universiteit. Verder wil ik de vrienden van de kandidaturen scheikunde aan de Uhasselt en deze van de licenties aan de KU Leuven bedanken voor de toffe kameraadschap en voor de nodige nota's die ze mij terbeschikking stelden indien ik de lessen niet kon volgen. Ook de proffen van de KU Leuven ben ik erkentelijk voor de steun na mijn ernstig auto-ongeval.

Nu we aan "het doctoraat" zelf gekomen zijn, wil ik in de eerste plaats Peter Adriaensens, mijn promotor, en Jan Gelan, mijn co-promotor, bedanken. Bedankt voor het vertrouwen en de grote mate van vrijheid die jullie mij geschonken hebben en voor de uitstekende wetenschappelijke begeleiding de voorbije jaren. In het begin was het niet gemakkelijk om te werken met de ingewikkelde NMR apparatuur, maar uiteindelijk is het toch enigszins gelukt. Naast de waardevolle tips en vele discussies wil ik jullie ook uitvoerig bedanken voor het zorgvuldig doornemen van artikels en presentaties, alsook het leesbaar maken van deze thesis in de Engelse taal. Voor de financiële steun heb ik gedurende de voorbije 6 jaar kunnen rekenen op de Universiteit Hasselt, waarvoor ik natuurlijk zeer erkentelijk ben. Robert Carleer bedank ik voor de financiële steun tijdens een voorafgaand overbruggingsjaar; ik heb ook zeer veel plezier beleefd aan de vele grappen en het uitwisselen van verhalen betreffende de gemaakte bergvakanties.

De voorbije bijna 6.5 jaar heb ik steeds een heel toffe en aangename werksfeer kunnen ervaren. Ik heb hierbij eigenlijk nooit het gevoel gehad dat ik echt aan het werken was, zeker met de vele andere jobs die ik reeds gedaan had zoals metaalarbeider, winkelbediende, magazijnier en produktiearbeider als referentiepunt in gedachte. Dit goede gevoel werd mede gemaakt door de leuke

contacten met de vele vrienden, collega's en proffen niet alleen van de onderzoeksgroep Organische en Polymere Scheikunde, maar ook van de andere onderzoeksgroepen (TOES, anorganische en de materiaal fysici), het secretariaat SBG en didactiek Scheikunde. Het opsommen van al de personen die gedurende deze 6.5 jaar mijn pad gekruisd hebben zou dan ook een enorme lijst opleveren; om niet het risico te lopen er enkele te vergeten zal ik dit dan ook niet doen. Toch wil ik iedereeen via deze van harte bedanken. Toch wil ik mijn dank extra benadrukken aan de drie personen die, naast Peter, een grote bijdrage hebben geleverd aan dit werk. Ten eerst aan Koen Van Vinckenroye. Koen, je hebt mij niet alleen de basis van vloeistof NMR uitgelegd, maar ook een oneindig aantal keren geholpen met allerlei informatica problemen en wanneer ik een of andere NMR toestel niet aan de praat kreeg. Ook Guy Reggers wil ik bedanken voor de vele DSC's, die uiteindelijk een grote meerwaarde gegeven hebben aan de inhoud van dit werk. Tenslotte gaat mij grote dank uit aan Sabine Bertho. Sabine, jouw vele bijdrages hebben dit werk enorm verrijkt. Niet alleen kon ik rekenen op de talloze TEM en SAED opnames, ook ben ik blij dat we op het einde nog een aantal zonnecellen via doctor blading hebben kunnen maken. De snelle respons via mail op de vele vragen die ik je stelde was tevens zeer leerzaam. Nogmaals Koen, Guy en Sabine bedankt!
Tot slot wil ik ook mijn ouders, broers, overige familie en vrienden even bedanken voor hun steun en interesse in hetgeen ik de laatste jaren allemaal heb uitgespookt. Ik weet dat jullie zeer trots op mij zijn.

Bedankt allemaal!